Theoretical investigation of photon manipulation for quantum computing and quantum information processing

by

Chenxu Liu

B.S. in Physics, Nankai University, 2013

Submitted to the Graduate Faculty of

the Dietrich School of Arts and Sciences in partial fulfillment

of the requirements for the degree of

Doctor of Philosophy

University of Pittsburgh

2020

UNIVERSITY OF PITTSBURGH

KENNETH P. DIETRICH SCHOOL OF ARTS AND SCIENCES

This dissertation was presented

by

Chenxu Liu

It was defended on

June 16th 2020

and approved by

David Pekker, Assistant Professor, Department of Physics and Astronomy

M.V. Gurudev Dutt, Associate Professor, Department of Physics and Astronomy

Roger Mong, Assistant Professor, Department of Physics and Astronomy

Arthur Kosowsky, Professor, Department of Physics and Astronomy

Paul Leu, Associate Professor, Swanson school of Engineering

Dissertation Advisors: David Pekker, Assistant Professor, Department of Physics and Astronomy,

M.V. Gurudev Dutt, Associate Professor, Department of Physics and Astronomy

Theoretical investigation of photon manipulation for quantum computing and quantum information processing

Chenxu Liu, PhD

University of Pittsburgh, 2020

Quantum computing and quantum information processing are fast developing fields. As more and more qubits are integrated into the quantum computing systems, a deeper understanding and more careful modeling of the dynamics of these quantum systems in presence of driving and/or loss are necessary, not only for optimizing existing quantum devices, but also for designing and achieving novel method for more precise manipulation of these quantum systems. Our work investigating these quantum systems is inspired by quantum optics, a field focused on the quantum description of light and light-matter interactions.

In this thesis, we use the theoretical toolboxes provided by quantum optics as well as condensed matter theory to investigate and model realistic quantum systems. Specifically, we focus on the Nitrogen-vacancy centers in diamond crystal, a Josephson parametric amplifier (that uses Josephson junctions as its non-linear elements), and plasmonic nanowire system. With the knowledge of the dynamics of these systems, we proposed single-photon heralded two-NV center quantum gates; designed and optimized the superconducting circuit for a Josephson parametric amplifier to improve the amplifier's saturation power; and designed new methods for robust light manipulation using topologically protected plasmonic modes. All the devices that we study are either ready to be implemented in experiments or have already been built. Further, as discussed in this thesis, our theoretical analysis of NV-centers can be extended to similar device types like solid-state defect centers, while our analysis of Josephson parametric amplifiers can be extended to other types of superconducting circuit systems.

Table of contents

List of tables

List of figures

1.0 Introduction

The central topic of this thesis is the application of the tools of quantum optics to quantum computers and other quantum information processing devices.

The creation of the laser, a much more coherent light source as compared to most light sources that preceded it, highlighted the quantum nature of light and light-matter interaction. Consequently, there has been significant work on the development of quantum optics, a subject that studies the quantum nature of light and the light-matter interaction. Specifically, quantum optics focuses on the full quantum theory for systems that have loss and decoherence; a set of powerful theoretical tools is provided to understand and model driven-dissipative systems. With a better understanding of light-matter systems, more precise quantum manipulations can be applied to different quantum systems to prepare the system into a specific quantum states, to perform gate operations, information processing, etc.

Quantum computers are expected to use the power of quantum entanglement to achieve significant speedup as compared to classical computers. Ever since the idea of using quantum computers to simulate quantum systems was proposed in 1981 by Richard Feynman [1], the development of quantum computing systems that are able to perform reliable calculations is one of the dreams of several generations of physicist.

The speedup that can be achieved by quantum computers can be quantified by investigating computational complexity. In Section 1.1, we will briefly introduce the computational complexity classes in computation theory. We describe computational complexity classes of classical and quantum computers and highlight where quantum computing brings significant speedup as compared to classical computing.

Achieving fault tolerant quantum computing is not only significant to solve some the hard problems in classical computation theory, but is also important, via simulation of quantum systems [2, 3], for providing better understanding of nature itself, e.g. to understand thermalization of highly disordered systems [4, 5, 6, 7], the excited states of many-body strong correlated systems and black hole physics [8, 9, 10]. Over the past decade the pace of quantum computing research has significantly accelerated, and moved into industrial labs (See

Table. 1). The latest state-of-the-art quantum computing systems have up to 54 qubits, although these are still quite noisy. Last year, a Google machine performed a complex computing task that is impossible to achieve in a realistic time with classical computers [11] achieving so-called "quantum supremacy". However, there are significant unsolved problems on our road toward large-scale, fault tolerant quantum computer for reliable quantum simulation and algorithms. What's more, there does not exist solid answers for the questions which system, e.g. superconducting qubit systems, cold atoms systems or other systems, and which method, directly coupling or via intermediate particles and measurements, for gate operation is the best quantum system and gate schemes for fault-tolerant quantum computing. To pave the road for a practical quantum computer, on one hand, the new error correction schemes for quantum computing systems are required to fight against the quantum loss channels, on the other hand, a more thorough understanding of the dynamics of the qubits with couplings and novel methods to efficiently and precisely control the qubits are required. Quantum optics, which also focus on the driven-dissipative systems, provides the toolbox to understand and analyze these physical systems.

While in the process of construction of quantum computers, since the loss and decoherence of the quantum system cannot be fully eliminated, the quantum signal can have low signal-to-noise ratio. Further, to readout the calculation result from a quantum computer, usually requires precise detection of the quantum states of the qubits. The investigation of how to robustly transmit, manipulate and precisely acquire quantum information (detect the states of the qubits) of the quantum systems are becoming increasingly significant.

On the road towards the goal of quantum computing, the understanding of the physical system is essential to know the limitation of the system itself and optimize the physical system for better computing and information processing capabilities. In this thesis, we apply the theoretical tools, including quantum optics and other condensed matter techniques, to three specific physical systems, (1) Nitrogen-Vacancy centers in diamond crystal, (2) superconducting circuits and (3) nano-plamonc systems. In these quantum systems, we apply the theoretical tools, especially the quantum optics, to build deeper understanding and modeling of these physical systems and using these knowledge to achieve (1) quantum gate operation for the qubits made by NV center electronic states, (2) understanding and

Table 1: A list of major quantum computing projects of commercial companies. The qubit number is based on the most recent usable/commercial systems of the corresponding company. The notation "–" means no available quantum computing chip (processor) is available yet. IonQ has 79 qubits addressable in the trapped ion setup.

Company	Qubit number (year)	Chip system	Computing scheme
Google	54 qubits (2019) [11]	Superconducting qubit	Universal gate based
IBM	53 qubits (2020) [12]	Superconducting qubit	Universal gate based
Intel	49 qubits (2018) [13]	Superconducting qubit	Universal gate based
Rigetti	31 qubits (2020) [14]	Superconducting qubit	Universal gate based
Microsoft	– (2017) [15]	Topological quantum computing using Majorana Fermions	Universal gate based
IonQ	79 qubits* (2019) [16]	Trapped ions	Universal gate based
D-Wave	2000 qubits (2017) [17]	Superconducting devices	Quantum annealing

optimizing the performance of the quantum device for better quantum information processing and (3) robust light manipulation using topological plasmonic modes.

The thesis discusses the application of the theory modeling and analysis to these physical systems and propose experimental realizable gate schemes, optimization of the performance of the quantum devices and control on the quantum systems, to shed light towards the advances in quantum information processing and quantum computers. The theoretical treatment of these quantum systems are not limited to the specific devices, but can be easily generalized to the other related systems.

In the following sections, we at first give a brief introduction to the computation com-

plexity classes in Section 1.1. We introduce the computational complexity classes P, NP and BPP for traditional computing systems and BQP class for quantum computers. We explicitly point out the quantum algorithms can give significant improvement to some of the hard problems in traditional computation theory. Even though the computation theory is not a focus of the thesis, with the introduction of the classical and quantum complexity classes, we hope to give a flavor to the power of the quantum computers, which motivates the research on quantum computing and information processing.

In the later sections, we give brief introductions to the physical systems discussed in the following chapters of the thesis. Specifically, in Section 1.2, we briefly introduced the Nitrogen-Vacancy centers in diamond crystal. In Section 1.3, solid-state superconducting-circuit systems and amplifiers based on Josephson nonlinearities are introduced. In Section 1.4, a brief introduction to the topological modes in nano-plasmonic systems is given.

1.1 Computation classes and quantum algorithms with significant speedup

In this section, we give a brief introduction to the computation complexity classes. We mainly focus on the complexity class P, NP, BPP and define the NP-complete problems in a informal way. The discussion and definition of the complexity classes mainly follows Refs. [18, 19].

The investigation of the computational complexity classes is to understand the complexity of the different computational problems and the bounds of the computational efficiency of the algorithms for these problems. In the discussion of the complexity classes, only the decision problems, i.e., the problems whose answer is binary, either yes or not, are considered. It does not limit the generality of the discussion because all the other problems can be reduced to decision problems.

For computing the problem in a classical computer, the problem needs to be encoded into a sequence of binary strings as the inputs for the computer, or the so-called Turing Machine (TM), a model that consists of the essential components of standard computation. The problems that take these encoded binary strings as input are called concrete problems.

If the input size of a concrete problem has size N and the problem can be solved in time order $O(N^k)$ on the deterministic TM, where k is a constant that does not depend on the size of the input, the problem is polynomial-time solvable. The computational complexity class P is formally defined as the set of the polynomial-time solvable concrete problems, i.e., the complexity class P can be thought of as a set of problems that can be solved in polynomial time using a classical computer. The example of the problems in complexity class P consists of sorting an unsorted list, breadth first traversal and depth first traversal of a binary tree, Dijkstra algorithm for graphs, etc.

Other than the problems that are known in complexity class P, there are harder problems. Among all these problems, the problems that can be verified when they are provided a possible answer to the question on a deterministic TM in polynomial time forms the complexity class NP. If a problem is solvable in polynomial time, it can be easily verified in polynomial time, so the problems in class P is in class NP, i.e., class P is a subset of NP. However, since solving a problem is usually harder than verifying a given solution of the problem, it is widely assumed that there are problems that can be polynomial-time verified, but cannot polynomial-time solvable, i.e., the class P is a proper subset of class NP. Within the NP problems, there is a set of problems, which all the problems in NP class can be polynomial-time reducible to these problems. The set of these problems is NP-complete problems. Note that when a problem A can be reducible to another problem B[1], the problem A is "no harder than" problem B [19]. Therefore, the NP-complete problems are considered to be the hardest problems in NP class and if a polynomial-time algorithm is found to be able to solve one of them, all the problems in NP can be solved in polynomial time, i.e., NP = P. If NP $\neq$ P, there is no polynomial-time algorithm to solve the NP-complete problems, which means the NP-complete problems cannot be exact and efficiently solved by classical computers [19, 18]. The examples of NP-complete problems include cliques of undirected graphs, vertex cover of undirected graphs, the travelling salesman problem, etc.

[1]The definition for NP class, NP-Complete and reducibility are rigorously defined using the formal-language framework in Ref. [19], where the possible inputs for the problems are abstracted as the possible strings of a language. A language is a set of all possible strings using allowed symbols (like the basic states on the tape of a Turing machine, we restricted our symbols to be {0, 1} for the this discussion). Especially, the language L_1 can be polynomial-time reducible to another language L_2, if there exists a polynomial-time computable function f such that for all the strings x in language L_1 *iff* $f(x)$ is a string in L_2, noted as $L_1 \leq_p L_2$. If language L is NP-complete, it must be in NP class and for any language $L_1 \in$ NP, $L_1 \leq_p L$.

Another important complexity class for traditional computation is BPP, i.e., bounded error probabilistic polynomial time. It consists of the problems that can be solved on a probabilistic TM with a bounded error 1/3 for each run[2] [18, 22]. The relation between BPP and NP is still an active research area in computational complexity study. But the problems in BPP can be considered as the problems that can be efficiently solved using a classical computer [18].

Quantum computers should be able to perform significantly better than their classical counterparts on certain tough problems. Some examples of this quantum speed up include Shor's algorithm [23, 24], Grover's algorithms [25], and Simon's algorithm [26]. Shor's algorithm focus on the integer prime factorization problem. The integer prime factorization problem is an NP problem, however, it is widely suspected that it is not a problem in P, nor an NP-complete problem either. Its best-known time complexity is sub-exponential in classical computers. But with Shor's algorithm, the problem can be solved in polynomial time, which provides a considerable speedup turning a super-polynomial problem into a polynomial problem. Grover's algorithm focuses on searching an unstructured database. For a classical method, the database with N entries needs to be examined one-by-one, which gives a complexity $O(N)$. Grover's algorithm, on the other hand, improves the complexity to $O(\sqrt{N})$, which is a quadratic improvement. Simons's algorithm which focuses on Simon's problem [26], a problem that requires an exponential number of queries on a black-box function in a classical algorithms, uses only polynomial number of queries with quantum algorithm. Simons's algorithm demonstrates the power of quantum computing to provide exponential speed up on NP-hard problems in classical computation theory.

To further understand the power of the quantum computing, a new complexity class, BQP complexity class (bounded-error quantum polynomial-time) is proposed. BQP class is defined as the problems that can be solved with a bounded error 1/3 using a polynomial

[2]For a standard (deterministic) TM, when the symbol and the TM state is determined, the action to the TM state is unique. A non-deterministic TM is a TM that allows to have multiple possible actions for a single symbol read out from the tape and the state of the current TM. The performed action is determined by a probability distribution on all possible actions. The probabilistic TM is a special type of non-deterministic TM, in which the possible actions are binary. The formal definition of a non-deterministic TM can be found in Chapter 4.5 of Ref. [20]. And the definition for probabilistic TM can be found in Chapter 8.2 of Ref. [21] and Chapter 10.2 of Ref. [22].

size quantum circuit[3] [18, Pages 200-202]. The problems in BQP are the most interesting problems which are expected to be efficiently solved by quantum computers. Currently, it is suspected that with quantum computing, we may not be able to solve all NP and NP-hard problems. But constructing large-scale quantum computers that implement these algorithms and designing new quantum algorithms that can provide significant speedup to hard problems in classical computation, and moving the problems into BQP class is still the main goals of quantum computing algorithm research.

In recent quantum computing research, with more and more qubits being integrated into the quantum computing systems (see Table 1), the power of the quantum computing systems is also increasing. The state-of-the-art systems are still not able to achieve fault tolerant universal quantum computing to implement complicated algorithms in BQP class to experimentally demonstrate the quantum speedup, however, some tasks which are considered to be hard in classical computation theory, e.g. the computation of a single amplitude (in specific basis) of the state of a general quantum circuit [29], sampling the output from a quantum system [30, 31], etc., are expected to be solvable using the current available quantum system. Therefore, the power of the quantum computing can be demonstrated experimentally to go beyond the capability of the classical computers (so called quantum supremacy) [32, 11], especially, using the Boson sampling problem [11]. Further, the Quantum Approximate Optimization Algorithm, which can be applied to max-cut problem, is also expected to be able to demonstrate the quantum supremacy with near-term devices [33, 34, 35].

1.2 Nitrogen-Vacancy centers in diamond crystal

In this section, we briefly introduce the Nitrogen-Vacancy (NV) centers in diamond and its application in quantum computing and quantum information process.

Nitrogen-Vacancy (NV) center is a type of defect color center in diamond crystal. It

[3]The BQP class can also be defined similar to BPP class, instead of using the classical Turing machine, it uses a quantum Turing machine [27]. In Ref. [28], Yao pointed out that "any function computable in polynomial time by a quantum Turing machine has a polynomial-size quantum circuit". So these two definition of BQP are equivalent.

consists of diamond crystal in which a nitrogen atom replaces a carbon atom and one of the four nearby carbon atoms is missing. The properties of NV centers in diamond make them one of the most promising candidates for quantum computing and quantum information processing. The most significant properties for NV centers that are beneficial for quantum computing and quantum information processing include: (1) The ground state of NV center electronic states is a spin triplet with total spin number $S = 1$. The ground state has a zero magnetic field splitting 2.87 GHz, which are well separated in room temperature and can be precisely initialized, addressed and manipulated by optical and microwave methods. The manipulation of the electronic states of NV centers was experimentally demonstrated in Ref. [36, 37, 38, 39] at room temperature. (2) NV centers also have very long spin coherence time ($\sim$ 1.8 ms in isotopically pure samples) [40] which is beneficial for performing long sequence of quantum gate operations for quantum computing and quantum information processing. (3) The NV centers can be easily fabricated in diamond crystal. (4) The NV centers electronic spin states can easily couples to the external magnetic field and the energy of the states are affected by temperature. Further, NV centers can exists in nano-size diamond crystals, which can be easily integrated in biological systems. These advantages also make NV centers widely used as magnetic sensors and thermal censers in the field of quantum sensing [41, 42, 43].

The study of the NV centers starts in 1976. In Ref. [44], Davies *et al* investigated the spectral property of the diamond crystal with defects and identified the transition that corresponded to the NV^- ground state to the electronic excited states. Follow this work, several spectral studies of the NV^- defect centers led to the understanding of the electronic structure of this system [45, 46, 47]. In Ref. [48], Gruber *et al* experimentally collect the fluorescence from individual NV centers using a scanning confocal optical microscope, which opens the word for using individual NV centers as single-photon sources or single qubits for quantum computing and quantum information processing. In the works that followed [49, 50, 51], the photon intensity self-correlation (g^2) was measured, and especially in Ref. [51], it was explicitly demonstrated that the NV centers can be used as a stable single-photon source, which is important for quantum optics experiments, quantum information processing using photons and measurement based quantum computing using photons. Further, the electronic

states of the NV centers can be optically initialized and the electronic states can be optically read-out [36, 37]. The fact that NV center electronic states can be manipulated and initialized optically makes it more controllable for quantum computing and information processing. Following the work in Ref. [52], in which the coherent coupling between the NV electronic spin and the nuclear spin of nearby ^{13}C was reported, the seminal work of Dutt *et al*, Ref. [38], showed that NV center electronic states combined with the nearby ^{13}C nuclear spin can be used as a long-lasting and controllable quantum register. Further, the entanglement of emitting photon states and the electronic state of NV center was experimentally demonstrated [53], which sheds light on using the NV centers for quantum information processing experimentally. The investigation of the usage of the NV centers, both the electronic states, the nuclear spin states and the emitted photons in quantum information processing, become increasingly popular and interesting [39, 54, 55, 56, 57]. Further, the quantum entanglement of two NV center electronic states, using the photon-heralded methods, has also been demonstrated in experiments [58, 59]. With the coherence of the emitted photon polarization and the electronic spin states, the research on using NV center as a photon source to generate photonic cluster states for measurement based quantum computing also highlights the role of NV center in quantum computing [60, 61].

1.3 Superconducting circuits and Josephson parametric amplifiers

Superconducting circuits, which consist of superconducting wires and Josephson junctions, are one of the most promising systems for quantum computing and quantum information processing. The superconducting circuit systems have multiple advantages, (1) the bulk of the superconducting circuits are made of superconducting wires, which have extremely low loss when transmitting current, (2) the coupling between superconducting circuits elements is relatively easily introduced, which makes the system itself be easily integrated together to form large scale multi-qubit systems, (3) the design and fabrication of superconducting circuits on chip is not technically difficult [62]. The key element of the superconducting circuit is the Josephson junctions, which consists of two bulk superconductors and a thin barrier

in between. In 1962, B. D. Josephson pointed out that two bulk superconductors that are coupled through a thin barrier can (1) exhibit an oscillating current when a DC voltage bias is applied across the junction (the AC Josephson effect) and (2) can carry a current without dissipation when phase biased (the DC Josephson effect) [63].

The DC Josephson effect introduces nonlinearity into microwave circuits, which can be used to turn harmonic oscillators into anharmonic oscillators. The anharmonic oscillators can then be made to act like artificial two-level atoms, also known as qubits. In experiments, there are various realization of the superconducting qubits, e.g. the transmon qubits [64, 65, 66, 67], flux qubit [68, 69, 70, 71, 72], fluxonium qubits [73], etc, which are available for quantum computing and quantum information process.

On the other hand, the nonlinearity of the Josephson junctions also provides a resource for nonlinear coupling of different spatial microwave modes in a superconducting circuit. It can play the role of the nonlinear media in nonlinear optics, but provides much stronger nonlinearity. If one of the spatial microwave modes is strongly pumped, through the nonlinearity provided by the Josephson junction, the different spatial modes can be parametrically coupled. The Josephson parametric amplifier takes advantage of the parametric coupling process to provide photon gain to the signal mode of the amplifier from the pump mode.

Various Josephson Parametric Amplifier (JPA) circuits have recently been investigated. These designs includes JPAs based on Superconducting Nonlinear Asymmetric Inductive eLements (SNAILs) [74, 75, 76, 77]), flux pumped Superconducting QUantum Interference Devices (SQUIDs) [78, 79, 80, 81, 82], and the Josephson Parametric Converters (JPCs) [83, 84, 85, 86, 87]). There are also designs for amplifiers that do not use cavities, e.g. the traveling wave parametric amplifier (TWPA) [88, 89, 90]. For all these Josephson parametric amplifiers, there is one remaining question to be used for large scale quantum information processing, which is the maximum power of the input signal that the amplifiers can still gives a constaint gain. In this thesis, we will address this problem of the system.

1.4 Topological modes in plasmonic nano-structures

The interface between two electronic materials with topologically distinct band structures necessarily supports a topologically protected mode [91, 92, 93]. The robustness of this mode arises from global symmetries like parity, space inversion, and time reversal [94, 95]. In electronic systems, the topology of the electronic band structures can be controlled relatively easily by either using materials properties (e.g. picking a suitable semiconductor [96]) or by materials engineering (e.g, by making hybrid structures like quantum wells out of suitable materials [97]). The combination of robustness of topological edge modes and the relative ease of fabrication has resulted in an explosion of interest in these systems with applications ranging from decoherence-free quantum state manipulation [98] to electronic device design [99, 100, 101].

Following the seminal work of [102], it was realized that topological band structures can also exist in photonic systems. These ideas have been explored in a number of theoretical proposals [103, 104, 105, 106, 107, 108, 109]. They have also been realized experimentally in the following photonic crystal systems: gyromagnetic photonic crystal at microwave frequencies [110], coupled whispering gallery mode optical resonators [111], optical waveguides [112, 113], and plasmonic arrays [114, 115, 116].

The analysis of Refs. [112], which provides a mapping between electronic systems and paraxial light propagation in photonic and plasmonic systems, inspired a number of works. Here, we are concerned with the one-dimensional topological model of Su-Schrieffer-Heeger (SSH) [117, 118], which was originally used to describe electron motion in polyacetylene chains. The SSH model hosts topologically protected modes on domain boundaries, the protection being provided by the sub-lattice (or chiral) symmetry which belongs to the AIII-class of [94]. The mapping inspired by Rechtsman et al's work was adopted to the SSH model and explored experimentally in plasmonic nanowire arrays [114, 119] as well as photonic crystals [113]. The propagation of plasmonic topological modes in graphene nanowires was also explored theoretically in [120]. These works serve to establish the existence of optical topological defect modes.

The following of sections of this thesis is structured as follows. In Chapter 2, we re-

view the theory of quantum optics and open quantum system. especially some of the key assumptions and the results of quantum optics treatment of driven-dissipative systems. In Chapter 3, we discuss our investigation of the NV center systems, with the understanding of the electronic states of negatively charged NV centers, we proposed single-photon heralded two-NV center quantum gates. We also evaluate the gate performance using quantum trajectory method. In Chapter 4, we investigate the the dynamic of the Josephson ring modulator based Josephson parametric amplifier. We theoretically investigate how the nonlinearity provided by the Josephson junctions controls the saturation power of the amplifier. We further design the device and optimize its saturation power by ~ 15 dB compare to the previously experimentally fabricated JPAs. In Chapter 6, we introduce a mapping between the paraxial plasmonic light and the lower dimensional time evolution of the electronic systems. We design the metallic nanowire geometry to construct topological protected plasmonic modes, similar to the SSH model in electronic systems. We further use the topologically protected edge mode to achieve a waveguide, a spacial mode filter and beam splitter. In Chapter 7, we present a brief conclusion of the main results.

2.0 Theory of open quantum systems: a quantum description of dissipation and decoherence

In this chapter, we review basic quantum optics, some of the main assumptions, the various regimes, and the main results in the treatment of the quantum systems that experience dissipation and decoherence. Rather than focusing on the rigorous derivation, we focus on the physical arguments of the validity of the assumptions and the key conditions for the assumptions to be reasonable in quantum optics systems. The discussion in this chapter mainly follows Refs. [121, 122, 123, 124].

2.1 Paradigm of quantum optical systems

In the general discussion of loss and decoherence in quantum systems, we assume that the total system which is under consideration consist of two parts: (1) a subsystem which contains a few degrees of freedom (DOF), which is the model for the quantum systems we care about and (2) the rest of the system that has a large number of DOFs which the model treats as the surrounding environment of the quantum system. We use the Hamiltonian H_s to describe the subsystem (1) and $H_{\rm B}$ [B for bath] to describe the rest of the system (2). From now on, to be consistent with the quantum optics treatment, we will refer to the subsystem (1) as the system and the rest of the system (2) as the bath (or reservoir) of the system.

The system and the bath can couple through a coupling Hamiltonian V. Here we assume the coupling strength between the system and the bath is weak, i.e., the dynamics of the system-bath coupling is much slower than the dynamics of the system and bath.

2.2 Master equation of the quantum systems with dissipation

With the model described in Sec. 2.1, the dynamics of the system and bath in the interaction picture is,

$$\partial_t R^{(I)}(t) = -i \left[V,\, R^{(I)}(t)\right], \tag{2.1}$$

where $R^{(I)}(t)$ is the density operator for both the system and the bath, which is given by $R^{(I)}(t) = U^\dagger R(t) U$, where $U = e^{-i(H_\mathrm{S}+H_\mathrm{B})t}$. We assume $\hbar = 1$.

Formally integrate Eq. (2.1), which gives,

$$R^{(I)}(t) = R^{(I)}(t = t_0) - i \int_{t_0}^{t} \left[V(t'),\, R^{(I)}(t')\right] dt' \tag{2.2}$$

and we plug back to Eq. (2.1),

$$\partial_t R^{(I)}(t) = -i \left[V(t), R^{(I)}(t_0)\right] - \int_{t_0}^{t} \left[V(t),\, \left[V(t'),\, R^{(I)}(t')\right]\right] dt' \tag{2.3}$$

Note that up to this point our description is exact.

Using this method, we can expand the equation of motion for the system and bath in orders of the coupling strength. But to exactly solve this equation, it is hardly any easier than the original Eq. (2.1). By solving Eq. (2.1), we not only know the dynamics of the system, but also know the dynamics of the bath.

As the system and bath evolves, in reality, due to the existence of the system-bath coupling, the system will be entangled with the bath. The exact time evolution of the whole system and bath cannot be separated. However, in almost all the realistic quantum optics systems, the dynamics of the bath is neither interesting to us, nor traceable in experimental observation. Only the system itself can be measured and observed. If only the system itself is observed, the system is in a mixed state, which can be described by its density operator

$$\rho = \mathrm{tr}_\mathrm{B} \{R\} \tag{2.4}$$

where ρ is the density operator for the system itself and R is the density operator for the system and bath together. The notation tr_B is the partial trace over the bath DOFs. So our goal is to know how the state of the system evolves in terms of its density operator ρ without solving the exact time-evolution of the system and bath. In the following, we will

make assumptions and apply approximations to simplify the Equation of motion (EOM) by constructing effective dynamics of the system itself to reflect the effect of the actual system-bath coupling, and finally eliminate the bath DOFs from the system dynamics.

To achieve the goal, we at first assume that the system-bath coupling strength is weak compared to the dynamics of the system and bath. This approximation is Born approximation [124]. As in a quantum optics system, the frequency scale of the system dynamics are typically in optical regime and so as the bath dynamics, while the system-bath coupling is much slower than the optical frequency, the Born approximation is typically applicable to quantum optical systems.

In addition, with the assumption that the bath is much larger than the system, or even the bath itself is infinite, along with the Born approximation, the finite excitation and information exchanged from the system to the bath only changes the bath state slightly from the initial bath state. So we can approximate the state of the bath at any time in the time scale that we interested in by the initial state of the bath (which can be either a pure state or a mix state). As a result, the state of the system and bath can be approximated by

$$R(t) \sim \rho(t) \otimes \rho_{\mathrm{B}}(t_0) \tag{2.5}$$

We further assume that the initial state of the system and bath is not an entangled state, i.e., $R(t_0) \sim \rho(t_0) \otimes \rho_{\mathrm{B}}(t_0)$. With the approximation Eq. (2.5), after taking partial trace on the bath DOFs in Eq. (2.3), the EOM for the system is

$$\begin{aligned} \partial_t \rho^{(I)}(t) = & -i \,\mathrm{tr}_{\mathrm{B}} \left\{ \left[V(t), \rho^{(I)}(t_0) \otimes \rho_{\mathrm{B}}^{(I)}(t_0) \right] \right\} \\ & - \mathrm{tr}_{\mathrm{B}} \left\{ \int_{t_0}^{t} \left[V(t), \left[V(t'), \rho^{(I)}(t') \otimes \rho_{\mathrm{B}}^{(I)}(t_0) \right] \right] dt' \right\} \end{aligned} \tag{2.6}$$

where super-index (I) is to show the density operators are in interaction picture.

We would to stress again that even though the approximation Eq. (2.5) is applied, because of the actual entanglement of the system and bath DOFs due to the system-bath coupling, after eliminating the bath, the system itself will not undergo unitary time-evolution, instead it will suffer loss and decoherence. If the system is initialize in a pure state, it may evolve into a mixed state in presence of the system-bath coupling, even under the approximation Eq. (2.5).

Here we want to highlight why this treatment is able to model the loss process of the system itself. Notice that the bath itself may have a large bandwidth and it is much larger than the system. When the excitation from the system is exchanged to the bath, it will take much longer time for it to return back to the system. If the time scale we care about (given by the dynamics of the system) is much slower than this revival time, the excitation from the system can be considered as being lost, even though the whole system and bath experience unitary time evolution. Note that if the bath DOF is infinite, the recurrence time would be infinite. Therefore, the information (excitation) lost into the bath will never come back to the system.

With further assumptions that explicitly define the bath initial states and the system-bath coupling Hamiltonian, we can perform the partial trace of the bath DOFs and the time integral to achieve the explicit form of master equation for the system itself. Especially in this treatment, if the system-bath coupling has a broad bandwidth coupling and the coupling strength as well as the density of states of the bath in the coupling window is smooth, the Markov approximation can also be applied. With the Markov approximation, the coupling strength and the bath density of states are approximated by constants (i.e., independent of the frequency), which causes the bath time-correlation can be approximated by $\delta(t-t')$. With the Markov approximation, the system density operator in Eq. (2.6) can be replaced by $\rho^{(I)}(t)$. We will carefully examine the Markov approximation in next section.

With the Born-Markov approximations, the equation of motion of motion for the system density operator can be, in general, written in Lindblad form,

$$\partial_t \rho(t) = -i\ [H_s, \rho(t)] - \sum_m \frac{\Gamma_m}{2} \left(\hat{L}_m^\dagger \hat{L}_m \rho(t) + \rho \hat{L}_m^\dagger \hat{L}_m - 2\hat{L}_m \rho(t) \hat{L}_m^\dagger \right) \tag{2.7}$$

where $\rho(t)$ is the system density operator, H_s is the system coupling Hamiltonian, $\hat{L}_m$ is a system operator, which is the quantum jump operator for the corresponding process and Γ_m is the transition rates of the corresponding process. The master equation Eq. (2.7) is referred as Lindblad master equation (or Lindbladian) and the terms that appears because of the system-bath coupling (the second term on the right hand side of the Eq. (2.7), which has quantum jump operators) are called Lindblad terms. Suppose the system is a single-mode cavity and the cavity couples to a vacuum photon bath. Due to the cavity-bath coupling, the

cavity photon will experience photon loss, i.e., the cavity photon can leak out of the cavity and loss into the bath. In this system, the quantum jump operator for the cavity photon loss is the photon operator $\hat{a}$ of the cavity mode. The terms that describes the photon loss is

$$\Gamma\mathcal{D}[\hat{a}]\rho \equiv -\frac{\Gamma}{2}\left(\hat{a}^\dagger\hat{a}\rho + \rho\hat{a}^\dagger\hat{a} - 2\hat{a}\rho\hat{a}^\dagger\right) \tag{2.8}$$

where $\mathcal{D}[\hat{a}]\rho$ is commonly referred as dissipator of the loss process.

2.3 An example of master equation derivation

In this section, we consider a simple physical system, a two-level atom couples to a single-mode cavity field, to demonstrate how to derive the master equation for an open quantum system. In this specific system, the single mode cavity field is considered to be the bath of the quantum system, the two level atom. The EOM for the whole system is

$$\partial_t R = -i[H, R], \tag{2.9}$$

where R is the density operator for the whole system (atom + cavity field), and the Hamiltonian is

$$H = H_0 + H_{\text{int}} \tag{2.10a}$$

$$H_0 = \frac{1}{2}\omega_0\sigma_z + \sum_k \omega_k a_k^\dagger a_k \tag{2.10b}$$

$$H_{\text{int}} = \sum_k i\kappa_k \left[a_k^\dagger\sigma_- - \sigma_+ a_k\right], \tag{2.10c}$$

where a_k ($a_k^\dagger$) are the corresponding lowering and raising operators for the cavity mode with wave vector k, and the operator σ_z, σ_- and σ_+ are atomic operators. We assume the dispersion relation of the system is given by $\omega_k = v_p|k|$, where v_p is the wave speed for the cavity field, and the cavity field is in the vacuum state. We further assume the initial state of the whole system is in $R(t=0) = \rho(t=0) \otimes |\text{vac}\rangle\langle\text{vac}|$, where ρ is the density operator for the two-level atom, and $|\text{vac}\rangle$ is the vacuum state of the cavity field.

The EOM for the whole system in the interaction picture is

$$\partial_t R^{(I)} = -i[H_{\rm int}^{(I)}, R^{(I)}] \tag{2.11a}$$

$$H_{\rm int}^{(I)} = \sum_k i\kappa_k \left\{ a_k^\dagger \sigma_- \exp\left[i(\omega_k - \omega_0)t\right] - \sigma_+ a_k \exp\left[-i(\omega_k - \omega_0)t\right] \right\}. \tag{2.11b}$$

To derive the master equation for the atom, we explicitly perform the partial trace over the bath DOFs in Eq (2.6) for this system. Notice that $\langle a_k \rangle = \langle a^\dagger \rangle = 0$ for the vacuum cavity field, the first order term is zero.

To calculate the second order terms in Eq. (2.6), we need to expand the commutator relations and perform the time integration and sum over different k mode explicitly. Note that the commutator can be expanded into

$$\begin{aligned} \left[H_{\rm int}(t),\, \left[H_{\rm int}(t'),\, \rho^{(I)}(t')\rho_{\rm B}\right]\right] &= H_{\rm int}(t)H_{\rm int}(t')\rho^{(I)}(t')\rho_{\rm B} + \rho^{(I)}(t')\rho_{\rm B}H_{\rm int}(t)H_{\rm int}(t') \\ &= -H_{\rm int}(t)\rho^{(I)}(t')\rho_{\rm B}H_{\rm int}(t') - H_{\rm int}(t')\rho^{(I)}(t')\rho_{\rm B}H_{\rm int}(t), \end{aligned} \tag{2.12}$$

where $\rho_{\rm B} = |{\rm vac}\rangle\langle{\rm vac}|$ is the bath density operator. When we take the partial trace over the bath DOFs, we notice that

$${\rm tr}_{\rm B}\left(a_k a_{k'}^\dagger \rho_{\rm B}\right) \equiv \langle a_k a_{k'}^\dagger \rangle_{\rm B} = \delta_{k,k'}, \qquad {\rm tr}_{\rm B}\left(a_k^\dagger a_{k'} \rho_{\rm B}\right) \equiv \langle a_k^\dagger a_{k'} \rangle_{\rm B} = 0. \tag{2.13}$$

In the first term in Eq. (2.12), the only term that survive after the partial trace over the bath DOFs is

$${\rm tr}_{\rm B}\left\{H_{\rm int}(t)H_{\rm int}(t')\rho^{(I)}(t')\rho_{\rm B}\right\} = \sum_{k,k'} \kappa_k \kappa_{k'} \sigma_+\sigma_- \rho^{(I)}(t') e^{i(\omega_0-\omega_k)t} e^{i(\omega_{k'}-\omega_0)t'} \langle a_k a_{k'}^\dagger \rangle \tag{2.14a}$$

$$= \sum_k \kappa_k^2 \sigma_+\sigma_- \rho^{(I)}(t') e^{i(\omega_0-\omega_k)(t-t')}. \tag{2.14b}$$

To further calculate the summation of all the k modes, we approximate

$$\sum_k \to \frac{L}{2\pi}\int dk = \frac{L}{\pi v_p}\int d\omega_k \tag{2.15}$$

where L is the length of the cavity, which is assumed to be large, c is the speed of light inside the cavity field. We assume the atom will couples to the cavity modes propagating on both direction, which causes an extra factor 2 when it is converted to frequency integral. With

the finite system-bath coupling bandwidth, we assume that κ_k is only nonzero in the range that $\omega_k \in (\omega_0 - \Gamma/2, \omega_0 + \Gamma/2)$.

With the Born-Markov approximation, we assume that the coupling strength of the atom and the cavity field is smooth such that in the coupling bandwidth, the coupling strength κ_k can be well approximated by κ_{k_0}, where $k_0 = \omega_0/c$. Further, we assume the coupling bandwidth Γ is much larger than the time scale for the system dynamics (especially the system dynamics caused by the system-bath coupling), the integral of frequency can be approximated by a delta function, i.e.,

$$\sum_k \kappa_k^2 \sigma_+\sigma_-\rho^{(I)}(t')e^{i(\omega_0-\omega_k)(t-t')} \sim \frac{L\kappa_{k_0}^2}{2\pi v_p}\sigma_+\sigma_-\rho^{(I)}(t')\int_{\omega_0-\frac{\Gamma}{2}}^{\omega_0+\frac{\Gamma}{2}} e^{i(\omega_0-\omega_k)(t-t')}d\omega_k \tag{2.16a}$$

$$\sim \frac{2L\kappa_{k_0}^2}{v_p}\sigma_+\sigma_-\rho^{(I)}(t')\delta_\Gamma(t-t') \tag{2.16b}$$

where $\delta_\Gamma(t-t')$ is assumed to be a "finite-width" delta function, i.e., the function can be assumed to be a delta function when we integrate this function with another function that slowly changes in the time scale given by the width Γ.

Therefore the contribution from the first term in Eq. (2.12) to the master equation is

$$-\int_{t_0}^{t} \mathrm{tr}_\mathrm{B}\left\{H_\mathrm{int}(t)H_\mathrm{int}(t')\rho^{(I)}(t')\rho_\mathrm{B}\right\} \sim -\frac{1}{2}\frac{2L\kappa_{k_0}^2}{c}\sigma_+\sigma_-\rho^{(I)}(t) \tag{2.17}$$

where we use the fact that the dynamics of the system state caused by the system-bath coupling is much slower than the bandwidth Γ, such that $\delta_\Gamma(t-t')$ is approximated by a real delta function $\delta(t-t')$.

Similarly, if we use the same procedure to calculate the contribution for the rest of three terms in Eq. (2.12), by define the decay rate $\gamma = 2L\kappa_{k_0}^2/v_p$, the master equation for the atom density operator is

$$\partial_t\rho^{(I)}(t) = -\frac{\gamma}{2}\left(\sigma_+\sigma_-\rho^{(I)}(t) + \rho^{(I)}(t)\sigma_+\sigma_- - 2\sigma_-\rho^{(I)}\sigma_+\right) = \gamma\mathcal{D}[\sigma_-]\rho^{(I)}, \tag{2.18}$$

where $\mathcal{D}[\sigma_-]\rho$ is the dissipator for the atom decay, which is similar as Eq. (2.8). Similarly, for a single-mode light field couples to vacuum photon bath can be treated in the same way.

2.4 Quantum Langevin equation and input-output relation

For simplicity, in the discussion of this section, we assume the bath is a single-mode photon bath with Hamiltonian

$$H_{\mathrm{B}} = \int \omega\, b^{\dagger}(\omega) b(\omega) d\omega \tag{2.19}$$

where $b(\omega)$ is the bath operator with frequency ω, which satisfy commutation relation $[b(\omega), b(\omega')] = \delta(\omega - \omega')$. Note that the bath can be easily expended to multi-mode cases, e.g. a 1D infinite long waveguide, 3D free space electromagnetic field, etc. In these case, the wave-vector k (or $\vec{k}$ for 3D electromagnetic field) is a better index to label the bath operators, i.e.,

$$H_{\mathrm{B}} = \int \omega(k)\, b^{\dagger}(k) b(k) dk \tag{2.20a}$$

$$[b(k), b(k')] = \delta(k - k'), \tag{2.20b}$$

where the mode frequency $\omega(k)$ is given by the dispersion relation. In this scenario, when we transform the integral of all the modes wave-vector k to the integral of frequency ω, the density of state $D(\omega)$ is needed. The Markov approximation also requires that the density of state should also be smooth and slow varying inside the system-bath coupling bandwidth as we discussed in previous section (section 2.2).

The system-bath coupling is assumed to be linear and in the form of

$$V = i \int_{\omega_0 - \Gamma}^{\omega_0 + \Gamma} \kappa(\omega) \left[b^{\dagger}(\omega) a - a^{\dagger} b(\omega) \right] d\omega \tag{2.21}$$

where a and $a^{\dagger}$ are the system operators, ω_0 is the optical frequency of the system and Γ gives the system-bath coupling bandwidth.

With the system Hamiltonian H_{S}, the Heisenberg equations for the operators can be written as

$$\partial_t b(\omega, t) = -i\omega b(\omega, t) + \kappa(\omega) a(t) \tag{2.22a}$$

$$\partial_t c(t) = -i[c(t), H_{\mathrm{S}}] + \int_{\omega_0 - \Gamma}^{\omega_0 + \Gamma} \kappa(\omega) \left\{ b^{\dagger}(\omega, t)[c(t), a(t)] - [c(t), a^{\dagger}(t)] b(\omega, t) \right\} d\omega \tag{2.22b}$$

where $c(t)$ is an arbitrary system operator. We explicitly write down the time variable t to show that these operators are in the Heisenberg picture.

We can formally integrate the equations of bath operators $b(\omega, t)$ using the field operator in the past (i.e., $t > t_0$) as

$$b(\omega, t) = \exp[-i\omega(t - t_0)]b(\omega, t_0) + \kappa(\omega) \int_{t_0}^{t} \exp[-i\omega(t - t')]a(t')dt' \tag{2.23}$$

and plug back to the EOMs for the system operator and get

$$\begin{aligned} \partial_t c(t) = & -i[c(t), H_{\mathrm{S}}] \\ & + \int \kappa(\omega) \left[e^{i\omega(t-t_0)} b^\dagger(\omega, t_0)[c(t), a(t)] - [c(t), a^\dagger(t)] e^{-i\omega(t-t_0)} b(\omega, t_0) \right] d\omega \\ & + \int d\omega \int_{t_0}^{t} dt' \left\{ \kappa^2(\omega) \left(e^{i\omega(t-t')} a^\dagger(t')[c(t), a(t)] - [a(t), c(t)] e^{-i\omega(t-t')} a(t') \right) \right\} \end{aligned} \tag{2.24}$$

where the integration of the frequency should be understood from $(\omega_0 - \Gamma)$ to $(\omega_0 + \Gamma)$.

To further simplify the equations of motion, we apply the first Markov approximation [122], in which we assume the system-bath coupling is smooth in the whole bandwidth, such that the coupling strength can be approximated by a constant, i.e., $\kappa(\omega) \sim \sqrt{\gamma/(2\pi)}$, where γ is a constant and does not depend on the frequency ω. With the first Markov approximation, the integration over the whole coupling bandwidth can be performed in the last term in Eq. (2.24). Note that since the frequency integration is not from $-\infty$ to $+\infty$, the integration of the frequency does not give an exact $\delta(t - t')$ function. Instead, the integration result can be thought of as a function which is peaked around $t = t'$, but has a finite width on the order of Γ, which is noted as $\delta_\Gamma(t - t')$. If the function (operator) in the time integration changes much slower than Γ, we can approximately treat $\delta_\Gamma(t - t')$ as a $\delta(t - t')$, otherwise, extra care should be paid.

However, in general, the Heisenberg picture system operators changes in the frequency of optical frequency ω_0. In typical quantum optics systems, the bandwidth Γ cannot be comparable to the optical frequency ω_0 (otherwise the coupling strength cannot be considered a smooth function of frequency and the first Markov approximation is invalid). However, if we transform to the interaction picture of the system operators, where the fast optical frequency

oscillations are removed, we appreciate the fact that the integration of the frequency ω will give an extra phase term that cancels all the fast oscillating terms in the time integral,

$$\int_{t_0}^{t} dt'\gamma/(2\pi) \int_{\omega_0-\Gamma}^{\omega_0+\Gamma} d\omega e^{-i\omega(t-t')} a(t') \sim \frac{1}{2}\gamma a(t). \tag{2.25}$$

Based on Eq. (2.25), the final result of the integration matches the situation where we assume the coupling bandwidth is "large" and the frequency integration can be extended to $-\infty$ to $+\infty$. But the above discussion of the Markov approximation relies on the existence of the frequency hierarchy that $\omega_{\mathrm{S,c}} \ll \Gamma \ll \omega_0$, where $\omega_{\mathrm{S,c}}$ is the system coupling dynamic frequency [124].

Apply the first Markov approximation on the middle terms of Eq. (2.6), with further definition of the "input" field as

$$b_{\mathrm{in}}(t) = \frac{1}{\sqrt{2\pi}} \int_{\omega_0-\Gamma}^{\omega_0+\Gamma} e^{-i\omega(t-t_0)} b(\omega, t_0), \tag{2.26}$$

the quantum Langevin equation can be written as

$$\partial_t c(t) = -i[c(t), H_{\mathrm{S}}] - [c(t), a^\dagger(t)] \left[\frac{\gamma}{2} + \sqrt{\gamma} b_{\mathrm{in}}\right] + \left[\frac{\gamma}{2} + \sqrt{\gamma} b_{\mathrm{in}}^\dagger\right] [c(t), a(t)] \tag{2.27}$$

Further, we can also formly integrate the equation of bath operators $b(\omega, t)$ using the field operator in the future (i.e., $t < t_1$) as

$$b(\omega, t) = \exp[-i\omega(t-t_1)] b(\omega, t_1) - \kappa(\omega) \int_t^{t_1} \exp[-i\omega(t-t')] a(t') dt' \tag{2.28}$$

and define the "output" field as

$$b_{\mathrm{out}}(t) = \frac{1}{\sqrt{2\pi}} \int_{\omega_0-\Gamma}^{\omega_0+\Gamma} e^{-i\omega(t-t_1)} b(\omega, t_1). \tag{2.29}$$

The quantum input-output relation can be found as [124, 122],

$$b_{\mathrm{out}}(t) - b_{\mathrm{in}}(t) = \sqrt{\gamma} a(t). \tag{2.30}$$

How do we apply the quantum input-output formalism? Consider a superconducting artificial atom [which acts as the system] to a single mode transmission line [which acts as the bath]. If we send a microwave tone on the to the transmission line, we can solve how the tone interacts with the superconducting artificial atom, and compute the output

field. If the input tone is classical, we can approximate the input field operators using their classical mean values. On the other hand, if the input signal has quantum noise, or if the noise is one of the features we want to consider, we can leave the input and output field as operators and compute the correlation function of the output field operator expectation value, auto-correlation functions, etc.

2.5 Quantum trajectory method

To numerically solve the master equation of an open quantum system, we can expand the density operator of the system as a matrix using the eigen-states of the quantum system, and directly time evolve the master equation numerically. This is the numerical method we applied to analyze the Josephson micromaser, which will be discussed in Chapter 5. In addition, especially for a quantum system whose Hilbert space is so large that the density matrix cannot be efficiently stored, the quantum trajectory method provides a more efficient way to numerically solve the master equation. Further, with a slight modification of the quantum trajectory method, we can also simulate the open quantum system which is being observed, in which the measurement gives back-action to the system. This is the main method we used to calculate the Nitrogen-vacancy center unitary gate properties in Chapter 3. In this section, we discuss the quantum trajectory method.

As we discussed in Section. 2.2, the system master equation can be written in Lindblad form as Eq. (2.7). Here we can slightly rewrite the Lindblad master equation as

$$\partial_t \rho(t) = -i \left(H_{\text{eff}} \rho(t) - \rho(t) H_{\text{eff}}^\dagger \right) + \sum_m \left(\sqrt{\Gamma_m} \hat{L}_m \right) \rho(t) \left(\sqrt{\Gamma_m} \hat{L}_m^\dagger \right) \tag{2.31}$$

where the effective Hamiltonian for the dissipative system H_{sys} is

$$H_{\text{sys}} = H_s - i \sum_m \frac{\Gamma_m}{2} \hat{L}_m^\dagger \hat{L}_m. \tag{2.32}$$

Note that this effective system Hamiltonian is no longer Hermitian. With this non-Hermitian system Hamiltonian, the system will experience loss or (and) decoherence. Consider the cavity photon loss process discussed at the end of Sec. 2.2, in which the jump operator is

the cavity photon operator $\hat{a}$. The non-Hermitian term in the effective Hamiltonian decays the population of non-zero photon number states. However, the density operator should still keep unit trace, which is guaranteed by the last term in Eq. (2.31), which increases the population of the one-photon lower state by the amount of population loss from the upper photon states. This is the reason why this term is usually referred to as recycle term.

In the rest of this section, we give the essence of the quantum trajectory method and then we show that the quantum trajectory method will give the same time evolution as the master equation shown in Eqs. (2.7) and (2.31). The discussion in this section mainly follows Ref. [124].

In the quantum trajectory method, we treat the system to always be in a pure state at the coarse time steps δt. The state of the system can be be represented by $|\psi(t)\rangle$ at different time steps. But the time evolution of the system state is stochastic instead. Each sample of the stochastic time evolution of the system is treated as a possible "trajectory" of the system evolution, and the actual system state that can be measured (which is a mixed state) is given by the ensemble average of all these possible trajectories.

For each trajectory, we initialize the system to the same state $|\psi(t=0)\rangle$. For each time step, the system evolves to state

$$|\psi_m(t+\delta t)\rangle \propto |\tilde{\psi}_m(t+\delta t)\rangle \equiv \left(\sqrt{\Gamma_m \delta t}\hat{L}_m\right)|\psi(t)\rangle \tag{2.33}$$

with probability p_m, where

$$p_m = \langle\tilde{\psi}_m(t+\delta t)|\tilde{\psi}_m(t+\delta t)\rangle = \Gamma_m \delta t \langle\psi(t)|\hat{L}_m^\dagger \hat{L}_m|\psi(t)\rangle, \tag{2.34}$$

or evolve to the state

$$|\psi_0(t+\delta t)\rangle \propto |\tilde{\psi}_0(t+\delta t)\rangle \equiv (1 - i\, H_{\rm sys}\delta t)|\psi(t)\rangle, \tag{2.35}$$

with probability $(1 - \sum_m p_m)$. Note that after each time step, the state of the system needs to be renormalized.

To see that this time evolution is identical to the master equation in the first order of δt, the density matrix after a single time step of the above stochastic evolution is

$$\begin{aligned}\rho(t+\delta t) &= \sum_m p_m |\psi_m\rangle\langle\psi_m| + (1-p)|\psi_0\rangle\langle\psi_0| \\ &= \sum_m p_m \frac{|\tilde{\psi}_m\rangle}{\sqrt{p_m}} \frac{\langle\tilde{\psi}_m|}{\sqrt{p,}} + (1-p)\frac{|\tilde{\psi}_0\rangle}{\sqrt{1-p}}\frac{\langle\tilde{\psi}_0|}{\sqrt{1-p}}\end{aligned} \tag{2.36}$$

where $|\psi_0\rangle$ and $|\psi_1\rangle$ are given by Eqs. (2.35) and (2.33) with proper renormalization, respectively. After expressing the Eq. (2.36) using the density operator at time t, i.e., $\rho(t) = |\psi(t)\rangle\langle\psi(t)|$,

$$\begin{aligned}\rho(t+\delta t) =& \rho(t) - i\left(H_{\text{eff}}\rho(t) - \rho(t)H_{\text{eff}}^\dagger\right)\delta t + H_{\text{sys}}\rho(t)H_{\text{sys}}^\dagger \delta t^2 \\ &+ \sum_m \left(\sqrt{\Gamma_m}\hat{L}_m\right)\rho(t)\left(\sqrt{\Gamma_m}\hat{L}_m^\dagger\right)\delta t.\end{aligned} \tag{2.37}$$

Compare Eq. (2.37) with Eq. (2.31), these two methods agree up to the linear order of δt and should be identical in the limit of $\delta t \to 0$.

The actual state of the system, in general, should be a mixed state, which is given by the ensemble average of the trajectories. The physical quantities represented by operator $\hat{O}$ measured at time t is given by

$$\langle\hat{O}(t)\rangle = \text{tr}\left[\hat{O}\rho(t)\right]$$

.

To evaluate the system state and the physical quantities at time t_f using quantum trajectory method, we can initialize multiple trajectories at initial time t_0 with the same initial state $|\psi(t_0)\rangle$ and time evolve each trajectories according to the stochastic evolution rule till final time t_f. Then the mean value of the quantity $\langle O(t_f)\rangle$ is

$$\langle\hat{O}(t_f)\rangle = \frac{1}{N}\sum_{i=1}^{N}\langle\psi_i(t_f)|\hat{O}|\psi_i(t_f)\rangle, \tag{2.38}$$

where i is the index for different trajectories and N is the total number of trajectories.

If the master equation is linear, i.e., it could be expressed in the form of $\partial_t \rho = \mathcal{L}\rho$, the quantum regression theorem applies. In the quantum regression theory, if the single-time average of a system operator O_i satisfies

$$\langle O_i(t+\tau)\rangle = \sum_j c_j(\tau)\langle O_j(t)\rangle \tag{2.39}$$

the two time correlation function for two system operators O_i and O_k, based on quantum regression theorem, is

$$\langle O_i(t+\tau)O_k(t)\rangle = \sum_j c_j(\tau)\langle O_j(t)O_k(t)\rangle. \tag{2.40}$$

With quantum regression theorem, the two-time correlation function, e.g. $\langle A(t+\tau)B(t)\rangle$ where A and B are system operators, can also be calculated using quantum trajectory method. In each quantum trajectories, the system is initialized to its initial state, $|\psi_0\rangle$ and stochastically time-evolve to time t. The state of the system is now noted as $|\phi(t)\rangle$. Then four auxiliary states are created at this time,

$$|\psi_\pm^{\mathrm{R}}(t)\rangle = \frac{1}{\sqrt{\mu_\pm^{\mathrm{R}}}}\left(1 \pm B\right)|\phi(t)\rangle \tag{2.41a}$$

$$|\psi_\pm^{\mathrm{I}}(t)\rangle = \frac{1}{\sqrt{\mu_\pm^{\mathrm{I}}}}\left(1 \pm iB\right)|\phi(t)\rangle \tag{2.41b}$$

where B is the system operator in two-time correlation function, $\mu_\pm^{\mathrm{R(I)}}$ are the normalization factors for each state. Then based on the master equation, these four auxiliary states are stochastically time evolve to time $(t+\tau)$. The two-time correlation function is calculated by the trajectory average of [125, 124]

$$C(t+\tau) = \frac{1}{4}\left(\mu_+^{\mathrm{R}}c_+^{\mathrm{R}} - \mu_-^{\mathrm{R}}c_-^{\mathrm{R}} - i\mu_+^{\mathrm{I}}c_+^{\mathrm{I}} + i\mu_-^{\mathrm{I}}c_-^{\mathrm{I}}\right), \tag{2.42}$$

where the parameters

$$c_\pm^{\mathrm{R(I)}} = \langle\psi_\pm^{\mathrm{R(I)}}(t+\tau)|A|\psi_\pm^{\mathrm{R(I)}}(t+\tau)\rangle. \tag{2.43}$$

To understand why this approach works, we notice that the trajectory average of a single term is to calculate a two-time correlation function, e.g. the first term,

$$\mu_+^{\mathrm{R}}c_+^{\bar{\mathrm{R}}} \sim \langle\psi_0|e^{-\mathcal{L}t}(1+B^\dagger)e^{\mathcal{L}\tau}Ae^{\mathcal{L}\tau}(1+B)e^{\mathcal{L}t}|\psi_0\rangle. \tag{2.44}$$

where $\mathcal{L}$ is the superoperator given by the master equation. Eq. (2.44) can be expanded into four terms, the only term that survive after combining all four terms in Eq. (2.42) is

$$C(t^{-}+\tau) = \mathrm{Tr}\left\{e^{-\mathcal{L}(t+\tau)}Ae^{\mathcal{L}\tau}Be^{\mathcal{L}t}\rho_0\right\} = \langle A(t+\tau)B(t)\rangle, \tag{2.45}$$

where $\rho_0 = |\psi_0\rangle\langle\psi_0|$ is the initial state density operator.

Compare the quantum trajectory method with the directly time evolve the master equation using the system density matrix, the quantum trajectory method requires less memory. To see that, if the system state under investigation is in a N-dimensional Hilbert space, the pure state of the system can be represented by a N-dimensional vector. But using the density matrix, we need $N \times N$ coefficients to store. Further, even with the quantum trajectory method, for some systems, e.g. the 100 spin-half particles, the state space can be much larger than the computer memory. To deal with these system, the quantum trajectory method can be easily integrate with the matrix-product-state representation of the many-body wave function to reduce the memory cost. But since each time-evolution of the system is a single trajectory of the trajectories ensemble, the time evolution needs to be run for many times to build a relative reliable statistics to give prediction of the system dynamics.

3.0 Single-photon heralded 2-qubit unitary gates for pairs of Nitrogen-Vacancy centers in diamond

3.1 Introduction

Quantum computers are expected to achieve significant speedup compare to classical computers to hard problems in classical computation theory [see Sec. 1.1 for detailed discussion]. The key resource that enables quantum speedup is quantum entanglement. In order to generate and harness this resource, it is essential to build high fidelity multi-qubit quantum gates.

The electronic spin associated with the nitrogen-vacancy (NV) centers in diamond is a promising qubit candidate for solid-state quantum computing. The spin states are well defined, have long spin relaxation and coherence times, and can be optically addressed for qubit initialization and readout for quantum operations. The qubits can be manipulated using either optical or microwave drive fields. However, a key missing ingredient for NV center quantum computing is an experimental demonstration of a high-fidelity 2-qubit unitary gate between NV centers at remote locations in the diamond lattice.

There are two main directions that have been investigated for coupling pairs of NV centers. The first direction, which has been proposed theoretically [126], relies on collective dynamics of spin-chains to deterministically generate couplings between two remote NV centers. The second direction, which has been investigated both theoretically and experimentally, generates entanglement between two NV centers using a heralded method. Cabrillo *et al.* showed that measurement can be used to project two-qubit quantum state of atoms into an entangled state in Ref. [127]. The idea of heralded probabilistic entanglement generation was also theoretically proposed and studied in Refs. [128, 129, 130, 131, 132, 133]. The quantum entanglement of two NV centers using heralded method has also been explored experimentally. Bernien *et al.* observed quantum entanglement of spins of two NV centers [58]. In a related work, Lee et al. demonstrated the entanglement of vibrational modes of two macroscopic diamonds (but not NV centers) [134]. Pfaff *et al.* experimentally

entangled spin states of two NV-centers, which they used for quantum teleportation [135]. Hensen et al. experimentally performed the Bell inequality test via entangling two separated NV-center spin states [59]. It is important to point out that the measurement of the photon in Refs. [58, 135, 59] is effectively a parity projector that projects the NV centers into a maximally entangled state. The limitation of this approach is that while it can be used to generate entanglement, it cannot be used to construct a 2-qubit unitary gate.

Inspiration for our work comes from a previous theoretical proposal for constructing a heralded probabilistic 2-qubit unitary gate using generic atoms [136]. Specifically, Protsenko et al. showed that quantum interference can be used to construct a 2-qubit unitary gate by controlling the relative phase of the photons emitted by the two atoms. This interference principle was later proposed for building 2-qubit gates between a pair of atoms in optical cavities coupled by linear optics [132].

In this chapter, we propose an alternative 2-qubit unitary gate for Nitrogen-Vacancy (NV) centers in diamond heralded by a single scattered photon. Further, we predict that there exists a "magic" frequency which suppresses spin-state preserving scattering transitions in favor of spin-flipping scattering transitions and a "balance" point where two spin-state flipping scattering transitions are equal. Utilizing these frequencies, in combination with a single mode diamond waveguide to collect and interfere the scattered photons, enables the proposed 2-qubit gate to achieve high fidelity and high success probability. For success probability approaching unity, the gate fidelity is $\sim 92\%$, while for fidelity approaching unity the success rate approaches $\sim 34\%$.

A key advantage of our scheme is that, unlike the schemes in Refs. [58, 135, 59] that rely on two-photon Hong-Ou-Mandel interference, the success of our entangling unitary gate is heralded by a single photon detection. For example, if our protocol were implemented with bulk optics and microfabricated solid-immersion lenses in diamond as has been previously demonstrated, the detection probability is $p \sim 10^{-4}$ [58], and with a conservative repetition rate $\sim$ 20 kHz, this would result in a successful entangling gate operation every 0.5 seconds. By contrast, entanglement events occur every 10 minutes in the two-photon heralded schemes, which represents orders of magnitude improvement in the clock rate. With further improvements in collection efficiency using e.g. the nanobeam waveguides that we propose

and analyze in this paper, and fast electronics, we can potentially achieve kHz - MHz clock rates that would be comparable to superconducting qubit quantum information processors.

This chapter is organized as follows. In Sections 3.2 and 3.3 we describe the main ingredients of our 2-NV center unitary gate. In Section 3.2, we focus on the proposed experimental setup and how to use interference to construct a unitary gate. In Section 3.3, we argue for the existence of a "magic" frequency at which qubit state-preserving transitions are suppressed and a "balance" frequency at which qubit state-flipping transitions are balanced. We propose four gate operation schemes, three utilizing the "magic" frequency and one the "balance" frequency, and analyzed their fidelity, success probability and unitarity. In Section 3.4, we analyze the success probability and fidelity of the 2-qubit unitary gate with possible experimental imperfections. We first build a qualitative understanding of the processes involved in the qubit dynamics and their effects on gate fidelity. Then we perform a quantitative analysis using the quantum trajectory method. Details of the proposed waveguide geometry, photon collection efficiency, transition rate calculations and further discussion of gate fidelity can be found in Section 3.5. We draw conclusions and present an outlook in section 3.6.

3.2 Proposed experimental setup for a 2-NV unitary gate

The experimental setup that we propose for a 2-qubit unitary gate using spin states of two NV centers is shown in Fig. 1(a). The two NV centers are embedded into a single-mode diamond waveguide, and are selected so that they are separated by $(2n+1)/4$-wavelengths, where n is an integer. The separation ensures that the emitted photons have $\pi/2$ phase difference when they are captured by the detectors. Both NV centers are aligned so that their x, y, and z-directions [137] (i.e., the $[11\bar{2}]$, $[1\bar{1}0]$, $[\bar{1}\bar{1}\bar{1}]$, direction of the diamond crystal) match the x, y, and z-directions of the waveguide (see Fig. 1(c)). State-flipping transitions in both NV centers are pumped by a continuous-wave laser applied transverse to the waveguide [in Fig. 1(a)]. The diamond waveguide collects and interferes the state-flipping scattered photons from the NV centers. Two detectors detect the photons collected by the waveguide from both ends to improve the detection efficiency. We note that depending on whether the

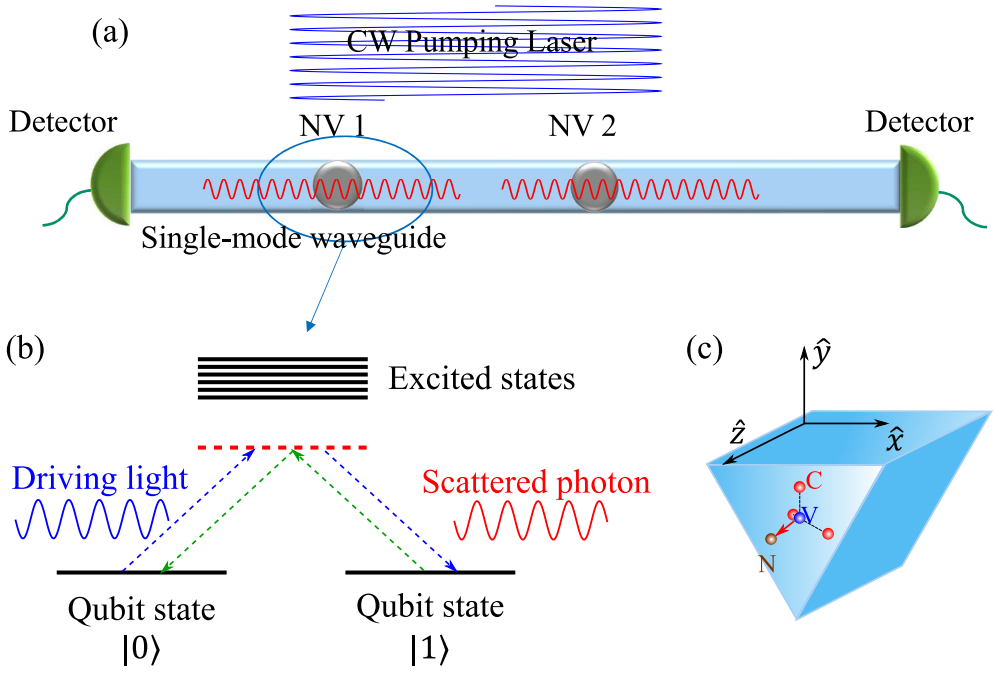

Figure 1: (a) Schematic illustration for the proposed heralded two NV center quantum gate. A sketch of the level diagram of NV centers is shown in (b). The NV centers can undergo scattering transitions to flip the qubit states and emit scattered photons when they are driven by an off-resonance continuous wave (CW) pump laser. The two NV centers with quarter wavelength separation are in a single-mode diamond waveguide. The waveguide collects and interferes the scattered photons emitted from the NV centers. The detectors monitor the scattered photons collected by the diamond waveguide. The unitary gate operation is heralded by the detection of a photon. (c) The coordinate system of an NV center (red spheres – carbon; blue – vacancy; brown – nitrogen), relative to the crystallographic axes of the diamond waveguide. The $\hat{x}$, $\hat{y}$ and $\hat{z}$ directions of the NV center match those of the waveguide, e.g. the $[\bar{1}\bar{1}\bar{1}]$ direction of diamond crystal (the red vector from the nitrogen to the vacancy) coincides with the axial direction of the waveguide.

detector on the left or on the right captures the photon we obtain slightly different unitary gates, which we discuss below.

We begin by reviewing why the $\pi/2$ phase is critical to achieve a unitary gate [136]. Assume that the NV centers have suitable state-flipping transitions which flip the qubit state between $|0\rangle$ and $|1\rangle$ and emit indistinguishable photons [Fig. 1(b)]. Next, suppose that there is a phase difference of χ in the optical path from the two NV centers to the detector (on the right). Consider the two initial states $|0,0\rangle$ and $|1,1\rangle$. If the detector on the right clicks, the output states are $|0,1\rangle + e^{i\chi}|1,0\rangle$ and $|1,0\rangle + e^{i\chi}|0,1\rangle$. In order for our 2-qubit gate to be unitary, these two output states must be orthogonal, hence $\chi = \pi/2 + n\pi$ where n is an integer. Similar logic applies to the cases in which the initial states are $|1,0\rangle$ and $|0,1\rangle$.

When the right detector clicks, the unitary 2-qubit gate is described by the matrix:

$$G_r = \frac{1}{\sqrt{2}} \begin{pmatrix} 0 & 1 & i & 0 \\ 1 & 0 & 0 & i \\ i & 0 & 0 & 1 \\ 0 & i & 1 & 0 \end{pmatrix}, \tag{3.1}$$

in the $|0,0\rangle$, $|0,1\rangle$, $|1,0\rangle$ and $|1,1\rangle$ basis. On the other hand if the left detector clicks we obtain the gate described by the matrix:

$$G_l = \frac{1}{\sqrt{2}} \begin{pmatrix} 0 & i & 1 & 0 \\ i & 0 & 0 & 1 \\ 1 & 0 & 0 & i \\ 0 & 1 & i & 0 \end{pmatrix}. \tag{3.2}$$

Note that if we wanted to obtain G_r, but the left detector clicks instead, we can apply the single-qubit operation $X_1 \otimes X_2$ to both qubits to convert the gate operation in Eq. (3.2) to the gate operation in Eq. (3.1). We note that G_r can be expressed in terms of the control-Z (CZ) gate and single-qubit gates as

$$G_r = \frac{1+i}{\sqrt{2}}(H \otimes H)\left(S^{-1} \otimes S\right)\mathrm{CZ}(H \otimes H), \tag{3.3}$$

where H is the Hadamard gate and S is the single-qubit $\pi/2$ phase gate

$$H = \frac{1}{\sqrt{2}} \begin{pmatrix} 1 & 1 \\ 1 & -1 \end{pmatrix}, \qquad S = \begin{pmatrix} 1 & 0 \\ 0 & i \end{pmatrix}, \tag{3.4}$$

and therefore, our two-qubit gate, in combination with the available NV single-qubit gates, forms a universal gate set.

3.3 Scattering transitions of an NV center for unitary 2-qubit gates

The main missing ingredient for constructing a 2-qubit gate with NV centers is finding suitable state-flipping transitions between qubit states of NV centers that emit indistinguishable scattering photons. In this section, we explore the electronic structure of NV centers and argue for the existence of suitable transitions.

Detailed information on electronic structures of NV centers can be found in Ref. [137, 138] and in 3.5.2 of our paper. The electronic levels, including fine-structure, of NV centers in diamond crystals without strain is shown in Fig. 2(a). The electronic ground state of NV center is a spin triplet. The spin-spin interaction breaks the degeneracy of the NV electronic ground state and splits the state $|g_1\rangle = |g, S_z = 0\rangle$ from the states $|g_2\rangle = \frac{1}{\sqrt{2}}(|g, S_z = +1\rangle + |g, S_z = -1\rangle)$ and $|g_3\rangle = \frac{1}{\sqrt{2}}(|g, S_z = +1\rangle - |g, S_z = -1\rangle)$ by the zero field splitting $D/h = 2.87$ GHz. The manifold of excited states spans several GHz and consists of four discrete sets of states with six states in total [see Fig. 2(a)]. These excited states can be labeled by the irreducible representation of the C_{3V} group and the S_z quantum number. To simplify notation, we label them $|e_j\rangle$, where $j = 1$ to 6. We note that in the presence of spin-spin (SS) interactions S_z is not a good quantum number for the lowest four excited states. However, as the SS interaction results in only a slight mixing between $S_z = \pm 1$ states and $S_z = 0$ states we label the eigenstates $|e_1\rangle$, $|e_2\rangle$, $|e_3\rangle$ and $|e_4\rangle$ by the dominant S_z component.

We propose to use the two-fold degenerate $S_z = \pm 1$ spin states, $|g_2\rangle$ and $|g_3\rangle$, as the logic 0 and 1 qubit states. We use scattering transitions pumped by an off-resonant laser to

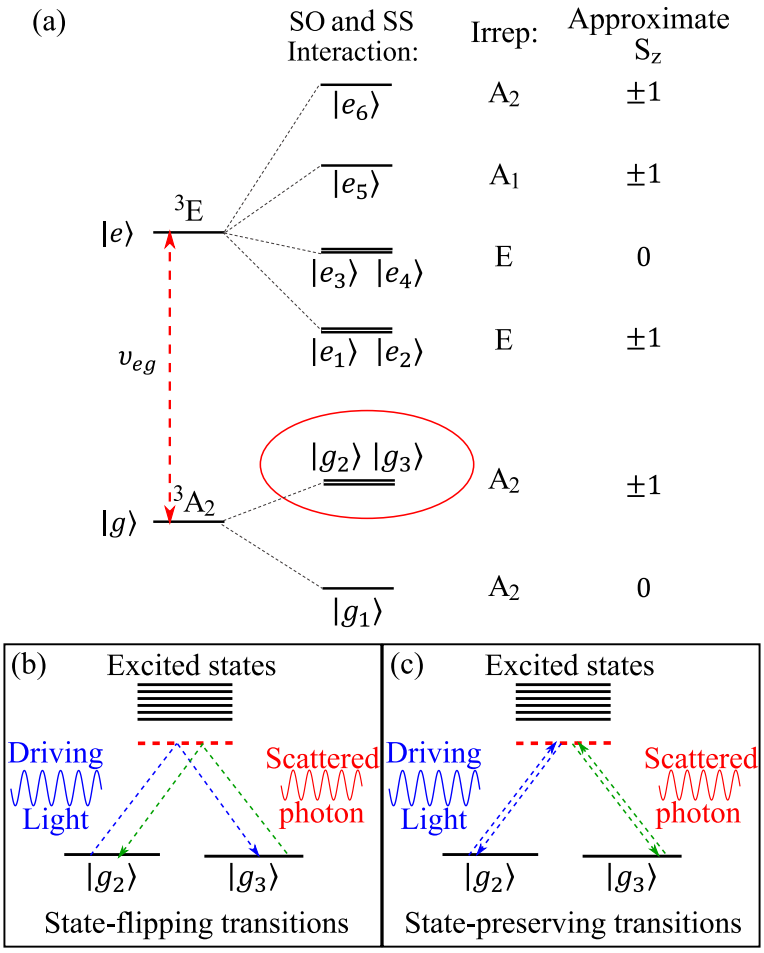

Figure 2: The sketch of the level diagram of NV center electronic states is shown in (a). The electronic ground state $|g\rangle$ and excited state $|e\rangle$ splits due to the spin-orbit (SO) and spin-spin (SS) interactions with the corresponding irreducible representations (*irrep*) of the C_{3V} group and approximated S_z quantum number. We choose to use state $|g_2\rangle = \frac{1}{\sqrt{2}}(|+1\rangle + |-1\rangle)$ and state $|g_3\rangle = \frac{i}{\sqrt{2}}(|+1\rangle - |-1\rangle)$ as the qubit states. We demonstrate the state-flipping transitions in (b) and state-preserving transitions in (c). The state-flipping transitions are the transitions that flips between qubit states $|g_2\rangle$ and $|g_3\rangle$. The other two transitions that does not flip NV states are the state-preserving transitions.

drive transitions between states $|g_2\rangle$ and $|g_3\rangle$ and hence flip the logic state [Fig. 2(b)]. The scattered photons from the two state-flipping transitions have the same frequency because the states $|g_2\rangle$ and $|g_3\rangle$ are energetically degenerate. There are two more scattering transitions that can occur in principle, i.e., Rayleigh scatterings. These two transitions do not flip the qubit state [Fig. 2(c)] and hence we call these transitions state-preserving transitions. The scattered photons emitted from these two transitions have the same frequency as the ones from state-flipping transitions. To ensure successful 2-qubit gate operation we must ensure that the detectors only click on state-flipping and not state-preserving transitions.

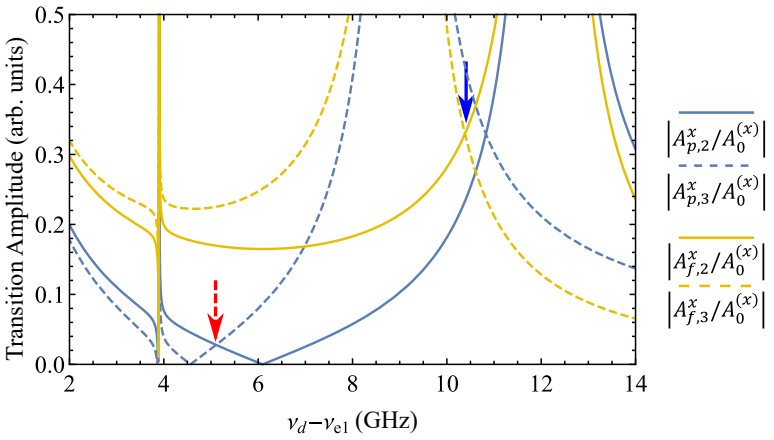

Figure 3: The magnitudes of state-preserving and state-flipping transition amplitudes given in the R.H.S of Eq. (3.7) (blue lines) and Eq. (3.9) (yellow lines) as we shift the driving light frequency ν_d. There are two frequency points that draw our attention: (1) the "magic" point (labeled by red dashed arrow) at which the two state-preserving transition amplitudes are strongly suppressed, (2) the "balance" point (labeled by blue solid arrow), where two state-flipping transition amplitudes are balanced.

The two ingredients that go into the calculation of the optical transition rates are: (1) the dipole matrix elements between NV center ground and excited states and (2) the interference between virtual excitations of the various excited states.

The results of the rate calculations for the state-flipping and state-preserving transitions, as a function of the drive frequency, are plotted in Fig. 3. We find that as we tune the drive frequency the interference between virtual excitation paths results in the significant

variation of the transition rates. We identify two special frequencies: first, there is a "magic" frequency for which the state-preserving transitions are approximately turned off. Second, there is a "balance" point frequency for which the two state-flipping transition rates are equal. We present the outline of the transition rate calculation in Section 3.3.1 (the details are presented in 3.5.2). Next, we discuss four different schemes for building a 2-qubit gate using the two special drive frequencies and different configurations of polarizers in the collection path. Specifically, we discuss how different schemes can be used to optimize gate fidelity, success probability, and unitarity. In Sections 3.3.2 and 3.3.3 we discuss gates schemes $M1$, $M2$ and $M3$ that utilize "magic" frequency drive light. The three schemes differ by drive light polarization and collection path configuration which let us optimize either gate success probability or gate unitarity. In Section 3.3.4, we discuss the gate scheme $B1$, that utilizes driving light frequency which makes the two state-flipping transitions balanced. We summarize the configurations of the four gate operation schemes in Table. 2.

Table 2: The configurations of the four gate operation schemes. We list the driving light frequency and polarization, and the collection path polarizer orientation for each schemes. Polarizations that appear in brackets are alternative to the ones that appear with no brackets.

Gate schemes	Drive frequency	Drive polarization	Collection path filter polarization
$M1$	"magic" point	$\hat{x}\,(\hat{y})$	$\hat{y}\,(\hat{x})$
$M2$	"magic" point	$\hat{x}+\hat{y}\,(\hat{x}-\hat{y})$	$\hat{x}-\hat{y}\,(\hat{x}+\hat{y})$
$M3$	"magic" point	$\hat{x}+\hat{y}\,(\hat{x}-\hat{y})$	$\hat{x}+\hat{y}\,(\hat{x}-\hat{y})$
$B1$	"balanced" point	$\hat{x}\,(\hat{y})$	$\hat{y}\,(\hat{x})$

3.3.1 Transition rate calculation: interference of virtual excitation paths

The dipole moment matrix after taking spin-orbital (SO) and spin-spin (SS) interaction into account can be written as

$$\frac{\hat{\mathbf{p}}}{p_0} = \begin{pmatrix} -F_{21}\hat{x} & F_{21}\hat{y} & F_{22}\hat{x} & F_{22}\hat{y} & -F_{23}\hat{y} & F_{23}\hat{x} \\ F_{21}\hat{y} & F_{21}\hat{x} & -F_{22}\hat{y} & F_{22}\hat{x} & F_{23}\hat{x} & F_{23}\hat{y} \end{pmatrix}. \tag{3.5}$$

Here, p_0 is the scale of the dipole moment; the matrix is written in the basis $\hat{p}_{ij} = \langle g_i | \hat{\mathbf{p}} | e_j \rangle$, where $i = 1$ for $|g_2\rangle$, $i = 2$ for $|g_3\rangle$ and $j = 1$ to 6 for excited states $|e_1\rangle$ to $|e_6\rangle$; and the factors F_{21}, F_{22}, F_{23} are three dimensionless parameters from the microscopic NV center Hamiltonian, $F_{21} = 0.7062$, $F_{22} = 0.0363$, $F_{23} = 1/\sqrt{2}$ (see Ref. [137] and 3.5.2 for details).

The scattering transition rates between the states $|g_2\rangle$ and $|g_3\rangle$ can be calculated using second order Fermi's golden rule. According to Eq. (3.5), if the driving light is linearly polarized along $\hat{x}$ or $\hat{y}$ direction, the photons from state-preserving transitions have the same polarization as the incoming light, while the photons from the state-flipping transitions have orthogonal polarization. Therefore, the state-flipping scattering photons can be distinguished from state-preserving scattering photons by polarization. In general, the result of perturbation theory can be expressed as

$$|g_j\rangle |\hat{\sigma}_1\rangle_i \xrightarrow{H_{\text{scatter}}} A_{p,j}^{\hat{\sigma}_1} |g_j\rangle |\hat{\sigma}_1\rangle_o + A_{f,j}^{\hat{\sigma}_1} |g_k\rangle |\hat{\sigma}_2\rangle_o \tag{3.6}$$

where $j, k = 1, 2$ and $j \neq k$, A's represent the transition amplitudes, the incoming drive light is in the polarization state $\hat{\sigma}_1$, and the outgoing light in the waveguide is in the polarization state $\hat{\sigma_1}$ or $\hat{\sigma_2}$ [1].

Let us consider the case in which the driving light is linearly polarized along either $\hat{x}$ or $\hat{y}$ direction, and hence $\langle \hat{\sigma}_1 | \hat{\sigma}_2 \rangle = 0$. We present the generic case in 3.5.3. Assuming the driving light frequency is ν_d, based on the dipole moment matrix, the state-preserving transition amplitudes can be worked out as,

$$\frac{A_{p,2}^x}{A_0^{(x)}} = \frac{A_{p,3}^y}{A_0^{(y)}} = \frac{1}{\Delta_1} F_{21}^2 + \frac{1}{\Delta_3} F_{22}^2 + \frac{1}{\Delta_6} F_{23}^2 \tag{3.7a}$$

[1] As we discuss in 3.5.1, the transverse directions of the NV centers are aligned to the transverse directions of the waveguide, which leads to the $\hat{x}$ and $\hat{y}$ directions of the dipole moment to couple to two different guided modes of the waveguide.

$$\frac{A^x_{p,3}}{A^{(x)}_0} = \frac{A^y_{p,2}}{A^{(y)}_0} = \frac{1}{\Delta_2}F^2_{21} + \frac{1}{\Delta_4}F^2_{22} + \frac{1}{\Delta_5}F^2_{23} \tag{3.7b}$$

where the $\Delta_i = \epsilon_{e,i} - \epsilon_g - h\nu_d$ is the energy mismatch, $\epsilon_{e,i}$, ϵ_g are the energy of the excited state $|e_i\rangle$ and the ground state $|g_2\rangle$, $|g_3\rangle$. As we shift the driving light frequency ν_d, the energy detuning of each excited level (Δ_i) changes. Two scale factors, $A^{(x)}_0$ and $A^{(y)}_0$, are defined as $A^{(\sigma)}_0 = p^2_0 E_{d,\sigma}\mathcal{E}_0 u_0$, where $E_{d,\sigma}$ is the driving light electric field along $\hat{\sigma}$ direction, $\mathcal{E}_0 = \sqrt{h\nu_d/(2\varepsilon_0)}$ is the electric field associated with a single photon in the waveguide, u_0 is the normalized waveguide mode profile at the location of the NV centers (see Eq. (3.44) in 3.5.3) We assume that the electric fields of the two guided modes have the same u at the location of the NV centers. In 3.5.3, we show that there is a region inside the waveguide where the two modes have balanced coupling to the NV centers. See 3.5.3 for details. In the following discussion, we assume these two parameters, $A^{(x)}_0$ and $A^{(y)}_0$, are equal. We also notice that the equality relations

$$\frac{A^x_{p,2}}{A^{(x)}_0} = \frac{A^y_{p,3}}{A^{(y)}_0}, \quad \frac{A^y_{p,2}}{A^{(y)}_0} = \frac{A^x_{p,3}}{A^{(x)}_0} \tag{3.8}$$

hold if $|\langle g_2|\hat{\mathbf{p}}|e_i\rangle| = |\langle g_3|\hat{\mathbf{p}}|e_i\rangle|$ for all excited states.

Similarly, the state-flipping transition amplitudes are,

$$\frac{A^x_{f,2}}{A^{(x)}_0} = \frac{A^y_{f,3}}{A^{(y)}_0} = -\frac{1}{\Delta_1}F^2_{21} - \frac{1}{\Delta_3}F^2_{22} + \frac{1}{\Delta_6}F^2_{23} \tag{3.9a}$$

$$\frac{A^x_{f,3}}{A^{(x)}_0} = \frac{A^y_{f,2}}{A^{(y)}_0} = \frac{1}{\Delta_2}F^2_{21} + \frac{1}{\Delta_4}F^2_{22} - \frac{1}{\Delta_5}F^2_{23} \tag{3.9b}$$

Note that these two equality relations $\frac{A^x_{f,2}}{A^{(x)}_0} = \frac{A^y_{f,3}}{A^{(y)}_0}$ and $\frac{A^y_{f,2}}{A^{(y)}_0} = \frac{A^x_{f,3}}{A^{(x)}_0}$ do not rely on the special symmetry in dipole moment elements. We plot the magnitudes of the R.H.S. of the Eq. (3.7) and Eq. (3.9) in Fig. 3 as we shift the driving light frequency ν_d.

3.3.2 M1 2-qubit gate scheme: "magic" frequency, $\hat{x}$-polarized drive light

As we shift the driving light frequency ν_d, we notice that there is a "magic" point where both state-preserving transition rates are highly suppressed because of the destructive interference between the virtual paths through the different excited states (see Fig. 3).

When we use an $\hat{x}$ polarized driving light, the scattered photons from state-preserving transitions are polarized along the $\hat{x}$ direction, while the polarization of the photons from state-flipping transitions are orthogonal, i.e., along $\hat{y}$. We can use a polarizer to further filter the state-flipping photons from the state-preserving photons. Heralding on the photons coming through the polarizer, we achieve a 2-qubit gate on the NV centers. This is our proposed gate scheme $M1$.

At the "magic" frequency the transition amplitudes satisfy $A^x_{p,2} = -A^x_{p,3} > 0$, $A^x_{f,2} < 0$ and $A^x_{f,3} > 0$. Therefore we define $A^x_{p,2} = -A^x_{p,3} = A_p > 0$ and define

$$A_1 \equiv |A^x_{f,2}| = -A^x_{f,2},\ A_2 \equiv |A^x_{f,3}| = A^x_{f,3}. \tag{3.10}$$

Since the state-preserving transition amplitudes satisfies $A^x_{p,2} = -A^x_{p,3} > 0$, we can also define $A_p = A^x_{p,2} = -A^x_{p,3}$.

At the "magic" frequency, however, the two state-flipping transition amplitudes are not balanced. These two unbalanced transition amplitudes cause the resulting gate to be slightly non-unitary. Assuming the polarizer is perfect and the right detector captures the heralding photon, the 2-qubit gate is described by the matrix,

$$G^{(1),\mathrm{ub}}_r = \begin{pmatrix} 0 & A_2 & iA_2 & 0 \\ -A_1 & 0 & 0 & iA_2 \\ -iA_1 & 0 & 0 & A_2 \\ 0 & -iA_1 & -A_1 & 0 \end{pmatrix} \tag{3.11}$$

in the basis $|g_2; g_2\rangle$, $|g_2; g_3\rangle$ and $|g_3; g_2\rangle$ and $|g_3; g_3\rangle$. If we have two balanced state-flipping transitions, i.e., $A_1 = A_2$, after proper normalization, the gate operation is a 2-qubit unitary

gate, and it can be written as

$$G_r^{(1),\mathrm{b}} = \frac{1}{\sqrt{2}} \begin{pmatrix} 0 & 1 & i & 0 \\ -1 & 0 & 0 & i \\ -i & 0 & 0 & 1 \\ 0 & -i & -1 & 0 \end{pmatrix} \tag{3.12}$$

where we write down the gate operation in the same basis as Eq. (3.11). Notice that this gate operation is different from the one shown in Eq. (3.1). This is because of the negative state-flipping transition amplitude $A_{f,2}^x$. This gate is also equivalent to CZ gate combining with single qubit gates as,

$$G_r^{(1),\mathrm{b}} = \frac{1+i}{\sqrt{2}} \left((S^{-1}H) \otimes (SH)\right) \mathrm{CZ} \left((HS^{-1}) \otimes (HS)\right) \tag{3.13}$$

where S, H are single qubit phase gate and Hadamard gate shown in Eq. (3.4). When the two transition amplitudes are not balanced, i.e., $A_1 \neq A_2$, the gate operation shown by Eq. (3.11) is not unitary.

Now we calculate the entanglement fidelity of our 2-qubit gate. Notice that both the entanglement fidelity and the average fidelity, which can be relatively easily calculated, is proven to be related [139, 140]. Here, we use the entanglement fidelity for the quantum channel to evaluate the quality of our gate [141]. Consider a quantum channel $\mathcal{E}$ acting on quantum system Q. Suppose there is another quantum system R and there is a maximally entangled state $|\phi\rangle$ on system QR. The entanglement fidelity is defined as:

$$F_e(\mathcal{E}_Q) = \langle\phi| \left[\mathcal{I}_R \otimes \mathcal{E}_Q\right] \left(|\phi\rangle \langle\phi|\right) |\phi\rangle \tag{3.14}$$

where $\mathcal{I}_R$ is the action of the identity operation on the system R and $\mathcal{E}_Q$ is the action of the quantum channel on the system Q. In our scenario we considered a 2-qubit gate operation instead of a quantum channel to transfer a quantum state. We adapt the above definition to the entanglement fidelity of an imperfect quantum gate operation $\mathcal{G}$ as compared to the ideal quantum gate operation $\mathcal{U}$ via:

$$F_e(\mathcal{U}_Q, \mathcal{G}_Q) = \langle\phi| \left[\mathcal{I}_R \otimes (\mathcal{U}_Q^\dagger \circ \mathcal{G}_Q)\right] \left(|\phi\rangle \langle\phi|\right) |\phi\rangle \tag{3.15}$$

where $\mathcal{U}_Q$ is the desired unitary gate operation on system Q and $\mathcal{G}_Q$ is the non-ideal gate operation, notation $\circ$ stands for composition of gate operations. Note that the quantum operation $\mathcal{G}$ should be trace preserving, though it may be non-unitary. For example, the quantum operation $\mathcal{G}$, corresponding to the gate $G_r^{(1),\mathrm{ub}}$, on the system density operator ρ is,

$$\mathcal{G}_r^{(1),\mathrm{ub}}(\rho) = \frac{G_r^{(1),\mathrm{ub}} \rho \left[G_r^{(1),\mathrm{ub}}\right]^\dagger}{\mathrm{Tr}\left[G_r^{(1),\mathrm{ub}} \rho \left[G_r^{(1),\mathrm{ub}}\right]^\dagger\right]} \tag{3.16}$$

To apply the definition above to a two-qubit system, we need another two-qubit system in order to construct a maximally entangled state over the four-qubits. We choose the state $|\phi\rangle = \sum_{j=1}^{4} \frac{1}{2} |j_R\rangle |j_Q\rangle$, where $|j\rangle$ is $|g_2; g_2\rangle$, $|g_2; g_3\rangle$, $|g_3; g_2\rangle$, $|g_3; g_3\rangle$ for $j = 1$ to 4 on corresponding 2-qubit systems. With the transition amplitudes calculated at the "magic" frequency as $A_1 \sim 0.1696$ and $A_2 \sim 0.2252$, the entanglement fidelity of our gate operation shown in Eq. (3.11) is

$$F_e(\mathcal{G}_r^{(1),\mathrm{b}}, \mathcal{G}_r^{(1),\mathrm{ub}}) = \frac{(A_1 + A_2)^2}{2(A_1^2 + A_2^2)} \sim 0.981. \tag{3.17}$$

3.3.3 M2 & M3 2-qubit gate schemes: "magic" frequency, $\hat{x} \pm \hat{y}$-polarized drive light

In this subsection, we discuss two schemes, $M2$ and $M3$, to perform the 2-qubit gate operation at the "magic" frequency. In the $M2$ scheme, we choose $(\hat{x} + \hat{y})$ polarized driving light with a $(\hat{x} - \hat{y})$ polarizer (mode filter) on the collection path. In the $M3$ scheme, we also choose $(\hat{x} + \hat{y})$ polarized diving light, but use $(\hat{x} + \hat{y})$ polarizer. Scheme $M2$ results in a slightly non-unitary gate with higher success probability as compared to scheme $M3$. Scheme $M3$, on the other hand, results in a 2-qubit gate that is exactly unitary, but has a low success probability. We note that similar schemes can be constructed with the alternative choice of $(\hat{x} - \hat{y})$ polarized drive light.

To understand the gate operation when we rotate the driving light polarization, we need to know the scattered photon polarization. Suppose the driving photon is in state $|\hat{\sigma}_d\rangle = \cos(\theta) |\hat{x}\rangle_i + \sin(\theta) e^{i\phi} |\hat{y}\rangle_i$. According to Eq. (3.6), if an NV center is initialized in $|g_2\rangle$

state, the final states of the NV center and the scattered photon are

$$\begin{aligned} |g_2\rangle \otimes |\hat{\sigma}_d\rangle &\xrightarrow{H_{\text{scatter}}} |\Psi_{2;\hat{\sigma}_d}\rangle \\ &= |g_2\rangle \left(\cos(\theta) A^x_{p,2} |\hat{x}\rangle + \sin(\theta) e^{i\phi} A^y_{p,2} |\hat{y}\rangle\right) \\ &+ |g_3\rangle \left(\cos(\theta) A^x_{f,2} |\hat{y}\rangle + \sin(\theta) e^{i\phi} A^y_{f,2} |\hat{x}\rangle\right) \end{aligned} \tag{3.18}$$

where we use notation $|\Psi_{2,\hat{\sigma}_d}\rangle$ to show the final state of the NV center and the scattered photon when the initial state of NV center is $|g_2\rangle$ and the drive light is $|\hat{\sigma}_d\rangle$. Using the $\hat{\sigma}_d$ polarized driving light to pump the transition from a single NV center in state $|g_2\rangle$, the state-preserving scattered photon is in state $|\hat{\sigma}^p_2\rangle \propto \cos(\theta) A^x_{p,2} |\hat{x}\rangle + \sin(\theta) e^{i\phi} A^y_{p,2} |\hat{y}\rangle$ up to a normalization constant, while the state-flipping scattered photon is in state $|\hat{\sigma}^f_3\rangle \propto \cos(\theta) A^x_{f,2} |\hat{y}\rangle + \sin(\theta) e^{i\phi} A^y_{f,2} |\hat{x}\rangle$. Similarly, the state of the photons from the scattering process with initial state $|g_3\rangle$ are $|\hat{\sigma}^p_3\rangle \propto A^x_{p,3} \cos(\theta) |\hat{x}\rangle + A^y_{p,3} \sin(\theta) |\hat{y}\rangle$ for state-preserving photons, and $|\hat{\sigma}^f_3\rangle \propto A^x_{f,3} \cos(\theta) |\hat{y}\rangle + A^y_{f,3} \sin(\theta) e^{i\phi} |\hat{x}\rangle$ for state-flipping photons.

As we rotate the driving light from the $\hat{x}$ to $\hat{y}$ direction, the scattered photons from two state-flipping transitions do not have the same polarization, i.e., $\langle \hat{\sigma}^f_2 | \hat{\sigma}^f_3 \rangle \neq 1$ after the proper normalization of states $|\hat{\sigma}^f_2\rangle$ and $|\hat{\sigma}^f_3\rangle$. This occurs because the transition amplitudes $A^x_{f,2} = A^y_{f,3} \neq A^y_{f,2} = A^x_{f,3}$. Therefore, we need a polarizer on the collection path to erase the quantum information carried by the state-flipping photons. If the NV center in state $|g_i\rangle$ is pumped with $|\hat{\sigma}_d\rangle$ drive light and the polarizer in the collection path only allows photons in the state $|p\rangle = -\sin(\alpha) |\hat{x}\rangle_o + \cos(\alpha) e^{i\beta} |\hat{y}\rangle_o$, then the final state of the NV center heralded by a photon detection is $|\psi^{\hat{p}}_{i,\hat{\sigma}_d}\rangle \propto \langle p | \Psi_{i;\hat{\sigma}_d}\rangle$.

By rotating the driving light polarization to the direction $(\hat{x} + \hat{y})$, i.e., $|\hat{\sigma}_d\rangle_i = |+\rangle = \frac{1}{\sqrt{2}}(|\hat{x}\rangle_i + |\hat{y}\rangle_i)$, we balance the state-flipping transition rates. In this case, the state-preserving photons are polarized along $(\hat{x} - \hat{y})$ direction, and the state-flipping photons are polarized at a small angle $\pm\theta$ to the $(\hat{x} - \hat{y})$ direction, the sign being determined by the initial state of the NV center (see Fig. 4).

In scheme $M2$, we erase quantum information carried by the state-flipping photon by inserting a polarizer along the $(\hat{x} - \hat{y})$ direction in the collection path. In scheme $M3$ we use $(\hat{x} + \hat{y})$ polarizer instead.

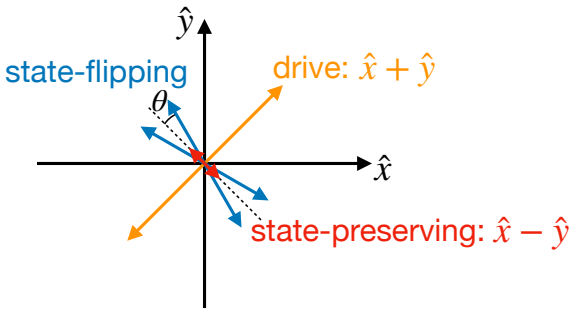

Figure 4: Polarization diagram for drive light polarized along $(\hat{x}+\hat{y})$. State-preserving scattered photons are polarized along $(\hat{x}-\hat{y})$. State flipping scattered photons are polarized in a direction $\pm\theta$ away from $(\hat{x}-\hat{y})$ (the sign being determined by the initial state of the NV center).

We now analyze scheme $M2$ and come back to scheme $M3$ below. The polarizer only allows photons in the state $|p\rangle = |-\rangle = \frac{-1}{\sqrt{2}}(|\hat{x}\rangle_o - |\hat{y}\rangle_o)$ to reach the detector. Using the relation of the transition amplitudes in Eq. (3.10), the transformation of a single NV center state after the detector captures a heralding scattered photon is described by:

$$T_s = \frac{\bar{A}}{\sqrt{A_p^2 + \bar{A}^2}} \begin{pmatrix} A_p/\bar{A} & -1 \\ 1 & -A_p/\bar{A} \end{pmatrix} \tag{3.19}$$

in the basis $|g_2\rangle$ and $|g_3\rangle$, where $\bar{A}$ is the average state-flipping transition amplitude defined as $\bar{A} = (A_1 + A_2)/2$.

Again, assuming the right detector captures a photon, the 2-qubit gate can be described by the matrix,

$$G_r^{(2)} = \frac{\bar{A}}{N} \begin{pmatrix} \frac{-(1+i)A_p}{\bar{A}} & 1 & i & 0 \\ -1 & \frac{(1-i)A_p}{\bar{A}} & 0 & i \\ -i & 0 & \frac{(i-1)A_p}{\bar{A}} & 1 \\ 0 & -i & -1 & \frac{(1+i)A_p}{\bar{A}} \end{pmatrix} \tag{3.20}$$

in the basis of $|g_2; g_2\rangle$, $|g_2; g_3\rangle$ and $|g_3; g_2\rangle$ and $|g_3; g_3\rangle$, where the normalization constant is defined as $N^2 = 2(A_p^2 + \bar{A}^2)$. Note that this gate is still not unitary. The non-unitarity is

due to the existence of the residual state-preserving photons that cannot be filtered out from the scattered light. However, since we are working at the "magic" frequency of the driving light where the state-preserving transitions are highly suppressed, the gate unitarity is only slightly broken. By the same argument as in Section 3.3.2, with state-preserving transition amplitude $A_p \sim 0.0278$, the entanglement fidelity of this gate is

$$F_e = \frac{\bar{A}^2}{\bar{A}^2 + A_p^2} \sim 0.981. \tag{3.21}$$

Since the polarization of the state-flipping photon is not aligned to the $(\hat{x} - \hat{y})$ direction exactly, the existence of the polarizer causes the desired photons to have a loss probability, which decreases the gate success probability. In an ideal experimental setup, the gate operation fails if the first state-flipping photon fails to pass the polarizer. Therefore, we calculate the probability that a photon emitted from the NV centers successfully passes the polarizer to estimate the gate success probability. This probability is given by:

$$P_- = \langle - | \operatorname{Tr}_{\mathrm{NV}}(\rho) | - \rangle = \frac{\bar{A}^2 + A_p^2}{\left(A_1^2 + A_2^2\right)/2 + A_p^2} \tag{3.22}$$

where ρ is the density operator for the NV centers and the scattered photon at the time when the scattering process has occurred but the photon has not gone through the polarizer, $|-\rangle = \frac{1}{\sqrt{2}}\left(-|\hat{x}\rangle + |\hat{y}\rangle\right)$ is the photon state that are allowed to pass the polarizer, $\mathrm{Tr}_{\mathrm{NV}}$ is the partial trace over all degrees of freedom of NV centers. In this case, the success probability of our gate is 98.1%.

Scheme $M3$ is similar to scheme $M2$, except that we orient the polarizer along $(\hat{x} + \hat{y})$ direction to only allow photons in state $|p\rangle = |+\rangle = \frac{1}{\sqrt{2}}(\hat{x} + \hat{y})$ to pass the polarizer. In this case, the gate is perfectly unitary (when operated at the "magic" frequency). Following arguments similar to the $M2$ scheme above, we find that the 2-qubit gate, conditioned on a click in the right detector, is described by the matrix:

$$G_r^{(3)} = \frac{1}{\sqrt{2}} \begin{pmatrix} 0 & 1 & i & 0 \\ 1 & 0 & 0 & i \\ i & 0 & 0 & 1 \\ 0 & i & 1 & 0 \end{pmatrix}. \tag{3.23}$$

Note that this gate operation exactly matches Eq. (3.1).

However, since the scattered photons from state-flipping transitions are nearly polarized along $(\hat{x} - \hat{y})$ direction, the component along the direction $(\hat{x} + \hat{y})$ is small, which causes a low gate success probability as most state-flipping photons are stopped by the polarizer. Similar to the previous case, the gate success probability is calculated as:

$$P_+ = \langle + | \operatorname{Tr}_{NV}(\rho) | + \rangle = \frac{(A_1 - A_2)^2 / 4}{(A_1^2 + A_2^2)/2 + A_p^2} \sim 1.9\,\%. \tag{3.24}$$

3.3.4 B1 2-qubit gate scheme: "balance" frequency drive light

Because of the orthogonality of the dipole moment matrix discussed at the beginning of Section 3.3.2, the scattered photons from state-preserving and state-flipping transitions can be fully distinguished by polarization if the driving light is along $\hat{x}$ or $\hat{y}$ direction. Therefore, besides the "magic" frequency of the driving light, we can find a frequency point for the driving light to give us balanced state-flipping transitions and use a polarizer to discard the state-preserving photons. This "balanced" point is shown in Fig. 3 by the blue arrow. If the driving light is polarized along $\hat{x}$ direction, at the "balance" frequency, the state-flipping transition amplitudes satisfy $A^x_{f,2} = A^x_{f,3}$. Combining this fact with a polarizer along $\hat{y}$ direction in the collection path, if the right detector captures the scattered photon, the 2-qubit unitary gate is described by the matrix

$$G_r^{(4)} = \frac{1}{\sqrt{2}} \begin{pmatrix} 0 & 1 & i & 0 \\ 1 & 0 & 0 & i \\ i & 0 & 0 & 1 \\ 0 & i & 1 & 0 \end{pmatrix} \tag{3.25}$$

in the same basis as Eq. (3.11).

Unlike in scheme $M3$ that was described in the previous subsection, in scheme $B1$ the state-preserving transition rate is comparable to the state-flipping transition rate. We now point out that the existence of state-preserving transitions, though the scattered photons from these transitions are completely filtered out, decoheres the initial states of the NV centers.

To understand the decoherence mechanism associated with the state-preserving transitions, we construct the master equation to describe the time evolution of the NV center. We assume the NV centers are driven by a $\hat{x}$ polarized light and the polarizer in the collection path is along $\hat{y}$ direction. For simplicity, we assume the emitted photons only couple to the right propagating modes of the waveguide and are detected by the right detector. Since the state-preserving photons are polarized along $\hat{y}$, while the state-flipping photons are polarized along $\hat{x}$, they couple to two different waveguide modes (see 3.5.1 for details). We further assume the driving light is weak and far-detuned from the excited states, so we can construct an effective Hamiltonian to describe the scattering process where only ground states $|g_2\rangle$ and $|g_3\rangle$ of NV centers appear (see 3.5.3 for details). Therefore, we can treat each NV center as a two-level system. We further treat the two waveguide modes as two thermal baths at temperature zero and trace out the photon degrees of freedom, so that the master equation for the NV centers is:

$$\partial_t \rho = B\left(2\hat{L}\rho\hat{L}^\dagger - \hat{L}^\dagger\hat{L}\rho - \rho\hat{L}^\dagger\hat{L}\right) \tag{3.26a}$$

$$+ B\left(2\hat{G}\rho\hat{G}^\dagger - \hat{G}^\dagger\rho\hat{G} - \hat{G}\rho\hat{G}^\dagger\right),$$

$$\hat{L} = A^{(x)}_{f,2}\left(i\sigma^{(1)}_{23} + \sigma^{(2)}_{23}\right) + A^{(x)}_{f,3}\left(i\sigma^{(1)}_{32} + \sigma^{(2)}_{32}\right), \tag{3.26b}$$

$$\hat{G} = A^{(x)}_{p,2}\left(i\sigma^{(1)}_{22} + \sigma^{(2)}_{22}\right) + A^{(x)}_{p,3}\left(i\sigma^{(1)}_{33} + \sigma^{(2)}_{33}\right), \tag{3.26c}$$

where $\hat{L}$ and $\hat{G}$ are two jump operators describing the state-flipping transitions and state-preserving transitions respectively, the operator $\sigma^{(i)}_{jk}$ is the operator acting on i-th NV center and flips NV state from $|g_j\rangle$ to state $|g_k\rangle$, i.e., $\sigma^{(i)}_{jk} = |g_k\rangle\langle g_j|$ for i-th NV center, and $B = \frac{2\pi n_{\text{eff}}}{c\hbar^2}$ is a constant, where n_{eff} is the mode effective refractive index (see Eq. (3.53) in 3.5.3). We find that the second term in the master equation involving $\hat{G}$ causes the off-diagonal elements of the two-NV density matrix to decay if the state-preserving transitions are not balanced. This means that if our initial state is prepared in an entangled state of two NV centers, the entanglement between the two NV centers is destroyed by these undetected state-preserving transitions, which will also limit our gate operation time at this frequency point.

We can also calculate the gate success probability using a similar method to the one illustrated by Eq. (3.22) and Eq. (3.24), which we find to be 37.4%. Note that the success probability is a "first-photon" success probability, which means we know in advance

the scatter has happened and a single scattered photon has already been emitted into the waveguide mode. In the more realistic case, we can only monitor the detector and we have no information whether the state-preserving transitions happens or not. Gate fidelity and success probability for this case will be discussed in Section. 3.4 using quantum trajectory method.

3.4 2-qubit gate fidelity and success probability

In this section, we analyze the fidelity and success probability of our proposed 2-qubit gate for NV centers with possible experimental imperfections. First of all, we notice that NV centers have a phonon side bind which causes Raman scatterings. However, these scattered photons do not have same frequencies as the driving light so that we can filter out and also monitor these photons. The existence of the phonon side band decreases the gate success probability, but does not decrease the gate fidelity. In the following discussion, we ignore the phonon side band and mainly focus on (1) the imperfect scattered photon collection and detection efficiency of the experimental setup, (2) the unbalanced state-flipping transition rates, and (3) possible population loss from the $|g_2\rangle$ and $|g_3\rangle$ manifold. We use quantum trajectory simulations with continuous measurement of the scattered photons to estimate the output state fidelity and success probability with different gate operation schemes and photon collection strategies. In the simulations we use the transition amplitudes calculated at the corresponding driving light frequency and take different types of imperfections together into consideration.

3.4.1 Imperfect scattered photon collection and detection efficiency

Unlike the quantum entanglement proposals in Ref. [127, 128, 129, 130, 131], when applying a unitary gate to two NV centers, in general, we do not know in advance which states these NV centers are. Therefore the NV centers cannot be reset back to initial input state to re-apply the gate operation. It is critical to detect the first state-flipping photon from

the two NV centers to perform the unitary gate operation successfully. One possible error source in real experiment for our proposed 2-qubit gate is the imperfect photon collection and detection efficiency of the experimental setup, which we now discuss.

If the detection efficiency of the setup is imperfect, any loss of the heralding photons indicates that undetected state-flipping transitions occurred on either of the two qubits. After missing one or several scattered photons, a photon detection projects the NV centers into an undesired 2-qubit state, which degrades the gate fidelity. To estimate the quality of the gate operation with imperfect photon detection efficiency, we perform quantum trajectory calculation with continuous measurement of the scattered photons to numerically investigate the gate fidelity and success probability.

In our model, because we only consider the scattering between the states $|g_2\rangle$ and $|g_3\rangle$, we treat NV centers as 2-level systems by using the effective Hamiltonian for the scattering process (see 3.5.3 for details). For simplicity, we ignore other imperfections, i.e., our 2-qubit gate is working at a fictitious driving frequency at which two state-preserving transitions are perfectly suppressed and the two state-flipping transitions are balanced. Therefore, the transition amplitudes in Eq. (3.26) satisfy $A^x_{p,2} = A^x_{p,3} = 0$ and $A^x_{f,2} = A^x_{f,3} \equiv A$ and thus the master equation can be written as,

$$\frac{\partial \rho}{\partial t} = -\frac{\Gamma}{2}\left(\hat{L}^\dagger \hat{L}\rho + \rho \hat{L}^\dagger \hat{L} - 2\hat{L}\rho\hat{L}^\dagger\right) \tag{3.27a}$$

$$\hat{L} = i\sigma^{(1)}_{23} + \sigma^{(2)}_{23} + i\sigma^{(1)}_{32} + \sigma^{(2)}_{32} \tag{3.27b}$$

where $\Gamma = B|A|^2$ is the state-flipping transition rates, $\sigma^{(i)}_{jk} = |g_k\rangle\langle g_j|$ is the operator for i-th NV transiting from state $|g_j\rangle$ to state $|g_k\rangle$ with $j, k = 2, 3$. Because in the present consideration, the two state-flipping transitions are balanced, the output state fidelity for all possible input states should be the same and hence the output state fidelity for a certain input state is the gate fidelity. We choose state $|\psi_i\rangle = |g_2\rangle \otimes |g_2\rangle$ as the input state. We labels the 2-NV state $|g_i\rangle \otimes |g_j\rangle$ as $|g_i; g_j\rangle$.

To calculate the output state fidelity of input state $|\psi_i\rangle = |g_2; g_2\rangle$, at the beginning of each trajectory, we initialize both NV centers in $|g_2\rangle$ state and stochastically evolve the two NV centers according to the master equation in Eq. (3.27) conditioned on the measurement result from the detector. When a photon is emitted from NV center, it has probability η to

be detected by the detector, otherwise the photon is lost into the bath. The photon detection is a projection measurement, with the jump operator $\hat{L}$ in Eq. (3.27) as the measurement projector. When a scattered photon is detected by the detector, the density matrix collapses to $\rho' \propto \hat{L}\rho\hat{L}^\dagger$ up to a normalization constant. It is obvious that if the detection efficiency $\eta = 1$, the gate operation is a 2-qubit unitary gate described by G_r in Eq. (3.1).

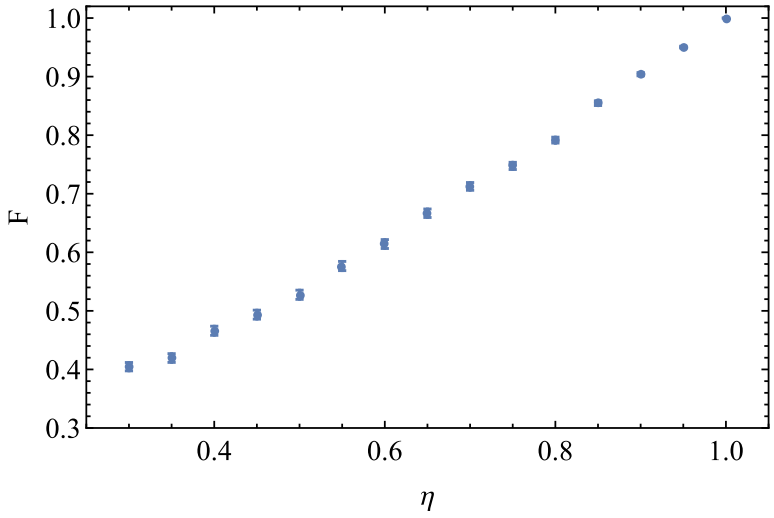

Figure 5: Unitary gate fidelity, F, drops as overall scattered photon collection efficiency, η, decreases with the first gate operation strategy (see main text).

The first strategy to perform the 2-qubit unitary gate is to run the trajectory until we receive a photon by the detector. In real experiment, it is equivalent to running the experiments until a photon is detected without limiting the collection time window. When a photon is detected, we stop the time evolution of the trajectory and calculate the output state fidelity using the target state $|\psi_t\rangle = G_r |\psi_i\rangle = \frac{1}{\sqrt{2}} (|g_2; g_3\rangle + i |g_3; g_2\rangle)$. Since we do not limit the total time to end the protocol, we always have a positive detection result and thus the gate is always considered as success. However, the gate fidelity suffers from the missing photon cases. We ran 1000 independent trajectories in total to build up statistics for the gate fidelity. The gate fidelity as a function of overall photon detection efficiency (η) is shown in Fig. 5. The numerical simulation matches our expectation that as the collection efficiency drops, it becomes more and more likely that the first scattered photon is missed, and hence the overall output state fidelity drops. When the collection efficiency $\eta = 1$, the

fidelity is 1. The fidelity drops to 0.5 when the overall photon detection efficiency drops to $\eta \sim 0.45$. Based on the proposed geometry of the diamond waveguide, we calculate the overall collection efficiency of the diamond waveguide to be 85% (see Appendix for details). At the 85% photon collection efficiency, the gate fidelity is 0.8547 ± 0.0040.

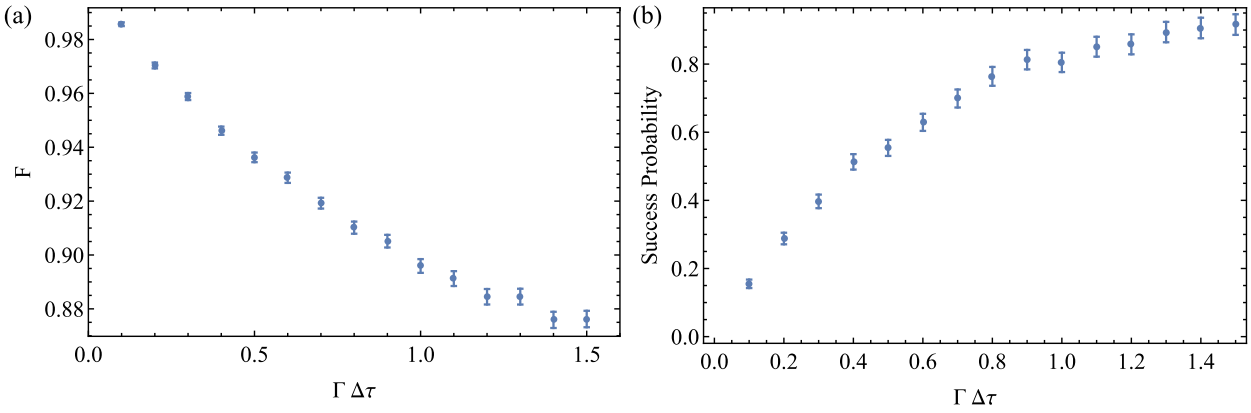

Figure 6: The missing scattered photon cases degrade the gate fidelity when photon detection efficiency is imperfect. Using the second gate operation strategy (see main text), the the gate fidelity [in (a)] and success probability [in (b)] is investigated numerically as a function of maximum collection time window ($\Delta\tau$). The overall photon detection efficiency is 85%.

The second strategy aims to improve gate fidelity with an imperfect photon detection efficiency, by limiting the maximum photon collection time window. This will help to rule out missing photon cases and improve the fidelity of the 2-qubit gate operation. However, as we decrease the collection window, it is possible not to detect any photons within the time bin, and hence the gate success probability is expected to drop as we shrink the collection window. We numerically investigate the output state fidelity and success probability as we change the duration of collection window. We use the same quantum trajectory method with a collection efficiency η to stochastically time evolve the master equation in Eq. (3.27). We still use the state $|\psi_i\rangle = |g_2; g_2\rangle$ as the input state and $|\psi_t\rangle = \frac{1}{\sqrt{2}}(|g_2; g_3\rangle + i\,|g_3; g_2\rangle)$ as the target state. If we get a positive detection result within the collection window, we stop the trajectory and measure the output state fidelity. Otherwise, if no scattered photon is detected till the end of the collection window, we reckon the gate fails and stop the trajectory. The

numerically calculated average gate fidelity and gate success probability with $\eta = 0.85$ as we change the collection window is plotted in Fig. 6(a) and Fig. 6(b) respectively. The average gate fidelity improves as we shrink the collection window, but the success probability drops, as we expected. For example, if we choose the collection window $\Gamma\Delta\tau = 0.1$, the fidelity can be improved to 0.9857 ± 0.0007, however, the success probability of the gate decreases to 0.155. To conclude, this gate operation strategy trades the successful probability for high gate fidelity.

We want to point out that Ref. [142] shows that constructing a graph or cluster state requires a minimum success probability of 1/3. In our numerical simulations this threshold can be met by setting the collection window to be $\Gamma\Delta\tau = 0.3$, which results in the gate success probability of 0.397 and an average output state fidelity of 0.9588 ± 0.0013.

3.4.2 Unbalanced state-flipping transitions

In the above calculation, we assumed that the two state-flipping transition rates are balanced. However, this assumption does not have to hold. For example, in scheme $M1$, which we discuss in Section 3.3.2, the transition rates for the two state-flipping transitions are different. Furthermore, the state-flipping transition rates of two NV centers may also be different (e.g. due to different coupling strength to the waveguide modes). In Section 3.3.2, we considered the gate fidelity when the state-flipping transitions rates are not equal, but two NV centers are identical. In this subsection we consider a more general case when the two state-flipping transitions of two NV centers emit indistinguishable scattered photons, but the rates can be different. We analyze the gate operation and the gate fidelity.

When the state-flipping transition rates are different from one NV center to the other one, we use $A_1^{(i)}$ and $A_2^{(i)}$ to note the transition amplitude for state-flipping transitions from $|g_2\rangle$ to $|g_3\rangle$ and $|g_3\rangle$ to $|g_2\rangle$ of i-th NV center. Here we assume there is no state-preserving transitions and detection efficiency is 1 to only focus on the imperfection caused by the unbalanced state-preserving transitions. We also assume the state-flipping transition amplitudes are all positive.

Similar to the previous subsection, we assume the scattered photons only couples to the

right-propagating modes, and thus the master equation of the two NV centers in this case is similar to the master equation shown in Eq. (3.26) as,

$$\frac{\partial \rho}{\partial t} = -\frac{B}{2}\left(\hat{L}^\dagger \hat{L}\rho + \rho \hat{L}^\dagger \hat{L} - 2\hat{L}\rho\hat{L}^\dagger\right) \tag{3.28a}$$

$$\hat{L} = iA_1^{(1)}\sigma_{23}^{(1)} + A_1^{(2)}\sigma_{23}^{(2)} + iA_2^{(1)}\sigma_{32}^{(1)} + A_2^{(2)}\sigma_{32}^{(2)} \tag{3.28b}$$

When a photon is captured by the detector, it corresponded to a projection measurement onto the NV centers which is described by the jump operator $\hat{L}$. Therefore the gate operation can be described by the matrix,

$$\hat{L} = \begin{pmatrix} 0 & A_2^{(2)} & iA_2^{(1)} & 0 \\ A_1^{(2)} & 0 & 0 & iA_2^{(1)} \\ iA_1^{(1)} & 0 & 0 & A_2^{(2)} \\ 0 & iA_1^{(1)} & A_1^{(2)} & 0 \end{pmatrix} \tag{3.29}$$

in the same basis as Eq. (3.11). We can use the same method as discussed in Section 3.3.2 to estimate the gate fidelity. We can define $\bar{A}$ as the average of these four state-flipping transition amplitudes as $\bar{A} = \sum_{i,j} A_j^{(i)}/4$ and the derivations of each specific transition amplitude from this average amplitude by $\delta_{i,j} = A_j^{(i)} - \bar{A}$. When the four transition amplitudes are not severely unbalanced, i.e., $\left|\delta_{i,j}/\bar{A}\right| \ll 1$, we can expand the output state fidelity in series of $\delta_{i,j}/\bar{A}$. In general, the gate fidelity will drop linearly as $\delta_{i,j}^2/\bar{A}^2$ increases. As we see from Section 3.3.2, when $A_i^{(1)} = A_i^{(2)}$, the deviation of the transition amplitudes $\delta_{i,1} = -\delta_{i,2} \equiv \delta$. The gate fidelity can then be expanded as,

$$F = \frac{\bar{A}^2}{\bar{A}^2 + \delta^2} \sim 1 - \frac{\delta^2}{\bar{A}^2} \tag{3.30}$$

Let's also discuss the case when two state-flipping transition amplitudes for a single NV center are balanced, however, the same transitions for different NV centers have a constant transition amplitude offset. In this case, we assume $A_j^{(1)} = \bar{A} - \delta$, and $A_j^{(2)} = \bar{A} + \delta$. The gate fidelity is also given by Eq. (3.30).

3.4.3 Overall output state fidelity

In this subsection, we evaluate the gate quality by numerically simulating the output state fidelity and success probability with the four possible gate operation schemes discussed in Section 3.3 combined with the two proposed collection strategies discussed in Section 3.4.1. The four gate operation schemes are summarized in Table. 2. The two collection strategies are collecting the photon (1) without and (2) with a maximum collection window $\Delta\tau$.

With all four gate operation schemes, we explore the output state fidelity when state $|\psi_1\rangle = |g_2; g_2\rangle$, $|\psi_2\rangle = |g_2; g_3\rangle$ and $|\psi_3\rangle = \frac{1}{\sqrt{2}}(|g_2; g_2\rangle + i\,|g_3; g_3\rangle)$ as the gate input states using quantum trajectory simulation with continuous measurement on the scattered photons. We set the overall collection efficiency of the photons through the polarizer to 85%. The gate average fidelity and gate success probability without and with a maximum collection time window $\Delta\tau = 0.1/\bar{\Gamma}_f$ is shown in Table 3. Here, $\bar{\Gamma}_f$ is the average state-flipping transition rates, $\bar{\Gamma}_f = (A_1^2 + A_2^2)/2$, where A_1 and A_2 is the absolute value of the state-flipping transition amplitudes at the working frequency [see Eq. (3.6)]. We also listed the output state fidelity with corresponding gate operation schemes with perfect photon detection efficiency and infinite pump power for reference, which set a theoretical upper bound for the output state fidelity in the corresponding cases.

To estimate the gate fidelity of the different schemes we use the worst output state fidelity in Table 3. $M3$ and $B1$ are two schemes that are perfectly unitary in ideal conditions. When we don't setup a finite collection window, since the gate operation scheme $M3$ suffers low success probability, even with perfect collection efficiency, the output state fidelity drops significantly from unity. This is because most of the detected photons are from the long-time scatter events, i.e., the NV center system tends to relax to its steady state before the heralding photon is detected. Therefore, it is equivalent to applying the gate to the steady state of the master equation, which gives an output state fidelity ≈ 0.25. If we don't limit the collection window, the gate operation scheme $B1$ has significantly different output state fidelity when the input state is $|\psi_1\rangle$ (or $|\psi_2\rangle$) and $|\psi_3\rangle$. This is because the undetected state-preserving transitions decohere the input state, even though they do not flip the NV spin states and their photons are perfectly separated from the state-flipping photons. The

Table 3: Output state fidelity and gate success probability for input states $|\Psi_1\rangle = |g_2; g_2\rangle$, $|\Psi_2\rangle = |g_2; g_3\rangle$, $|\Psi_3\rangle = \frac{1}{\sqrt{2}}(|g_2; g_2\rangle + i\,|g_3; g_3\rangle)$ with the four gate operation schemes, $M1$, $M2$, $M3$ and $B1$ (see Table. 2), when the photon collection efficiency is perfect (labeled Perfect Collection), imperfect with an infinite photon collection time window (labeled $\eta = 0.85, \bar{\Gamma}_f \Delta\tau = \infty$), and imperfect with a finite photon collection time window (labeled $\eta = 0.85, \bar{\Gamma}_f \Delta\tau = 0.1$). Note for the case of perfect collection, and the case of imperfect collection with infinite photon collection time window $P = 1$.

Input State	Perfect Collection	$\eta = 0.85$ $\bar{\Gamma}_f \Delta\tau = \infty$	$\eta = 0.85$ $\bar{\Gamma}_f \Delta\tau = 0.1$	
	F	F	F	P
$M1$				
$\|\Psi_1\rangle$	1.0	0.848 ± 0.004	0.9896 ± 0.0006	0.106
$\|\Psi_2\rangle$	0.981	0.837 ± 0.005	0.9704 ± 0.0005	0.164
$\|\Psi_3\rangle$	0.981	0.824 ± 0.005	0.9665 ± 0.0006	0.156
$M2$				
$\|\Psi_1\rangle$	0.981	0.819 ± 0.005	0.9683 ± 0.0006	0.172
$\|\Psi_2\rangle$	0.981	0.824 ± 0.005	0.9678 ± 0.0006	0.166
$\|\Psi_3\rangle$	0.981	0.823 ± 0.005	0.9683 ± 0.0006	0.169
$M3$				
$\|\Psi_1\rangle$	1.0	0.255 ± 0.002	0.916 ± 0.004	0.0037
$\|\Psi_2\rangle$	1.0	0.256 ± 0.002	0.902 ± 0.004	0.0035
$\|\Psi_3\rangle$	1.0	0.255 ± 0.002	0.911 ± 0.004	0.0033
$B1$				
$\|\Psi_1\rangle$	1.0	0.859 ± 0.004	0.9870 ± 0.0006	0.172
$\|\Psi_2\rangle$	1.0	0.857 ± 0.004	0.9842 ± 0.0007	0.153
$\|\Psi_3\rangle$	1.0	0.571 ± 0.006	0.906 ± 0.004	0.150

input state $|\psi_3\rangle$ decoheres to an equal mixture of states $|g_2; g_2\rangle$ and $|g_3; g_3\rangle$, which makes the output state-fidelity drop to ≈ 0.5. The finite collection time window helps to discard the long-time detection events, which improves the output-state fidelity significantly, especially for the gate operation scheme $M3$.

Gate operation schemes $M1$ and $M2$ are not perfectly unitary even in the ideal case. However, since the polarizer setup has little probability to block the state-flipping photons and the state-preserving transitions are highly suppressed due to the "magic" frequency of the driving light, these two schemes behave much better when the collection time is not limited. When we have a finite collection window, the output state fidelity also improves. Compared to the gate operation schemes $M3$ and $B1$, the schemes $M1$ and $M2$ have better output state fidelity.

We comment that schemes $M3$ and $B1$ can, in principle, reach sufficiently high fidelity so as to overcome the error correction threshold. This would make it possible to implement error correction codes like the surface code [143, 144]. At present, achieving this goal requires (1) significant progress in optical single photon detectors and (2) device optimization that is closely tied to the device fabrication process.

3.4.4 Population loss due to the transition out of the $|g_2\rangle$, $|g_3\rangle$ manifold

Any process that transfers population out of $|g_2\rangle$ and $|g_3\rangle$ manifold, i.e., to the other states like $|g_1\rangle$, results in no further photon detections after this "leakage" transition happens. This will degrade the success probability of the gate. There are two possible leakage paths, (1) by the Raman scattering process to state $|g_1\rangle$, (2) by exciting to the NV electronic excited states then by the non-radiative relaxation through the meta-stable states of NV centers to $|g_1\rangle$.

To examine the effect of spin Raman transition from logic states $|g_2\rangle$ and $|g_3\rangle$ to state $|g_1\rangle$, we refer to the dipole matrix in Eq. (3.41) in 3.5.2, and calculate the leakage transition amplitudes as,

$$\frac{A^x_{l,2}}{A^{(x)}_0} = \frac{1}{\Delta_1} F_{21} F_{11} - \frac{1}{\Delta_3} F_{22} F_{12} \tag{3.31a}$$

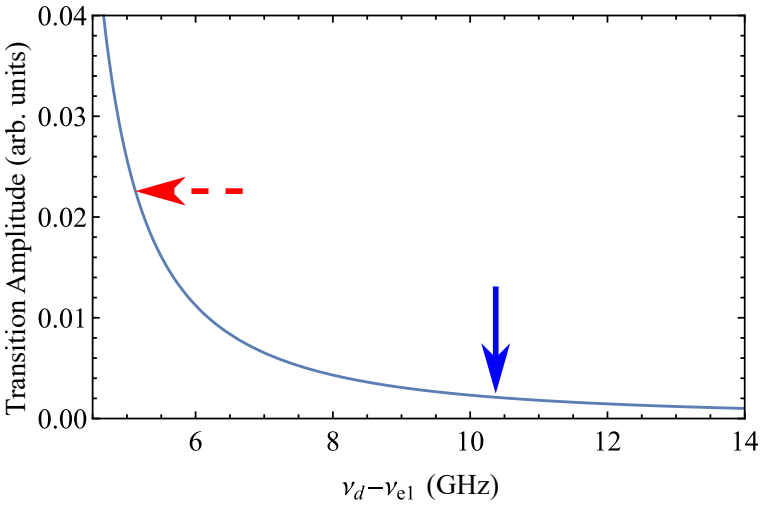

Figure 7: We study the population leakage from state $|g_2\rangle$ and $|g_3\rangle$ manifold into state $|g_1\rangle$ state caused by spin-Raman transitions. We plot the transition rate under the same pumping laser as in Fig. 3. The "magic" frequency is pointed out by the red dashed arrow while the "balance" frequency is labeled by the blue solid arrow. The population leakage rate by spin-Raman transition is much slower than the state-flipping transitions shown in Fig. 3 and hence we do not expect to see large population within the detection window.

$$\frac{A^y_{l,2}}{A^{(y)}_0} = -\frac{1}{\Delta_1}F_{21}F_{11} + \frac{1}{\Delta_3}F_{22}F_{12} \tag{3.31b}$$

$$\frac{A^x_{l,3}}{A^{(y)}_0} = -\frac{1}{\Delta_2}F_{21}F_{11} + \frac{1}{\Delta_4}F_{22}F_{12} \tag{3.31c}$$

$$\frac{A^y_{l,3}}{A^{(x)}_0} = -\frac{1}{\Delta_1}F_{21}F_{11} + \frac{1}{\Delta_3}F_{22}F_{12} \tag{3.31d}$$

Where $F_{11} = 0.0513$ and $F_{12} = 0.9987$ are two dimensionless parameters from the dipole moments between eigenstates of spin-orbit and spin-spin Hamiltonian of single NV centers (see Eq. (3.41) in 3.5.2), Δ_i are the energy mismatch for excited level $|e_i\rangle$. If we consider the fact that the excited states $|e_1\rangle$ and $|e_2\rangle$, $|e_3\rangle$ and $|e_4\rangle$ are energetically degenerate, i.e., $\Delta_1 = \Delta_2$, $\Delta_3 = \Delta_4$, these four transition amplitudes satisfies $-\frac{A^x_{l,2}}{A^{(x)}_0} = \frac{A^y_{l,2}}{A^{(y)}_0} = \frac{A^x_{l,3}}{A^{(y)}_0} = \frac{A^y_{l,3}}{A^{(x)}_0}$. We plot the magnitude of R.H.S of Eq. (3.31) in Fig. 7, and label the "magic" point and "balance" point by red dashed and blue solid arrows respectively. At the "balance" point, the leak transition amplitudes are two orders of magnitudes smaller than the state-flipping transition amplitudes and hence have little impact on the gate operation scheme $B1$. The population of the NV centers in ground states $|g_2\rangle$ and $|g_3\rangle$ decays slowly to $|g_1\rangle$ due to the existence of the leakage transitions, which sets a maximum gate operation window to avoid significant population loss.

At the "magic" point, the leak transition amplitudes are comparable to the state-preserving transition amplitudes. Note that this suppression is not due to the interference. Instead, it is mainly suppressed by the small mixing of excited spin $S_z = 0$ states with spin $S_z = \pm 1$ states that caused by the spin-spin interaction [137]. Compared to the state-flipping transition amplitudes, the leakage transition amplitudes are approximately ten times smaller than the state-flipping transition amplitudes. The gate operation schemes working at the "magic" frequencies are not severely affected.

To quantitatively estimate the effect of the non-radiative relaxation process, we approximate the dynamics of NV centers with the metastable spin-singlet states as a three-level system, ground state $|0\rangle$, excited state $|1\rangle$ and meta-stable state $|2\rangle$. The transition between states $|0\rangle$ and $|1\rangle$ are driven by an off-resonance classical laser field. The non-radiative relaxation process from state $|1\rangle$ to meta-stable state $|2\rangle$ are modeled by the coupling to a thermal

optical phonon bath with temperature zero. Therefore the dynamics can be described by the master equation

$$\partial_t \rho = -i(2\pi)\left[-\delta\sigma_{00} + \Omega_R\left(\sigma_{01} + \sigma_{10}\right),\, \rho\right] + \mathcal{L}\rho, \tag{3.32a}$$

$$\mathcal{L}\rho = -\frac{\Gamma_{NR}}{2}\left(\sigma_{11}\rho + \rho\sigma_{11} - 2\sigma_{21}\rho\sigma_{12}\right), \tag{3.32b}$$

where operators σ_{ij} are defined by $\sigma_{ij} = |i\rangle\langle j|$, $h\delta = \epsilon_1 - \epsilon_0 - h\nu_d$ is the detuning of the drive field, ϵ_i is the energy of the state $|i\rangle$, $h\Omega_R = p_0 E_d$ is the Rabi frequency, p_0 is the dipole moment for the optical transition between $|0\rangle$ and $|1\rangle$, which is approximated as $p_0 \approx 5.2$ Debye (see 3.5.3 and Ref. [145]), E_d is the driving light electric field, Γ_{NR} is the non-radiative relaxation rate from state $|1\rangle$ to $|2\rangle$.

We estimate the non-radiative relaxation rate Γ_{NR} by the lifetime of the excited levels of NV centers. In Ref. [138], a six-level model is introduced to describe the NV center electronic structure. The excited manifold is simplified as two states with quantum number $S_z = 0$ and $S_z = \pm 1$, with measured lifetime 12.0 ns and 7.8 ns respectively [146]. We further assume that the excited state $S_z = 0$ has no relaxation path to the meta-stable state and the radiative relaxation from excited states back to ground states of NV centers are the same, and hence the non-radiative relaxation rate from excited state $S_z = \pm 1$ can be estimated using the difference of the lifetimes of these two excited states as $\Gamma_{\mathrm{NR}} \approx 44.9$ MHz.

We approximate the detuning by the smallest detuning of our driving light, to one of the four excited states with $S_z \sim \pm 1$, i.e., $|e_1\rangle$, $|e_2\rangle$, $|e_5\rangle$ and $|e_6\rangle$. If our proposed gate is working at the "magic" frequency of the driving light, the detuning $\delta \approx 3.95$ GHz for a $\hat{y}$ polarized driving light and 5.11 GHz for a $\hat{x}$ polarized driving light. Clearly, $\Gamma_{\mathrm{NR}}/\delta \ll 1$, so that we work in the dressed-state basis and then treat the Lindblad term $\mathcal{L}\rho$ in Eq. (3.32) as a perturbation.

In our previous treatment of scattering transitions, we implicitly assumed that the Rabi frequency is small compared to detuning, i.e., $\Omega_R/\delta \ll 1$. The dressed state basis for the Hamiltonian in Eq. (3.32) is $|-\rangle \sim |0\rangle - \frac{\Omega_R}{\delta}|1\rangle$ and $|+\rangle \sim |1\rangle + \frac{\Omega_R}{\delta}|0\rangle$. If all the population is in state $|0\rangle$ at the beginning, we would expect most of the population will be remain in the state $|-\rangle$ after we start driving the Rabi oscillation. Since the non-radiative relaxation removes the population in state $|1\rangle$ only, the decay rate for the population in state $|-\rangle$ is

$\Gamma_- \sim \Gamma_{\mathrm{NR}}\sigma_{11}\left|-\right\rangle\left\langle-\right|\sigma_{11} \sim \Gamma_{\mathrm{NR}}\frac{\Omega_R^2}{\delta^2} \propto E_d^2$. As we show in 3.5.3, the state-flipping transition rate at the "magic" point is $\Gamma_t \sim \Gamma_0 \propto E_d^2$, we can calculate the ratio between the lower state-flipping transition rates versus the non-radiative relaxation rate as $\Gamma_t/\Gamma_- \sim 1.63$ and 0.975 for $\hat{x}$ and $\hat{y}$ polarized driving light respectively, which are independent of the driving strength E_d. These two ratios set a hard limit on the collection time window of the scattered photon before the population is lost.

We perform the same calculation at the "balance" point, and determine the hard limit on the collection window. As the "balance" point is located between the excited states $|e_5\rangle$ and $|e_6\rangle$, this balance frequency for gate operation is more vulnerable to population loss. The transition ratio Γ_t/Γ_- is calculated as 0.744 and 0.412 for $\hat{x}$ and $\hat{y}$ polarized driving light at "balance" point. We summarize the parameters we used and the results in Table 4 for reference.

3.5 Detailed calculation for two-qubit gate schemes for NV centers

3.5.1 Waveguide modes and the NV center coupling strength

In this section of the appendix, we analyze the triangular diamond waveguide and its mode profiles. The triangular diamond waveguide we proposed in our paper has 300 nm edge. The diamond waveguide can be experimentally fabricate using anisotropic plasma etching [147]. The mode profiles are calculated by solving eigenproblem of discretized transverse Maxwell equation using Lumerical Mode solution solver. There are only two degenerate guided modes at the "magic" frequency. The mode profiles are shown in Fig. 8. The modes are normalized according to,

$$\int dxdy\epsilon_r(x,y)\vec{E}_m^*(x,y)\cdot\vec{E}_n(x,y) = \delta_{m,n} \tag{3.33}$$

where indices m and n are for modes, ϵ_r is the relative permittivity.

To calculate the light collection efficiency of the diamond waveguide, we treat the NV-center as a dipole moment $\vec{p} = |p|\cdot\hat{p}$ located at position $\vec{r}_0$, where $\hat{p}$ is the unit vector along

Table 4: Summary of the parameters we used for estimating the effect of the non-radiative relaxations. We also listed the smallest frequency detuning when the drive light is at the "magic" frequency and the "balanced" frequency and the corresponding ratio between lower state-flipping transition rate versus the non-radiative relaxation rate, Γ_t/Γ_-.

NV-center electronic dipole moment	p_0	5.2 Debye
Non-radiative relaxation rate for NV excited states	Γ_{NR}	44.9 MHz
$\hat{x}$-polarized drive at "magic" frequency	detuning δ	5.11 GHz
	transition rates ratio Γ_t/Γ_-	1.63
$\hat{y}$-polarized drive at "magic" frequency	detuning δ	3.95 GHz
	transition rates ratio Γ_t/Γ_-	0.975
$\hat{x}$-polarized drive at "balance" frequency	detuning δ	3.45 GHz
	transition rates ratio Γ_t/Γ_-	0.744
$\hat{y}$-polarized drive at "balance" frequency	detuning δ	2.57 GHz
	transition rates ratio Γ_t/Γ_-	0.412

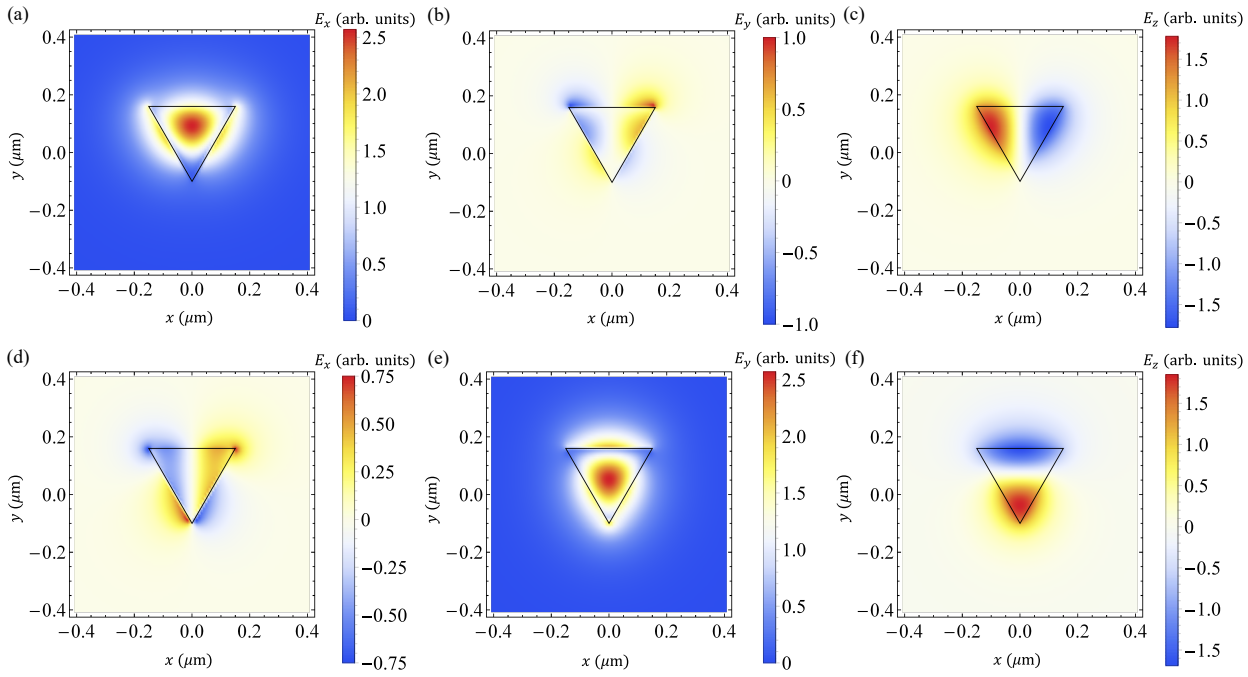

Figure 8: The mode profiles of the triangular diamond waveguide. The waveguide has 300 nm edge. The diamond waveguide supports two degenerate propagating modes. Mode 1 E_x, E_y and E_z components are plotted in (a) to (c), while mode 2 components are plotted in (d) to (f).

the dipole moment. We only consider the dipole interaction between NV-centers and the modes inside the waveguide. If we have a well defined mode in the cross-section, whose electric field is $\vec{E}_n(\vec{r})$, the emission rate from the NV-center to this mode Γ_n is proportional to $|p|^2 \cdot |\vec{E}_n(\vec{r}_0) \cdot \hat{p}|^2$. For a complete set of orthonormal modes in space with frequency of emission light $\{\vec{E}_n(\vec{r})\}$, the total rate can be calculated as $\Gamma_{\text{total}} = \sum_n |p|^2 \cdot |\vec{E}_n(\vec{r}_0) \cdot \hat{p}|^2$. Therefore, the collection efficiency of the waveguide is,

$$\eta(\vec{r}_0) = \frac{\sum_n' |\vec{E}_n(\vec{r}_0) \cdot \hat{p}|^2}{\sum_n |\vec{E}_n(\vec{r}_0) \cdot \hat{p}|^2}, \tag{3.34}$$

where $\sum_n'$ is the summation over the guided modes only, an $\sum_n$ is the summation over all the modes in the complete set of orthonormal modes.

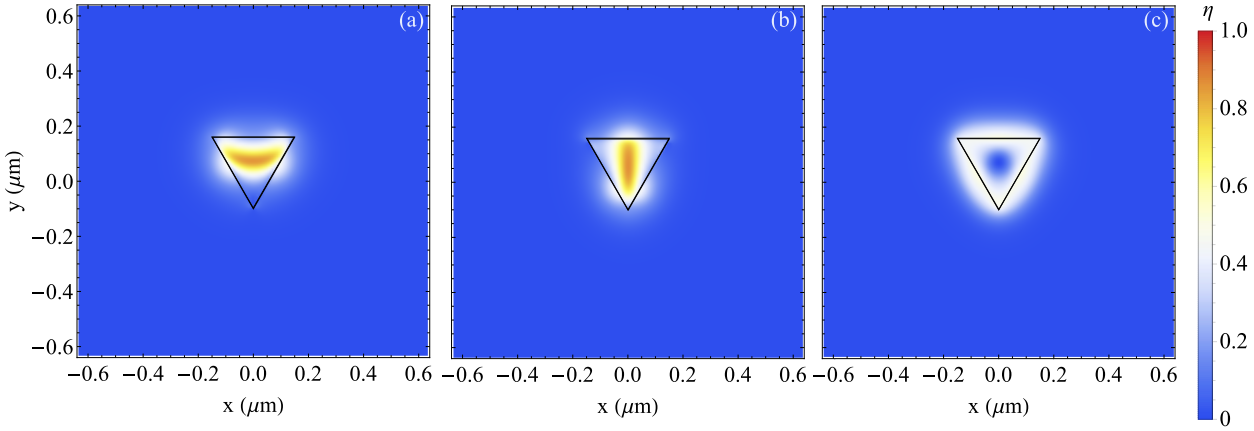

Figure 9: The diamond waveguide collection efficiency of the Raman photon emitted from a NV-center located in the cross-section of the waveguide. The NV-center is modeled as a dipole moment. The black triangle labeled in the plot shows the diamond waveguide boundary. The collection efficiency of photons when the dipole moment is pointing along x, y and z direction is plotted in (a), (b) and (c).

In the numerical approach, we cannot solve an infinite large region. Instead, we solve the modes using a finite size cross-section region. The boundary condition around the region is chosen as perfect matched layer (PML) to simulate the infinite space. We plot the collection efficiency of the diamond waveguide with a dipole moment pointing along x, y and z direction at different position in this cross-section in Fig. 9. From the figure, the collection efficiency

for a NV-center whose electric dipole moment is along the x or y direction is $\eta \approx 0.86$. However, when the dipole moment is pointing along z direction, the collection efficiency is poor because a dipole moment pointing along z direction mainly radiates in a direction transverse to the direction of the waveguide.

Assuming the NV center is centered in the waveguide, i.e., $x, y \sim 0$, and the NV center is orientated as Fig. 1(c) shows, the optical dipole moment is along the transverse direction of the waveguide. According to Fig. 9, the NV center optical transitions with $\hat{x}$ dipole moment strongly couples to the mode 1 and almost no coupling to mode 2, while the transitions with $\hat{y}$ dipole moment strongly couples to the mode 2 and almost no coupling to mode 1.

3.5.2 Dipole moment of NV-centers without external magnetic field

In this section, we discuss the NV center dipole moment matrix for optical transitions between electronic ground and excited state of NV centers with spin-orbit, spin-spin interactions, and with strain field in diamond crystal. We assume there is no magnetic field applied to the NV center. Here, we follow the notation of Ref. [137], which gives a detailed review of the electronic properties of negatively charged NV centers. We want to stress that the directions $\hat{x}$, $\hat{y}$ and $\hat{z}$ in this section are the intrinsic directions of an NV center. The direction $\hat{z}$ is defined as the axial direction of NV center, i.e., the direction along the nitrogen atom and the vacancy site, which is the [111] direction of the diamond crystal.

The NV center electronic fine states structure is shown in Fig. 3(a) of our main paper. Here we assume the dipole moment operator $\hat{\vec{p}}$ between the molecule orbits of NV-centers are,

$$\langle e_x | \hat{\vec{p}} | a_1 \rangle = p_0 \cdot \hat{x} \quad , \quad \langle e_y | \hat{\vec{p}} | a_1 \rangle = p_0 \cdot \hat{y} \tag{3.35}$$

where $|a_1\rangle$, $|e_x\rangle$ and $|e_y\rangle$ are molecule orbits of NV centers [137], $\hat{x}$ and $\hat{y}$ are unit vector pointing along x or y direction. We note that the state $|e_y\rangle$ has intrinsic dipole moment and $\langle e_x | \hat{\vec{p}} | e_y \rangle$ is non-zero. However, since we only consider the transition between spin-triplet ground states and excited states of an NV center, the assumption in Eq. (3.35) is enough. The equality of the magnitude of these two dipole moment is guaranteed by Wigner-Echart theorem.

Using Eq. (3.35) with Table 1 (and Table A.1) in Ref. [137], we can calculate the dipole moment operators between the electronic fine levels of ground and excited states. Here we only consider spin 1 states whose energy is inside the diamond band gap. Because the dipole transition does not interact with spin degree of freedom, the spin projection along z direction should be invariant. The non-zero dipole moment operator elements between definite orbital symmetry states are:

$$\langle A_2, 1, 0| \hat{\vec{p}} |E_x, 1, 0\rangle = p_0 \cdot \hat{y} \tag{3.36a}$$

$$\langle A_2, 1, 0| \hat{\vec{p}} |E_y, 1, 0\rangle = p_0 \cdot \hat{x} \tag{3.36b}$$

$$\langle A_2, 1, +1| \hat{\vec{p}} |E_x, 1, +1\rangle = p_0 \cdot \hat{y} \tag{3.36c}$$

$$\langle A_2, 1, +1| \hat{\vec{p}} |E_x, 1, +1\rangle = p_0 \cdot \hat{x} \tag{3.36d}$$

$$\langle A_2, 1, -1| \hat{\vec{p}} |E_x, 1, -1\rangle = p_0 \cdot \hat{y} \tag{3.36e}$$

$$\langle A_2, 1, -1| \hat{\vec{p}} |E_x, 1, -1\rangle = p_0 \cdot \hat{x} \tag{3.36f}$$

Here the states are labeled as $|k, S, S_z\rangle$, where k labels the lattice symmetry group irreducible representations, S is the spin quantum number, S_z is the z-direction spin projection quantum number. These states can be found in Ref. [137] Table 1 and Table A.1. For completeness, we list them using hole representation here,

$$|A_2, 1, 0\rangle = \left(|e_x \bar{e_y}\rangle + |\bar{e_x} e_y\rangle\right)/\sqrt{2} \tag{3.37a}$$

$$|E_x, 1, 0\rangle = \left(|\bar{a_1} e_x\rangle + |a_1 \bar{e_x}\rangle\right)/\sqrt{2} \tag{3.37b}$$

$$|E_y, 1, 0\rangle = \left(|\bar{a_1} e_y\rangle + |a_1 \bar{e_y}\rangle\right)/\sqrt{2} \tag{3.37c}$$

$$|A_2, 1, 1\rangle = |\bar{e_x} \bar{e_y}\rangle \tag{3.37d}$$

$$|E_x, 1, 1\rangle = |\bar{a_1} \bar{e_x}\rangle \tag{3.37e}$$

$$|E_y, 1, 1\rangle = |\bar{a_1} \bar{e_y}\rangle \tag{3.37f}$$

$$|A_2, 1, -1\rangle = |e_x e_y\rangle \tag{3.37g}$$

$$|E_x, 1, -1\rangle = |a_1 e_x\rangle \tag{3.37h}$$

$$|E_y, 1, -1\rangle = |a_1 e_y\rangle \tag{3.37i}$$

where the bar denotes spin-down.

Similarly, we can also find the dipole moment operators between definite spin-orbital symmetry states which are shown in Table 1 of Ref. [137]. The states $|g_1\rangle$, $|g_2\rangle$ and $|g_3\rangle$ are used to label states $\Phi^{\mathrm{SO}}_{1,A_1}$, $\Phi^{\mathrm{SO}}_{2,E,x}$ and $\Phi^{\mathrm{SO}}_{2,E,y}$ in Ref. [137] respectively. Since these states do not mix under spin-orbit and spin-spin interactions, we write them down explicitly here for ease of use later,

$$|g_1\rangle = |A_2, 1, 0\rangle \tag{3.38a}$$

$$|g_2\rangle = \frac{-1}{\sqrt{2}} \left(|A_2, 1, 1\rangle - |A_2, 1, -1\rangle\right) \tag{3.38b}$$

$$|g_3\rangle = \frac{-i}{\sqrt{2}} \left(|A_2, 1, 1\rangle + |A_2, 1, -1\rangle\right). \tag{3.38c}$$

We also write down the excited fine levels with definite spin-orbit symmetry, which we label $|e_1\rangle$ to $|e_6\rangle$ here (these are labeled $\Phi^{\mathrm{SO}}_{5,E,x}$, $\Phi^{\mathrm{SO}}_{5,E,y}$, $\Phi^{\mathrm{SO}}_{6,E,x}$, $\Phi^{\mathrm{SO}}_{6,E,x}$, $\Phi^{\mathrm{SO}}_{7,A_2}$ and $\Phi^{\mathrm{SO}}_{8,A_1}$ in Ref. [137]):

$$\begin{aligned} |e_1\rangle = \Phi^{\mathrm{SO}}_{5,E,x} = \frac{1}{2}[&-i \left(|E_x, 1, 1\rangle + |E_x, 1, -1\rangle\right) \\ &- \left(-|E_y, 1, 1\rangle + |E_y, 1, -1\rangle\right)] \end{aligned} \tag{3.39a}$$

$$\begin{aligned} |e_2\rangle = \Phi^{\mathrm{SO}}_{5,E,y} = \frac{1}{2}[&- \left(-|E_x, 1, 1\rangle + |E_x, 1, -1\rangle\right) \\ &+ i \left(|E_y, 1, 1\rangle + |E_y, 1, -1\rangle\right)] \end{aligned} \tag{3.39b}$$

$$|e_3\rangle = \Phi^{\mathrm{SO}}_{6,E,x} = -|E_y, 1, 0\rangle \tag{3.39c}$$

$$|e_4\rangle = \Phi^{\mathrm{SO}}_{6,E,y} = |E_x, 1, 0\rangle \tag{3.39d}$$

$$\begin{aligned} |e_5\rangle = \Phi^{\mathrm{SO}}_{7,A_2} = \frac{1}{2}[&\left(-|E_x, 1, 1\rangle + |E_x, 1, -1\rangle\right) \\ &+ i \left(|E_y, 1, 1\rangle + |E_y, 1, -1\rangle\right)] \end{aligned} \tag{3.39e}$$

$$\begin{aligned} |e_6\rangle = \Phi^{\mathrm{SO}}_{8,A_1} = \frac{1}{2}[&-i \left(|E_x, 1, 1\rangle + |E_x, 1, -1\rangle\right) \\ &+ \left(-|E_y, 1, 1\rangle + |E_y, 1, -1\rangle\right)] \end{aligned} \tag{3.39f}$$

The non-zero dipole moment operator matrix elements can be calculated for states of definite spin-orbital (SO) symmetry using the molecular orbitals. The dipole moment operators

between the SO ground and excited state are labeled $\hat{\vec{p}}_{i,j} = \langle g_i | \hat{\vec{p}} | e_j \rangle$, and can be represented as a matrix:

$$\hat{\vec{p}}_{i,j} = p_0 \cdot \begin{pmatrix} \mathbf{0} & \mathbf{0} & \hat{x} & \hat{y} & \mathbf{0} & \mathbf{0} \\ -\frac{\hat{x}}{\sqrt{2}} & \frac{\hat{y}}{\sqrt{2}} & \mathbf{0} & \mathbf{0} & -\frac{\hat{y}}{\sqrt{2}} & \frac{\hat{x}}{\sqrt{2}} \\ \frac{\hat{y}}{\sqrt{2}} & \frac{\hat{x}}{\sqrt{2}} & \mathbf{0} & \mathbf{0} & \frac{\hat{x}}{\sqrt{2}} & \frac{\hat{y}}{\sqrt{2}} \end{pmatrix}. \tag{3.40}$$

Here **0** indicates forbidden in dipole transitions. Note, this dipole moment operator matrix is consistent with the group symmetry prediction shown in Table A.4 of the Ref. [137].

Furthermore, the spin-orbit interaction and spin-spin (SS) Hamiltonian given in the basis of SO states can be found in Ref. [137] Table 2 and Table 3. Due to the large energy separation between the electronic ground states and excited states, the matrix elements out of the block of ground states or excited states are ignored, i.e., the perturbation theory can applied to the electronic ground states and excited states separately. The perturbation Hamiltonian for SO and SS interactions in ground state manifold, $V_g = V_g^{(\mathrm{SO})} + V_g^{(\mathrm{SS})}$, is diagonal, which means the states $|g_1\rangle$, $|g_2\rangle$ and $|g_3\rangle$ are still the eigenstates of the NV-center with SO interaction ($V_g^{(\mathrm{SO})}$) and SS interaction ($V_g^{(\mathrm{SS})}$). However, the perturbation Hamiltonian in the excited state manifold, $V_e = V_e^{(SO)} + V_e^{(SS)}$, is not diagonal. Besides affecting the level splitting, the perturbation interaction Hamiltonian results in mixing of the excited state.

We can find a unitary matrix U_e to diagonalize the excited state perturbation Hamiltonian V_e by $U_e V_e U_e^\dagger$. The eigenstates of the new basis can be transformed from the SO basis by applying the unitary matrix U_e to the SO basis. Therefore, the dipole moment operator between the ground states and the new excited states can be found by treating $\left(\hat{\vec{p}}_{i,j}\right)$ in Eq. (3.40) as a matrix and applying $\left(\hat{\vec{p}}_{i,j}\right) \cdot U_e^\dagger$. After taking the SS interactions into consideration, the excited state $|e_1\rangle$ mixes with state $|e_3\rangle$, state $|e_2\rangle$ mixes $|e_4\rangle$, which results in small but non-zero dipole moment matrix elements between ground states $|g_2\rangle$ and $|g_3\rangle$ to the excited states $|e_3\rangle$ and $|e_4\rangle$. The eigenstates that diagonalize the SO and SS interaction Hamiltonian in NV electronic excited states are noted as SS basis of the NV center excited states and they are labeled as $|\tilde{e}_i\rangle$ for $i = 1$ to 6. Note that the notation $|e_i\rangle$ in our main paper refers to the SS basis states instead. The dipole moment operator between NV ground

states and SS basis states of excited states is

$$\frac{\hat{\vec{p}}}{p_0} = \begin{pmatrix} -F_{11}\hat{x} & -F_{11}\hat{y} & F_{12}\hat{x} & F_{12}\hat{y} & \vec{0} & \vec{0} \\ -F_{21}\hat{x} & F_{21}\hat{y} & -F_{22}\hat{x} & F_{22}\hat{y} & -F_{23}\hat{y} & F_{23}\hat{x} \\ F_{21}\hat{y} & F_{21}\hat{x} & F_{22}\hat{y} & F_{22}\hat{x} & F_{23}\hat{x} & F_{23}\hat{y} \end{pmatrix} \tag{3.41}$$

where $F_{11} = 0.0513$, $F_{12} = 0.9987$, $F_{21} = 0.7062$, $F_{22} = 0.0363$, $F_{23} = 1/\sqrt{2}$.

The strain field ($\vec{\xi}$) can also affect the NV electronic states. The strain field interactions to the NV electronic ground states are much smaller than the interactions to the excited states. Therefore we ignore the strain interaction to the NV ground states and only consider the excited state mixing due to the strain field. According to Ref. [137], axial strain field (ξ_z) does not mix the excited states, it only shifts the energy of the excited states and hence the dipole moment matrix does not change. However, the interaction Hamiltonian due to transverse strain field ξ_x and ξ_y has off-diagonal matrix elements in the SO basis of excited states, which means the transverse strain field mixes the SO basis of excited states.

Assume the transverse strain field is small so that the group symmetry of NV center is still preserved. The interaction Hamiltonian for $\hat{x}$-direction strain field is

$$H(\xi_x) = \begin{pmatrix} 0 & 0 & 0 & 0 & 0 & -E \\ 0 & 0 & 0 & 0 & E & 0 \\ 0 & 0 & E & 0 & 0 & 0 \\ 0 & 0 & 0 & -E & 0 & 0 \\ 0 & E & 0 & 0 & 0 & 0 \\ -E & 0 & 0 & 0 & 0 & 0 \end{pmatrix} \tag{3.42}$$

in the basis of the SO basis states, where E is the interaction strength introduced by $\hat{x}$ direction strain field. From the Hamiltonian, the excited state $|e_1\rangle$ mixes with state $|e_6\rangle$, state $|e_2\rangle$ mixes with state $|e_5\rangle$. Since the dipole moment between the states $|e_1\rangle$, $|e_6\rangle$ and ground states has the same direction, we should expected that the dipole moment elements between SS basis states $\langle\tilde{e}_1|\,\hat{\vec{p}}\,|g_j\rangle$ and $\langle\tilde{e}_6|\,\hat{\vec{p}}\,|g_j\rangle$ for $j = 2, 3$ does not change directions, which can be easily checked after diagonalize the SO, SS with the strain field coupling Hamiltonian.

Similar to the $\langle\tilde{e}_2|\,\hat{\vec{p}}|g_j\rangle$ and $\langle\tilde{e}_5|\,\hat{\vec{p}}|g_j\rangle$. Besides, due to the perturbation introduced by $\hat{x}$-direction strain field, the degeneracy of excited states $|\tilde{e}_1\rangle$ and $|\tilde{e}_2\rangle$ as well as the degeneracy of states $|\tilde{e}_3\rangle$ and $|\tilde{e}_4\rangle$ is broken.

The Hamiltonian for small $\hat{y}$-direction strain field in diamond crystal is,

$$H(\xi_y) = \begin{pmatrix} 0 & 0 & 0 & 0 & -E & 0 \\ 0 & 0 & 0 & 0 & 0 & -E \\ 0 & 0 & 0 & -E & 0 & 0 \\ 0 & 0 & -E & 0 & 0 & 0 \\ -E & 0 & 0 & 0 & 0 & 0 \\ 0 & -E & 0 & 0 & 0 & 0 \end{pmatrix} \tag{3.43}$$

where E is the interaction energy due to the $\hat{y}$ direction strain field. The $\hat{y}$ direction strain field mixes the excited state $|e_1\rangle$ with $|e_5\rangle$, state $|e_2\rangle$ with $|e_6\rangle$ and state $|e_3\rangle$ with $|e_4\rangle$. The dipole moment $\langle\tilde{e}_i|\,\hat{\vec{p}}|g_j\rangle$ for $i = 1$ to 6 and $j = 2, 3$ does not point along $\hat{x}$ or $\hat{y}$ directions any more. Instead, the dipole moment between the same excited state and the two ground states $|g_2\rangle$ and $|g_3\rangle$ are no longer orthogonal. This feature of the dipole moment matrix causes that the scattering light from state-preserving and state-flipping transitions are not polarized along perpendicular directions.

3.5.3 Transition rates and scattered photon polarization

In this section, we present the details of the scattering rate calculation. To estimate the magnitude of the dipole moment, we modeled the relaxation from the electronic excited state with $S_z = 0$ (e.g $|e_3\rangle$), back to ground state with $S_z = 0$ (e.g. $|g_1\rangle$) as a two-level system spontaneous relaxation process. If we ignore the slow relaxation processes from state $|e_3\rangle$ to the other two ground state levels $|g_2\rangle$ and $|g_3\rangle$, then the lifetime of state $|e_3\rangle$, which is 13 ns [138], can be used to estimate the value of dipole moment. The magnitude of dipole moment estimated based on this method is $|p| = e|d| = 5.2$ Debye [145], where e is the electron charge.

As we pointed out in 3.5.1 and 3.5.2 the NV center dipole moments for optical transition between ground and excited states are along the transverse direction. Therefore, we choose

to match the axial direction of NV centers ($\hat{z}$ direction) to the waveguide $\hat{z}$ direction to have optimum coupling efficiency. We also choose to match the NV center intrinsic transverse directions $\hat{x}$ and $\hat{y}$ with the waveguide transverse direction $\hat{x}$ and $\hat{y}$ as Fig. 1(c) shows.

To calculate the scattering transition rates between ground states $|g_2\rangle$ and $|g_3\rangle$, we consider a single NV center residing inside an infinitely long waveguide shown in 3.5.1. The quantized guided waveguide mode in a length L waveguide, with wavevector along the waveguide axial direction k_z and mode index m is [148]:

$$\hat{E}_{k_z,m} = \mathcal{E}_0(k_z)\vec{u}_{k_z,m}(x,y)a_{k_z,m}\frac{1}{\sqrt{L}}e^{ik_z z - i\omega_{k_z}t} + h.c., \tag{3.44}$$

where $a_{k_z,m}$ is the annihilation operator for photons with k_z and mode m, ω_{k_z} is the angular frequency of the mode photon, which can be determined by the waveguide dispersion relations, $\mathcal{E}_0(k_z) = \sqrt{\hbar\omega_{k_z}/2\varepsilon_0}$ in which ε_0 is the vacuum permittivity, $\vec{u}_{k_z,m}(x,y)$ is the mode profile on the cross section of the waveguide. The mode profile is normalized according to the normalization condition,

$$\int dxdy\, \varepsilon_r(x,y)\vec{u}^*_{k_z,m}(x,y)\cdot\vec{u}_{k_z,n}(x,y) = \delta_{m,n} \tag{3.45}$$

To simplify the calculation, we assume the NV centers only couple to the driving light and the waveguide modes, and ignore the coupling to the non-guided modes. We further assume the driving light is a classical field while the waveguide modes are quantized. The interaction Hamiltonian is,

$$H_{\text{int}} = H_{\text{drive}} + H_{\text{guide}} \tag{3.46a}$$

$$H_{\text{drive}} = \left[\sum_{i,j}\vec{E}^*_d(\vec{r}_0)\cdot\hat{\vec{p}}_{i,j}\,|g_i\rangle\langle e_j|\,e^{i(\omega_d-\omega_{ej,gi})t} + h.c.\right] \tag{3.46b}$$

$$H_{\text{guide}} = \left[\sum_{i,j}\sum_{k_z}\sum_{m_k}\mathcal{E}_0(k_z)\left(\vec{u}_{k_z,m_k}(\vec{r}_0)\cdot\hat{\vec{p}}^*_{i,j}\right)a_{k_z,m}\,|e_j\rangle\langle g_i|\,e^{i\left(\omega_{ej,gi}-\nu_{\vec{k},\lambda}\right)} + h.c.\right]. \tag{3.46c}$$

H_{drive} is for the interaction between the NV center and the driving light. The classical electromagnetic field, $\vec{E}(\vec{r})e^{i\omega_d t}$, is the driving laser light. $\hat{\vec{p}}_{i,j}$ is defined as $\langle g_i|\,\hat{\vec{p}}\,|e_j\rangle$, where $|e_j\rangle$ is the eigenstates of electronic excited state of NV center. H_{guide} is for the interaction with the waveguide guided modes, $\vec{r}_0$ is the position of the NV center. The summation index

$i = 1$ to 3, while index $j = 1$ to 6. The mode index m goes through all the guided modes in the waveguide with wave vector k_z.

Note that the photon scattering process from ground state $|g_i\rangle$ to the ground state $|g_{i'}\rangle$ is a second order process. We use second order Fermi's golden rule to calculate the transition rates. Assuming that initially there are no photons in the guided modes, and hence the initial state is $|\Psi_i\rangle = |g_i\rangle \otimes |0\rangle$, where $|0\rangle$ is the vacuum guided mode fields, while the scattering final state is $|\Psi_f\rangle = |g_{i'}\rangle \otimes |1_m\rangle$, where $|1_m\rangle$ is the state for one photon inside the guided mode m. Based on the second order Fermi's Golden Rule, the transition rate from initial state $|g_i\rangle \otimes |0\rangle$ to final state $|g_{i'}\rangle \otimes |1_m\rangle$ is,

$$\Gamma_{i\to i'} = \frac{2\pi}{\hbar}\delta(\epsilon_f - \epsilon_i) \times \left| \sum_{j=1}^{6} \langle \Psi_f | \frac{H_{\text{guide}} |e_j\rangle |0\rangle \langle 0| \langle e_j| H_{\text{drive}}}{\hbar\omega_d + \epsilon_{g,i} - \epsilon_{e,j}} |\Psi_i\rangle \right|^2 \tag{3.47}$$

where $\epsilon_{g,i}$ and $\epsilon_{e,j}$ are for the energy of NV states $|g_i\rangle$ and $|e_j\rangle$, ω_d is the driving light angular frequency. We define an effective Hamiltonian for Raman transition as,

$$\begin{aligned} H_{\text{eff}} &= \sum_{j=1}^{6} \frac{H_{\text{guide}} |e_j\rangle |0\rangle \langle 0| \langle e_j| H_{\text{drive}}}{\hbar\omega_d + \epsilon_{g,i} - \epsilon_{e,j}} \\ &= \sum_{k_z,m} \sum_{j=1}^{6} \frac{\mathcal{A}_{k_z,m}(\vec{r}_0)}{\Delta_j} \left(\hat{u}_{k_z,m} \cdot \hat{p}_{i',j}\right)^* \left(\hat{\lambda}_d \cdot \hat{p}_{i,j}\right) a^\dagger_{k_z,m} \end{aligned} \tag{3.48}$$

where $\mathcal{A}_{k_z,m}(\vec{r}_0)$ is a constant defined as $\mathcal{E}_0(k_z) u^*_{k_z,m} E_d p_0^2$, energy mismatch Δ_j is defined as $\hbar\omega_d + \epsilon_{g,i} - \epsilon_{e,j}$. The variable $u_{k_z,m}$ is the magnitude of the waveguide mode with wave-vector k_z and mode index m at the NV position $\vec{r}_0$, $\hat{u}_{k_z,m}$ is the unit vector along the electric field of the mode at the NV center location, $\hat{p}_{i,j}$ is defined as $\hat{p}_{i,j} = \vec{p}_{i,j}/p_0$ in which $\vec{p}_{i,j}$ is the dipole moment operator elements between ground state $|g_i\rangle$ and excited $|e_j\rangle$. The driving field magnitude at the NV location is noted as E_d, while its polarization direction is labeled as $\hat{\lambda}_d$. The transition amplitude can be written as $\langle \Psi_f | H_{\textbf{eff}} | \Psi_i \rangle$.

As we pointed out in 3.5.1, at the "magic" frequency, there are only two guided modes supported by the diamond waveguide. Further, mode 1 and mode 2 only have non-zero E_x or E_y components respectively (when the NV center is centered in the waveguide: $x, y \sim 0$). Therefore, the transitions with $\hat{x}$ dipole and transitions with $\hat{y}$ dipole couple to different modes. If we also assume that at the NV center location, $E_x(\vec{r}_0)$ of mode 1 is equal to $E_y(\vec{r}_0)$

of mode 2, the constant $\mathcal{A}$ does not depend on mode number m. If we only considered the modes which respect the energy conservation, and use $\hat{x}$ polarized light to drive the transitions, the effective Hamiltonian can be written as,

$$\begin{aligned}\frac{H_{\text{eff},k_{z0}}}{\mathcal{A}_{k_{z0}}} = &\left(\frac{F_{21}^2}{\Delta_1}+\frac{F_{22}^2}{\Delta_3}+\frac{F_{23}^2}{\Delta_6}\right)|g_2\rangle\langle g_2|\, a^\dagger_{k_{z0},2} + \left(\frac{F_{21}^2}{\Delta_2}+\frac{F_{22}^2}{\Delta_4}+\frac{F_{23}^2}{\Delta_5}\right)|g_3\rangle\langle g_3|\, a^\dagger_{k_{z0},2} \\ &+\left(\frac{-F_{21}^2}{\Delta_1}+\frac{-F_{22}^2}{\Delta_3}+\frac{F_{23}^2}{\Delta_6}\right)|g_3\rangle\langle g_2|\, a^\dagger_{k_{z0},1} + \left(\frac{F_{21}^2}{\Delta_2}+\frac{F_{22}^2}{\Delta_4}+\frac{-F_{23}^2}{\Delta_5}\right)|g_2\rangle\langle g_3|\, a^\dagger_{k_{z0},1}\end{aligned} \tag{3.49}$$

where we adopt the dipole moment operator expression in Eq. (3.41). The first and second terms give the state-preserving transitions, while the third and fourth terms give the state-flipping transitions. According to Eq. (3.49), photons from state-preserving transitions and state-flipping transitions have perpendicular polarizations, and hence they couple to two different modes. Similarly, if the driving light is polarized along $\hat{y}$ direction, following the same argument, it is easy to show that the photons from state-preserving transitions are coupled to mode 2, while photons from state-preserving transitions are coupled to the mode 1 instead. The orthogonal polarization of photons is a feature that originates in the orthogonal dipole moment between the ground states $|g_2\rangle$, $|g_3\rangle$ and the same excited state $|e_j\rangle$, i.e.,

$$\langle g_2|\,\hat{\vec{p}}|e_j\rangle \cdot \langle g_3|\,\hat{\vec{p}}|e_j\rangle = 0 \tag{3.50}$$

for $j = 1$ to 6 (we call this property orthogonality). The perturbation on the excited state energy, the dipole moment elements and the $\hat{x}$ direction strain field interaction, does not change this dipole moment property, and hence orthogonal polarization of photons is still expected from state-preserving and state-flipping transitions. If this feature does not persist, e.g. adding $\hat{y}$ direction strain field, the photons coming from state-flipping and state-preserving transitions become non-orthogonally polarized.

The "magic" point is the point where both state-preserving transitions are highly suppressed. According to the Eq. (3.49), this requires,

$$\frac{F_{21}^2}{\Delta_1}+\frac{F_{22}^2}{\Delta_3}+\frac{F_{23}^2}{\Delta_6} = 0 \tag{3.51a}$$

$$\frac{F_{21}^2}{\Delta_2}+\frac{F_{22}^2}{\Delta_4}+\frac{F_{23}^2}{\Delta_5} = 0 \tag{3.51b}$$

However, there is no driving light frequency that can satisfy both equations. Instead, we choose to minimize the larger rates of these two transitions to improve the gate fidelity, i.e., to minimize

$$\mathrm{Max}\left[\left|\frac{F_{21}^2}{\Delta_1}+\frac{F_{22}^2}{\Delta_3}+\frac{F_{23}^2}{\Delta_6}\right|,\left|\frac{F_{21}^2}{\Delta_2}+\frac{F_{22}^2}{\Delta_4}+\frac{F_{23}^2}{\Delta_5}\right|\right].$$

We found this is equivalent to solving the equation:

$$\left(\frac{F_{21}^2}{\Delta_1}+\frac{F_{22}^2}{\Delta_3}+\frac{F_{23}^2}{\Delta_6}\right)^2=\left(\frac{F_{21}^2}{\Delta_2}+\frac{F_{22}^2}{\Delta_4}+\frac{F_{23}^2}{\Delta_5}\right)^2, \tag{3.52}$$

which gives the frequency of the "magic" point used in the main manuscript.

The transition rates at the "magic" point can be calculated using Fermi's golden rule. We sum over all the possible k_z and m to get the transition rate from the initial state $|g_i\rangle$ to final state $|g_{i'}\rangle$:

$$\Gamma_{i\to i'}=\frac{\pi n_{\mathrm{eff}}\omega_d p_0^4|u|^2|E_d|^2}{c\hbar\varepsilon_0}\times\left|\sum_{j,m}\frac{1}{\Delta_j}\left(\hat{u}_m\cdot\hat{p}_{i',j}\right)^*\left(\hat{\lambda}_d\cdot\hat{p}_{i,j}\right)\right|^2. \tag{3.53}$$

Here, n_{eff} is the effective refractive index for the modes at the frequency of the driving light, the dispersion relation of the guided modes at the driving light frequency is $\omega=(c/n_{\mathrm{eff}})k_z$. We also assume the NV center is located at a point where the E_x field of mode 1 is equal to the E_y field of mode 2, which is represented as u, while the E_y of mode 1 and E_x of mode 2 is zero. The unit vectors $\hat{u}_m$ and $\hat{\lambda}_d$ shows the direction of the guided field in waveguide and the driving field at the NV location. To convert the term inside $|\ldots|^2$ to a dimensionless parameter, we define $\Delta_j=h\nu_0\tilde{\Delta}_j$ where $\nu_0=1$ GHz. Therefore we can define a rate constant Γ_0 and a dimensionless parameter $\mathcal{G}_{i,i'}$ so that the transition rate $\Gamma_{i\to i'}=\Gamma_0\mathcal{G}_{i,i'}(\omega_d)$, where

$$\Gamma_0=\frac{n_{\mathrm{eff}}\omega_d p_0^4|u|^2|E_d|^2}{4\pi c\hbar^3\varepsilon_0\nu_0} \tag{3.54}$$

$$\mathcal{G}_{i,i'}=\left|\sum_{j,m}\frac{1}{\tilde{\Delta}_j}\left(\hat{u}_m\cdot\hat{p}_{i',j}\right)^*\left(\hat{\lambda}_d\cdot\hat{p}_{i,j}\right)\right|^2 \tag{3.55}$$

By solving the mode profiles at the "magic" frequency, the effective refractive index of these two modes are $n_{\mathrm{eff}}=1.580$. At $x=0$, after properly normalize the mode fields using Eq. (3.45), we can find a point which satisfies our assumptions, i.e., $E_{x,1}(y_0)=E_{y,2}(y_0)$ (see Fig. 10). At this point, $u=2.4847\,\mu\mathrm{m}^{-1}$. We estimate the electric field of the driving light by a $1\,\mu$W plane wave focused with a $1\,\mu\mathrm{m}^2$ region. The transition rate constant is calculated as $\Gamma_0=20.78$ MHz.

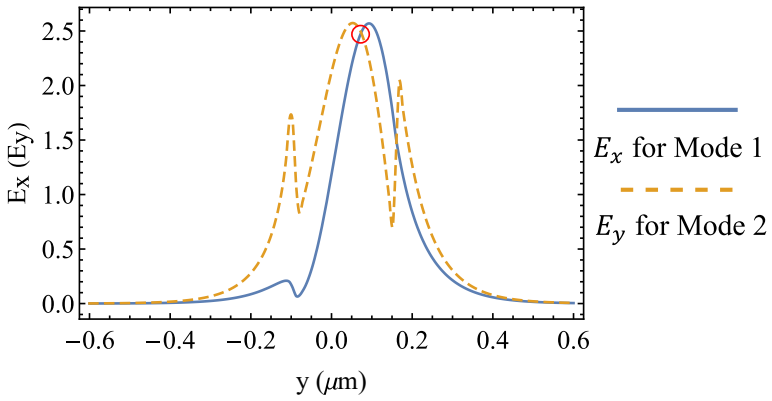

Figure 10: E_x component of mode 1 and E_y component of mode 2 at $x = 0$ of the waveguide. We can find a point (red circle) that satisfies $E_{x,1} = E_{y,2}$.

3.5.4 Gate fidelity and tolerance of the magic point against NV electronic state perturbation

In this section, we provide a more detailed discussion and analysis of how perturbations to NV electronic states affect the drive frequency (especially the "magic" frequency) and the gate fidelity. We focused on three types of perturbations: (1) shifts of the excited state energy /effect of an NV center, (2) perturbation of the dipole moment matrix elements and (3) small transverse strain fields inside the diamond crystal. We also analyze how each of the perturbation affects the polarization of the emitted photons. We mainly focus on the effect of perturbation at the "magic" point and explore how these perturbations affect gate fidelity for the gate operation schemes $M1$, $M2$, and $M3$.

First, we consider perturbations that shift the energy of NV excited states. Since this type of perturbations does not affect the dipole moment between the ground states and excited states, the orthogonal property of scattered photon polarizations that are utilized by $M1$ and $B1$ are preserved. However, shifts of the excited state energies changes the transition amplitudes and hence may shift the position of the "magic" point. Changes in the state-flipping amplitudes affect the imbalance of the two state-flipping transitions rates, thus affect gate fidelity in scheme $M1$. Changes of the state-preserving transition amplitudes

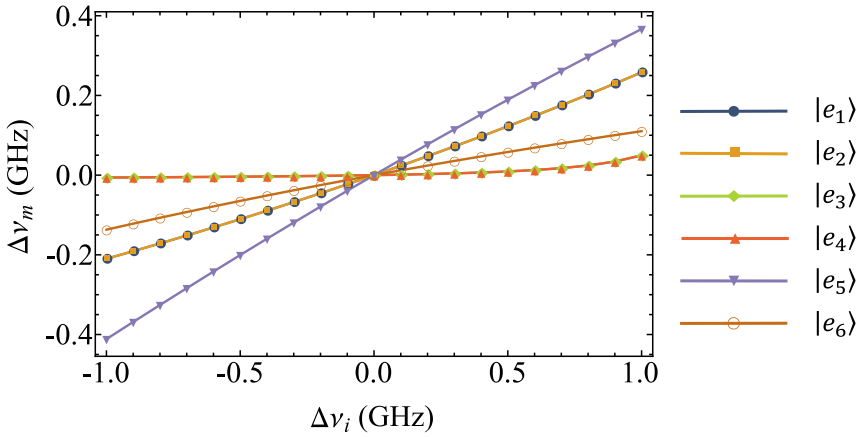

Figure 11: Tolerance of the "magic" point to shifts of the fine levels of the NV excited states. We perturb the energy of each level ($\Delta E_{e,i}$) by ± 1 GHz. We plot the shift of the "magic" frequency relative to the unperturbed case as we perturb the energy of each excited state.

affect the suppression at the "magic" frequency, which affects the gate fidelity of scheme $M2$.

To quantitatively explore the effects of the shifting of NV center electronic excited states, we artificially shift the energy of the excited states $|e_1\rangle$ to $|e_6\rangle$ one-by-one by ± 1 GHz, while leave the dipole moments unchanged. With the energy level perturbation, we search around the original "magic" frequency to find a new "magic" frequency that minimize both state-flipping transition amplitudes. The shift of the "magic" frequency as we shift each of the excited state energies is plotted in Fig. 11.

Assuming that the imbalance of the two state-flipping transition amplitudes is small, i.e., $\frac{|A_1 - A_2|}{A_1 + A_2} \ll 1$, where A_1 and A_2 are defined in Eq. (3.10), enables us to expand the gate fidelity of scheme $M1$ as:

$$F_{e,1} = \frac{(A_1 + A_2)^2}{2\left(A_1^2 + A_2^2\right)} = \frac{\bar{A}^2}{\bar{A}^2 + \Delta A^2} \sim 1 - \frac{\Delta A^2}{\bar{A}^2} \tag{3.56}$$

where $\bar{A} = (A_1 + A_2)/2$ and $\Delta A = |A_1 - A_2|/2$. We calculate the gate infidelity $(1 - F_{e1})$ in each cases with gate operation scheme $M1$ and show it in Fig. 12(a). As we shift each excited state energy of the NV center by ± 1 GHz, the gate fidelity of gate operation scheme

$M1$ is only slightly affected. In the worst case, when we shift the energy of state $|e_2\rangle$ by $+1$ GHz, the gate fidelity drops to ~ 0.96.

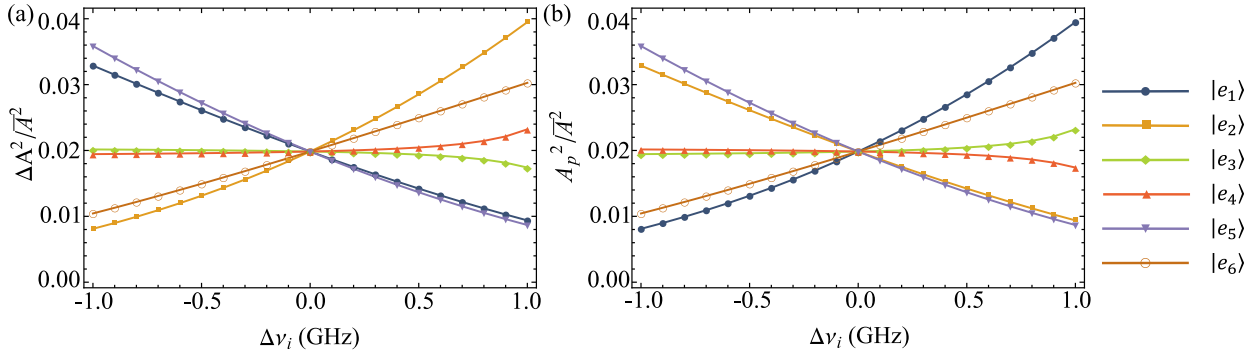

Figure 12: Shifting the energy of excited states also affects the state-preserving and state-flipping transition rates. In (a), we plot the gate infidelity of scheme $M1$ due to the imbalance in the state-flipping transition rates as we perturb the energy of each excited state. In (b), we plot the gate infidelity of scheme $M2$ caused by the leakage of the state-preserving photons as we perturb the energy of each excited state.

The gate operation scheme $M2$ is not affected by the imbalance of state-flipping transitions. However, because the state-preserving transition relation $\frac{A^x_{p,2}}{A^{(x)}_0} = \frac{A^y_{p,3}}{A^{(y)}_0} = -\frac{A^y_{p,2}}{A^{(y)}_0} = -\frac{A^x_{p,3}}{A^{(x)}_0}$ holds, when drive light is polarized along $(\hat{x}+\hat{y})$ direction, the state-preserving scattered photons are still along $(\hat{x}-\hat{y})$ direction, which causes leakage of the state-preserving photons to the detector. Since we are working at the "magic" point where the state-preserving transitions are highly suppressed, we can also expand the gate fidelity of gate operation scheme $M2$ as:

$$F_{e,2} = \frac{\bar{A}^2}{\bar{A}^2 + A_p^2} \sim 1 - \frac{A_p^2}{\bar{A}^2} \tag{3.57}$$

where A_p is the magnitude of the state-preserving transition amplitudes. In Fig. 12(b), we plot the gate infidelity of the scheme $M2$. When shifting energy of state $|e_1\rangle$ by $+1$ GHz, the gate infidelity increases ~ 0.04. Again, the gate operation fidelity is only slightly affected by the excited state energy level shifting.

Scheme $M3$ is not effected by shifting the excited state levels. Because the dipole moment is not affected, when the drive light is polarized along $(\hat{x}+\hat{y})$ direction, the state-preserving

photons are still polarized along $(\hat{x}-\hat{y})$ direction. The collection path polarizer along $(\hat{x}+\hat{y})$ can fully eliminate the state-preserving photons. The polarizations of the two types of state-flipping photons still deviated from $(\hat{x}-\hat{y})$ direction by $\pm\theta$ (see Fig. 4), where θ is determined by the imbalance of the state-flipping transitions. However, since these two directions are centered on the direction $(\hat{x}-\hat{y})$, after the polarizer, the two state-flipping transition rates are balanced.

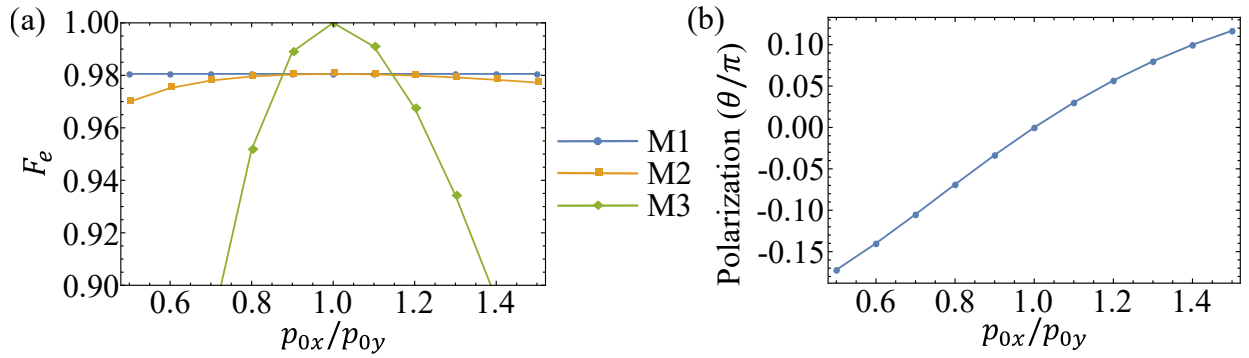

Figure 13: We plot the entanglement gate fidelity for gate operation schemes $M1$ to $M3$ at the "magic" frequency of the drive light when we add dipole moment mismatch in (a). If the NV centers are driven by a $(\hat{x}+\hat{y})$ polarized light, because the four transition amplitudes are not all balanced, the two kinds of state-preserving photons, i.e., $|g_2\rangle \to |g_2\rangle$ and $|g_3\rangle \to |g_3\rangle$, are no longer polarized along $(\hat{x}-\hat{y})$ direction. We plot the polarization angle of the state-preserving photons with respect to $(\hat{x}-\hat{y})$ direction as a function of dipole mismatch in (b).

Second, we explore the effect of perturbations that modify the dipole moments of the NV centers. In 3.5.2, we constructed the dipole moment using Eq. (3.35). Let $\langle e_x|\,\hat{\vec{p}}\,|a_1\rangle = p_{0x}\cdot\hat{x}$, $\langle e_y|\,\hat{\vec{p}}\,|a_1\rangle = p_{0y}\cdot\hat{y}$, then C_{3v} symmetry in combination with the Wigner-Eckart theorem guarantees that $p_{0x} = p_{0y}$, which is consistent with the assumptions in Eq. (3.35). Here we assume there might be certain types of perturbations that break this relation and give $p_{0x}/p_{0y} \neq 1$. Notice, that these perturbations break the state-preserving amplitudes relation, i.e., $|\langle g_2|\,\hat{\mathbf{p}}\,|e_i\rangle| \neq |\langle g_3|\,\hat{\mathbf{p}}\,|e_i\rangle|$, which voids the origin of the equality of state-preserving transition amplitudes in Eq. (3.8). Therefore, we will have four different state-preserving

transition amplitudes. If we assume $p_{0y} = p_0$, as we shift p_{0x}, in dipole moment matrix in Eq. (3.41), the components along $\hat{y}$ direction do not change, while the components along $\hat{x}$ change by a factor $O_x = p_{0x}/p_0$ and hence the state-preserving transition amplitudes become $\tilde{A}^x_{p,2} = O_x^2 A^x_{p,2}$ and $\tilde{A}^x_{p,3} = O_x^2 A^x_{p,3}$.

At the unperturbed "magic" point, the state-preserving transition amplitudes satisfy $\frac{A^x_{p,2}}{A^{(x)}_0} = \frac{A^y_{p,3}}{A^{(y)}_0} = -\frac{A^y_{p,2}}{A^{(y)}_0} = -\frac{A^x_{p,3}}{A^{(x)}_0}$. Under the dipole moment perturbation we obtain:

$$\frac{\tilde{A}^x_{p,2}}{A^{(x)}_0} = -\frac{\tilde{A}^x_{p,3}}{A^{(x)}_0} = O_x^2 \frac{\tilde{A}^y_{p,3}}{A^{(y)}_0} = -O_x^2 \frac{\tilde{A}^y_{p,2}}{A^{(y)}_0}. \tag{3.58}$$

Even through we cannot suppress all four state-preserving transition amplitudes to the same level, we can still achieve a good suppression for $\tilde{A}^x_{p,2}$ and $\tilde{A}^x_{p,3}$ at the original "magic" point if the dipole mismatch factor O_x is close to identity and hence we still use this drive frequency point as a "magic" point under perturbation.

We also notice that the orthogonality property of the dipole matrix persists, i.e.,

$$\langle g_2 | \hat{\mathbf{p}} | e_j \rangle \cdot \langle g_3 | \hat{\mathbf{p}} | e_j \rangle = 0 \tag{3.59}$$

for $j = 1$ to 6. Due to this feature, if the drive is polarized along $\hat{x}$ or $\hat{y}$ direction, the state-flipping photons are polarized along the direction perpendicular to state-preserving photons. Hence, the drive and polarizer setup in $M1$ can fully eliminate the state-preserving Raman photons from the collection path. Moreover, according to the state-flipping transition amplitudes in Eq. (3.9), when the perturbation gives mismatch factor $O_x \neq 1$, the state-flipping transition amplitudes are all enhanced (or shrunk) by a factor of O_x. Based on Eq. (3.56), the gate fidelity for scheme $M1$ is not affected by the dipole moment perturbation, as shown in Fig. 13(a).

When the drive is polarized along $(\hat{x} + \hat{y})$ direction, due to the fact that the four state-preserving transition amplitudes in Eq. (3.58) are not all equal at "magic" point, the state-preserving photons are not polarized along $(\hat{x} - \hat{y})$. We plot the deviation of the state-preserving transition photon polarization direction from $(\hat{x} - \hat{y})$ as the dipole mismatch changes in Fig. 13(b). Due to the rotation of the polarization direction of state-preserving photons, the state-preserving transition amplitudes seen after a $(\hat{x} - \hat{y})$ polarizer also varies.

However, as the state-flipping transition amplitudes after the polarizer is much larger than the state-preserving transitions amplitudes, the gate operation scheme $M2$ is tolerant to small dipole mismatch as shown in Fig. 13(a). When the dipole moment mismatch is large (e.g. ~ 0.5), the gate fidelity of $M2$ drops by ~ 0.01.

The gate fidelity of scheme $M3$ is strongly affected by the dipole moment perturbation as shown in Fig. 13(a). The polarizer setup in $M3$ is along $(\hat{x}+\hat{y})$ direction, which blocks most of the state-flipping photons. However, under the dipole moment perturbation, the state-preserving photons are not polarized along $(\hat{x}-\hat{y})$ direction, which breaks the unitarity of scheme $M3$. Further, the leakage of the state-preserving photons through the polarizer can be as strong as the state-flipping photons, which strongly affects the gate fidelity. Since the two kinds of state-preserving photons are linearly polarized along the same direction, it is possible to rotate the polarizer on the collection path to completely eliminate the state-preserving photons. However, the two state-flipping transitions seen after the polarizer are not balanced anymore. In this way, we can improve the fidelity of scheme $M3$, but the gate is no longer perfectly unitary.

Third, we consider perturbations due to a strain field in the diamond crystal. A strain field applied along the $\hat{x}$ ($\hat{y}$) direction mixes the NV excited states via the perturbation Hamiltonian Eq. (3.42) (Eq. (3.43)). The strain field also acts on the ground state manifold, however, it only shifts the energy of the $|g_2\rangle$ and $|g_3\rangle$ states. Here, we ignore the impact of the strain fields on the ground states and only focus on the excited states. Due to the mixing of the excited states, the dipole moment matrix does not preserve the property $|\langle g_2|\,\hat{\mathbf{p}}\,|e_i\rangle| = |\langle g_3|\,\hat{\mathbf{p}}\,|e_i\rangle|$ and hence we expect the four state-preserving transition amplitudes to be different. Moreover, in the presence of a strain field, it is impossible to find a frequency point to make all four transitions balanced. Instead, in the vicinity of the unperturbed "magic" frequency, there is a window of drive frequencies in which the state-preserving transitions are suppressed. Therefore, we can still use the unperturbed "magic" point as the drive frequency in the presence of a weak strain field.

Strain field applied in the $\hat{x}$ direction mixes the states $|e_1\rangle \leftrightarrow |e_6\rangle$, and $|e_2\rangle \leftrightarrow |e_5\rangle$. Note, the dipole moments between a certain ground state and the two excited states that are being mixed have the same direction. Hence, while the magnitude of the dipole moment between

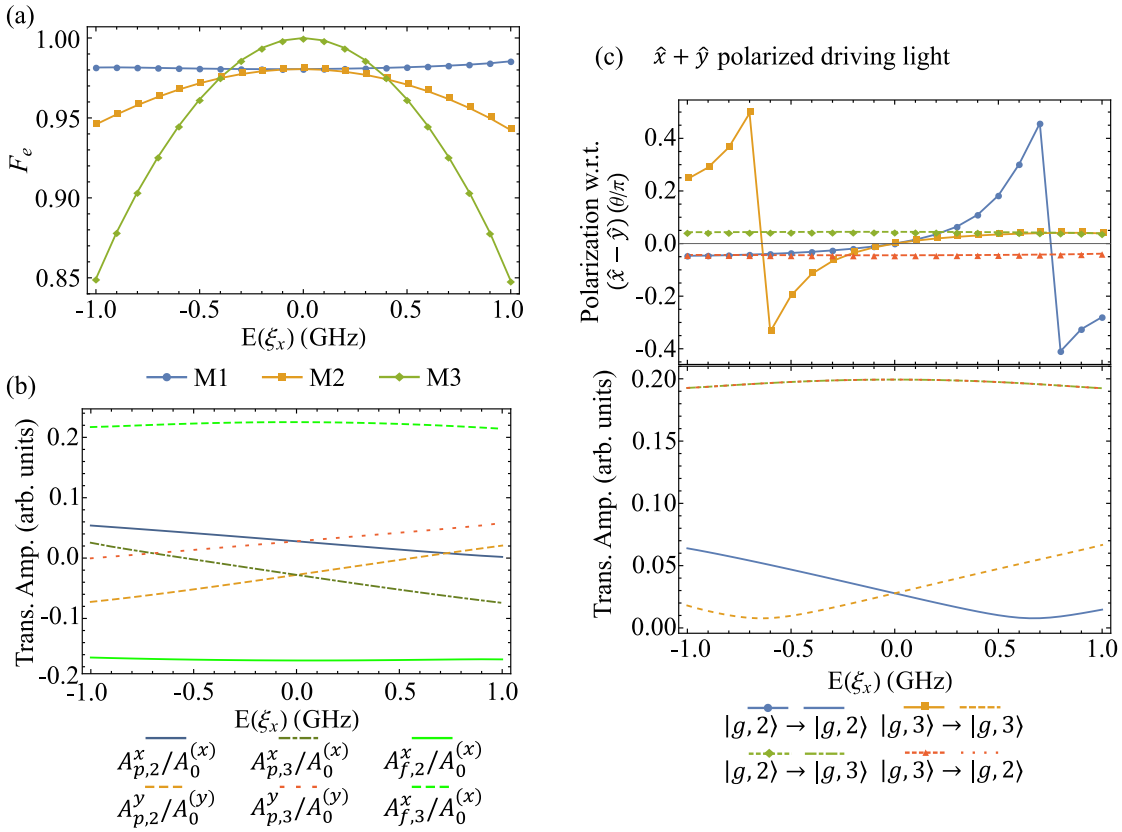

Figure 14: We add $\hat{x}$ direction strain fields in diamond crystal to induce interaction with strength $E(\xi_x)$ [see Eq.(3.42). The gate entanglement fidelity of schemes $M1$, $M2$ and $M3$ are plotted in (a) for $\hat{x}$ direction strain field. In (b), we apply $\hat{x}$ polarized driving light and plot the transition amplitudes (Trans. Amp.) as a function of the $\hat{x}$ direction strain field, ξ_x. We observe that the two state-flipping transition amplitudes are unbalanced and weakly affected by the strain. In (c), we apply $(\hat{x}+\hat{y})$ polarized driving light, and plot the polarization angles of state-preserving and state-flipping photons with respect to the $(\hat{x}-\hat{y})$ direction (top panel) and the magnitude of the state-preserving and state-flipping transition amplitudes (bottom panel) as a function of the $\hat{x}$ direction strain field. Note that the magnitudes of two state-flipping transition amplitudes (top lines in the bottom panel) are the same as we perturb the x-direction strain field.

ground and excited states is affected by strain, its direction is not. Therefore, the orthogonal properties of the dipole moment [see Eq. (3.50)] are preserved with the $\hat{x}$ direction strain field perturbation.

In Fig. 14(a) we plot the gate entanglement fidelity for schemes $M1$, $M2$, and $M3$ as a function of strain in the $\hat{x}$ direction [expressed via the matrix element E in Eq. (3.42)]. We observe that strain has essentially no effect on the $M1$ scheme, weak effect on the $M2$ scheme, and strong effect on the $M3$ scheme.

To understand the effect of the $\hat{x}$ strain field on the gate fidelity, we begin by plotting its effect on the non-zero state-preserving and state-flipping transition amplitudes at the "magic" frequency [see Fig. 14(b)]. We observe that in the presence of a small $\hat{x}$ strain field the state-flipping transitions are only slightly affected [see the bright green (the top and bottom) lines in Fig. 14(b)], while the state preserving transition amplitudes are still suppressed [see the middle four lines in Fig. 14(b)].

In scheme $M1$, state-preserving photons can be blocked by the polarizer on the collection path due to the orthogonality property of the dipole moment matrix elements. As the state-flipping transitions are only slightly affected by the $\hat{x}$ direction strain field, the gate fidelity of $M1$ is almost flat [see the blue curves with dots in Fig. 14(a)].

When the drive is polarized along $(\hat{x}+\hat{y})$ direction, since the transition amplitudes $A^x_{f,2}$ and $A^x_{f,3}$ only slightly affected by the $\hat{x}$ strain field [see Fig. 14(b)], neither the rates nor the polarizations of the state-flipping photons are heavily affected [see green curve with diamond markers and red curve with triangles in Fig. 14(c) top panel]. However, the $\hat{x}$ strain field shifts the four state preserving transition amplitudes a lot, which causes the increase of the state-preserving transition rates [see blue solid line and orange dashed line in Fig. 14(c) bottom panel]. Note that the polarization of the state-preserving photons points along $(\hat{x}-\hat{y})$ direction without strain field is because that the state-preserving transition amplitudes satisfy $A^x_{p,2} = A^y_{p,3} = -A^y_{p,2} = -A^x_{p,3}$ at the "magic" point. The non-zero $\hat{x}$ strain field destroys this feature, which causes the polarization of the state-preserving photons deviates from $(\hat{x}-\hat{y})$ direction [see blue curves with dots and orange curve with square markers in Fig. 14(c) top panel].

In $M2$, the polarizer on the collection path is along $(\hat{x}-\hat{y})$ direction, which still al-

lows most of the state-flipping photons passing through. In non-perturbed case, the state-preserving photons are polarized along $(\hat{x} - \hat{y})$ direction, which can pass the collection path polarizer for certain. With the $\hat{x}$ strain field perturbation, the more the polarization of the state-preserving photons deviates from $(\hat{x} - \hat{y})$ direction, the less probable the photon can pass the collection path polarizer. However, the x-direction strain field also boost the generation rates of the state-preserving photons [see Fig. 14(c) bottom panel]. Combining these two factors, the overall gate fidelity for scheme $M2$ drops to ~ 0.95 as the x-direction strain field increases to 1 GHz [see Fig. 14(a)].

However, in scheme $M3$, the collection path $(\hat{x} + \hat{y})$ polarizer blocks most of the state-flipping photons, which makes this scheme fragile to the leaking state-preserving photons. The key for the success of $M3$ in the non-perturbed case is the fact that state-preserving photons is polarized along $(\hat{x} - \hat{y})$ direction. However, as we increase the $\hat{x}$ strain field, the polarization of the state-preserving photons are not exactly aligned $(\hat{x} - \hat{y})$ direction [see Fig. 14(c) top panel], which deteriorates the gate fidelity as shown in Fig. 14(a).

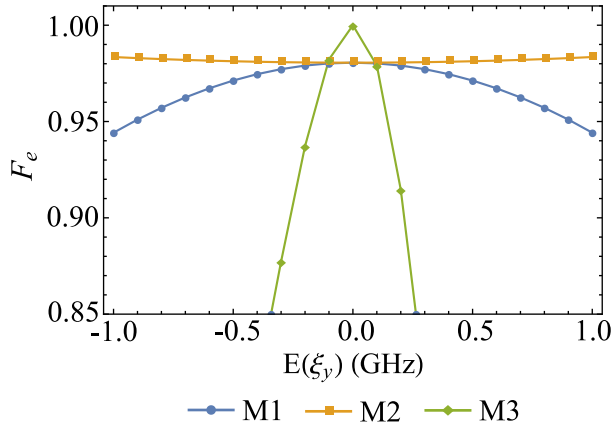

Figure 15: We add $\hat{y}$ direction strain fields in diamond crystal to induce interaction with strength $E(\xi_y)$ [see Eq.(3.43)]. The gate entanglement fidelity of schemes $M1$, $M2$ and $M3$ are plotted in (b).

The entanglement gate fidelity F_e when $\hat{y}$ direction strain field is applied to the diamond crystal is plotted in Fig. 15. The $\hat{y}$ direction strain field mixes the states $|e_1\rangle \leftrightarrow |e_5\rangle$, $|e_2\rangle \leftrightarrow |e_6\rangle$, and $|e_3\rangle \leftrightarrow |e_4\rangle$. The mixing of the states results in the loss of the dipole moment

orthogonality property. Therefore, for drive photons polarized along $\hat{x}$ direction the state-preserving photons are not necessarily polarized along $\hat{x}$, nor the state-flipping photons along $\hat{y}$. The polarization of both state-preserving photons and state-flipping photons relative to the $\hat{y}$ direction is plotted in Fig. 16(a) top panel. As we vary the $\hat{y}$ direction strain field, the polarization of the two kinds of state-flipping photons remains nearly along the $\hat{y}$ direction [see the green curve with diamond markers and the red curve with triangle markers in Fig. 16(a) top panel], but the polarization of state-preserving photons changes significantly [see the blue curve with dots and the orange curve with square markers in Fig. 16(a) top panel].

For scheme $M1$ (with $\hat{x}$ polarized drive), there are two main sources of error: (1) unbalanced state-flipping transitions as before and (2) $\hat{y}$ photons from state-preserving transitions that leak past the polarizer. We plot the polarization angle with respect to the $\hat{y}$ direction and the magnitude of the transition amplitudes for both state-preserving and state-flipping transitions in Fig. 16(a). As we increase the perturbation of y-direction strain field, the state-preserving transition amplitudes are slightly increased [see the blue solid line and the orange dashed line in Fig. 16(a) bottom panel]. Combining with the fact that polarization of the state-preserving photons are no longer along $\hat{x}$ direction exactly [see the blue curves with dots and the orange curves with square markers in Fig. 16(a) top panel], the leaking state-preserving photons to the detector decreases the gate fidelity to ~ 0.95 as we change $\hat{y}$ direction strain field to $\sim \pm 1$ GHz.

Similarly, when the drive is along $(\hat{x} + \hat{y})$ direction, the polarization features that were utilized in gate operation schemes $M2$ and $M3$ are no longer valid. We plot the deviation of the polarization angle of all scattered photons with respect to the polarizer direction in $M2$, i.e., $(\hat{x} - \hat{y})$, in the top panel of Fig. 15. The polarization of the state-flipping photons are slightly affected by the $\hat{y}$-direction strain field, while the state-preserving photon polarization rotates $\sim 54^\circ$ as we increase $\hat{y}$-direction strain field to ± 1 GHz. The amplitudes of the state-preserving and state-flipping transitions are plotted in the bottom panel of Fig. 16(b). We observe that the transition amplitudes are only slightly affected by the applied $\hat{y}$-direction strain field. Therefore, to understand the effect of y-direction strain field on schemes $M2$ and $M3$, we mainly focus on the rotation of the scattered photon polarizations.

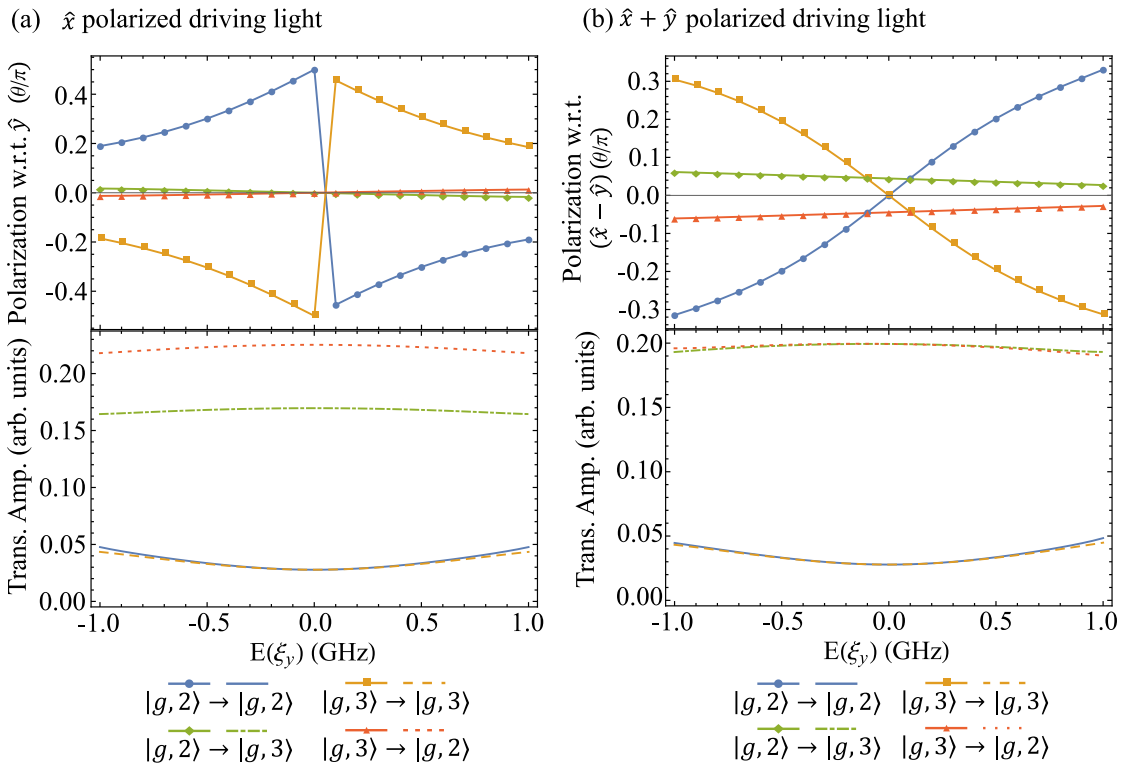

Figure 16: We add $\hat{y}$ direction strain fields in diamond crystal to induce interaction with strength $E(\xi_y)$ [see Eq.(3.43)]. In (a), we apply $\hat{x}$ polarized driving light and plot the polarization angles of the state-preserving and state-flipping photons with respect to the $\hat{x}$ direction (top panel) and the magnitude of the state-preserving and state-flipping transition amplitudes (bottom panel) as a function of the $\hat{y}$ direction strain field. In (b), we apply $(\hat{x}+\hat{y})$ polarized driving light and plot the polarization angles of the state-preserving and state-flipping photons to the $(\hat{x}-\hat{y})$ direction (top panel) and the magnitude of the state-preserving and state-flipping transition amplitudes (bottom panel) as a function of the $\hat{y}$ direction strain field. Note that the curves for the magnitudes of the two state-flipping transition amplitudes are overlapped (top curves in the bottom panel). The curves of two state-preserving transition amplitudes are overlapped (bottom curves in the bottom panel).

The main error source in scheme $M2$ without perturbation is the leakage of state-preserving photons past the polarizer in the collection path. As we change the $\hat{y}$-direction strain field, the state-preserving transitions are only slightly affected, while the polarization of the state-preserving photons rotates away from the collection path polarizer direction, i.e., $(\hat{x} - \hat{y})$ direction [see Fig. 16(b)]. The state-preserving photons thus have a smaller probability to get past the polarizer in the collection path. Consequently, the gate fidelity for scheme $M2$ slightly improves as a result of $\hat{y}$-direction strain field perturbation, as we show in Fig. 15.

On the other hand, the perfect gate fidelity of scheme $M3$ in the absence of perturbation is based on the fact that all state-preserving photons are polarized along $(\hat{x} - \hat{y})$ direction and hence are stopped by the polarizer in the collection path (along with most of the state-flipping photons). Large rotation angle of the state-preserving photon polarization makes the leakage rate of the state-preserving photons comparable to that of the state-flipping photons. This quickly degrades the gate fidelity as we show in Fig. 15.

3.6 Summary and outlook

In this chapter, we proposed a 2-qubit unitary quantum gate to achieve quantum logic operations using two NV centers. We theoretically analyzed how a photon is scattered by an NV center, taking care of the interference between different excitation paths. We found that for scattering rates between two electronic spin states ($|S_z = \pm 1\rangle$) there are two special frequencies for the driving light: a "magic" frequency at which the state conserving scattering rate is suppressed and a "balanced" frequency at which the state-flipping transition rates are equal. We analyzed the gate unitarity, fidelity and success probability for each of the schemes with possible experimental imperfections. When the photon collection efficiency is ~ 0.85, the gate fidelity of the most reliable scheme can reach ~ 0.97 when we impose a photon collection window $0.1/\bar{\Gamma}_f$, where $\bar{\Gamma}_f$ is the averaged state-flipping transition rate. While decreasing the photon collection window can improve the gate fidelity, the corresponding decrease in the success probability will have to be mitigated by some other means to ensure

we stay above the threshold for cluster or graph-state quantum computing. The proposed scheme could also be extended to other qubits such as Silicon-vacancy in diamond, or to localized vibronic states of the NV or other defect centers where the larger energy splittings can allow for quantum computing even at room temperature.

4.0 Optimizing Josephson ring modulator based Josephson parametric amplifiers via full Hamiltonian control

4.1 Introduction

Amplification is a key element in quantum sensing and quantum information processing. For example, readout of superconducting qubits requires a microwave amplifier that adds as little noise to the signal as possible [149], ideally approaching the quantum limit [150, 151, 152]. Recently, low-noise parametric amplifiers powered by the nonlinearity of Josephson junctions have been realized and are in regular use in superconducting quantum information experiments [153, 154, 78, 83, 84, 155, 156, 157, 158, 159].

To evaluate the performance of a practical parametric amplifier there are three aspects that are equally important: (1) added noise at the quantum limit [152, 83, 84, 155, 156, 160], (2) broad-band amplification [161, 162, 160, 163, 164], and (3) high saturation power [165, 84, 87, 166, 167, 85, 75, 168], i.e., the ability to maintain desired gain for a large input signal power [169]. The last requirement has been especially hard to achieve in Josephson parametric amplifiers and will be the focus of this paper.

In previous works on Josephson parametric amplifiers, it was assumed that saturation power is limited by pump depletion [165, 84, 87, 166, 168]. This is a natural explanation, as the amplifier gain is a very sensitive function of the flux of the applied pump photons. Thus, as the input power is increased, and more pump photons are converted to signal photons, the gain falls. However, in Refs. [167, 85, 75, 170] it was pointed out that the fourth order nonlinear couplings (i.e., the Kerr terms), inherent in Josephson-junction based amplifiers, can also limit the saturation power. These terms induce a shift in the mode frequencies of the amplifier as a function of signal power, which can cause the amplifier to either decrease or increase its gain. Thus, we adopt the definition of saturation power as the lowest input power that causes the amplifier's gain to either increase or decrease by 1dB, which we abbreviate as $P_{\pm 1\mathrm{dB}}$.

In this chapter, we address the question: for a given device, does pump depletion, Kerr

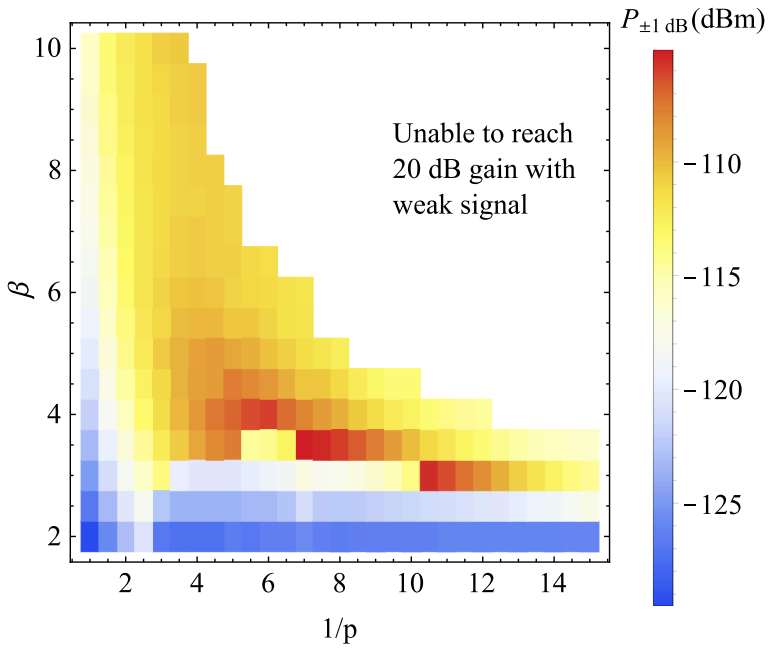

Figure 17: The saturation power for the JRM-based Josephson parametric amplifier with various JRM inductance ratio β and participation ratio p. The amplifier has a sweet spot, in which saturation power is maximal, in the low β and intermediate p regime regime; Optimizing β and p, we find saturation power of $P_{\pm 1\ \mathrm{dB}} \sim -104.8$ dBm at $\beta \approx 3.5$, $1/p \approx 7.0$. For small p and large β, the amplifier is not able to reach the desired reflection gain (of 20 dB); this region is labeled in white. In the intermediate p regime ($1/p \sim 4$ to 10), as we lower β, the saturation power first increases, hits the sweet spot, and then abruptly drops. To understand this behavior we refer to Fig. 28a, which shows that the gain at large signal powers tends to increase as β decreases. This trend is at first beneficial to the amplifier, as the gain vs. signal power curve flattens out. However, at even lower β the gain tends to increase with signal power (a feature that we call the "shark-fin") resulting in the amplifier saturating to 21 dB (see Fig. 28a, $\beta = 3$ curve) and hence the saturation power abruptly decreasing. The sweet spot of the saturation power is located at the edge of the this "reflection gain boost" regime.

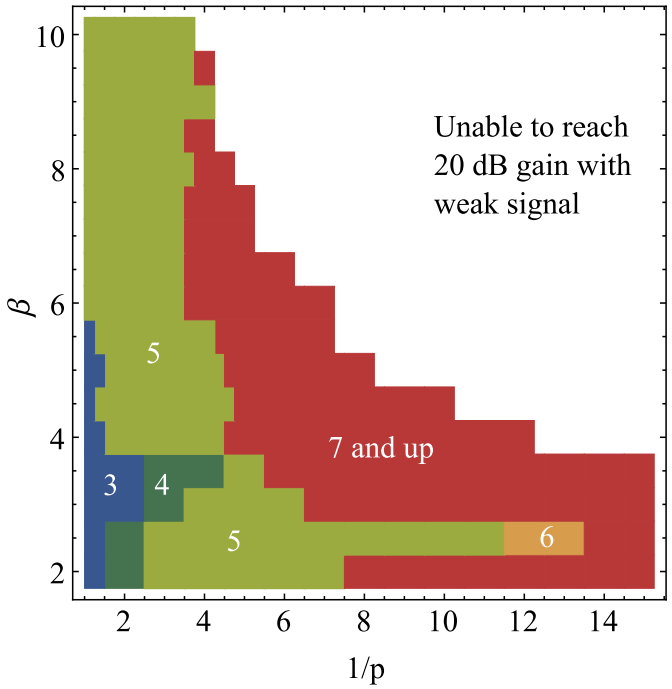

Figure 18: The minimum truncation order needed to converge small-signal reflection gain of the amplifier to 20 ± 0.3 dB. In our main text, we show that the convergence order of small-signal reflection gain gives a good prediction on the convergence order of the saturation power (see Fig. 28b & c). In the small-β, large-p corner, the third order truncation is enough to make the time-solver convergence to the desired 20 dB reflection gain. While as we decrease the participation ratio, the higher and higher order is needed to converge the truncated theory, which shows that the full-order simulation is needed to predict the performance of the amplifier near the sweet spot.

terms, or higher-order nonlinearities limit the saturation power $P_{\pm 1\mathrm{dB}}$? Yet how do we tame these limitations to optimize the device by maximizing $P_{\pm 1\mathrm{dB}}$? Our analysis and results are generally applicable for all amplifiers based on third-order couplings, including JPAs based on Superconducting Nonlinear Asymmetric Inductive eLements (SNAILs) [74, 75, 76, 77]), flux pumped Superconducting QUantum Interference Devices (SQUIDs) [78, 79, 80, 81, 82], and the Josephson Parametric Converters (JPCs) [83, 84, 85, 86, 87]). These techniques we develop may also be of use in the simulation of non-cavity based amplifiers, such as the traveling wave parametric amplifier (TWPA) [88, 89, 90].

In the JPC, three microwave modes (a,b,c) are coupled via a ring of four Josephson Junctions [the so-called Josephson Ring Modulator (JRM), see Fig. 19(b) shaded part, for example]. A third-order coupling ($g_3\varphi_a\varphi_b\varphi_c$) between the fluxes ($\varphi_i$) of three microwave modes is obtained by applying a static magnetic flux to the JRM ring. Phase-preserving gain is obtained by pumping one mode (typically c) far off resonance at the sum frequency of the other two (a and b), with the gain amplitude being controlled by the strength of the pump drive.

We now discuss the main results of our investigation, which are summarized in Figs. 17 and 18. Previously, descriptions of JPC's relied on expanding the nonlinear couplings between the three microwave modes in a power series of cross- and self- couplings. The power series was truncated at the lowest possible order, typically fourth (i.e., corresponding to the cross- and self-Kerr terms) [84, 156, 85, 162]. In the present chapter, we compare these power series expansions with the exact numerical solutions in the framework of semi-classic input-output theory. Our first main finding is that there is indeed a sweet spot for operating a JPA, see Fig. 17, at which $P_{\pm 1\mathrm{dB}}$ is maximized. The sweet spot appears for moderate values of the two circuit parameters: participation ratios $p \sim 1/7$ and shunt inductance ($\beta = L_\mathrm{J}/L_\mathrm{in} \sim 3.5$, where L_in is the shunt inductance, $L_\mathrm{J} = \varphi_0/I_0$ is the Josephson inductance, $\varphi_0 = \hbar/2e$ is the reduced flux quantum, and I_0 is the Josephson junction critical current). Our second main finding is that in the vicinity of the sweet spot nonlinear terms up to at least 7th order are comparable in magnitude and hence truncating the power series description at fourth order is invalid, see Fig. 18. The second main result can be interpreted from two complementary perspectives. First, the sweet spot corresponds to high pump pow-

ers and hence the energy of Josephson junctions cannot be modeled by a harmonic potential anymore. Second, different orders of the power series expansion have either a positive or a negative effect on the gain as a function of signal power; when the magnitudes of terms at different orders are comparable the terms cancel each other resulting in a boost of $P_{\pm 1\mathrm{dB}}$. We hypothesize that the second main finding is a generic feature for Josephson junction based parametric amplifiers.

Before moving to a detailed development of our theory, we provide a summary of the key steps of our investigation and outline the structure of our paper.

We begin by noting that in addition to the above-mentioned parameters p and β, the magnetic flux through the JRM $\varphi_{\mathrm{ext}} = (2\pi/\varphi_0)\Phi_{\mathrm{ext}}$ is another important control parameter. For conventional JRMs [84, 83], at non-zero values of applied flux there are non-zero cross- and self-coupling at all orders (4th, 5th, etc.). However, we have recently realized that a linearly-shunted variant of the JRM [156, 162] can null all even-order couplings at a special flux bias point ($\varphi_{\mathrm{ext}} = 2\pi$), which we call the Kerr nulling point. The same nulling is also observed in SNAIL-based devices [74]. In the context of a JPC with participation ratio $p < 1$, even couplings come back but remain much smaller than at generic values of φ_{ext}. Therefore throughout this paper, we focus on φ_{ext} at or in the vicinity of the Kerr nulling point.

We calculate the saturation power using semi-classical equations of motion for the microwave modes, which are derived using input-output theory from the Lagrangian for a lumped-circuit model of the JPA. When we consider higher than third-order couplings, these equations are not generally analytically solvable. To analyze the saturation power for a given set of parameters, we compare numerical integration of the full nonlinear equations to solutions of various, artificially truncated versions of the equations obtained using both numerical integration and perturbation theory. We begin by investigating the effects of pump depletion. To do so, we analyze the dynamics of all the modes with interactions truncated at third order. Using classical perturbation theory to eliminate the dynamics of the pump mode (c), we find, in contradiction with the basic understanding of pump 'depletion', that the first corrections are a complex fourth order cross-Kerr coupling between modes a and b, and an associated two-photon loss process in which pairs of a and b photons decay

into the c mode, that effectively *increase* the pump strength. The dynamically generate Kerr terms act similarly to the intrinsic Kerr terms, including giving rise to saturation to higher gain when the pump mode frequency is positively detuned from the sum frequency. Further, in the shunted JRM, we can partially cancel the real part of the dynamically generated Kerr by tuning the applied flux near the Kerr nulling-point so as to generate an opposite sign intrinsic Kerr. Thus, the presence of judicious intrinsic Kerr can be a virtue, and the ultimate pump 'depletion' limit is set by the imaginary Kerr and two-photon loss. Increasing the β value of the JRM reduces these effects and increase the JPCs saturation power. Away from the nulling point, these depletion effects are overwhelmed by the intrinsic Kerr effects, and the device is Kerr-limited in agreement with our previous results.

Next, we perform calculations with full nonlinearity, and find that saturation power stops increasing at high β. We find that this is primarily due to certain 5th order terms of the form $(\varphi_a^2 + \varphi_b^2)\,\varphi_a\varphi_b\varphi_c$. These terms modulate the effective parametric coupling strength as a function of the input signal power thus shifting the amplifier away from the desired gain by increasing the effective parametric coupling (in fact, throughout this work we failed to identify a scenario in which the amplifier 'runs out of pump power').

To suppress the strength of these terms relative to the desired third order coupling, we introduce an additional control knob by adding outer linear inductors L_{out} in series with the JRM. The participation ratio $p = L_{\text{JRM}}/(2L_{\text{out}} + L_{\text{JRM}})$, where L_{JRM} is the effective inductance of the JRM, controls what fraction of the mode power is carried by the JRM. Decreasing p results in the suppression of all coupling terms; however, the higher-order coupling terms decrease faster than the lower order ones. Thus, if the saturation power is limited by intrinsic 5th order terms, we can increase the saturation power by decreasing the participation ratio p. We remark that as the pump power is increased, the cross-coupling terms result in a shift of the JPA frequencies that must be compensated, which we do for each value of p and β. Tuning both p and β we can find a sweet spot for the operation of the JPC, as discussed above.

In general, the mode frequencies shift with applied pump power. This, combined with the fact that JPAs can function with pump detunings comparable to the bandwidth of the resonators on which they are based, makes comparing theory and experiment very complicated.

For concreteness, our simulations vary the applied pump and signal frequencies to identify the bias condition which requires minimum applied pump power to achieve 20 dB of gain. These points can be readily identified in experiment [85]. However, there has been a recent observation in SNAIL-based JPAs that deliberate pump detuning can additionally enhance device performance [76], and serve as an *in situ* control to complement the Hamiltonian engineering we discuss in this work.

This paper is organized as follows. In Sec. 4.2, we focus on the closed model of JPA circuit (without input-output ports). We start by reviewing the basic theory of circuits with inductors, capacitors and Josephson junctions in subsection 4.2.1. In subsection 4.2.2, we include the external shunted capacitors with JRM, and present the normal modes of the JPA circuit model using Lagrangian dynamics. In Section 4.3, we further include the input-output ports into the circuit model of the JPA, and construct the equations of motion to describe the dynamics of the circuit. In Section 4.4, we investigate the limitation on the saturation power of the JPA without external series inductors. Specifically, we analyze the 3rd order theory using both numerical and perturbative approaches in Sec. 4.4.3. We compare these results with the effect of Kerr nonlinearities in Sec. 4.4.4 and identify the dynamically generated Kerr terms and the two-photon loss processes. Intrinsic fifth- and higher-order nonlinear couplings are investigated in Sec. 4.4.5. We put these results together in Sec. 4.4.1 and identify which effect is responsible for limiting the saturation power in different parametric regimes. In Sec. 4.5 we consider the consequence of the series inductors outside of it. We show that the series inductors, which suppress the participation ratio of the JRM, can be used to improve the dynamic range of the JRM. We discuss how to optimize the saturation power of the JPA, taking into account both series inductors and full nonlinearities in Section 4.6. In Sec. 4.7, we further explore how the saturation power is affected by the magnetic field bias, the modes' decay rates and stray inductors in series of the Josephson junction in JRM loop. We provide an outlook on the performance of Josephson junction based amplifiers in Section 4.9.

4.2 Equations of motion for circuits made of Josephson junctions

In this section, we review the theory of lumped circuits elements. We start from the Lagrangian treatment of single circuit elements in subsection 4.2.1. Then in subsection 4.2.2, we work on the JRM and the closed JPA circuit model and solved the normal mode profiles of the JRM.

4.2.1 Lagrangian description of linear inductance, Josephson junctions and capacitors

The equations of motion (EOM) that describe the dynamics of a circuit with Josephson junctions, inductors, and capacitors can be derived using the formalism of Lagrangian dynamics, which naturally leads to Kirchhoff's law. We use the dimensionless flux on each node of the circuit, $\varphi_j(t) = \frac{1}{\phi_0}\int_{-\infty}^{t} V_j(t')dt'$, as the set of generalized coordinates. The Lagrangian $\mathcal{L}[\{\varphi_j, \dot{\varphi}_j\}]$ is defined as

$$\mathcal{L} = T[\{\dot{\varphi}_j\}] - U[\{\varphi_j\}], \tag{4.1}$$

where T is the kinetic energy associated with the capacitors and U is the potential energy associated with the inductors and the Josephson junctions. Using Fig. 19(a) to define the nodes and current direction for each type of circuit element, we observe that each capacitor contributes

$$E_C = \frac{C}{2}\phi_0^2\left(\dot{\varphi}_1 - \dot{\varphi}_2\right)^2 \tag{4.2}$$

to $T[\{\dot{\varphi}_j\}]$, while each inductor and each Josephson junction contributes

$$E_L = \frac{\phi_0^2}{2L}(\varphi_2 - \varphi_1)^2, \tag{4.3}$$

$$E_{\mathrm{J}} = -\phi_0 i_c \cos\left(\varphi_2 - \varphi_1\right), \tag{4.4}$$

to $U[\{\varphi_j\}]$, where i_c is the critical current of the Josephson junctions. The current across a capacitor is

$$-\frac{1}{\phi_0}(\delta E_C/\delta\varphi_1) = \frac{1}{\phi_0}(\delta E_C/\delta\varphi_2)$$

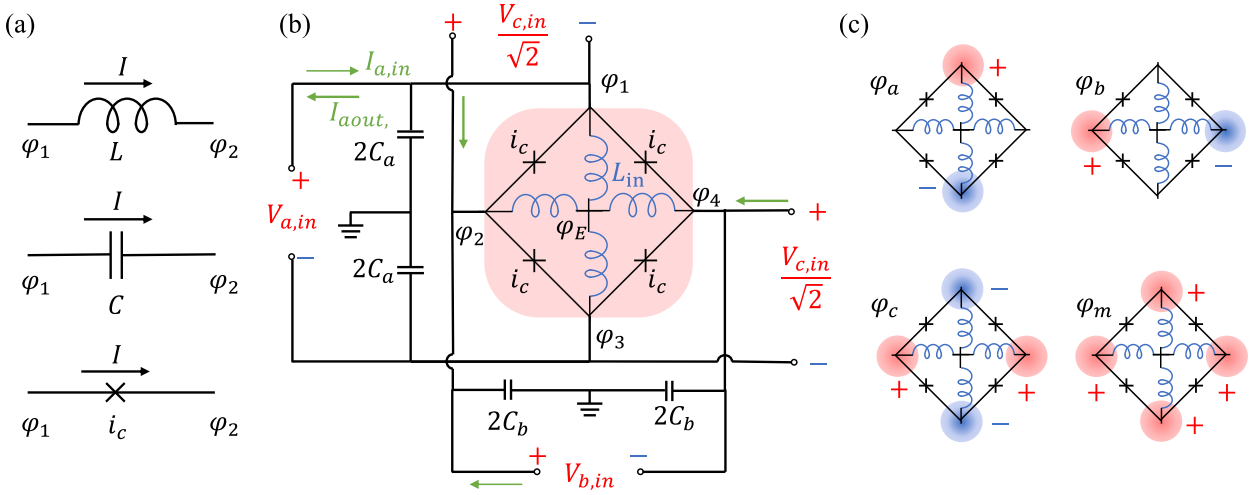

Figure 19: In (a) we show the typical circuit elements that we will focus on in this paper, a linear inductor with inductance L, a capacitor with capacitance C and a Josephson junction with critical current i_c. The node phase and the convention for the current is labeled on each element drawings. The circuit model for the JRM-based JPA circuit is shown in (b). The circuit model for a linear inductance shunted Josephson Ring Modulator (JRM) is shaded in red. We connected the linear inductance shunted JRM with the capacitors and the input-output ports. We assume the normal modes are symmetrically driven by the ports. For the port corresponds to mode φ_a, we use the green arrows to show the input and output (reflected) current flow direction. For b-mode, we only use the green arrow to show the flow direction of the input current. The connection of the c-port is not shown in the plot. The c-port also drives the corresponding mode profile symmetrically. The corresponding normal modes, including three nontrivial modes φ_a, φ_b and φ_c and one trivial mode φ_m, are shown in (c).

, while the current across an inductor is

$$\frac{1}{\phi_0}(\delta E_L/\delta\varphi_1) = -\frac{1}{\phi_0}(\delta E_L/\delta\varphi_2)$$

and across a Josephson junction

$$\frac{1}{\phi_0}(\delta E_{\rm J}/\delta\varphi_1) = -\frac{1}{\phi_0}(\delta E_{\rm J}/\delta\varphi_2).$$

Using the Lagriangian $\mathcal{L}$ of the circuit elements, the current that flows out of each node of the circuit is

$$J_j = -\frac{1}{\phi_0}(\delta\mathcal{L}/\delta\varphi_j).$$

To obtain the equations of motion (EOMs) we extremize the action by setting $J_j = 0$, which corresponds to enforcing Kirchhoff's law.

Next, we apply the Lagrangian formalism to derive the potential energy of the linear-inductor-shunted JRM, the key component at the heart of the JPA, shown in Fig. 19(b), which is shaded in red. The potential energy of the JRM circuit [1] is

$$E_{\mathrm{JRM}} = \frac{\phi_0^2}{2L_{\mathrm{in}}}\sum_{j=1}^{4}\left(\varphi_j - \varphi_E\right)^2 - \phi_0 i_c \sum_{i=1}^{4}\cos\left[\varphi_{i+1} - \varphi_i - \frac{\varphi_{\mathrm{ext}}}{4}\right], \tag{4.5}$$

where φ_j's are the phases of the superconductors on the nodes [see Fig. 19(b)] and we adapt the convention that $\varphi_5 = \varphi_1$ for the summation. The external magnetic flux though the JRM circuit Φ_{ext} controls the parameter $\varphi_{\mathrm{ext}} = \Phi_{\mathrm{ext}}/\phi_0$. Applying Kirchhoff's law to node E, we obtain $\varphi_E = \frac{1}{4}\left(\varphi_1 + \varphi_2 + \varphi_3 + \varphi_4\right)$.

4.2.2 Normal modes of the Josephson parametric amplifier

In this sebsection, we focus on the equations of motion of the closed circuit model of the JPA (i.e., ignore the input-output ports) and analyze the normal mode profile of the JPA circuit (see Fig. 19(b), but without input ports).

The potential energy of the shunted JRM was derived in the previous subsection, see Eq. (4.5). The kinetic energy associated with the capacitors [Fig. 19(b)], Eq. (4.2), is

$$E_c = \phi_0^2\left(C_a\dot{\varphi_1}^2 + C_b\dot{\varphi_2}^2 + C_a\dot{\varphi_3}^2 + C_b\dot{\varphi_4}^2\right), \tag{4.6}$$

Which gives the Lagrangian $\mathcal{L} = E_c - E_{\mathrm{JRM}}$. The EOM of this closed circuit can be constructed using Lagrange's equation, e.g. for a node flux φ_j,

$$2C_j\ddot{\varphi}_j + \frac{1}{L_{\mathrm{in}}}\left(\varphi_j - \varphi_E\right) + \frac{1}{L_{\mathrm{J}}}\left[\sin\left(\varphi_j - \varphi_{j+1} + \frac{\varphi_{\mathrm{ext}}}{4}\right)\right.$$

[1] Throughout our paper, we make the assumption that the JRM circuit is symmetric, that is all four inner inductors are identical and all four Josephson junctions are identical.

$$-\sin\left(\varphi_{j-1}-\varphi_j+\frac{\varphi_{\rm ext}}{4}\right)\Big]=0, \tag{4.7}$$

where φ_j is the node phases, $j=1,2,3,4$, and we use the index convention that $\varphi_0=\varphi_4$, $\varphi_5=\varphi_1$. According to the Fig. 19(b), the node capacitance are $C_1=C_3=C_a$ and $C_2=C_4=C_b$. The Josephson inductance $L_{\rm J}=\phi_0/i_c$.

To analyze the normal modes of the circuit, we assume we have chosen suitable values for the parameters so that the ground state of the circuit is $\varphi_1=\varphi_2=\varphi_3=\varphi_4=0$, and expand in small oscillations to obtain a linearized set of EOMs around the ground state. The corresponding normal coordinates, which we denote as $[\varphi_M]$ in vector form, are related to the node fluxes via $[\varphi]=[\mathcal{A}].[\varphi_M]$, where transformation matrix $[\mathcal{A}]$ is

$$[\mathcal{A}]=\begin{pmatrix} 1 & \frac{1}{2} & 0 & -\frac{C_b}{(C_a+C_b)} \\ 1 & 0 & \frac{1}{2} & \frac{C_a}{(C_a+C_b)} \\ 1 & -\frac{1}{2} & 0 & -\frac{C_b}{(C_a+C_b)} \\ 1 & 0 & -\frac{1}{2} & \frac{C_a}{(C_a+C_b)} \end{pmatrix}, \tag{4.8}$$

and the flux coordinates vectors are defined as $[\varphi]=(\varphi_1,\varphi_2,\varphi_3,\varphi_4)^{\intercal}$ and $[\varphi_M]=(\varphi_m,\varphi_a,\varphi_b,\varphi_c)^{\intercal}$. Inverting this transformation, we obtain the expression for the normal modes in terms of the node fluxes,

$$\varphi_a=\varphi_1-\varphi_3, \tag{4.9a}$$

$$\varphi_b=\varphi_2-\varphi_4, \tag{4.9b}$$

$$\varphi_c=-\frac{1}{2}\left(\varphi_1+\varphi_3-\varphi_2-\varphi_4\right) \tag{4.9c}$$

$$\varphi_m=\frac{C_a}{2(C_a+C_b)}\left(\varphi_1+\frac{C_b}{C_a}\varphi_2+\varphi_3+\frac{C_b}{C_a}\varphi_4\right). \tag{4.9d}$$

The profiles for the normal modes, φ_a, φ_b, φ_c and φ_m are sketched in Fig. 19(c). The normal mode φ_m has zero frequency and it is not coupled with any of the other three modes [see Eq. (4.11)]. Therefore, φ_m is a trivial mode, which can be safely ignored in our following discussion. The corresponding frequencies for the other three nontrivial modes are

$$\omega_a^2=\frac{L_{\rm J}+2L_{\rm in}\cos\left(\frac{\varphi_{\rm ext}}{4}\right)}{2C_aL_{\rm in}L_{\rm J}}, \tag{4.10a}$$

$$\omega_b^2=\frac{L_{\rm J}+2L_{\rm in}\cos\left(\frac{\varphi_{\rm ext}}{4}\right)}{2C_bL_{\rm in}L_{\rm J}}, \tag{4.10b}$$

$$\omega_c^2 = \frac{C_a + C_b}{C_a C_b} \cdot \frac{L_{\rm J} + 4L_{\rm in}\cos\left(\frac{\varphi_{\rm ext}}{4}\right)}{4L_{\rm in}L_{\rm J}}. \tag{4.10c}$$

With the coordinate transformation given by the model matrix $[\mathcal{A}]$ [see Eq. (4.8)], we can re-write the potential energy of the JPA (the energy of JRM circuit) using the normal modes φ_a, φ_b and φ_c, as

$$\begin{aligned} E_{\rm JRM} = &-4E_{\rm J}\left[\cos\left(\frac{\varphi_a}{2}\right)\cos\left(\frac{\varphi_b}{2}\right)\cos\left(\varphi_c\right)\cos\left(\frac{\varphi_{\rm ext}}{4}\right)\right. \\ &\left.+\sin\left(\frac{\varphi_a}{2}\right)\sin\left(\frac{\varphi_b}{2}\right)\sin\left(\varphi_c\right)\sin\left(\frac{\varphi_{\rm ext}}{4}\right)\right] \\ &+\frac{\phi_0^2}{4L_{\rm in}}\left(\varphi_a^2+\varphi_b^2+2\varphi_c^2\right) \end{aligned} \tag{4.11}$$

where $E_{\rm J} = \phi_0 i_c$ is the Josephson energy.

We observe from Eq. (4.11) that the four Josephson junctions on the outer arms of the JRM provide nonlinear couplings between the normal modes of the circuit. Assuming that the ground state of the circuit is $\varphi_a = \varphi_b = \varphi_c = 0$, and it is stable as we tune the external magnetic flux bias, we can expand the nonlinear coupling terms around the ground state as

$$\begin{aligned} E_{\rm JRM} \sim &\left[\frac{\phi_0^2}{4L_{\rm in}} + \frac{E_{\rm J}}{2}\cos\left(\frac{\varphi_{\rm ext}}{4}\right)\right]\left(\varphi_a^2+\varphi_b^2\right) + \left[\frac{\phi_0^2}{2L_{\rm in}} + 2E_{\rm J}\cos\left(\frac{\varphi_{\rm ext}}{4}\right)\right]\varphi_c^2 \\ &-E_{\rm J}\sin\left(\frac{\varphi_{\rm ext}}{4}\right)\varphi_a\varphi_b\varphi_c - \frac{1}{96}E_{\rm J}\cos\left(\frac{\varphi_{\rm ext}}{4}\right)\left(\varphi_a^4+\varphi_b^4+16\varphi_c^4\right) \\ &+\frac{1}{16}E_{\rm J}\cos\left(\frac{\varphi_{\rm ext}}{4}\right)\left(\varphi_a^2\varphi_b^2+4\varphi_a^2\varphi_c^2+4\varphi_b^2\varphi_c^2\right)+... \end{aligned} \tag{4.12}$$

Because of the parity of the cosine and sine functions, the cosine terms in Eq. (4.11) contribute the even order coupling terms while the sine terms contributes the odd order coupling terms. The nonlinear couplings are controlled by the external magnetic flux bias $\varphi_{\rm ext}$. The third order nonlinear coupling is the desired term for a non-degenerate Josephson parametric amplifier, while all the higher order couplings are unwanted. The Kerr nulling point [74, 162] is achieved by setting the external magnetic flux to $\varphi_{\rm ext} = 2\pi$ (and assuming that the ground state $\varphi_a = \varphi_b = \varphi_c = 0$ remains stable), and we find that all the even order nonlinear couplings are turned off.

4.3 Input-output theory of the Josephson parametric amplifier

The linear-inductor shunted JRM described in the previous section is the core elements of the Josephson parametric amplifier. In order to build the JPA, we add input-output lines and external parallel capacitors to the JRM, see Fig. 19(b). In Section 4.5 we will extend the description of the JPA by adding stray and series inductors to the JRM.

In order to fully model the JPA, we need to describe the input-output properties of the JPA circuit. In Subsec. 4.3.1 we introduce input-output theory, and apply it to the problem of modeling drive and response of the JPA. In Subsec. 4.3.2 we present the full nonlinear equations of motion that describe the JPA circuit.

4.3.1 Input-output relation for the Josephson parametric amplifier

To solve the full dynamics of the JPA with amplification process, we need to be able to describe the microwave signals that are sent into and extracted (either reflected or transmitted) from the circuit. Therefore, we need to connect the input-output ports to the JPA circuit and include the description of them in the EOMs.

To simplify the problem, we assume that the drives perfectly match the profiles of the corresponding normal modes, as shown schematically for modes a and b in Fig. 19(a). Take mode a as an example. We send in a microwave signal with the amplitude of the voltage $V_{a,\mathrm{in}} = \phi_0\dot{\varphi}_{a,\mathrm{in}}$ into the port for this mode. The corresponding current flow from the transmission line to the amplifier is $I_{a,in} = \frac{V_{a,in}}{Z_a}$, where Z_a is the impedance of the transmission line. The voltage applied to node 1 and node 3 are $V_1 = \frac{\phi_0}{2}\dot{\varphi}_{a,\mathrm{in}}$ and $V_3 = -\frac{\phi_0}{2}\dot{\varphi}_{a,\mathrm{in}}$, respectively. While the output microwave signal has output voltage amplitude $V_{a,\mathrm{out}} = \phi_0\dot{\varphi}_{a,\mathrm{out}}$ and the output current is $I_{a,\mathrm{out}} = \frac{V_{a,\mathrm{out}}}{Z_a}$.

At the nodes which connect to the transmission line, e.g. nodes 1 and 3 for a mode, the voltage and current should be single-valued. This requirement induces an input-output condition

$$V_{a,\mathrm{in}} + V_{a,\mathrm{out}} = V_a = V_1 - V_3 \tag{4.13a}$$

$$I_{a,\mathrm{in}} - I_{a,\mathrm{out}} = I_{1,a} = -I_{3,a}, \tag{4.13b}$$

where $I_{1,a}$ ($I_{3,a}$) is the net current flow into node 1 (3) of the amplifier from the port. Because the output signals should be determined by the input signals, we eliminate the output variables from the input-output relation so that it can be combined with the current relation inside the JRM to construct the EOMs for the open circuit model

$$I_{1,a} = -I_{3,a} = \frac{2V_{a,\text{in}}}{Z_a} - \frac{\phi_0\left(\dot{\varphi}_1 - \dot{\varphi}_3\right)}{Z_a}. \tag{4.14}$$

Given the the drives (inputs), we can solve for the mode fluxes using the EOMs, and then obtain the outputs using the input-output relations. For example, the output voltage on port a is determined by

$$V_{a,\text{out}} = \phi_0\left(\dot{\varphi}_1 - \dot{\varphi}_3\right) - V_{a,\text{in}}. \tag{4.15}$$

In the remainder of this paper we focus on the reflection gain of the JPA which is obtained from a phase-preserving amplification process. The input signal to be amplified by the JPA is a single-frequency tone. The amplified output is the reflected signal at the same frequency. Using the Josephson relation relating voltage and flux, we observe that the reflected voltage gain is equal to the reflected flux gain. Therefore, we use the input-output relation for the mode flux, e.g. for port a we have

$$\varphi_{a,\text{out}} = \varphi_1 - \varphi_3 - \varphi_{a,\text{in}}. \tag{4.16}$$

The analysis of input-output ports for mode b and c is similar. For b-port we have

$$I_{2,b} = -I_{4,b} = \frac{2V_{b,\text{in}}}{Z_b} - \frac{\phi_0\left(\dot{\varphi}_2 - \dot{\varphi}_4\right)}{Z_b} \tag{4.17a}$$

$$V_{b,\text{out}} = \phi_0\left(\dot{\varphi}_2 - \dot{\varphi}_4\right) - V_{b,\text{in}}, \tag{4.17b}$$

and for c-port

$$\begin{aligned} I_{2,c} &= I_{4,c} = -I_{1,c} = -I_{3,c} \\ &= \frac{\sqrt{2}V_{c,\text{in}}}{Z_c} - \frac{\phi_0}{2Z_c}\left(\dot{\varphi}_2 + \dot{\varphi}_4 - \dot{\varphi}_1 - \dot{\varphi}_3\right) \end{aligned} \tag{4.18a}$$

$$V_{c,\text{out}} = \frac{\sqrt{2}\phi_0}{2}\left(\dot{\varphi}_2 + \dot{\varphi}_4 - \dot{\varphi}_1 - \dot{\varphi}_3\right) - V_{c,\text{in}}. \tag{4.18b}$$

The extra factor $\sqrt{2}$ that app[ears for the c port is due to the microwave power being split 50/50 between the two transmission lines that drive all four nodes simultaneously.

When constructing the EOM with input-output ports, we should consider the current contribution from all the input-output ports together. For example, the net current injected through node 1 should have contributions from the drive applied to both ports for mode a and mode c, i.e., $I_{1,\mathrm{net}} = I_{1,a} + I_{1,c}$.

4.3.2 Full nonlinear equations of motion for the Josephson parametric amplifier

In this subsection, we combine the circuit model for JPA with the input-output relations to construct the full nonlinear EOMs of the JPA. We will take node 1 as an illustrative example and then give the full set of EOMs for the circuit. Note that the left hand side of the EOM for the closed circuit model of the JRM in Eq. (4.7) is equivalent to the current relation at node 1, except for a constant factor ϕ_0. To construct the EOM for the open circuit with all the driving ports, we should take the net current injected into node 1 to replace the right hand side of the Eq. (4.7). Applying this procedure to all nodes we obtain the EOMs

$$\ddot{\varphi}_1 + \frac{(3\varphi_1 - \varphi_2 - \varphi_3 - \varphi_4)}{8C_a L_{\mathrm{in}}} + \frac{1}{2C_a L_{\mathrm{J}}}\left[\sin\left(\varphi_1 - \varphi_2 + \frac{\varphi_{\mathrm{ext}}}{4}\right) - \sin\left(\varphi_4 - \varphi_1 + \frac{\varphi_{\mathrm{ext}}}{4}\right)\right] \tag{4.19a}$$

$$= \frac{1}{2C_a\phi_0}\left(I_{1,a} + I_{1,c}\right),$$

$$\ddot{\varphi}_2 + \frac{(3\varphi_2 - \varphi_1 - \varphi_3 - \varphi_4)}{8C_b L_{\mathrm{in}}} + \frac{1}{2C_b L_{\mathrm{J}}}\left[\sin\left(\varphi_2 - \varphi_3 + \frac{\varphi_{\mathrm{ext}}}{4}\right) - \sin\left(\varphi_1 - \varphi_2 + \frac{\varphi_{\mathrm{ext}}}{4}\right)\right] \tag{4.19b}$$

$$= \frac{1}{2C_b\phi_0}\left(I_{2,b} + I_{2,c}\right),$$

$$\ddot{\varphi}_3 + \frac{(3\varphi_3 - \varphi_1 - \varphi_2 - \varphi_4)}{8C_a L_{\mathrm{in}}} + \frac{1}{2C_a L_{\mathrm{J}}}\left[\sin\left(\varphi_3 - \varphi_4 + \frac{\varphi_{\mathrm{ext}}}{4}\right) - \sin\left(\varphi_2 - \varphi_3 + \frac{\varphi_{\mathrm{ext}}}{4}\right)\right] \tag{4.19c}$$

$$= \frac{1}{2C_a\phi_0}\left(I_{3,a} + I_{3,c}\right),$$

$$\ddot{\varphi}_4 + \frac{(3\varphi_4 - \varphi_1 - \varphi_2 - \varphi_3)}{8C_bL_{\text{in}}} + \frac{1}{2C_bL_{\text{J}}}\left[\sin\left(\varphi_4 - \varphi_1 + \frac{\varphi_{\text{ext}}}{4}\right) - \sin\left(\varphi_3 - \varphi_4 + \frac{\varphi_{\text{ext}}}{4}\right)\right] \tag{4.19d}$$

$$= \frac{1}{2C_b\phi_0}\left(I_{4,b} + I_{4,c}\right).$$

where the net currents injected from each of the ports to the corresponding nodes are given in Eqs. (4.14), (4.17) and (4.18). Using the transformation of Eq. (4.8) we obtain the EOMs using the normal modes

$$\ddot{\varphi}_a + \gamma_a\dot{\varphi}_a + \frac{\varphi_a}{2C_aL_{\text{in}}} + \frac{2}{C_aL_{\text{J}}}\left[\sin\left(\frac{\varphi_a}{2}\right)\cos\left(\frac{\varphi_b}{2}\right)\cos\left(\varphi_c\right)\cos\left(\frac{\varphi_{\text{ext}}}{4}\right)\right.$$
$$\left. - \cos\left(\frac{\varphi_a}{2}\right)\sin\left(\frac{\varphi_b}{2}\right)\sin\left(\varphi_c\right)\sin\left(\frac{\varphi_{\text{ext}}}{4}\right)\right] = 2\gamma_a\partial_t\varphi_{a,\text{in}}(t) \tag{4.20a}$$

$$\ddot{\varphi}_b + \gamma_b\dot{\varphi}_b + \frac{\varphi_b}{2C_bL_{\text{in}}} + \frac{2}{C_bL_{\text{J}}}\left[\cos\left(\frac{\varphi_a}{2}\right)\sin\left(\frac{\varphi_b}{2}\right)\cos\left(\varphi_c\right)\cos\left(\frac{\varphi_{\text{ext}}}{4}\right)\right.$$
$$\left. - \sin\left(\frac{\varphi_a}{2}\right)\cos\left(\frac{\varphi_b}{2}\right)\sin\left(\varphi_c\right)\sin\left(\frac{\varphi_{\text{ext}}}{4}\right)\right] = 2\gamma_b\partial_t\varphi_{b,\text{in}}(t) \tag{4.20b}$$

$$\ddot{\varphi}_c + \gamma_c\dot{\varphi}_c + \frac{\varphi_c}{C_cL_{\text{in}}} + \frac{4}{C_cL_{\text{J}}}\left[\cos\left(\frac{\varphi_a}{2}\right)\cos\left(\frac{\varphi_b}{2}\right)\sin\left(\varphi_c\right)\cos\left(\frac{\varphi_{\text{ext}}}{4}\right)\right.$$
$$\left. - \sin\left(\frac{\varphi_a}{2}\right)\sin\left(\frac{\varphi_b}{2}\right)\cos\left(\varphi_c\right)\sin\left(\frac{\varphi_{\text{ext}}}{4}\right)\right] = \sqrt{2}\gamma_c\partial_t\varphi_{c,\text{in}}(t) \tag{4.20c}$$

where we define the effective capacitance for the c mode as $C_c = \frac{4C_aC_b}{C_a+C_b}$. The mode decay rates γ_a, γ_b and γ_c are given by $\gamma_a = (C_aZ_a)^{-1}$, $\gamma_b = (C_bZ_b)^{-1}$ and $\gamma_c = \frac{C_a+C_b}{2C_aC_bZ_c}$. We convert the input-output relations of Eqs. (4.15), (4.17b) and (4.18b) into input-output relations for flux

$$\varphi_{a,\text{out}} = \varphi_a - \varphi_{a,\text{in}} \tag{4.21a}$$

$$\varphi_{b,\text{out}} = \varphi_b - \varphi_{b,\text{in}} \tag{4.21b}$$

$$\varphi_{c,\text{out}} = \sqrt{2}\varphi_c - \varphi_{c,\text{in}}. \tag{4.21c}$$

The response of the JPA can be fully described using Eqs. (4.20) and (4.21).

Finally, we point out that it is useful to use the normal modes of the JRM as the coordinates for writing the EOMs as it makes the analysis of the effects of the various orders of nonlinear coupling easier to understand. On the other hand, using the node fluxes as coordinates is useful as they are more naturally connected to Kirchhoff's law, especially when we want to include experimental imperfections.

4.4 Saturation power of a JPA (unit participation ratio)

In this section, we first obtain the saturation power of the JPA as described by the exact nonlinear EOMs discussed in subsection 4.3.2. Next, we analyze how higher-order nonlinear couplings affect the dynamics of the JPA with the goal of understanding which couplings control the saturation power of the parametric amplifier, to give us guidance on how to improve the saturation power.

We begin with Subsec. 4.4.1, in which we summarize our main results concerning the dependence of the saturation power on the parameter

$$\beta = L_{\rm J}/L_{\rm in}. \tag{4.22}$$

Specifically, we compare numerical solution of the full nonlinear model with numerical solutions of truncated models as well as perturbation theory results. We show that for small β the limitation on saturation power comes from dynamically generated Kerr-like terms, while for large β saturation power is limited by 5th order non-linearities of the JRM. The details of the analytical calculations are provided in the following subsections.

In Subsec. 4.4.2, we remind ourselves of the exact analytical solution for the ideal third order amplifier in which the signal is so weak that it does not perturb the pump (i.e., the stiff-pump case). Next, in Subsec. 4.4.3 we consider the case of a third order amplifier with input signal sufficiently strong such that it can affect the pump (i.e., the soft pump case). In this Subsection we construct a classical perturbation expansion (in which the stiff pump solution corresponds to the zeroth order solution and the first order correction) and find that it leads to the generation of an effective cross-Kerr term, and a pair of two-photon loss terms, one of which could be thought of as and imaginary cross-Kerr term. In Subsec. 4.4.4) we compare the effects of the dynamically generated terms to intrinsic Kerr terms. We analyze fifth and higher order couplings in Subsec. 4.4.5).

A note about notation: Throughout this section, we refer to the a-mode as the signal mode, b-mode as the idler mode, and c-mode as the pump mode with intrinsic frequencies ω_a, ω_b and ω_c. To simplify the discussion of the perturbative expansion, we only consider the case in which we assume that (1) the parametric amplifier is on resonance, i.e., $\delta = \omega_S - \omega_a = 0$

(where ω_S is the frequency of the signal tone) and $\varepsilon_p = \omega_P - (\omega_a + \omega_b) = 0$ (where ω_P is the pump tone frequency), so that $\omega_S = \omega_a$, $\omega_I = \omega_b$ and $\omega_P = \omega_a + \omega_b$, (2) the magnetic flux bias is set to the Kerr nulling point, i.e., $\varphi_{\text{ext}} = 2\pi$, (3) an input tone is only sent to the signal mode and there is no input to the idler mode.

4.4.1 Main result: saturation power as a function of β

In this subsection, we will compare the exact numerical solution of the full nonlinear EOMs of the JPA to various approximate solutions in order to identify the effects that limit saturation power.

For concreteness, we fix the following parameters: The magnetic field bias is fixed at $\varphi_{\text{ext}} = 2\pi$, the mode frequencies are fixed at $\omega_a/(2\pi) = 7.5$ GHz and $\omega_b/(2\pi) = 5.0$ GHz ($\omega_c/(2\pi) = 6.37$ GHz is fixed by the JPA circuit), the decay rates of the modes are fixed at $\gamma_a/(2\pi) = \gamma_b/(2\pi) = \gamma_c/(2\pi) = 0.1$ GHz, and the critical current of the Josephson junctions is fixed at $i_c = 1\,\mu$A. Throughout, we will set the amplitude of the pump to achieve 20dB reflection gain (at small signal powers). This leaves us with one independent parameter: the JRM inductance ratio β.

We shall now analyze saturation of the amplifier as a function of β. We find it convenient to use saturation input signal flux $|\varphi_{a,\text{in}}(\omega_a)|$ as opposed to $P_{\pm 1\text{dB}}$ because the former saturates to a constant value at high β while the latter grows linearly at high β. We note that the two quantities are related by the formula

$$P_{\pm 1\text{dB}} = \frac{\phi_0^2}{2Z_a} \left|\partial_t^2 \varphi_{a,\text{in}}(t)\right|^2 = \frac{1}{2} C_a \phi_0^2 \gamma_a \omega_a^2 \left|\varphi_{a,\text{in}}(\omega_a)\right|^2 . \tag{4.23}$$

At the nulling point, the EOMs do not explicitly depend on the Josephson junction critical current i_c. Therefore, the dynamics of the circuit in terms of the dimensionless fluxes φ_a, φ_b, and φ_c are invariant if we fix ω_a, ω_b, γ_a, γ_b, γ_c and β. However, i_c is needed to connect the dimensionless fluxes to dimensional variables. Specifically, the connection requires the mode capacitance, see Eq. (4.23). At the nulling point, the mode capacitance is set by the mode frequency and L_{in} [e.g. $C_a = 1/(\omega_a^2 L_{\text{in}})$] and L_{in} is set by i_c, see Eq (4.22). In the following, we will analyze saturation power in terms of dimensionless fluxes.

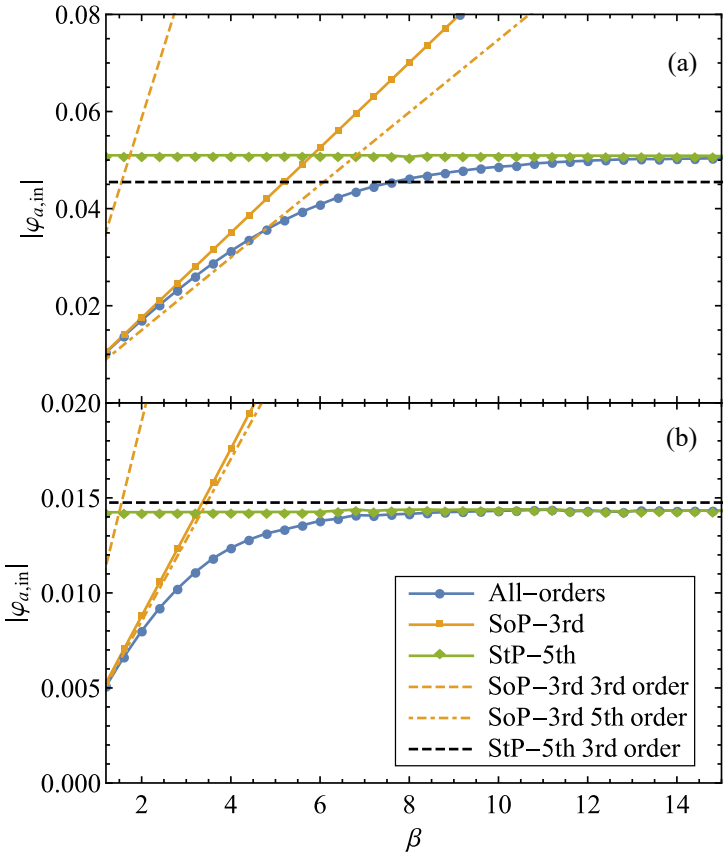

Figure 20: We plot the saturation flux $|\varphi_{a,\mathrm{in}}|$ of the JPA as we change JRM inductance ratio $\beta = L_{\mathrm{J}}/L_{\mathrm{in}}$. The amplifier saturates to 19 dB and 19.9 dB in (a) and (b) respectively. The saturation flux from numerical integration of full nonlinear EOMs, SoP-3rd order and StP-5th order nonlinear models of JPA is plotted as blue, orange and dark green solid lines in both subplots. The saturation fluxes are also obtained by the perturbation analysis for the SoP-3rd order and StP-5th order nonlinear models. We plot the third order and fifth order perturbation results as dashed lines and dash-dotted lines. In (a), the perturbation saturation fluxes do not agree well with the numerical ones. This is because the saturation fluxes are already out of the radius of convergence of the perturbation series. While in (b), they have a good agreement. Parameters chosen: $\varphi_{\mathrm{ext}} = 2\pi$, the mode frequencies $\omega_a/(2\pi) = 7.5$ GHz, $\omega_b/(2\pi) = 5.0$ GHz, mode decay rates $\gamma/(2\pi) = 100$ MHz for all three modes. The critical current is set to $i_c = 1$ μA. We tune the inner shunted inductance L_{in} to tune β.

In Fig 20 we plot the saturation flux as a function of β obtained using the full nonlinear EOMs as well as various truncated EOMs and perturbation theory. In panel (a) of the figure we use the conventional criteria that saturation occurs when the gain change by ± 1 dB, while in panel (b) we use the tighter condition that gain changes by ± 0.1 dB. We observe that the saturation flux has two different regimes. At small β the saturation flux grows linearly with β, while at high β it saturates to a constant.

To understand the limiting mechanisms in both β regimes, we compare the saturation flux $\varphi_{a,\text{in}}$ obtained from the numerical integration of full nonlinear EOMs with the various truncated EOMs. We mainly focus on two nonlinear truncated models: (1) soft-pump third order truncated model (SoP-3rd), in which the EOMs of the amplifier are obtained by truncating the Josephson energy to 3rd order in mode fluxes; (2) the stiff-pump fifth order truncated model (StP-5th), in which the Josephson energy is truncated to 5th order in mode fluxes and we ignore the back-action of the signal and idler modes on pump mode dynamics.

We begin by considering the small β regime. Comparing the saturation flux obtained from the numerical integration of full nonlinear EOMs with the above two truncated EOMs, we see that the saturation flux $\varphi_{a,\text{in}}$ of the full nonlinear EOMs most closely matches the EOMs of SoP-3rd order model of the amplifier, which indicates the soft-pump condition is the dominating limitation in this regime.

In the soft-pump model, saturation power is limited by the dynamically generated Kerr term. This term shifts the signal and idler modes off resonance as the power in these modes builds up. We describe the details of this process in Subsections 4.4.3 and 4.4.4. In the small β regime, the saturation flux of the amplifier increases as we increase β [see Fig. 20(a)]. This is because increasing β effectively decreases the nonlinear coupling strength of the amplifier and therefore decreasing the effective strength of the dynamically generated Kerr term. This conclusion is supported by comparing (see Fig. 20) the exact numerics on the SoP-3rd model (labeled SoP-3rd) with a perturbative analysis of the same model which captures the generated Kerr terms (labeled SoP-3rd 5th order).

In large β regime, the saturation flux obtained from full nonlinear model saturates to a constant value (see Fig. 20, "All-order" line). This behavior diverges from the prediction of the SoP-3rd order nonlinear model ("SoP-3rd" line) but it is consistent with the StP-5th

order nonlinear model ("StP-5th" line), which indicates that the dominating limitation in the large β regime is the intrinsic 5th order nonlinearity of the JRM energy. Perturbation theory analysis of the StP-5th order nonlinear model ("StP-5th 3rd order" and "StP-5th 5th order" lines, see Subsec. 4.4.5) indicates that the saturation flux depends on the ratio of the fifth order and the third order nonlinear couplings arising from the Josephson non-linearity, and is therefore independent of β. As we increase β, the limitation on the saturation power placed by the generated cross-Kerr couplings decreases and hence the mechanism limiting the amplifier's saturation flux changes from generated cross-Kerr couplings to fifth order nonlinearity of the JRM energy. The β at which the mechanism controlling saturation flux changes is controlled by the decay rates as $\beta \propto \gamma^{-1/2}$. For our choice of parameters this change of mechanism occurs at $\beta \sim 6$.

4.4.2 Ideal parametric amplifier, 3rd order coupling with stiff pump approximation

In this subsection, we remind ourselves with the solution of ideal parametric amplifier. The ideal parametric amplifier can be exactly solved in frequency domain such that we can also verify the reliability of the numerical solutions.

In an ideal parametric amplifier, the only coupling present is a third order coupling between the signal, idler and pump mode that results in parametric amplification. Further, the pump mode strength is considered to be strong compared to the power consumed by the amplification, such that the pump mode dynamics can be treated independently of the signal and idler modes. This approximation is commonly referred to as the "stiff-pump approximation" (StP). The EOMs to describe the parametric amplifier can be derived from the full nonlinear EOMs in Eq. (4.20) by expanding the nonlinear coupling terms to second order in mode fluxes φ's (2nd order in EOMs corresponding to 3rd order in Lagrangian). Under the stiff-pump approximation, we can effectively remove the three mode coupling terms in the EOM for the pump mode

$$\ddot{\varphi}_c + \gamma_c \dot{\varphi}_c + \omega_c^2 \varphi_c = \sqrt{2}\gamma_c \partial_t \varphi_{c,\mathrm{in}}(t). \tag{4.24}$$

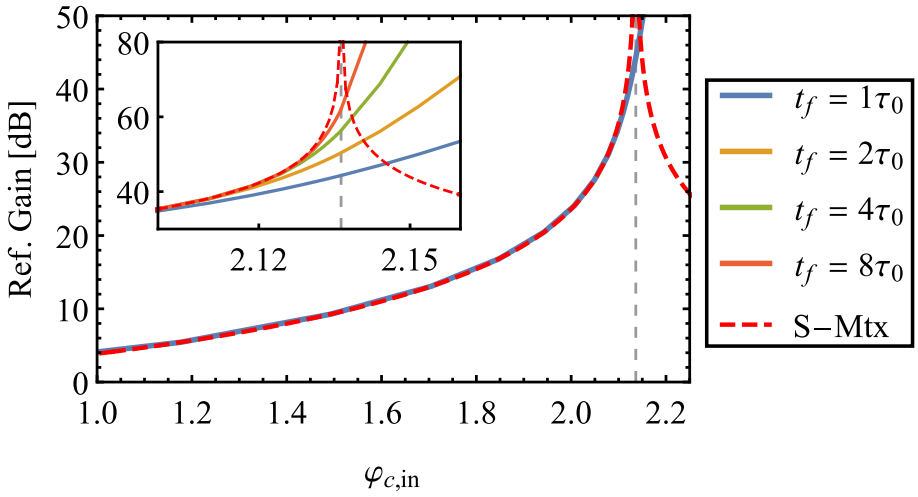

Figure 21: The reflection gain of an ideal parametric amplifier calculated by both scattering matrix (red dashed line) and time-domain numerical evolution (blue line). The response of the ideal amplifier can be faithfully simulated by the time-domain numerical method with a reasonable reflection gain. The black dashed line shows the bias point beyond which the amplifier is unstable. Our time-domain numerical solution start to deviated form the scattering matrix calculation at ~ 2.1. This is because the numerical accuracy of the time-domain solver. In the insert, we increase the final time t_f of the time-solver. We notice a better and better convergence to the analytical solution (red dashed line). This is caused by a numerical instability that occurs near the divergence point of the amplifier, Eq. (4.32). Parameters chosen: $\varphi_{\text{ext}} = 2\pi$, $\omega_a/(2\pi) = 7.5$ GHz, $\omega_b/(2\pi) = 5.0$ GHz, $\gamma_a = \gamma_b = \gamma_c = 2\pi \times 0.01$ GHz and $i_c = 1.0$ μA. Time constant $\tau_0 = 4000 f_a^{-1}$ where f_a is the signal mode frequency.

φ_c obtained from this equation acts as a time-dependent parameter in the EOMs for the a and b modes

$$\ddot{\varphi}_a + \gamma_a\dot{\varphi}_a + \omega_a^2\varphi_a - \frac{2\omega_a^2}{\beta}\varphi_b\varphi_c = 2\gamma_a\partial_t\varphi_{a,\mathrm{in}}(t), \tag{4.25a}$$

$$\ddot{\varphi}_b + \gamma_b\dot{\varphi}_b + \omega_b^2\varphi_b - \frac{2\omega_b^2}{\beta}\varphi_a\varphi_c = 2\gamma_b\partial_t\varphi_{b,\mathrm{in}}(t). \tag{4.25b}$$

Assuming the pump tone is $\varphi_{c,\mathrm{in}}(t) = \varphi_{c,\mathrm{in}}e^{-i\omega_P t} + c.c.$, we find that $\varphi_c(t) = \varphi_c(\omega_P)e^{-i\omega_P t} + c.c.$ where,

$$\varphi_c(\omega_P) = \frac{-i\sqrt{2}\gamma_c\omega_P}{\omega_c^2 - \omega_P^2 - i\gamma_c\omega_P}\varphi_{c,\mathrm{in}} \tag{4.26}$$

Substituting the c-mode flux φ_c in Eq. (4.25) the EOMs for a and b modes become linear and can be solved in the frequency domain. The Fourier components of the a and b modes, under the rotating-wave approximation, are

$$\varphi_a(\omega_a) = \frac{2\tilde{\gamma}_a\tilde{\gamma}_b}{\tilde{\gamma}_a\tilde{\gamma}_b - 4g^2\left|\varphi_c(\omega_P)\right|^2}\varphi_{a,\mathrm{in}} \tag{4.27a}$$

$$\varphi_b^*(\omega_b) = \frac{4ig\tilde{\gamma}_a\varphi_c^*(\omega_P)}{\tilde{\gamma}_a\tilde{\gamma}_b - 4g^2\left|\varphi_c(\omega_P)\right|^2}\varphi_{a,\mathrm{in}} \tag{4.27b}$$

where we define the dimensionless decay rates $\tilde{\gamma}_j = \gamma_j/\omega_j$, the dimensionless three-mode coupling strength $g = (1/\beta)\sin\left(\frac{\varphi_{\mathrm{ext}}}{4}\right) = 1/\beta$, which is obtained from a series expansion of the dimensionless potential energy

$$\mathcal{E}_{\mathrm{JRM}} \equiv \left[(\phi_0^2/L_{\mathrm{in}})\right]^{-1} E_{\mathrm{JRM}}. \tag{4.28}$$

Here we assume the input tone is $\varphi_{a,\mathrm{in}} = \varphi_{a,\mathrm{in}}e^{-i\omega_a t} + c.c.$ and there is no input into idler (b) mode.

The linear response of the ideal parametric amplifier is obtained using scattering matrix formalism. The EOMs of an ideal parametric amplifier can be written in matrix form as $[M].[\varphi] = 2[\tilde{\gamma}].[\varphi_{\mathrm{in}}]$, where

$$[M] = \begin{pmatrix} \tilde{\gamma}_a & -2ig\varphi_c(\omega_P) \\ 2ig\varphi_c^*(\omega_P) & \tilde{\gamma}_b \end{pmatrix}, \tag{4.29}$$

$$[\tilde{\gamma}] = \begin{pmatrix} \tilde{\gamma}_a & \\ & \tilde{\gamma}_b \end{pmatrix}. \tag{4.30}$$

The scattering matrix, which is defined by $[\varphi_{\rm out}] = [S].[\varphi_{\rm in}]$, is given by $[S] = 2[M^{-1}].[\tilde{\gamma}] - I_{2\times 2}$, where we have used the input-output relation $[\varphi] = [\varphi_{\rm in}] + [\varphi_{\rm out}]$ and $I_{2\times 2}$ is the 2×2 identity matrix,

$$[S] = \begin{pmatrix} \frac{2\tilde{\gamma}_a\tilde{\gamma}_b}{\tilde{\gamma}_a\tilde{\gamma}_b - 4g^2|\varphi_c(\omega_P)|^2} - 1 & -\frac{4ig\tilde{\gamma}_b\varphi_c(\omega_P)}{\tilde{\gamma}_a\tilde{\gamma}_b - 4g^2|\varphi_c(\omega_P)|^2} \\ \frac{4ig\tilde{\gamma}_a\varphi_c^*(\omega_P)}{\tilde{\gamma}_a\tilde{\gamma}_b - 4g^2|\varphi_c(\omega_P)|^2} & \frac{2\tilde{\gamma}_a\tilde{\gamma}_b}{\tilde{\gamma}_a\tilde{\gamma}_b - 4g^2|\varphi_c(\omega_P)|^2} - 1 \end{pmatrix}. \tag{4.31}$$

The reflection gain of the signal mode (in units of power) is defined as $G_0 = |[S]_{11}|^2$. To get large gain ($G_0 \gg 1$), the pump mode strength should be tuned to

$$2g\,|\varphi_c(\omega_P)| \sim \sqrt{\tilde{\gamma}_a\tilde{\gamma}_b}. \tag{4.32}$$

Alternatively, we can obtain the response of the JPA using time-domain numerical integration. First, we solve for the mode variables inside the JPA circuit with specific signal and pump inputs. Next, we use the input-output relation to find the output signal and then we obtain the reflection gain of the amplifier. Specifically, to solve the dynamics of the parametric amplifier, we set the input signal as $\varphi_{a,\rm in}(t) = \bar{\varphi}_{a,\rm in}\cos(\omega_S t)$ and $\varphi_{b,\rm in} = 0$, and numerically integrate the EOMs [Eq. (4.25)]. Here we note that $\bar{\varphi}_{a,\rm in} = 2\varphi_{a,\rm in}$, which is defined in Eq. (4.27). In Fig. 21, we show the comparison of the reflection gain obtained using numerical integration (red dashed line) and the scattering matrix solution (blue solid line). The two solutions start out identical. However, as we increase the pump mode strength $\varphi_{c,\rm in}$, we notice that as the reflection gain starts diverging ($G_0 \sim 35$ dB, see the insert of Fig. 21) from the analytical solution. This is because the numerical solver need a longer and longer time window to establish the steady-state solution of the nonlinear EOMs as we move towards the unstable point (vertical dashed line). To optimize the run time, here and later in the paper, we choose the time-window for our solver so that the numerical solution saturates for amplification of ~ 20 dB.

In the unstable regime the reflection flux on the signal mode diverges exponentially with time, as the amplifier will never run out of power under the StP approximation. Therefore, in this regime the time-domain solver gives a large unphysical reflection gain (as we cut it off at some large, but finite time).

4.4.3 JPA with third order coupling, relaxing the stiff-pump approximation

As we increase the input signal strength, the power supplied to the pump mode will eventually be comparable to the power consumed by amplification, where the amplifier will significantly deviate from the ideal parametric amplifier. In this subsection, we reinstate the action of the signal and idler modes on the pump mode. Since the pump mode strength is affected by the signal and idler mode strengths, we refer to it as the "Soft-pump" (SoP) condition.

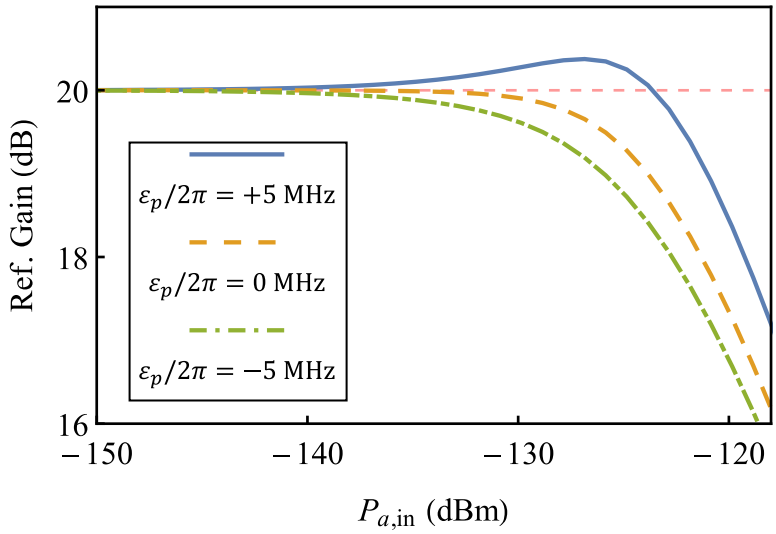

Figure 22: We consider the soft-pump condition with third order coupling and calculate the reflection gain of the amplifier. We slightly detune the pump drive frequency from the sum frequency of the signal and idler mode frequency. When the pump frequency detuning ε_p is negative (green dash-dotted line), the reflection gain is further suppressed compared with on-resonance drive (orange dashed line). However, when the pump frequency detuning is positive (blue line), the "shark fin" feature reappears, which was understood as the consequence of the existence of Kerr nonlinearity in the amplifier system.

The EOMs for the Soft-pump third order model of the JPA can be obtained by expanding the full nonlinear EOMs [Eq. (4.20)] and truncating all three EOMs to second order in mode fluxes. That is, we use Eq. (4.25) to describe a and b modes and modify Eq. (4.24) for the c

mode as

$$\ddot{\varphi}_c + \gamma_c \dot{\varphi}_c + \omega_c^2 \varphi_c - \frac{\omega_c^2}{\beta} \varphi_a \varphi_b = \sqrt{2} \gamma_c \partial_t \varphi_{c,\mathrm{in}}(t). \tag{4.33}$$

Unlike the StP approximation, the c mode flux φ_c can no longer be treated as a time-dependent parameter unaffected by a and b modes. While we can no longer obtain an exact analytical solution to these EOMs, we use perturbation theory as well as time-domain numerical integration to seek the dynamics of the amplifier.

In Fig. 22, we plot the reflection gain obtained by numerical integration. The reflection gain of the amplifier is no longer independent of the input signal power, instead we see that the reflection gain deviates from 20 dB as we increase the signal mode power. Moreover, as we change the detuning of the pump mode relative to the sum frequency of the signal and idler mode, the deviation of the reflection gain changes from negative to positive. While a deviation towards smaller gain (which occurs at negative or zero detuning) is consistent with the pump saturation scenario, a deviation towards higher gain (which occurs at positive detuning) is not. The "shark fin" feature we observe here, in which the gain first deviates up and then down, has been previously attributed to intrinsic Kerr couplings [85]. The fact that the "shark fin" reappears without an intrinsic Kerr term gives us a hint that SoP-3rd order couplings can generate an effective Kerr nonlinearity.

To fully understand the effect of the SoP condition, we use classical perturbation theory to analyze the dynamics of the circuit. Below, we explain the essential steps of the perturbation analysis. Then, we focus on the SoP-3rd order truncated model and compute the parametric dependence of the saturation flux of the amplifier.

4.4.3.1 Classical perturbation theory for the Josephson parametric amplifier

The small parameter in our perturbative expansion is the input fluxes to the signal and idler modes, $\varphi_{a,\mathrm{in}}$ and $\varphi_{b,\mathrm{in}}$. We can expand the mode fluxes in a series as

$$\varphi_j(t) = \varphi_j^{(0)}(t) + \varphi_j^{(1)}(t) + \varphi_j^{(2)}(t)... \tag{4.34}$$

for $j = a, b, c$. The EOM of the signal mode flux φ_a after series expansion is

$$\left(\partial_t^2 + \gamma_a \partial_t + \omega_a^2\right)\left(\varphi_a^{(1)}(t) + \varphi_a^{(2)}(t) + ...\right) - \frac{2\omega_a^2}{\beta}\left(\varphi_b^{(1)}(t) + \varphi_b^{(2)}(t) + ...\right) \times \left(\varphi_c^{(0)}(t) + \varphi_c^{(1)}(t) + ...\right) = 2\gamma_a \partial_t \varphi_{a,\text{in}}(t). \tag{4.35}$$

The idler and pump mode EOMs are similar.

In the absence of inputs to the signal and idler modes, we obtain the zeroth order solution of the EOMs. Since the amplifier should be stable, there should be no output in the signal and idler modes when there is no input, i.e., $\varphi_a^{(0)} = \varphi_b^{(0)} = 0$. Therefore, the only nonzero zeroth order solution is for the pump mode, which is given by

$$\ddot{\varphi}_c^{(0)} + \gamma_c \dot{\varphi}_c^{(0)} + \omega_c^2 \varphi_c^{(0)} = \sqrt{2}\gamma_c \partial_t \varphi_{c,\text{in}}(t). \tag{4.36}$$

This equation matches the StP c mode EOM [see Eq. (4.24)], the zeroth-order solution for φ_c is given in Eq. (4.26). We can then solve the higher corrections to signal, idler and pump mode fluxes by matching the terms in the EOMs order-by-order. For example, the equations for first order corrections $\varphi_a^{(1)}$ and $\varphi_b^{(1)}$ are identical to the ideal parametric amplifier, and hence they are given by the StP solution Eq. (4.27), while the first order correction to the pump mode flux is $\varphi_c^{(1)} = 0$.

As the first order correction to the pump mode is zero, there are no second order corrections to the signal and idler mode fluxes. While the second order correction to the pump mode has two frequency components: $\Sigma = \omega_S + \omega_I$ and $\Delta = \omega_S - \omega_I$ with Fourier components

$$\varphi_c^{(2)}(\Sigma) = f_\Sigma \frac{1}{\beta} \varphi_a^{(1)}(\omega_S) \varphi_b^{(1)}(\omega_I) \tag{4.37a}$$

$$\varphi_c^{(2)}(\Delta) = f_\Delta \frac{1}{\beta} \varphi_a^{(1)}(\omega_S) \varphi_b^{(1)*}(\omega_I), \tag{4.37b}$$

where the two dimensionless parameters f_Σ and f_Δ are defined as

$$f_\Sigma = \frac{\omega_c^2}{\omega_c^2 - \Sigma^2 - i\gamma_c \Sigma}, \tag{4.38a}$$

$$f_\Delta = \frac{\omega_c^2}{\omega_c^2 - \Delta^2 - i\gamma_c \Delta}. \tag{4.38b}$$

Both of these two frequency components contribute to the third order correction to the signal and idler mode flux with frequency ω_S and ω_I.

To obtain the third order corrections to the signal and idler mode fluxes we define an effective drive vector that is comprised of all the contributions from lower orders, utilizing Eq. (4.37) to express $\varphi_c^{(2)}$ in terms of $\varphi_a^{(1)}$ and $\varphi_b^{(1)}$

$$[\varphi_d^{(3)}] = \begin{pmatrix} 2g^2\left(f_\Delta + f_\Sigma\right)\varphi_a^{(1)}\left|\varphi_b^{(1)}\right|^2 \\ 2g^2\left(f_\Delta + f_\Sigma^*\right)\varphi_b^{(1)*}\left|\varphi_a^{(1)}\right|^2 \end{pmatrix}. \tag{4.39}$$

The third order correction to the signal and idler mode is given by $[\varphi^{(3)}] = [M^{-1}].[i].[\varphi_d^{(3)}]$, where $[M]$ is the same matrix as in the discussion of the ideal parametric amplifier Eq. (4.29), and $[i] = \mathrm{diag}\{i, -i\}$ is a diagonal 2×2 matrix. The signal mode 3rd order correction is

$$\begin{aligned}\varphi_a^{(3)} = \left(\frac{1}{\beta}\right)^2 \Big\{ & 2i[M^{-1}]_{11}\left(f_\Sigma + f_\Delta\right)\varphi_a^{(1)}\left|\varphi_b^{(1)}\right|^2 \\ & - 2i[M^{-1}]_{21}\left(f_\Sigma^* + f_\Delta\right)\varphi_b^{(1)*}\left|\varphi_a^{(1)}\right|^2\Big\}. \end{aligned} \tag{4.40}$$

Using this expression we obtain the corrections to the reflection gain up to second order $G^{(2)} = |\varphi_a^{(1)}(\omega_S) + \varphi_a^{(3)}(\omega_S) - \varphi_{a,in}|^2/|\varphi_{a,in}|^2$. Similarly, we can solve the perturbation theory order-by-order till the desired order.

Here we want to stress that we only focus on the main frequency components of signal and idler modes, i.e., $\varphi_a(\omega_a)$ and $\varphi_b(\omega_b)$ and ignore the higher order harmonics. This assumption is also applied when we consider the higher than 3rd order nonlinear couplings in the JPA truncated EOMs, e.g. in StP-Kerr nonlinear truncated model (discussed in subsec. 4.4.4) and StP-5th order truncated model (discussed in subsec. 4.4.5).

Further, we point out that the above discussion is easily generalized to the case when $\omega_S \neq \omega_a$, $\omega_I \neq \omega_b$ and (or) $\varphi_{\mathrm{ext}} \neq 2\pi$.

Next, we consider the question, how the perturbation on the reflection gain can be used to compute the saturation power of the amplifier. The saturation power is defined as the input power at which the amplifier's reflection gain changes by 1 dB. At the limit $\varphi_{a,\mathrm{in}} \to 0$, the reflection gain of the amplifier is noted as G_0, which is given by $G_0 = |\varphi_a^{(1)} - \varphi_{a,\mathrm{in}}|^2/|\varphi_{a,\mathrm{in}}|^2$.

As we increase the input signal strength $\varphi_{a,\text{in}}$ to reach 1 dB suppression of the reflection gain, the corrected gain (in power unit) should satisfy,

$$G = \frac{\left|\varphi_a^{(1)} + \varphi_a^{(c)} - \varphi_{a,\text{in}}\right|^2}{\left|\varphi_{a,\text{in}}\right|^2} = 10^{-0.1} G_0 \tag{4.41}$$

where $\varphi_a^{(c)}$ is the higher order corrections to the signal mode flux in perturbation theory. In the high gain limit ($G_0 \gg 1$), we can estimate the criteria by,

$$\left|\varphi_a^{(c)}\right| / \left|\varphi_a^{(1)}\right| = \epsilon \equiv 10^{-0.05} - 1. \tag{4.42}$$

Note ϵ depends on the definition of the threshold for the gain change at the amplifier saturation.

4.4.3.2 Perturbative analysis on SoP third order EOM

We apply the above perturbation analysis to SoP-3rd order truncated model to understand the mechanism of amplifier saturation in this model. Before we proceed to calculate the corrections to the reflection gain, we estimate the matrix elements in the inverse of the parametric matrix $[M]$ [see Eq. (4.29)] in high gain limit, i.e.,

$$G_A \equiv \sqrt{G_0} = 2\tilde{\gamma}_a [M^{-1}]_{11} - 1 = \frac{2\tilde{\gamma}_a \tilde{\gamma}_b}{\tilde{\gamma}_a \tilde{\gamma}_b - 4g^2 \left|\varphi_c(\omega_P)\right|^2} - 1 \gg 1. \tag{4.43}$$

Therefore, we can approximate $2\tilde{\gamma}_a [M^{-1}]_{11} \sim G_A$ and hence $\varphi_a^{(1)}(\omega_a) \sim G_A \varphi_{a,\text{in}}$. The matrix element $[M^{-1}]_{21}$ can be approximated by $-iG_A/(2\sqrt{\tilde{\gamma}_a \tilde{\gamma}_b})$, which can be seen from the relation $[M^{-1}]_{21} = -i2g\varphi_c^{(0)*}([M^{-1}]_{11})/\tilde{\gamma}_b$ and $\sqrt{\tilde{\gamma}_a \tilde{\gamma}_b} \sim 2g|\varphi_c^{(0)}|$.

The third order correction to signal mode strength is given by the Eq. (4.40), which becomes

$$\varphi_a^{(3)}(\omega_b) \sim 2\frac{g^2}{\tilde{\gamma}_a} G_A^4 \text{Im}(f_\Sigma) \varphi_{a,\text{in}}^3 \tag{4.44}$$

in the high gain approximation.

To calculate the saturation flux, we let $\varphi_a^{(3)} \sim \epsilon \varphi_a^{(1)}$ and solve for $\varphi_{a,\text{in}}$, where ϵ is given in Eq. (4.42). The saturation flux given by 3rd order perturbation is

$$\varphi_{a,\text{in},\pm 1 \text{ dB}} \sim G_0^{-3/4} \sqrt{\epsilon} \frac{\sqrt{\tilde{\gamma}_b}}{g} \text{Im}(f_\Sigma)^{-1/2}. \tag{4.45}$$

where G_0 is the small-signal reflection gain of the amplifier. The saturation flux given by third order perturbation theory of SoP-3rd nonlinear model is plotted as orange (light gray) dashed line in Fig. 20(a) [2]. We notice that the saturation flux predicted by 3rd order perturbation theory does not agree well with the numerical simulation ("SoP-3rd" line). The disagreement also occurs when we tighten the criteria for amplifier saturation to 0.1 dB (see Fig. 20(b) "SoP-3rd 3rd order" line).

To explain the disagreement between the perturbation theory and the numerical integration method, we correct the signal mode flux to the next non-zero order, which is at fifth order in $\varphi_{a,\text{in}}$. To solve the fifth order correction of signal and idler mode fluxes, we follow the same strategy as demonstrated above. The only nonzero fourth order correction is $\varphi_c^{(4)}$, with two frequency components, $\varphi_c^{(4)}(\Sigma)$ and $\varphi_c^{(4)}(\Delta)$. The fifth order correction to the signal mode strength $\varphi_a^{(5)}$ is

$$\varphi_a^{(5)} \sim \frac{g^4}{\tilde{\gamma}^2} G_0^{5/2} \text{Re}\left[f_\Sigma + f_\Delta\right]^2 \varphi_{a,\text{in}}^5 \tag{4.46}$$

where we use the fact that imaginary parts of f_Δ and f_Σ are much smaller than their real parts and hence we ignore the contribution from their imaginary parts. The saturation flux can be estimated by $|\varphi_a^{(5)}| \sim \epsilon |\varphi_a^{(1)}|$ as,

$$\varphi_{a,\text{in},\pm 1 \text{ dB}} \sim G_0^{-5/8} \frac{\sqrt{\tilde{\gamma}_b}}{g} \left[\frac{\epsilon}{2} \text{Re}(f_\Sigma + f_\Delta)^{-1}\right]^{1/4} \tag{4.47}$$

Compared with the saturation flux given by third order perturbation, the fifth order correction is more significant as f_Δ and f_Σ are almost real. However, in third order perturbation theory, the contribution of real parts of f_Δ and f_Σ is canceled, but they will appear in next order perturbation, which dominates the saturation.

The saturation flux correction till fifth order perturbation is obtained by directively solving Eq. (4.41) for $\varphi_{a,\text{in}}$, where the corrections of signal mode strength $\varphi_a^{(c)} = \varphi_a^{(3)} + \varphi_a^{(5)}$. The saturation flux corrected upto fifth order ["SoP-3rd 5th order" line in Fig. 20(a) and (b)] have better agreement with the numerical solution.

However, in both third order and fifth order perturbation analysis, the saturation flux with 1 dB gain change does not agree well with the numerical solution [see Fig. 20(a)].

[2] To be more accurate, we directly solve $\varphi_a^{(3)} = \epsilon \varphi_a^{(1)}$ without high-gain assumption for the perturbation curves in Fig. 20.

This is because the saturation flux for ± 1 dB is beyond the radius of convergence of the perturbation series. In order to validate the perturbation analysis, we tight the criteria for amplifier saturation to change of the amplifier gain by± 0.1 dB, which makes the signal flux to stay in the radius of convergence. In Fig. 20(b), the saturation flux corrected to fifth order ("SoP-3rd 5th order" line) has a much better agreement with the numerical methods ["SoP-3rd" line in Fig. 20(b)].

We notice that the saturation flux is inversely proportional to $g = 1/\beta$, and hence we expect that it can be increased by decreasing the three-mode coupling strength (increasing β). At the same time, the pump strength must be increased in order to reach G_0. This procedure, in effect, makes the pump stiffer.

4.4.4 Intrinsic and generated Kerr couplings

In this subsection, we comment on the generation of effective Kerr terms and compare it with the intrinsic cross-Kerr couplings in the Lagrangian. In the perturbation analysis, if we expand the pump mode strength to second order, the effective EOMs of the signal and idler modes contains a cross Kerr coupling term, in the form of $\varphi_a|\varphi_b|^2$ for the signal mode and $|\varphi_a|^2\varphi_b$ for the idler mode (see, e.g. Eq. (4.40)). We will show that these generated Kerr terms limit the saturation power (at least for small β).

To construct an understanding of this mechanism, we use perturbation theory to analyze the StP amplifier with an intrinsic cross Kerr k_{ab}, and compare it with the SoP-3rd order nonlinear amplifier. As we discussed in subsection 4.4.2, in the stiff pump approximation, we treat the pump mode flux, φ_c, as a time-dependent parameter that is independent of the signal and idler modes. The EOMs for the signal and idler modes can be obtained by adding the terms $4k_{ab}\varphi_a\varphi_b^2$ and $4k_{ab}\varphi_a^2\varphi_b$ to the left-hand-side of Eq. (4.25a) and (4.25b), respectively.

In perturbation analysis, following the discussion in the previous subsection, we expand the signal and idler mode fluxes in the order of $\varphi_{a,\mathrm{in}}$ and $\varphi_{b,\mathrm{in}}$. We further assume that the amplifier is stable, i.e., there is no output from the amplifier if there is no input, which gives the zeroth order solution of signal and idler modes as $\varphi_a^{(0)} = \varphi_b^{(0)} = 0$. The first order solution

of signal and idler mode fluxes repeats the solution of ideal parametric amplifier [Eq. (4.27)] and the next non-zero correction appears at third order. The corresponding drive term is

$$[\varphi_d^{(3)}] = \begin{pmatrix} 8k_{ab}\varphi_a^{(1)}(\omega_S)\left|\varphi_b^{(1)}(\omega_I)\right|^2 \\ 8k_{ab}\varphi_b^{(1)*}(\omega_I)\left|\varphi_a^{(1)}(\omega_S)\right|^2 \end{pmatrix}. \tag{4.48}$$

Comparing with Eq. (4.39), we see that the soft-pump condition gives an effective signal-idler Kerr coupling strength

$$k_{ab}^{\text{eff}} = \frac{1}{4}g^2\left[f_\Delta + \text{Re}(f_\Sigma)\right]. \tag{4.49}$$

We note that this effective Kerr coupling is complex as f_Δ is complex. We also observe that there is an additional term in Eq. (4.39), that we label $q_{ab}^{\text{eff}} = (1/4)g^2\text{Im}(f_\Sigma)$, which cannot be mapped onto a Kerr coupling (as the signal and idler parts have opposite sign).

Further, as the intrinsic cross Kerr coupling k_{ab} is real, the third order correction to the signal mode in StP cross-Kerr amplifier model is zero. If we proceed to next non-zero order correction to the signal and idler mode, and compare the drive term with the one from StP-3rd order truncated model in same perturbation order, we identify the same effective Kerr coupling strength as Eq. (4.49).

To check the correspondence and understand to what degree the saturation power of SoP-3rd order amplifier is limited by the generated effective Kerr coupling, we manually add an intrinsic cross Kerr coupling, $k_{ab}\varphi_a^2\varphi_b^2$, in the SoP-3rd order truncated Lagrangian, and observe the saturation power of the amplifier as we tune k_{ab} (see Fig 23(a) and (b), SoP-3rd line). We observe that in both small β (see Fig. 23(a), $\beta = 1.2$) and large β (see Fig. 23(b), $\beta = 10.0$), as we tune the intrinsic Kerr term, the saturation power is maximized at the point indicated by the dashed red line. This maximum corresponds to the value of the intrinsic Kerr term that best cancels the generated Kerr coupling ($k_{ab} = -\text{Re}[k_{ab}^{\text{eff}}]$) and hence provides a maximum boost to the saturation power. We also notice that the maximum peak on Fig. 23(a) has a shift from the full compensation point ($k_{ab} = -\text{Re}[k_{ab}^{\text{eff}}]$). This is caused by the existence of imaginary term of f_Σ. In perturbation analysis, if we turn off the imaginary part of f_Σ, the peak is perfectly centered at the full-compensation point.

We also compare the saturation power obtained with SoP 3rd order (blue solid lines) to the StP with intrinsic cross-Kerr term k_{ab} (orange dahsed lines). In order to make the

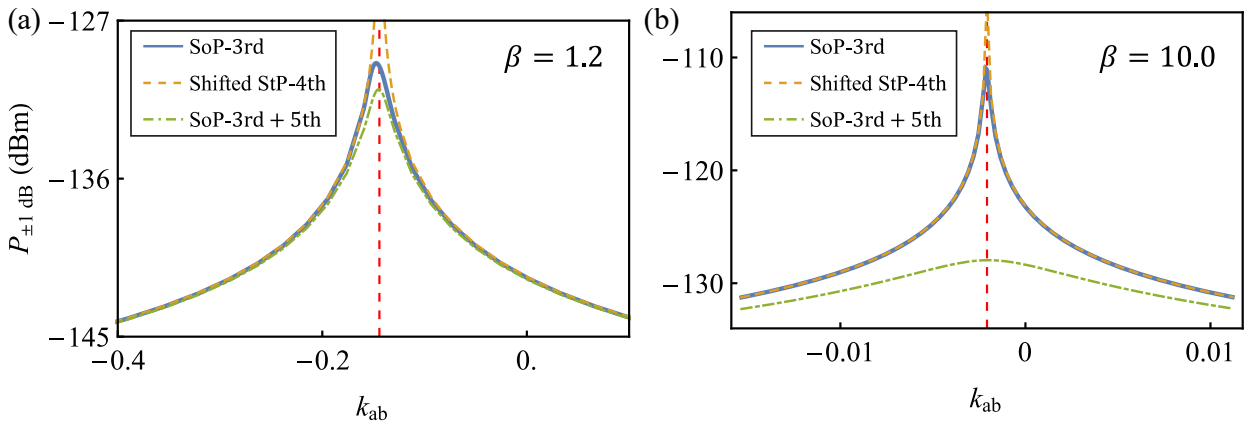

Figure 23: We compare three different cases, soft-pump with third order coupling (SoP-3rd), Stiff-pump with Kerr coupling (StP-4th) and soft pump truncated till the third order with fifth order couplings between signal and idler mode (SoP-3rd + 5th). For each cases, we manually turn on a cross-Kerr coupling k_{ab}. For StP-4th case, the plot is shifted by $-k_{ab}^{(\mathrm{eff})}$. The vertical red dashed line shows the location where the real part of the dynamically generated cross-Kerr is fully compensated by the intrinsic cross-Kerr coupling. The parameters chosen: $\omega_a/(2\pi) = 7.5$ GHz, $\omega_b/(2\pi) = 5.0$ GHz, $\gamma_j/(2\pi) = 100$ MHz. We set $\beta = 1.2$ [in (a)] and 10.0 [in (b)]. The critical current is $i_c = 1.0$ μA.

comparison more direct, we shift k_{ab} for the StP-Kerr amplifier by the computed value of the generated $\mathrm{Re}[k_{ab}^{\mathrm{eff}}]$ of the SoP-3rd order amplifier (i.e., we line up the peaks). We observe that away from the saturation power peak the two models are in good agreement, which supports the correspondence. Further, if we focus on $k_{ab} = 0$ point on the plot, i.e., the point at which SoP-3rd order model has no added intrinsic k_{ab}, the saturation power of SoP-3rd order amplifier (blue solid lines) matches the shifted StP cross-Kerr nonlinear amplifier (orange dashed lines) in both Fig. 23(a) and (b). Therefore, we conclude that it is indeed the generated Kerr coupling that is limiting the saturation power of the SoP-3rd order model.

However, near the saturation power maximum the two models diverge: the saturation power of the StP-Kerr amplifier becomes infinite as the intrinsic Kerr nonlinearity becomes zero, while the saturation power of the SoP-3rd order amplifier remains finite. This is caused

by the imagniary part of k_{ab}^{eff} and the q_{ab}^{eff}, which cannot be compensated by a real intrinsic cross-Kerr coupling k_{ab}.

We can understand the $\text{Im}[k_{ab}^{\text{eff}}]$ and the q_{ab}^{eff} terms as a two-photon loss channel, i.e., in which a photon in the signal mode and a photon in the idler mode combine and are lost in the pump mode. Both of the terms can be mapped to an imaginary energy which represents the decay of the signal and idler mode fluxes. Specifically, $\text{Im}(f_\Sigma)$ term represents the loss of a photon in signal mode and a photon in idler mode to a pump photon with frequency $\omega = \Sigma$, while $\text{Im}(f_\Delta)$ term represents the loss to a $\omega = \Delta$ pump photon.

4.4.5 Fifth and higher order nonlinearities

As we pointed out in Eq. (4.47), the saturation flux increases as we decrease the three-mode coupling strength g (by increase β). However, as we increase β, the saturation flux diverges from the SoP-3rd order model (see Fig. 20). This is because the saturation flux is so large that higher order nonlinear couplings becomes the limiting mechanism to the saturation flux. In this subsection, we focus on the higher order couplings and show how they limit the saturation flux of the amplifier.

At the Kerr nulling point, $\varphi_{\text{ext}} = 2\pi$, the Kerr couplings are turned off, and hence the next nonzero order of nonlinear couplings are fifth order in mode fluxes. The fifth order terms in the expansion of the dimensionless potential energy of the JRM, Eq. (4.28), are

$$\mathcal{E}_{\text{JRM}}^{(5)} = h_a\varphi_a^3\varphi_b\varphi_c + h_b\varphi_a\varphi_b^3\varphi_c + h_c\varphi_a\varphi_b\varphi_c^3, \tag{4.50}$$

where $h_a = h_b = \frac{1}{24\beta}\sin\left(\frac{\varphi_{\text{ext}}}{4}\right)$ and $h_c = \frac{1}{6\beta}\sin\left(\frac{\varphi_{\text{ext}}}{4}\right)$. To understand the direct effects of the fifth order couplings, we apply stiff-pump approximation and only include 3rd and 5th order nonlinear coupling terms into the EOMs (kerr couplings are turned off at $\varphi_{ext} = 2\pi$). Among the three fifth order terms, h_a and h_b terms are more significant as in stiff-pump approximation where c mode is treated as stiff, the term $h_c\varphi_c^2\varphi_a\varphi_b\varphi_c$ only shifts the pump mode flux to reach the desired gain G_0 and does not causes saturation. However, $h_a\varphi_a^2\varphi_a\varphi_b\varphi_c$ and $h_b\varphi_b^2\varphi_a\varphi_b\varphi_c$ terms dynamically shift the effective third order coupling strength as we increase the input signal power, which saturates the amplifier.

Again, we apply perturbation theory to analyze the StP-5th order amplifier following the discussion in subsection 4.4.3. The lowest order solution of the signal and idler mode fluxes are at first order, which repeats the solution of the ideal parametric amplifier. The next nonzero correction appears at third order with equation $[M].[\varphi^{(3)}] = -[i].[\varphi_d^{(3)}]$, where $[i]$ is a 2×2 diagonal matrix with elements $\{i, -i\}$ and the corresponding drive term is

$$[\varphi_d^{(3)}] = \begin{pmatrix} 12h_a\varphi_c \left|\varphi_a^{(1)}\right|^2 \varphi_b^{(1)*} + 6h_a\varphi_c^* \left(\varphi_a^{(1)}\right)^2 \varphi_b^{(1)} + 6h_b\varphi_c \left|\varphi_b^{(1)}\right|^2 \varphi_b^{(1)*} \\ 6h_a\varphi_c^* \left|\varphi_a^{(1)}\right|^2 \varphi_a^{(1)} + 12h_b\varphi_c^* \left|\varphi_b^{(1)}\right|^2 \varphi_a^{(1)} + 6h_b\varphi_c \left(\varphi_b^{(1)*}\right)^2 \varphi_a^{(1)*} \end{pmatrix}. \tag{4.51}$$

In the high-gain limit, the third order correction of the signal mode flux is

$$\varphi_a^{(3)} \sim 4\frac{h}{g}\left(1 + \frac{\tilde{\gamma}_a}{\tilde{\gamma}_b}\right) G_0^2 \varphi_{a,\mathrm{in}}^3, \tag{4.52}$$

where $h = h_a = h_b$ is the dimensionless fifth order coupling strength. Following the same method, we get an estimate on the saturation flux

$$\varphi_{a,\mathrm{in},\pm 1\mathrm{dB}} \sim \sqrt{\epsilon \frac{g}{4h}\left(1 + \frac{\tilde{\gamma}_a}{\tilde{\gamma}_b}\right)} G_0^{-3/4}. \tag{4.53}$$

We note that the ratio g/h is independent of β. As we increase β to reduce the limitation placed by SoP-3rd order model, Eq. (4.47), we eventually hit the limit that is given by StP-5th order nonlinear model, Eq. (4.53), i.e., the dominating limiting mechanisms on saturation flux switches.

To be more explicit, similar to the effective cross-Kerr compensation illustrated in subsec. 4.4.4, we add fifth order nonlinear coupling terms into the SoP-3rd order nonlinear model, which is labeled as "SoP-3rd+5th" in Fig. 23 (green lines). In the small β regime [Fig. 23(a)], except around the generated cross-Kerr full compensation region, the SoP-3rd+5th order nonlinear model closely follows the SoP-3rd order model, especially at $k_{ab} = 0$ point where there is no intrinsic k_{ab} added to both of the models. This indicates that at low β regime, the dominating limitation on the saturation power is given by the generated effective cross-Kerr coupling from the SoP-3rd order nonlinear coupling. However, when β is large [Fig. 23(b)], the saturation flux calculated from these two models disagrees. With additional fifth order nonlinear couplings, the saturation flux is heavily suppressed, which shows that the fifth

order nonlinear couplings dominates the SoP-3rd effects in limiting the saturation power of the amplifier.

Furthermore, in the large β regime, the fifth order nonlinear couplings in the JPA Lagrangian is the dominating limitation on the saturation power in full nonlinear EOMs of JPA among all the nonlinear couplings. To prove it, we numerically solve the saturation flux of the StP-5th order truncated model of JPA ("StP-5th" line in Fig. 20) and compare it with saturation flux obtained from the full nonlinear EOMs ("All-orders" line in Fig. 20). The saturation flux from StP-5th order model matches the saturation flux of full nonlinear JPA model in large β regime perfectly.

The saturation flux computed by numerical integration of StP-5th order nonlinear model is independent of parameter β, which agrees with the perturbation analysis. To further validate the perturbation theory, we plot the saturation flux from third order perturbation in Fig. 20(a) ("StP-5th 3rd order" line) for comparison. We notice that the perturbation result does not have a good quantitative agreement with the numerical solution. This is because the saturation flux is outside the radius of convergence of the perturbation series. If we tighten the criteria for amplifier saturation to the signal mode flux that causes the gain to change by ± 0.1 dB instead, the third order perturbation on StP-5th has much better agreement with the numerical solutions (see Fig. 20(b) "StP-5th" line and "StP-5th 3rd order" line). However, to perfectly match the numerical solution, we need next order correction, i.e., fifth order correction to signal mode flux. The result saturation flux is plotted in Fig. 20(b) as the red dot-dashed line.

Similarly, for the higher order nonlinear couplings in the Lagrangian, e.g. the seventh order in the Hamiltonian, we can still apply the perturbation theory to analyze the saturation flux. Here we focus on one of the seventh order couplings, $-l_{aa}\varphi_a^4\varphi_a\varphi_b\varphi_c$, to finalize the discussion. According to Eq. (4.12), l_{aa} is $\sin\left(\frac{\varphi_{\text{ext}}}{4}\right)/(1920\beta)$. We still consider the truncated EOMs of the amplifier under stiff-pump approximation.

Following the same procedures discussed above, the lowest order solution of signal and idler mode fluxes are in first order and are given by the ideal parametric amplifier solution in Eq. (4.27). However, the next nonzero correction to signal and idler mode fluxes appears

at fifth order with the corresponding drive term,

$$[\varphi_d^{(5)}] = 20\left|\varphi_a^{(1)}\right|^2 \begin{pmatrix} 3l_{aa}\left|\varphi_a^{(1)}\right|^2 \varphi_b^{(1)*}\varphi_c + 2\left(\varphi_a^{(1)}\right)^2 \varphi_b^{(1)}\varphi_c^* \\ l_{aa}\left|\varphi_a^{(1)}\right|^2 \varphi_a^{(1)}\varphi_c^* \end{pmatrix}. \tag{4.54}$$

The saturation flux given by this order of perturbation theory obeys

$$\varphi_{a,\mathrm{in},\pm 1\mathrm{dB}} \sim \left(\frac{g}{l_{aa}}\right)^{1/4} G_0^{-5/8}. \tag{4.55}$$

This limit does not depend on β either. With StP-7th order truncated nonlinear model, where we include 3rd, 5th and 7th order nonlinear couplings in JPA Lagrangian (even orders are turned off at $\varphi_{\mathrm{ext}} = 2\pi$), the existence of the 7th-order nonlinear couplings contributes to a small correction to the saturation flux at large β. However, the fifth order term remains the dominant factor in determining the saturation flux.

To conclude this section, for a JRM based JPA that is operated at the nulling point with fixed mode frequencies and mode linewidth, saturation flux can be increased by increasing β which suppresses the effects of generated Kerr couplings. As we move to large β regime, if we want to further improve the saturation power of the amplifier, we need to reduce the fifth and higher order nonlinear coupling strengths with respect to the third order coupling strength in the Lagrangian. In Ref. [85], we notice that the imperfect participation ratio $p \neq 1$ caused by nonzero linear inductance in series of JRM circuit, is one of the candidates for the suggested suppression, which will be discussed in the following sections.

4.5 Effects of participation ratio

In this section, we focus on the effects of reducing participation ratio by introducing outer linear inductors in series with the JRM circuit [L_{out} in Fig. 24].

When there are external resonators connected to the JRM, the flux injected from the microwave ports is shared between the JRM and the external resonators and hence the JRM nonlinearity is attenuated. To model this effect, four outer linear inductors L_{out} are added in series with the JRM circuit [see Fig. 24]. These inductors and the JRM can be treated as

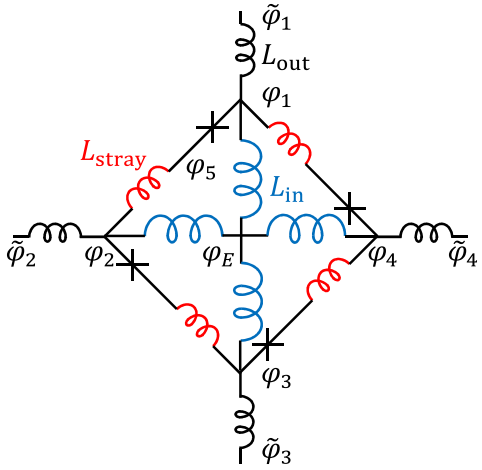

Figure 24: A more realistic circuit model for JRM, in which we include stray inductance L_{stray} in series of Josephson junctions and outer linear inductance L_{out} in series of JRM. The fluxes associated with each nodes are labeled on the plot.

a "flux-divider" type circuit. Further, as the input-output ports are connected to the outer nodes and there is no capacitors connecting the inner nodes to ground, we treat the fluxes of outer nodes ($\tilde{\varphi}_j$) as free coordinates, while the inner node fluxes (φ_j) are restricted by the Kirchhoff's current relation. The potential energy of JRM becomes

$$\begin{aligned} E &= E_{\text{out}} + E_{\text{JRM}} \\ &= \sum_j \frac{\phi_0^2}{L_{\text{out}}} \left(\tilde{\varphi}_j - \varphi_j\right)^2 + E_{\text{JRM}}(\varphi_1, \varphi_2, \varphi_3, \varphi_4). \end{aligned} \tag{4.56}$$

The EOM for node flux $\tilde{\varphi}_j$ are

$$\ddot{\tilde{\varphi}}_j + \frac{1}{C_j L_{\text{out}}} \left(\tilde{\varphi}_j - \varphi_j\right) = \text{IN}_j, \tag{4.57}$$

where $j = 1, 2, 3, 4$ and the node capacitance $C_j = C_a$ for $j = 1, 3$ and $C_j = C_b$ for $j = 2, 4$. The right hand side, IN_j is the corresponding input terms derived in Eq. (4.19) for each node

flux. The inner node fluxes φ_j are restricted by

$$\begin{aligned}\tilde{\varphi}_j =&\varphi_j + \zeta \left\{ \frac{1}{\beta} \sin\left(\varphi_j - \varphi_{j+1} + \frac{\varphi_{\text{ext}}}{4}\right) - \frac{1}{\beta} \sin\left(\varphi_{j-1} - \varphi_j + \frac{\varphi_{\text{ext}}}{4}\right) \right. \\ &\left. + \frac{1}{4}\left(3\varphi_j - \sum_{k\neq j} \varphi_k\right)\right\}\end{aligned} \tag{4.58}$$

where $\zeta = L_{\text{out}}/L_{\text{in}}$ and we apply index convention that $\varphi_0 = \varphi_4$, $\varphi_5 = \varphi_1$. As the symmetry of the JRM still persist, the normal mode profiles in terms of the outer node fluxes $\tilde{\varphi}$'s are identical to the ones without outer linear inductance, i.e., the normal mode coordinates are given by $[\tilde{\varphi}_M] = [\mathcal{A}^{-1}].[\tilde{\varphi}]$, where the model matrix $[\mathcal{A}]$ is identical to Eq. (4.8). This can also be derived from the linearization of the JPA's EOMs [Eq. (4.57)] and the constrains in Eq. (4.58). But the frequencies of the normal modes are shifted

$$\omega^2_{a,(b)} = \frac{1}{2C_{a,(b)}L_{\text{in}}} \frac{\beta + 2\cos\left(\frac{\varphi_{\text{ext}}}{4}\right)}{\beta + \beta\zeta + 2\zeta\cos\left(\frac{\varphi_{\text{ext}}}{4}\right)}, \tag{4.59a}$$

$$\omega^2_{c} = \frac{1}{C_c L_{\text{in}}} \frac{\beta + 4\cos\left(\frac{\varphi_{\text{ext}}}{4}\right)}{\beta + \beta\zeta + 4\zeta\cos\left(\frac{\varphi_{\text{ext}}}{4}\right)}, \tag{4.59b}$$

where $C_c = \frac{4C_aC_b}{C_a+C_b}$.

The question of how the nonlinear couplings shift when we add L_{out} into the JRM circuit is hard to directly analyze by the expanding the JRM potential energy in terms of normal modes around the ground state, as the constrains [Eq. (4.58)] are hard to invert. To obtain the nonlinear coupling strengths, we can either numerically calculate the derivatives of the potential energy with respect to the mode fluxes or using analytical perturbation expansion to get an approximate inversion relation of Eq. (4.58) and find the non-linear couplings. Here we stop at fourth-order non-linearities (in energy).

To solve the self-Kerr k_{jj} and cross-Kerr k_{ij} nonlinear coupling strengths, we can calculate the fourth order derivatives of the circuit potential energy E with respect to the normal coordinates $\tilde{\varphi}_a$, $\tilde{\varphi}_b$ and $\tilde{\varphi}_c$, i.e.,

$$k_{jj} = \frac{1}{24}\frac{\partial^4 \mathcal{E}}{\partial \tilde{\varphi}_j^4},\ k_{ij} = \frac{1}{4}\frac{\partial^4 \mathcal{E}}{\partial \tilde{\varphi}_i^2 \partial \tilde{\varphi}_j^2}. \tag{4.60}$$

where $\mathcal{E}$ is dimensionless energy of JRM circuit defined as $\mathcal{E} = (L_{\text{in}}/\phi_0^2)E$.

It is straightforward to use inner node fluxes to express the energy E in Eq. (4.56), and hence find an analytical expression for the derivatives with respect to inner node fluxes. However, to calculate derivatives with respect to the outer node fluxes requires the Jacobian matrix $[J] = [\frac{\partial\varphi}{\partial\tilde{\varphi}}]$, which effectively requires inversion of the constrains in Eq. (4.58).

To analytically solve this problem and give us a hint on the how the outer linear inductance will affect the nonlinear couplings, we apply the perturbation expansion around the ground state ($\tilde{\varphi}_j = 0$) to obtain an approximate inverse transformation and find the Jacobian. To simplify the discussion, we assume $C_a = C_b$. We note that this assumption does not affect the nonlinear coupling strengths which are independent of the c mode. Further, the method we discussed below can be easily generalized to the case when $C_a \neq C_b$.

We at first define a set of new variables using the normal mode transformation matrix $[\mathcal{A}]$, but use the inner node fluxes instead, noted as $[\varphi_M] = [\mathcal{A}^{-1}].[\varphi]$. Therefore, the relation in Eq. (4.58) using normal coordinates $[\tilde{\varphi}_M]$ and inner node coordinates $[\varphi_M]$ is

$$\tilde{\varphi}_j = (1+\zeta)\varphi_j + (2)\frac{2\zeta}{\beta}\frac{\partial}{\partial\varphi_j}\mathcal{E}^{(0)}_{\mathrm{JRM}} \tag{4.61}$$

where $\mathcal{E}^{(0)}_{\mathrm{JRM}}$ is given in Eq. (4.28), the factor (2) only exists for a and b modes. Here we only focus on the three nontrivial modes, $\tilde{\varphi}_a$, $\tilde{\varphi}_b$ and $\tilde{\varphi}_c$. The circuit ground state is assumed to be stable and at $\tilde{\varphi}_a = \tilde{\varphi}_b = \tilde{\varphi}_c = 0$ (which we confirm numerically). Further, at this stable ground state, the inner node fluxes are also zero. Since we only focus on the Kerr coupling strength in the vicinity of the ground state, the exact inner node fluxes that obey the inverse relation of Eq. (4.61) can be expanded in series of the small oscillations of the normal modes $\tilde{\varphi}_j$'s. That is, $\varphi_j \sim 0 + \varphi_j^{(1)} + \varphi_j^{(2)} + ...$

We plug the expansion of inner node fluxes back to Eq. (4.58) and match the terms with order-by-order. The lowest order solutions appear at the first order in normal coordinates

$$\varphi^{(1)}_{a,b} = \left[1+\zeta+\frac{2\zeta}{\beta}\cos\left(\frac{\varphi_{\mathrm{ext}}}{4}\right)\right]^{-1}\tilde{\varphi}_{a,b}, \tag{4.62a}$$

$$\varphi^{(1)}_{c} = \left[1+\zeta+\frac{4\zeta}{\beta}\cos\left(\frac{\varphi_{\mathrm{ext}}}{4}\right)\right]^{-1}\tilde{\varphi}_{c}. \tag{4.62b}$$

At this order, we can extract the definition of participation ratio for signal and idler mode as $p_{a,b} = \left[1+\zeta+\frac{2\zeta}{\beta}\cos\left(\frac{\varphi_{\mathrm{ext}}}{4}\right)\right]^{-1}$ and for pump mode as $p_c = \left[1+\zeta+\frac{4\zeta}{\beta}\cos\left(\frac{\varphi_{\mathrm{ext}}}{4}\right)\right]^{-1}$. If we bias the circuit at $\varphi_{\mathrm{ext}} = 2\pi$, all three participation ratios become $p_0 = \frac{1}{1+\zeta}$.

The second order correction to the inner node fluxes are

$$\varphi_a^{(2)} = p_a \frac{2\zeta}{\beta} \sin\left(\frac{\varphi_{\text{ext}}}{4}\right) \varphi_b^{(1)} \varphi_c^{(1)}, \tag{4.63a}$$

$$\varphi_b^{(2)} = p_b \frac{2\zeta}{\beta} \sin\left(\frac{\varphi_{\text{ext}}}{4}\right) \varphi_b^{(1)} \varphi_c^{(1)}, \tag{4.63b}$$

$$\varphi_c^{(2)} = p_c \frac{\zeta}{\beta} \sin\left(\frac{\varphi_{\text{ext}}}{4}\right) \varphi_a^{(1)} \varphi_b^{(1)}. \tag{4.63c}$$

The corresponding approximate inverse transformation of Eq. (4.58) is $\varphi_j \sim \varphi_j^{(1)}(\{\tilde{\varphi}\}) + \varphi_j^{(2)}(\{\tilde{\varphi}\})$ for $j = a, b, c$. At second order, it is sufficient to calculate the three mode coupling strength, as we only need at most the second order derivatives to the Jacobian matrix elements. The dimensionless three mode coupling strength are

$$g(\zeta) \equiv \frac{\partial^3 \mathcal{E}}{\partial\tilde{\varphi}_a \partial\tilde{\varphi}_b \partial\tilde{\varphi}_c} = p_a p_b p_c g(0), \tag{4.64}$$

where $g(0)$ is the three-mode coupling strength with unit participation ratio. Based on Eq. (4.64), decreasing the participation ratio by increasing L_{out} reduces the corresponding third order coupling strength, which is beneficial to reduce the limitation placed by the effective cross-Kerr nonlinearity generated by SoP-3rd order nonlinear couplings, and hence it is beneficial to improving the saturation power of the amplifier in the small β regime.

However, to calculate the fourth order derivatives, we need at least third order correction to the inner node fluxes. Following the same strategy, the third order correction of the inverse transformation for normal coordinate φ_a is

$$\begin{aligned}\varphi_a^{(3)} = \frac{p_a^4 \zeta}{12\beta} \cos\left(\frac{\varphi_{\text{ext}}}{4}\right) \tilde{\varphi}_a^3 + \frac{p_a^2 p_b^2 \zeta}{4\beta^2} \left[\beta \cos\left(\frac{\varphi_{\text{ext}}}{4}\right) + 8 p_c \zeta \sin^2\left(\frac{\varphi_{\text{ext}}}{4}\right)\right] \tilde{\varphi}_a \tilde{\varphi}_b^2 \\ + \frac{p_a^2 p_c^2 \zeta}{4\beta^2} \left[\beta \cos\left(\frac{\varphi_{\text{ext}}}{4}\right) + 4 p_b \zeta \sin^2\left(\frac{\varphi_{\text{ext}}}{4}\right)\right] \tilde{\varphi}_a \tilde{\varphi}_c^2\end{aligned} \tag{4.65}$$

and the relations for $\varphi_b^{(3)}$ and $\varphi_c^{(3)}$ can be derived similarly. The inverse relation from Eq. (4.58) is $\varphi_j \sim \varphi_j^{(1)}(\{\tilde{\varphi}\}) + \varphi_j^{(2)}(\{\tilde{\varphi}\}) + \varphi_j^{(3)}(\{\tilde{\varphi}\})$. The Kerr coupling strengths can be obtained from Eq. (4.60) with Jacobian derived from the perturbation expansion. For example k_{ab} is

$$k_{ab}(\zeta) = -\frac{\beta^3 \left\{\beta(1+\zeta)\cos\left(\frac{\varphi_{\text{ext}}}{4}\right) + 2\zeta\left[-3 + \cos\left(\frac{\varphi_{\text{ext}}}{4}\right) + 8\sin\left(\frac{\varphi_{\text{ext}}}{4}\right)\right]\right\}}{16\left[\beta + \beta\zeta + 2\zeta\cos\left(\frac{\varphi_{\text{ext}}}{4}\right)\right]^4 \left[\beta + \beta\zeta + 4\zeta\cos\left(\frac{\varphi_{\text{ext}}}{4}\right)\right]}. \tag{4.66}$$

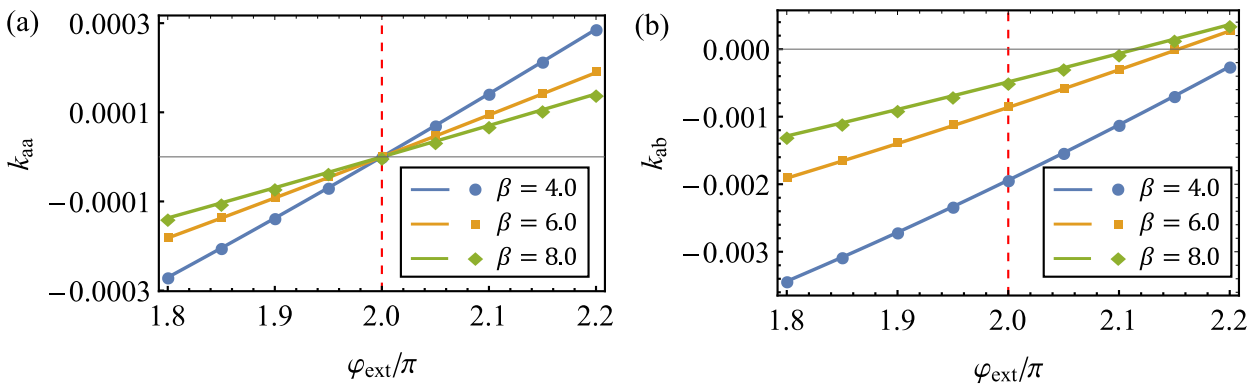

Figure 25: We calculate the Kerr coupling strength k_{aa} (a) and k_{ab} (b) as we sweep external magnetic field bias φ_{ext} when participation ratio $1/p = 1.1$. The perturbation solution (lines) and numerical solution (dots) agree well. In (a) for all three β values, the self-Kerr coupling strength k_{aa} can always be turned off at the Kerr nulling point $\varphi_{\text{ext}} = 2\pi$. However, in (c), we notice that the the magnetic field bias φ_{ext} to turn off cross-Kerr coupling k_{ab} depends on the choice of β. This means the exact Kerr nulling point of the does not exist any more when the participation ratio is not unity. Parameters chosen: three mode decay rates are $\gamma/(2\pi) = 0.1$ GHz, the critial current of the junctions is $i_c = 1.0$ μA. The outer linear inductance ratio $\zeta = 0.1$. The rest of the circuit elements are set by the mode frequencies at $\varphi_{\text{ext}} = 2\pi$, and they remains when we tune the external flux bias.

The self-Kerr coupling strength k_{aa} and the cross-Kerr coupling strength k_{ab} are plotted in Fig. 25(a) and (b), respectively. The Kerr nonlinear coupling strengths (k_{aa} and k_{ab}) are calculated via both numerical method (dots) and the above perturbation method (lines). In all three β values, the perturbation analysis matches the numerical solution well. Further, we notice that the self-Kerr coupling strength can still be turned off at the $\varphi_{\text{ext}} = 2\pi$ (Kerr nulling point) no matter what β value we choose [see Fig. 25(a)]. But the cross-Kerr couplings cannot be turned off at this magnetic bias point when participation ratio is not unity [see Fig. 25(b)].

The breakdown of the universal Kerr nulling point is also demonstrated by Eq. (4.66). The φ_{ext} that makes the numerator of Eq. (4.66) zero depends on the choice of β and

ζ. This indicates that as we turn the participation ratio to be smaller than unity, some nonlinear couplings that are previously killed by Kerr nulling point can reappear in the JPA Lagrangian. These extra nonlinear couplings are a consequence of the nonlinearity of the inner JRM circuit. As we mentioned, the JRM circuit with outer linear inductance shown in Fig. 24 can be treated as a phase divider, i.e., the phase across the outer nodes are divided to the phase across the outer linear inductors (L_{out}) and the phase across inner JRM nodes governed by the effective inductance of the inner JRM. Naively, if the divider is linear, we would expect the JRM with outer linear inductance generates nonlinear coupling strengths that are suppressed by the participation ratio (which does not depend on the mode flux), e.g. $k_{ab}(\zeta) = p_a^2 p_b^2 k_{ab}(0)$ and $k_{ab}(0) = 0$ is the cross-Kerr coupling strength of a JRM without outer linear inductance. However, as the effective inductance of inner JRM circuit is nonlinear, the total phase is not divided linearly, i.e., the more precise participation ratio defined as $p = \tilde{\varphi}/\varphi$ will change as the input flux oscillates as it is indeed a function of the outer node fluxes. Therefore, the normal modes experience extra nonlinearities as compared to the naive analysis. The re-apprearace of these extra nonlinearities will limit the saturation power of the amplifier.

However, for a general φ_{ext}, the Kerr couplings are suppressed roughly by $\sim p^4$. If we calculate one order up, the fifth order nonlinear coupling strength is suppressed by $\sim p^5$. This indicates that the non-unity participation ratio can help to suppress the higher order nonlinear couplings with respect to the third order, which is beneficial for improving the saturation power of the amplifier. We will focus on the quantitative understand of how these two factors compete with each other and further optimize the saturation power of the amplifier in next section.

4.6 Optimizing the JPA using participation ratio

As demonstrated in the above section, the outer linear inductance impacts the saturation power of the JPA in both negative and positive ways. In this section we describe the effects of the outer linear inductance quantitatively using numerics to obtain the saturation power

of the JPA as we sweep the JRM inductance ratio (β) and participation ratio (p).

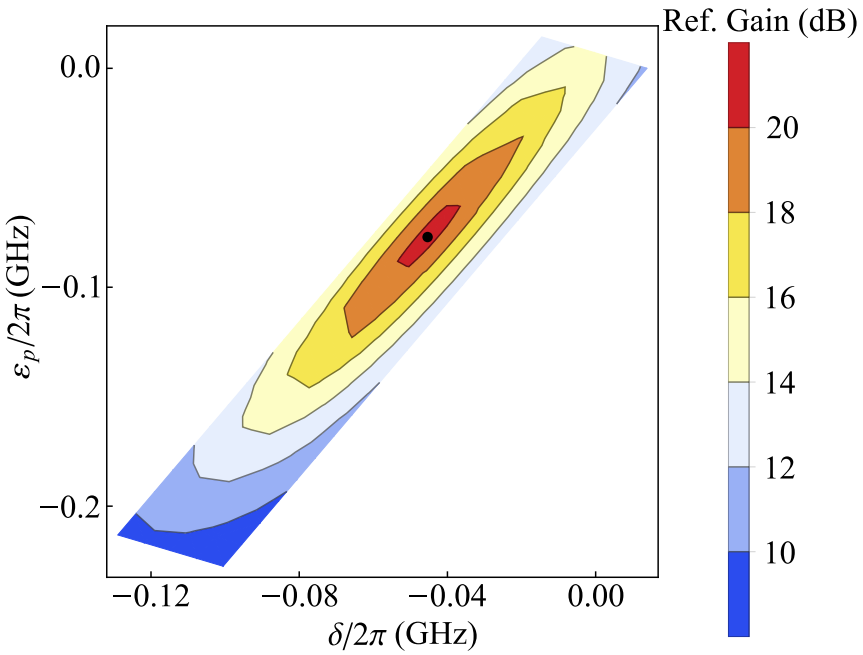

Figure 26: The optimization of the pump configuration. We sweep the signal mode detuning $\delta = \omega_S - \bar{\omega}_a$ and the pump tone detuning $\epsilon_p = \omega_P - (\bar{\omega}_a + \bar{\omega}_b)$ and fix the pump tone strength. The maximum gain is labeled by the black dot. The maximum gain is achieved when the signal tone matches the mode frequency and the pump mode matches the sum frequency of the signal and idler mode. The parameters used: $\gamma/2\pi = 0.2$ GHz, $\bar{\omega}_a/2\pi = 7.5$ GHz, $\bar{\omega}_b/2\pi = 5.0$ GHz, $\beta = 3.0$, $1/p = 8.0$.

Because of the presence of the outer linear inductance, even order nonlinear coupling terms reappears in the EOMs. The presence of these higher order couplings results in a shift of the mode frequencies. For example, the nonzero cross-Kerr coupling strength $k_{ac}\varphi_a^2\varphi_c^2$ and $k_{bc}\varphi_b^2\varphi_c^2$ causes the signal and idler mode frequencies to be dependent on the pump mode strength, which shifts the signal and idler mode frequencies away from the bare mode frequencies calculated from the normal mode analysis. To correctly pump the amplifier with the sum frequency of mode and idler mode frequencies and probe the signal with the correct signal mode frequency, as well as set the amplifier's small-signal reflection gain to 20 dB, we need to adjust the pump tone frequency and pump tone strength at the same time. Before we

perform the numerical calculation of the amplifier's reflection gain as we tune the input tone strength and extract the saturation power, we need to find the correct pump configurations and the signal mode frequency under that pump configuration.

To compensate for the frequency shifts and find the optimum pump configuration and corresponding signal mode frequency for JPA, we numerically optimize the pump tone frequency and strength. To solve this optimization problem, we notice that the amplifier is expected to consume the least pump tone input flux to reach the desired small-signal reflection gain when the amplifier is perfectly on resonance with its mode frequencies, i.e., $\omega_S = \omega_a$ and $\omega_P = \omega_a + \omega_b$. Therefore, we split the optimization process into two optimization tasks: (1) for a given input pump tone strength $\varphi_{c,\text{in}}$, find the optimimal pump tone frequency and signal mode frequency and (2) find the desired pump tone strength $\varphi_{c,\text{in}}$ to get 20 dB small-signal reflection gain with the corresponding optimized pump tone frequency. In (1), we fix the pump tone strength $\varphi_{c,\text{in}}$ and sweep signal tone and pump tone frequencies to find the parameters which maximize the reflection gain (a typical sweep is shown in Fig. 26). In (2), we use a binary search to find the desired pump strength $\varphi_{c,\text{in}}$ for 20 dB reflection gain.

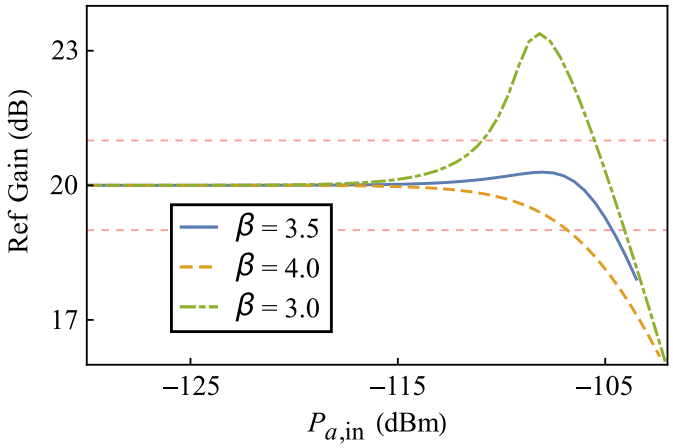

Figure 27: In this plot, we show the reflection gain of the amplifier as we increase the input signal power. We focus on a point which is away from the boundary shown in Fig. 24.

The resulting saturation power sweep of the JPA is shown in Fig. 17. In the large β regime ($\beta > 4.0$), as we decrease the participation ratio, the saturation power increases.

However, at the same time, the pump power for 20 dB reflection gain also increase, until the JRM reaches the full nonlinear regime and we cannot inject enough power to get 20 dB reflection gain anymore. However, in the low β regime ($\beta < 4.0$), when the participation ratio is less than unity, even though we firstly optimize the pump configuration to compensate for mode shifting, we still found that the reflection gain of the amplifier increases before it starts to drop ("shark fin"). This causes the amplifier to saturate as gain increases to 21 dB. If we move out of this regime by reducing the participation ratio or increase β, the "shark fin" reduces and we find a band of sweet spots of the JPA saturation power. The reflection gain of the JPA with configurations around one of the sweet spots is shown in Fig. 27, with the the blue curve corresponding to the sweet spot at $\beta = 3.5$, $1/p = 7.0$. As we decrease β to 3.0, the JPA saturates as gain touches 21 dB [green dash-dotted curve in Fig. 27], while as we increase β to 4.0 the "shark fin" disappears but the saturation power decreases.

To understand the dominating limitations placed by different nonlinear terms in the JPA Hamiltonian, especially around the sweet spot, we truncate the Hamiltonian order-by-order and analyze the performance of the truncated model. We keep the pump configurations identical to the full-order analysis and increase the truncation order from 3rd order to 8th order. In Fig. 28(a), we focus on the sweet spot $\beta = 3.5$, $1/p = 7.0$, and compare the truncated theory with the full-nonlinear solution. At small signal input, the nonlinear couplings up to 7th order are needed to converge to desired 20 dB reflection gain. This is a sign that the high order nonlinear coupling terms play an important role in the dynamics of the JPA. As we increase the signal power, the truncation to 4th order analysis does not show an obvious "shark fin" feature. However, when we include the higher order coupling terms, e.g. 5th to 8th, the "shark fin" appears. The truncated 5th order analysis supports another mechanism that causes the amplifier to saturate to 21 dB which is different from the one discussion in Ref. [85], that is the fifth order terms, e.g. $\varphi_a^2\varphi_a\varphi_b\varphi_c$ term, can shift the bias condition by shifting the effective third order coupling strength to drive the amplifier towards the unstable regime causing the reflection gain to rise. Further, as we discussed above, the external linear inductors breakdown the perfect nulling point for even order nonlinear couplings, the 6th order and 8th order terms can survive at the nulling point. From 5th order to 8th order truncation, the large signal input behavior oscillates, which is a sign that we are reaching

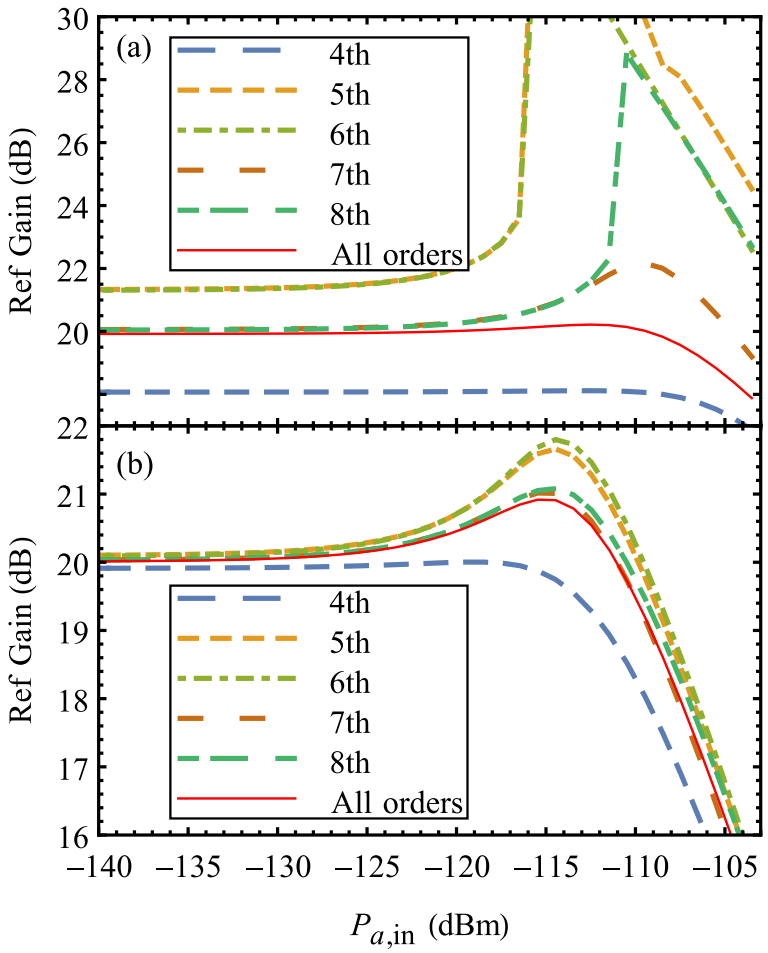

Figure 28: We test the reflection gain of the truncated model for $\beta = 4.5$ and $1/p \sim 4.0$ as we increase the input signal power $P_{a,\text{in}}$ in (a). In the calculation for the truncated model, we only truncate the JRM potential energy to the desired order, but fix the pump configuration as the full-order case. The reflection gain solved from truncated model also converge to the full-order analysis (red solid line) pretty well we truncated to 7th order. But as we decrease p further to push the configuration closer to the boundary ($1/p = 7.0$) in (b), the higher and higher order terms are needed to have a good approximation to the full-order performance.

the convergence point of the series expansion casued by the competition between different orders. We also compare it with a point away from the sweet spot in Fig. 28(b) ($\beta = 3.5$, $1/p = 4.0$). At this point, the 5th order truncation already converges to 20 dB reflection gain and the 7th order theory gives a good approximation to full order analysis with moderate input signal power. We conclude that the boost in performance of the amplifier at the sweet spot is a result of taking advantage of all orders, and hence cannot be modeled using a low order truncated theory.

4.7 Effects of tuning the external magnetic field, decay rates, and stray inductance

In this section, we further explore how the saturation power of the amplifier is affected by the magnetic field bias (φ_{ext}), the modes' decay rates (γ), and stray inductance in the JRM loop [L_{stray} in Fig. 24].

In Fig. 29, we plots the saturation power of the amplifier as we perturb the magnetic field bias and decay rates of JPA. Here we focus on the line of $1/p = 7.0$ in Fig. 29(a) and (b), and focus on the line of $\beta = 3.5$ in (c) and (d). In Fig. 29(a) and (c), we explore the effects of tuning the magnetic field bias. We at first set the JPA circuit parameters at $\varphi_{\text{ext}} = 2\pi$. We then operate the JPA at $\varphi_{\text{ext}} = 1.9\pi$ and $\varphi_{\text{ext}} = 2.1\pi$, respectively. We notice that as we perturb the magnetic field to $\varphi_{\text{ext}} = 1.9\pi$, the optimum saturation power is achieved at larger β values [see Fig. 29(a)] and smaller participation ratio p [see Fig. 29(c)]. By tuning β, the saturation power of the amplifier improves from -104.8 dBm to -103.9 dBm, while by tuning p, it improves to -104.1 dBm. This indicates that the optimal magnetic field bias occurs at somewhat lower magnetic field as compared to the Kerr nulling point. The corresponding sweet spot of the amplifier has larger β and lower p compare to the present setting.

In Fig. 29(b) and (d), we change the JPA modes' decay rates by 10 MHz to explore the effects of different decay rates to the JPA saturation power. In large β regime, increasing the JPA mode decay rates causes the regime in which we cannot obtain 20 dB (see Fig. 17) gain

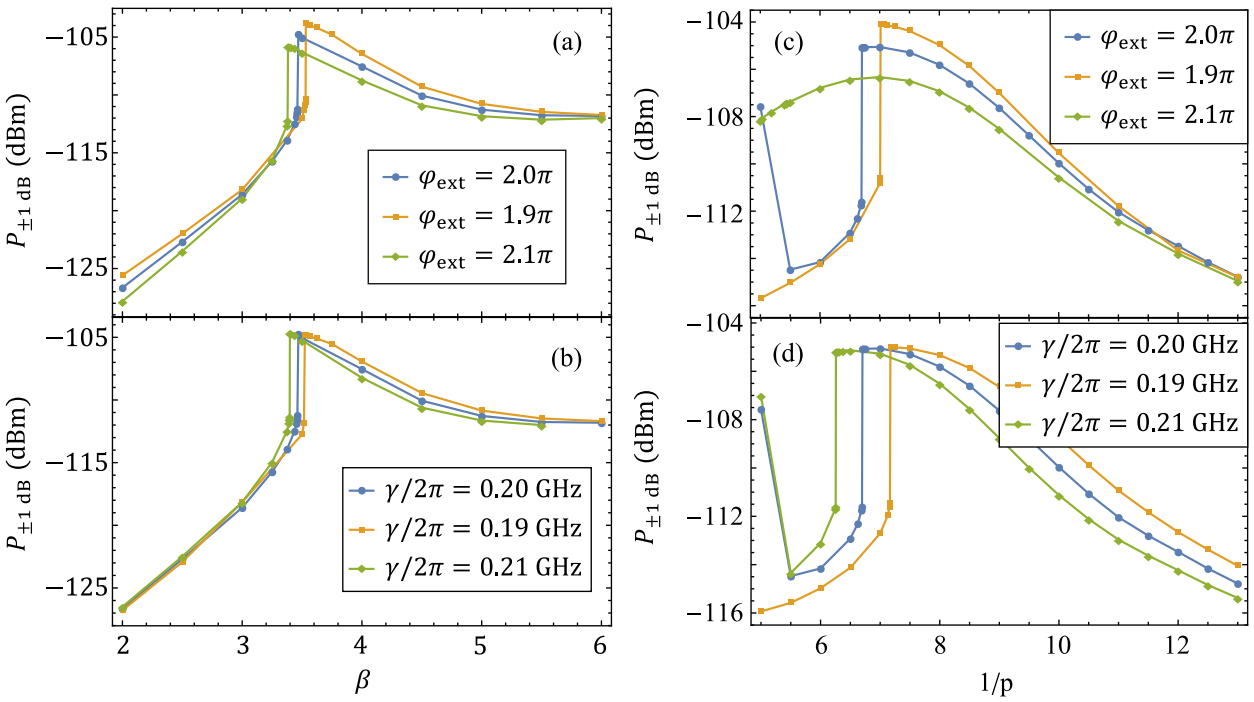

Figure 29: The saturation power of the JPA with external magnetic field bias and mode decay rates perturbation. In (a) and (c) we perturb the JPA external magnetic field bias from 2π by $\pm 0.1\pi$. We assume the JPA circuit parameters are fixed with bias $\varphi_{\mathrm{ext}} = 2\pi$, and then we operate the JPA at the perturbed magnetic field bias. In (b) and (d) we set the circuit parameters of JPA to change the modes' decay rates from $\gamma/2\pi = 0.2$ GHz by ± 10 MHz. In (a) and (b), we focus on the JPA settings with $1/p = 7.0$ and investigate the effect of the perturbation while in (c) and (d), we focus on the settings with $\beta = 3.5$.

to become larger. For example at $\gamma/2\pi = 0.21$ GHz, the JPA with $\beta = 6.0$ and $1/p = 7.0$ can no longer reach 20 dB reflection gain while a comparable JRM with $\gamma/2\pi = 0.20$ GHz could. The amplifier's optimum saturation power is also achieved at a lower β value as we increase the decay rates [see Fig. 29(b)]. However, as we tune the decay rates by ± 10 MHz, the maximum saturation power of the amplifier at $1/p = 7.0$ shows little change. Similarly, in Fig. 29(d), we perturb the modes' decay rates by ± 10 MHz on JPA with different p but a fixed β ($\beta = 3.5$). The amplifier's optimum saturation power is achieved at a lower p value

as we decrease the decay rates [see Fig. 29(d)]], while the maximum saturation power of the amplifier still shows little change.

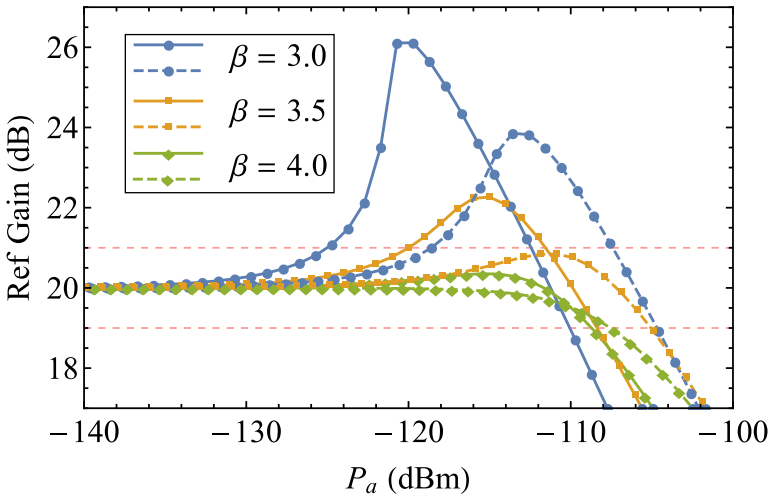

Figure 30: We compare the saturation power of the amplifier without stray inductance ($\alpha = 0$, dashed curves) and with stray inductance ($\alpha = 0.1$ slide curves). We tested three different settings of JPA, $\beta = 3.0$, 3.5 and 4.0, respectively. All of them have $1/p = 7.0$. We compare the reflection gain of the amplifier as we increase the signal power P_a. For all three cases, the saturation power is suppressed. The existence of the stray inductance enhances the shark fin, which causes the amplifier at previous sweet spot ($1/p = 7.0$ and $\beta = 3.5$) saturates to 21 dB instead.

Finally we consider the effect of stray inductors (L_{stray} in Fig. 25). We include stray inductance such that $\alpha = L_{\text{stray}}/L_J = 0.1$ and compare the reflection gain of the amplifier as we increase the signal power (P_a). Note that when the stray inductance is nonzero, the Kerr nulling point is shifted away from $\varphi_{\text{ext}} = 2\pi$ (see discussion in subsec. 4.8), especially, when $\alpha = 0.1$, the Kerr nulling point is at $\varphi_{\text{ext}} \sim 2.49\pi$. We will operator the JPA at this magnetic field bias when the participation ratio is not unity. In Fig. 30, we compare three different settings of JPA, $1/p = 7.0, \beta = 3.0$ (blue curves), $1/p = 7.0, \beta = 3.5$ (orange curves) and $1/p = 7.0, \beta = 4.0$ (green curves). In all three different sittings, we notice enhancement of the "shark fin", which causes the JPA at the previous sweet spot ($\beta = 3.5$, orange dashed curve) saturates to 21 dB instead, which greatly reduce the saturation power at this point

(from -104.8 dBm to -120 dBm). At $\beta = 4.0$, without stray inductors, the reflection gain of the amplifier monotonically decreases as the signal power increases (dashed green line), while at $\alpha = 0.1$ there is a shallow increases (see solid green line). Besides, the saturation power slightly drops from -107.5 dBm to -108.7 dBm.

4.8 The effect of stray inductance with unit participation ratio

In this section, we focus on the effect of the existence of nonzero stray inductance with unit participation ratio. This discussion is also provided in Ref. [162].

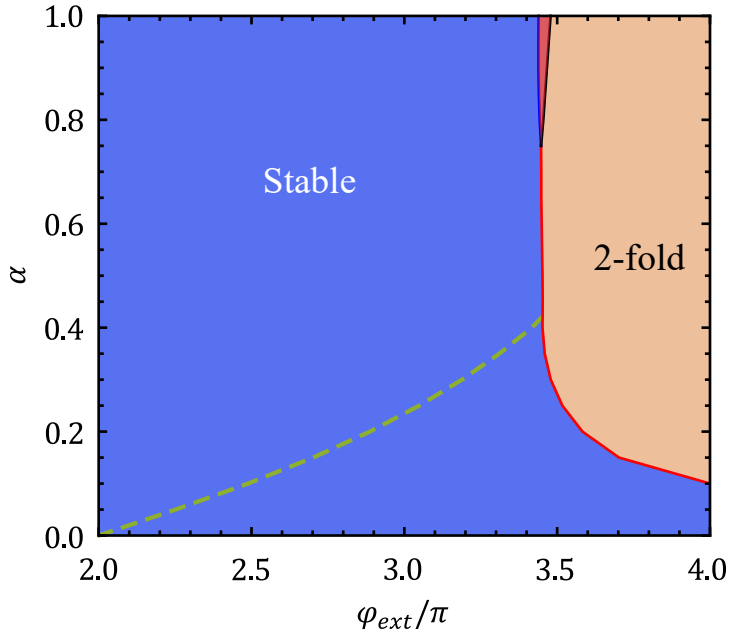

Figure 31: The stability diagram of the ground state of the JPA when we have nonzero stray inductance. We assume $L_{\text{out}} = 0$ and set $\beta = 4.0$. The blue region (labeled as "stable") shows the stable region of the JPA ground state, while in orange region (labeled as "2-fold"), the JPA ground state is doubly degenerate. In the red region (unlabeled region), JPA has four-fold degenerate ground state. The green line shows the position of the nulling point.

The circuit model of JRM circuit with stray inductance is in Fig 25(a). When the stray inductance is nonzero, similar to shunted JRM circuit, we can write the potential energy of

JRM circuit as,

$$E_{\mathrm{JRM}} = \frac{\phi_0^2}{2L_{\mathrm{in}}} \sum_j \left(\varphi_j - \varphi_E\right)^2 + \sum_j E_{\mathrm{arm}}\left(\delta_j\right), \tag{4.67}$$

where $\varphi_E = \frac{1}{4}(\varphi_1 + \varphi_2 + \varphi_3 + \varphi_4)$, the arm energy, E_{arm}, is the total energy of the stray inductor and the Josephson junction on one arm of the JRM, $\delta_j = \varphi_j - \varphi_{j+1} + \frac{\varphi_{\mathrm{ext}}}{4}$ is the total phase difference across the j-th arm. Take one of the arms as an example,

$$H_{\mathrm{arm}}(\delta_1) = \frac{\phi_0^2}{2L_{\mathrm{stray}}} \left(\varphi_1 - \varphi_5\right)^2 - \frac{\phi_0^2}{L_{\mathrm{J}}} \cos\left(\varphi_5 - \varphi_2 + \frac{\varphi_{\mathrm{ext}}}{4}\right), \tag{4.68}$$

where the phase on node φ_5 is constrained by the current relation at the corresponding node,

$$\delta_1 - \Delta\varphi = \alpha \sin\left(\Delta\varphi\right), \tag{4.69}$$

where $\alpha = L_{\mathrm{stray}}/L_{\mathrm{J}}$, $\delta_1 = \varphi_1 - \varphi_2 + \frac{\varphi_{\mathrm{ext}}}{4}$ is the total phase difference of the arm and $\Delta\varphi$ is the phase across the junction, defined as $\Delta\varphi = \varphi_5 - \varphi_2 + \frac{\varphi_{\mathrm{ext}}}{4}$. Suppose we focus on the case where the external magnetic flux is around 2π, when α is small ($\alpha < 2.80$), the nonlinear relation in Eq. (4.69) only has a single root when the total phase across the arm is determined.

To determine the self-Kerr k_{jj} and cross-Kerr k_{ij} coupling strengths, we can use the derivatives of the dimensionless JRM energy as,

$$k_{jj} = \frac{1}{24} \frac{\partial^4 \mathcal{E}_{\mathrm{JRM}}}{\partial \varphi_j^4},\ k_{ij} = \frac{1}{4} \frac{\partial^4 \mathcal{E}_{\mathrm{JRM}}}{\partial \varphi_i^2 \partial \varphi_j^2}. \tag{4.70}$$

Before we carry on the derivative, we appreciate the fact that the phase difference across the arms are linearly dependent on the node fluxes, and the node fluxes are linearly dependent on the normal mode coordinates. Since the inner linear inductance only contribute the energy which are quadratic to the node phases, there will be no contribution to the Kerr couplings. Because the four arms of the JRM is symmetric, the arm Hamiltonian for four arms should have identical form in terms of the phase difference δ. To finalize the calculation, the forth order derivatives with respect to normal modes in general can be calculated as,

$$\begin{aligned} \frac{\partial^4}{\partial \varphi_i^2 \partial \varphi_j^2} \mathcal{E}_{\mathrm{JRM}} &= \sum_l \frac{\partial^4}{\partial \varphi_i^2 \partial \varphi_j^2} \mathcal{E}_{\mathrm{arm}}(\delta_l) \\ &= \sum_l \left(\frac{\partial^4}{\partial \delta^4} \mathcal{E}_{\mathrm{arm}}\right) \left(\frac{\partial \delta_l}{\partial \varphi_i}\right)^2 \left(\frac{\partial \delta_l}{\partial \varphi_j}\right)^2. \end{aligned} \tag{4.71}$$

Therefore, for both self-Kerr couplings and cross-Kerr couplings, there is a common factor $\partial_\delta^4 \mathcal{E}_{\rm arm}$, so that the nulling point still exists at the external magnetic bias to let $\partial_\delta^4 \mathcal{E}_{\rm arm} = 0$.

However, as we increase the stray inductance α, which effectively decrease the inductance ratio β, it causes the ground state to be more and more unstable. Adding to it, increasing α causes the nulling point to shift from $\varphi_{\rm ext} = 2\pi$ to higher magnetic bias. At a relative large α, the nulling point may end up in the unstable regime and become unreachable in real experiment. In Fig. 31, we plot the ground state stability diagram as we change external magnetic flux and α, we further plot shifting of the nulling points as we change α [green curve in Fig 31]. In Fig. 31, we set the JRM inductance ratio $\beta = 4.0$ and when $\alpha \sim 0.4$, the nulling point hits the boundary of the unstable regime, which means the nulling point does not exist in experiment any longer.

4.9 Summary and outlook

In conclusion, we have investigated the nonlinear couplings of the JRM based JPA and how these different nonlinear couplings controls the performance of the parametric amplifier. In our analysis, we have adapted both perturbative and time-domain numerical methods to give us a full understanding of the circuit dynamics. By considering the full nonlinear Hamiltonian of the device, we show that we can fully optimize the performance of the amplifier, and achieve a $\sim$ 10 to 15 dB improvement of the saturation power of the JRM based JPA for a range of circuit parameters. Our method for numerically modeling multi-port circuits of inductors, capacitors, and Josephson junctions is also applicable to more complex circuits and pumping schemes, which can create JPAs with addition virtues such as extremely broad (and gain-independent) bandwidth and directional amplification [171, 79, 172, 160, 163, 162].

5.0 Theory of a Josephson micromaser: using the Josephson junction nonlinearity to exceed the Schawlow-Townes limit and generate quantum light

In this chapter we propose building a microwave laser (MASER) that uses elements of superconducting quantum computers: high quality factor cavities, transmon qubits as artificial atoms, and Josephson junctions as nonlinear coupling elements. The proposed maser explores a new direction in laser physics: the use of highly nonlinear elements to control light. As a demonstration, we show that we can design a maser with a linewidth that is ten times narrower than the Schawlow-Townes limits on the linewidth of conventional laser and maser systems.

The main components of a laser are a gain medium and a high quality cavity. The gain medium hosts atoms that can be pumped into a population inverted state (in which an excited level has higher occupation than the ground state) using an incoherent light source. Lasing occurs when the rate at which photons are emitted into the cavity exceeds the rate at which photons are lost from the cavity. This linear instability is re-stabilized by the depletion of the population inverted state, which is itself controlled by the rate of the incoherent pump. The linewidth of conventional lasers is limited by the noise inherent to the system, which has two main sources: the noise coming from photons entering the cavity and from photons leaving the cavity as laser light. The Schawlow-Townes limit is approached upon the minimization of these two sources of noise. It is precisely the reduction of these two noise sources, which we achieve by using inductors and Josephson junctions to engineering nonlinear couplings, that allows us to circumvent the Schawlow-Townes limit. In addition to being of fundamental interest, we envision that our new approach to laser physics will find applications in superconducting quantum machines and perhaps also in metrology.

Superconducting quantum devices that utilize Josephson effect are one of the most promising and mature technologies for achieving large-scale quantum computing. One of the shortcomings of this architecture is the lack of an on-chip (in-fridge) coherent microwave source. Instead, room temperature sources are used in conjunction with low temperature attenuators that reduce the thermal noise. This setup is inconvenient as (1) it requires a

large number of microwave lines to pass into the fridge and (2) the attenuators produce a considerable amount of heat that needs to be absorbed by the dilution refrigerator. The proposed micromaser provides for a very energy-efficient solution. It will only require noisy DC power to run (using the AC Josephson effect to pump the artificial atom) eliminating the need for AC lines. Further, it would operate at fridge temperatures, and hence would not need attenuation meaning that most of the pump power can be converted into coherent light. More broadly, the proposed maser could be used to generate quantum light, such as correlated photon pairs, which is an important resource for quantum information processing.

Finally, the proposed maser system could find applications in metrology, both as a low-noise system and as a system that can generate quantum light. The proposed maser itself could potentially be used as a time standard (accurate over short times). More speculatively, the maser principles could be applied to improve the performance of microwave atomic clocks.

5.1 Introduction

The nonlinearity of the Josephson junctions has been used to construct a number of qubit and quantum gate designs [173, 174, 64, 68, 69, 175, 176]. The ease of integration of the superconducting qubits and fast speed of the gate operation makes it one of the most attractive system for quantum computing. Further, with the development of the Josephson parametric amplifiers, which also take advantages of the nonlinearity of the Josephson junctions, the on-chip quantum computing and quantum information processing systems have been developed (IBM, Google, D-WAVE, etc, see Table. 1). However, an on-chip coherent microwave photon source (or maser) is still the missing component of the full on-chip superconducting circuit based solution for quantum computing and quantum information process.

The superconducting circuit qubits can be viewed as artificial atoms that have a two-level level structure, just like the two-level model for typical atoms in cavity-QED systems. Therefore, using the superconducting circuit qubits with the microwave cavity or resonators to achieve artificial atom-cavity coupling, and other quantum optics experiments, has been investigated [177, 178, 179, 180, 181]. Because the superconducting circuit system is different

from the atom-cavity picture of cavity-QED, it is also referred to as circuit-QED [182, 183]. With the success of the circuit-QED experiments involving qubit-resonator coupling, the question of whether lasing of the superconducting circuit can be achieved arises.

The problems of how to construct a maser using Josephson junction has been discussed for a long time. Hatakenaka and Kurihara discussed theoretically proposed a Josephson cascade micromaser using the Josephson effect in Ref. [184]. The coupling between Josephson junctions and cavities to be used for light generation was further explored theoretically and experimentally [185, 186, 187, 188, 189, 190, 191, 192]. Using a superconducting qubit as an artificial atom in a maser system, similar to the atomic laser model was theoretically proposed [193, 189]. This idea of using superconducting qubit as the laser pump media was experimentally demonstrated in Ref. [194], where Astafiev *et al* used a charge qubit coupling to a superconducting resonator, which acts as an atom inside the cavity, to construct a maser system. Following this work, with the strong coupling between the Josephson junction based superconducting qubit and the microwave resonator or cavity, the "single-atom maser" type system is further explored experimentally in Refs. [195] and theoretically [196] to achieve coherent light and quantum light generation from on-chip devices.

In this thesis, we proposed to use a pair of transmon qubits to construct an artificial atom for a Josephson maser system. Further, we proposed to use the nonlinearity provided by the Josephson junctions to generate nonlinear coupling not only between pump media and cavity, but also between the cavity and the bath (transmission line) to generate narrow-linewidth light. The linewidth of our proposed Josephson micromaser can be suppressed to ~ 10 times narrower than the Schawlow-Townes limit, which is the standard linewidth limit for a conventional laser.

Specifically, a conventional laser consists of three key ingredients, (1) the pump media which can be pump to have population inversion to pump the laser cavity, (2) the laser cavity which can be coherently pumped, (3) the bath of the cavity field, which is essential for laser output. For a typical atomic laser, the pump media is modeled by three-level atoms. The cavity is an optical cavity, which can be modeled by a single mode cavity. The bath of the cavity field, which is naturally to be considered as the electromagnetic field outside the cavity and can be modeled by a vacuum thermal bath. Further, to achieve an active laser,

the couplings between these three elements is needed. In a conventional laser, especially for an atomic laser, the cavity-atom and cavity-bath coupling are all linear couplings.

In superconducting circuit system, the strongly nonlinearity of the Josephson junction is the key to the construction of superconducting qubits. For example, a Josephson junction shunted by a capacitor (in parallel) can form a nonlinear harmonic oscillator, which is referred to as transmon qubit [64, 65]. Because of the strong nonlinearity, the photon that is on resonance to the transition from ground state to the first excited state, is far detuned from the transition between first excited state to the second excited states, which effectivly turns this non-linear resonator into a two-level system, i.e., a qubit.

Because of the nonlinearity of the transmon qubit, it can be treated as an artificial atom, which is easily mapped to the pump media in the atomic laser model. Meanwhile, in the Josephson circuit system, we can use either a superconducting coplanar waveguide resonator or microwave cavity to be the maser cavity. The cavity can couple to a transmission line, which acts the role of the output bath, to receive the output microwave light.

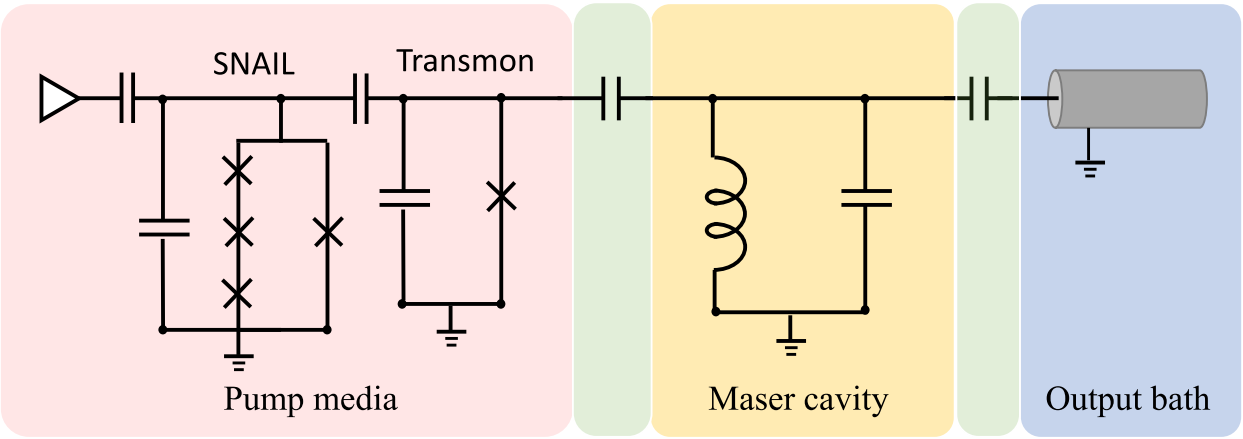

Figure 32: Conventional Josephson micromaser circuit model. In the model, a SNAIL qubit couples to a transmon qubit, which acts the role of the pump media. The LC resonator acts the role of the maser cavity, while the transmission is the output bath. These elements are linearly capacitivly coupled together.

Similar to a conventional atomic laser system, the different components of the Josephson micromaser, i.e., the transmon qubit, the cavity and the transmission line, can be capacitivly

coupled to achieve linear couplings and the Josephson micromaser can be built as shown in Fig. 32. Because the single photon transition between the ground and the second excited state of a transmon is forbidden, we will use an alternative transmon-type qubit which we will refer to as the SNAIL qubit. In the SNAIL qubit the Josephson junction of the transmon is replaced by a Superconducting Nonlinear Asymmetric Inductive eLement (SNAIL) [74], which has a third order nonlinearty that allows the SNAIL qubit to be pumped from the ground to the second excited state by a single photon. We will take this notion one step further by coupling a SNAIL qubit to a transmon qubit, and use the third order nonlinearity to drive both qubits to the first excited state. This process is discussed in details in Section. 5.5. The cavity of the Josephson micromaser can be modeled by LC resonator, whose frequency is set by $\omega_c = 1/\sqrt{L_c C_c}$. Using incoherent drive on the SANIL-transmon qubit pair, the transmon qubit can be pumped to have population inversion. Using linear coupling between the transmon qubit and the cavity, the cavity field can be pumped by the transmon qubit to achieve lasing. Through the linear coupling between the cavity and the transmission line, the laser light (microwave) is emitted from the cavity to the transmission line.

In Ref. [197], Wiseman showed that using the Susskind-Glogower operator [198] of the cavity field

$$\hat{e} = \sum_n |n\rangle\langle n+1|, \tag{5.1}$$

for atom-cavity coupling can remove the cavity field phase noise coming from the cavity pump process and suppress the linewidth of the laser field by a factor of 1/2 beyond the standard limit of the conventional laser light, i.e., the Schawlow-Townes limit. Inspired by Ref. [197], We examine the nonlinear couplings for not only the atom-cavity coupling, but also the cavity-bath coupling for our Josephson micromaser system and show that the nonlinear coupling can indeed suppress the linewidth of the laser light even further, beyond the 1/2 of the Schawlow-Townes limit.

With the nonlinearity of the Josephson junctions, the coupling between the cavity and the pump media, the cavity and the transmission line can be engineered. Instead of the linear capacitive coupling shown in Fig. 32, we can use Josephson junctions to provide the nonlinear couplings which can mimic the Susskind operator. Using nonlinear couplings, the

Josephson micromaser can emit not only coherent microwaves, but also light that is more quantum. Especially, in this chapter, we demonstrate that by replacing the linear coupling between the laser components (the green shaded region in Fig. 32) by nonlinear coupling circuits which consist of Josephson junctions and linear inductors, the Josephson micromaser light can have much narrower linewidth than the Schawlow-Townes limit.

In the following sections, we focus on the different components of the Josephson micromaser and the couplings between these components. Specifically, in Section 5.2, we introduce some of the helpful theorems and derivations that will be used in constructing the theoretical treatment of the Josephson micromaser. In Section 5.3, we review the linewidth suppression by the Susskind operator in Ref. [197], and we explore the case that using the Susskind operator for the cavity-bath coupling also. We show that the linewidth of the laser can be further suppressed. In Section 5.4, we discuss the second quantized treatment of the cavity field and the transmission line. Then we focus on the nonlinear coupling circuit and shows that the nonlinear coupling circuit can mimic the performance of the Susskind operator. In Section 5.5, we discuss the treatment of the Josephson micromaser pump media, i.e., the SNAIL qubit and the transmon qubit. We show that by the bath engineering on the transmon qubit using the SNAIL qubit as shown in Fig. 32, we can achieve the effective incoherent drive on the transmon qubit. In Section 5.6, we analysis the nonlinear coupling between the transmon qubit and the maser cavity. We also consider the quantum Josephson micromaser system as a whole and calculate the linewidth of the maser in Section 5.7. We show that the laser linewidth can be further suppressed beyond the 1/2 of the Schawlow-Townes limit. We conclude the chapter in Section 5.8.

5.2 Important theorems and derivation for Josephson micromaser system

In this section, we review some of the theorems and results which are helpful for the later discussion of the cavity-bath nonlinear coupling. In Section 5.2.1, we review the Baker-Campbell-Hausdorff formula. In Section 5.2.3 and 5.2.2, we discuss the treatment of the cosine of the field operators and how to expand the field operator cosine into normal ordered

terms.

5.2.1 Baker-Campbell-Hausdorff (BCH) formula

Suppose there are two operators $\hat{X}$ and $\hat{Y}$, the commutator of the operators satisfies

$$\left[\hat{X},[\hat{X},\hat{Y}]\right]=0=\left[\hat{Y},[\hat{X},\hat{Y}]\right] \tag{5.2}$$

Based on Baker-Campbell-Hausdorff formula,

$$\exp(\hat{X})\exp(\hat{Y})=\exp\left(\hat{X}+\hat{Y}+\frac{1}{2}[\hat{X},\hat{Y}]\right). \tag{5.3}$$

If we further assume that the commutator $[\hat{X},\hat{Y}]$ is a constant, the BCH formula can be simplified as

$$\begin{aligned}\exp(\hat{X})\exp(\hat{Y})&=\exp\left(\hat{X}+\hat{Y}\right)\exp\left(\frac{1}{2}[\hat{X},\hat{Y}]\right)\\ \Rightarrow\exp\left(\hat{X}+\hat{Y}\right)&=\exp(\hat{X})\exp(\hat{Y})\exp\left(\frac{1}{2}[\hat{X},\hat{Y}]\right).\end{aligned} \tag{5.4}$$

5.2.2 Transformation of a cosine of field operators

Suppose the Hermitian operator $\hat{X}$ acts on a N-dimensional Hilbert space, with eigenstates and eigenvalues

$$\hat{X}|x_i\rangle=x_i|x_i\rangle. \tag{5.5}$$

The operator is equivalently

$$\hat{X}=\sum_{i=1}^{N}x_i|x_i\rangle\langle x_i| \tag{5.6}$$

Suppose that the basis we are interested in is different from the eigenbasis of $\hat{X}$. Let the basis elements be denoted by $|n\rangle$, and the basis transformation by the unitary U. The operator $\hat{X}$ in this basis is

$$\hat{X}=\sum_{i,j}x_{ij}|i\rangle\langle j| \tag{5.7}$$

where x_{ij} is given by

$$x_{ij}=\sum_{i}x_kU_{ik}U^*_{jk} \tag{5.8}$$

where x_k's are the eigenvalues of $\hat{X}$.

Any function of the operator $\hat{X}$ can be expressed using its eigenstates $\{|x_i\rangle\}$ and eigenvalues x_i. For example for the case of the cosine function:

$$\cos \hat{X} = \sum_i \cos(x_i)|x_i\rangle\langle x_i|. \tag{5.9}$$

Applying this notion twice, we can express the cosine of an operator as the sum of exponentials of the operator

$$\cos(\hat{X}) = \sum_j \frac{1}{2}\left(e^{i\,x_j} + e^{-i\,x_j}\right)|x_i\rangle\langle x_i| = \frac{1}{2}\left(e^{i\,\hat{X}} + e^{-i\,\hat{X}}\right) \tag{5.10}$$

5.2.3 Expansion of the cosine of the field operators

In the treatment of the Josephson junction induced coupling between superconducting devices, especially for the quantized theory, the coupling Hamiltonian given by the Josephson junction contains the cosine of the phase operators. Note that the phase operator for an LC oscillator or a transmission line, similar to the position operator for the Harmonic oscillator, satisfies

$$\hat{\phi} = \tilde{\phi}_c(\hat{a} + \hat{a}^\dagger), \tag{5.11}$$

where $\tilde{\phi}_c$ is a constant of proportionality. However, direct analytical calculation using cosine of the operators is tough. If we directly expand the Hamiltonian in the order of $\tilde{\phi}_c$, it is hard to count the order in terms of the field operators. To see this, suppose we expand the Hamiltonian

$$H = -\cos\left[\tilde{\phi}_c(\hat{a} + \hat{a}^\dagger)\right], \tag{5.12}$$

in the order of $\tilde{\phi}_c$. Naively, the expansion would be

$$H \sim -\left(1 - \frac{1}{2}\tilde{\phi}_c^2(\hat{a} + \hat{a}^\dagger)^2 + \frac{1}{4!}\tilde{\phi}_c^4(\hat{a} + \hat{a}^\dagger)^4 + ...\right) \tag{5.13}$$

Note that because of the commutator relation of $\hat{a}$ and $\hat{a}^\dagger$, higher order terms in $\tilde{\phi}_c$ can contain lower orders in the field operators. However, especially when we want to calculate the mean value of the terms in vacuum state, the order in field operator expansion is more important to consider. To see this, we compare the second and fourth order terms in $\tilde{\phi}_c$ and

observe that both have terms that are constant and terms that are second order in the field operators.

$$\left(\hat{a}+\hat{a}^{\dagger}\right)^{2}=\hat{a}^{2}+\left(\hat{a}^{\dagger}\right)^{2}+2\hat{a}^{\dagger}\hat{a}+1 \tag{5.14a}$$

$$\begin{aligned}\left(\hat{a}+\hat{a}^{\dagger}\right)^{4}=&\hat{a}^{4}+\left(\hat{a}^{\dagger}\right)^{4}+4\hat{a}^{\dagger}\hat{a}^{3}+4\left(\hat{a}^{\dagger}\right)^{3}\hat{a}+6\left(\hat{a}^{\dagger}\right)^{2}\hat{a}^{2}\\&+6\left(\hat{a}^{\dagger}\right)^{2}+6\hat{a}^{2}+8\hat{a}^{\dagger}\hat{a}+5\end{aligned} \tag{5.14b}$$

To obtain an expansion in the order of field operator while the terms are aligned in normal order, we use the expansion of the operator cosine [Eq. (5.10)] combined with BCH formula [Eq. (5.4)],

$$\begin{aligned}H=&-\frac{1}{2}\left(e^{i\tilde{\phi}_c(\hat{a}+\hat{a}^{\dagger})}+e^{-i\tilde{\phi}_c(\hat{a}+\hat{a}^{\dagger})}\right)\\=&-\frac{1}{2}e^{-\tilde{\phi}_c^2/2}\left(e^{i\tilde{\phi}_c\hat{a}^{\dagger}}e^{i\tilde{\phi}_c\hat{a}}+e^{-i\tilde{\phi}_c\hat{a}^{\dagger}}e^{-i\tilde{\phi}_c\hat{a}}\right)\end{aligned} \tag{5.15}$$

where we use the fact that $\tilde{\phi}_c$ is real. In Eq. (5.15), the normal order of field operators is naturally guaranteed upon series expansion of the exponential of operators.

5.3 Narrowing of linewidth by nonlinear couplings

In this section, we consider the linewidth of the laser light. We start from the review of the conventional laser theory in Section 5.3.1 and 5.3.2. We construct the master equation of the conventional laser system in Section 5.3.1 and solve for the linewidth of the laser in Section 5.3.2. We also show that the linewidth of the conventional laser has a limit, which is referred as Schawlow-Townes limit. In Section 5.3.3, we first show that the nonlinear atom-cavity coupling can further suppress the linewidth of the laser light by a factor of 1/2 of the Schawlow-Townes limit, as pointed out in Ref. [197]. Then, we extend the linewidth suppression scheme of Wiseman in Ref. [197], and explore the possibility to further suppress the linewidth of laser light by applying nonlinear coupling not only between atom and cavity, but also between cavity and the bath. We conclude section 5.3.3 by showing that the linewidth of laser light can be decreased beyond the 1/2 of the Schawlow-Townes that was established in Ref. [197].

5.3.1 Master equation of conventional laser theory

In this subsection, we review the conventional laser theory to understand the laser linewidth. The theoretical treatment mainly follows the discussion in Chapter 11 of Ref. [121] and Chapter 16-17 of Ref. [199]. We will review the conventional laser model and then focus on the single-atom laser model for the Josephson micromaser proposed in Fig. 44. We will map the theoretical treatment of the single-atom model for the Josephson micromaser to the conventional laser model.

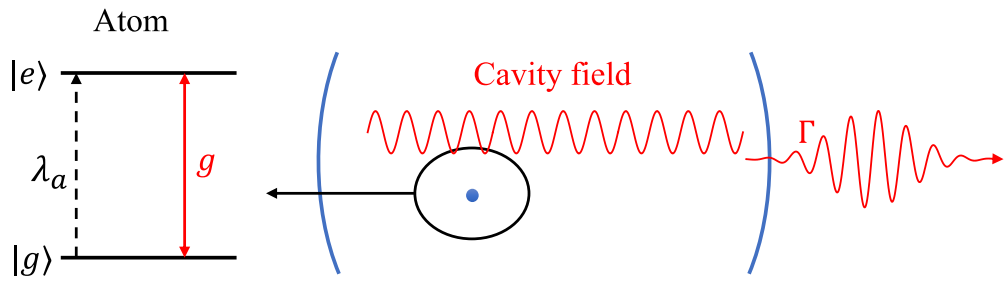

Figure 33: The sketch of the single-atom laser model for the linear Josephson micromaser given in Fig. 32.

A realistic model for the atomic laser is to model the pump media as a cluster of atoms. Two of the atom levels are the laser levels, between which the transition are coupled with the cavity field. The atoms can still be modeled by two-level atoms, and are effectively incoherently pumped from the lower laser level to the higher one. The detailed treatment of this laser model can be found in Chapter 11 of Ref. [121]. The sketch of the conventional atomic laser system is similar to the system shown in Fig. 33 except that the pump media is a cluster of atoms. Assume the pump media consists of N identical atoms, and the atoms couples to the cavity field by the Jaynes–Cummings Hamiltonian, i.e.,

$$V = \sum_i V_i = g\left(\sigma_+^{(i)} a + a^\dagger \sigma_-^{(i)}\right), \tag{5.16}$$

where we assume all the atoms couples to the field uniformly and the operator a and $a^\dagger$ are the lowering and raising operators for the cavity field and $\sigma_-^{(i)}$ and $\sigma_+^{(i)}$ are for the i-th atom. In this model, the direct coupling between the atoms are ignored, but the atoms can couple

through the cavity field. In addition to the cavity-atom coupling, there are also cavity loss and incoherent drive to the atoms, which can be described by the dissipators (which are superoperators that act on density matrices)

$$\mathcal{D}[a]\rho = -\frac{1}{2}\left(a^\dagger a\rho + \rho a^\dagger a - 2a\rho a^\dagger\right) \tag{5.17a}$$

$$\mathcal{D}[\sigma_+^{(i)}]\rho = -\frac{1}{2}\left(\sigma_-^{(i)}\sigma_+^{(i)}\rho + \rho\sigma_-^{(i)}\sigma_+^{(i)} - 2\sigma_+^{(i)}\rho\sigma_-^{(i)}\right). \tag{5.17b}$$

The state of the N atoms and the cavity field is described by its density operator R, which satisfies the the master equation,

$$\partial_t R = -i\sum_i [V_i, R] + \sum_i \lambda_a \mathcal{D}[\sigma_+^{(i)}]R + \Gamma_c \mathcal{D}[a]R, \tag{5.18}$$

where λ_a is the incoherent pumping rate and Γ_c is the cavity decay rate, and R is again the density operator for the cavity field and the N atoms in the cavity. To understand the property of the laser light, we want to reduce the equation of motion (EOM) for the cavity field and the pump atoms to an effective EOM of the cavity field itself. The cavity field itself can be described by its density operator $\rho = \mathrm{Tr}_A\{R\}$, where Tr_A is the partial trace over all the atomic degrees of freedom (DOFs). To perform the partial trace over the atomic DOFs on Eq. (5.18), we begin by focusing on the cavity-atom coupling term

$$\mathrm{Tr}_A\left\{\sum_i [V_i, R]\right\} = \sum_i \mathrm{Tr}_{(i)}\mathrm{Tr}_A^{(i)}[V_i, R] = \sum_i \mathrm{Tr}_{(i)}[V_i, \rho^i], \tag{5.19}$$

where $\mathrm{Tr}_{(i)}$ is the trace over the states of the i-th atom, $\mathrm{Tr}_A^{(i)}$ is the trace over all the DOFs of the pump atoms except for the i-th atom and $\rho^i = \mathrm{Tr}_A^{(i)}\{R\}$ is the density operator for the cavity field and the i-th atom. Similar to the second term in Eq. (5.18),

$$\mathrm{Tr}_A\left\{\sum_i \lambda_a \mathcal{D}[\sigma_+^{(i)}]R\right\} = \sum_i \mathrm{Tr}_i \lambda_a \mathcal{D}[\sigma_+^{(i)}]\rho^{(i)}. \tag{5.20}$$

We further assume that the pump media can be approximated by N atoms that are in the same state. This state is the average of the actual states of the atoms. Under this assumption, the cavity-pump media coupling can be treated as the cavity field couples to the mean state of the atoms. With this assumption, we can define an "averaged" density

operator for one of the atoms and the cavity field as $\tilde{\rho}$, where we ignore the index for the atom, as the atoms are all in the same state. The density operator $\tilde{\rho}$ is given by

$$\tilde{\rho} = \frac{1}{N}\sum_i \rho^{(i)} \tag{5.21}$$

and the state of the cavity is

$$\rho = \langle g|\tilde{\rho}|g\rangle + \langle e|\tilde{\rho}|e\rangle. \tag{5.22}$$

The effective master equation for the "averaged" atom-cavity density operator is

$$\partial_t\tilde{\rho} = -i[v,\tilde{\rho}] + \lambda_a\mathcal{D}[\sigma_+]\tilde{\rho} + \gamma_c\mathcal{D}[a]\tilde{\rho} \tag{5.23a}$$

$$v = g\left(\sigma_+ a + a^\dagger\sigma_-\right) \tag{5.23b}$$

where σ_+ and σ_- are the operators for the "averaged" atom Hilbert space.

For a typical laser model, the cavity decay is slow compared to the atom-cavity dynamics, in the following discussion, we ignore the cavity loss at first. After we write down the effective dynamics of the cavity field by adiabatically eliminate the atomic DOFs, the cavity loss is put back to the master equation of the cavity field.

The master equation Eq. (5.23) without cavity decay can be expanded in the state of this averaged atom and the cavity field, $|g(e)\rangle \otimes |n\rangle$ as,

$$\partial_t\tilde{\rho}_{en-1,en'-1} = -ig\left(\sqrt{n}\tilde{\rho}_{gn,en'-1} - \sqrt{n'}\tilde{\rho}_{en-1,gn'}\right) + \lambda_a\tilde{\rho}_{gn-1,gn'-1} \tag{5.24a}$$

$$\partial_t\tilde{\rho}_{gn,gn} = -ig\left(\sqrt{n}\tilde{\rho}_{en-1,gn'} - \sqrt{n'}\tilde{\rho}_{gn,en'-1}\right) - \lambda_a\tilde{\rho}_{gn,gn'} \tag{5.24b}$$

$$\partial_t\tilde{\rho}_{en-1,gn'} = -ig\left(\sqrt{n}\tilde{\rho}_{gn,gn'} - \sqrt{n'}\tilde{\rho}_{en-1,en'-1}\right) - \frac{\lambda_a}{2}\tilde{\rho}_{en-1,gn'} \tag{5.24c}$$

$$\partial_t\tilde{\rho}_{gn,en'-1} = -ig\left(\sqrt{n}\tilde{\rho}_{en-1,en'-1} - \sqrt{n'}\tilde{\rho}_{gn,gn'}\right) - \frac{\lambda_a}{2}\tilde{\rho}_{gn,en'-1}. \tag{5.24d}$$

Note that the density operator for the cavity field satisfies

$$\rho_{n,n'} = \tilde{\rho}_{gn,gn'} + \tilde{\rho}_{en,en'}, \tag{5.25}$$

and the time-evolution of the cavity field density operator satisfies

$$\begin{aligned}\partial_t\rho_{n,n'} = &-ig\left(\sqrt{n}\tilde{\rho}_{en-1,gn'} - \sqrt{n'}\tilde{\rho}_{gn,en'-1} + \sqrt{n+1}\tilde{\rho}_{gn+1,en'}\right.\\ &\left.-\sqrt{n'+1}\tilde{\rho}_{en,gn'+1}\right).\end{aligned} \tag{5.26}$$

To further the construction the master equation for the cavity field, the relation between the components of the averaged atom-cavity density operator and the cavity field density operator is required.

We can replace the last term in Eq. (5.24a) and get

$$\begin{aligned}\partial_t \tilde{\rho}_{en-1,en'-1} = &- ig\left(\sqrt{n}\tilde{\rho}_{gn,en'-1} - \sqrt{n'}\tilde{\rho}_{en-1,gn'}\right) + \lambda_a \rho_{n-1,n'-1} \\ &- \lambda_a \tilde{\rho}_{en-1,en'-1}.\end{aligned} \tag{5.27}$$

The laser system equations, Eq. (5.27) with Eqs. (5.24b), (5.24c) and (5.24d) form a closed set of equations for the components of the average atom-cavity field operator $\tilde{\rho}$, except for the component of the cavity field density operator $\rho_{n,n'}$. If we further assume that the dynamics of the cavity field is slow compared to the cavity-atom coupling, in this coarse-grained time step which is long compared to the cavity-atom dynamics, but short compared to the laser cavity field dynamics, $\rho_{n-1,n'-1}$ can be thought as a constant and the fast oscillation of the averaged atom-cavity density operator components is not important to the understanding of the time-evolution of the cavity field. This is a perfect scenario for adiabatic elimination, and therefore we set the time derivatives of $\tilde{\rho}$ to be zero. Then the averaged atom-cavity density operator components on the coarse-grained time steps satisfies

$$[\tilde{\rho}]_{n,n'} = [M]^{-1}_{n,n'}[\rho]_{n-1,n'-1} \tag{5.28}$$

where we express the above equations in matrix form,

$$[\tilde{\rho}]_{n,n'} = \begin{bmatrix} \tilde{\rho}_{en-1,en'-1} \\ \tilde{\rho}_{gn,gn'} \\ \tilde{\rho}_{en-1,gn'} \\ \tilde{\rho}_{gn,en'-1} \end{bmatrix}, \; [\rho]_{n,n'} = \begin{bmatrix} \lambda_a \rho_{n,n'} \\ 0 \\ 0 \\ 0 \end{bmatrix} \tag{5.29}$$

and

$$[M]_{n,n'} = \begin{bmatrix} -\lambda_a & & ig\sqrt{n'} & -ig\sqrt{n} \\ & -\lambda_a & -ig\sqrt{n} & ig\sqrt{n'} \\ ig\sqrt{n'} & -ig\sqrt{n} & -\lambda_a/2 & \\ -ig\sqrt{n} & ig\sqrt{n'} & & -\lambda_a/2 \end{bmatrix}. \tag{5.30}$$

With the Eq. (5.28), the dynamics of the cavity field [Eq. (5.26)] on the coarse time steps is

$$\partial_t \rho_{n,n'} = -\frac{\mathcal{N}'_{n,n'}\mathcal{A}}{1+\mathcal{N}_{n,n'}\mathcal{B}/\mathcal{A}}\rho_{n,n'} + \frac{\sqrt{nn'}\mathcal{A}}{1+\mathcal{N}_{n-1,n'-1}\mathcal{B}/\mathcal{A}}\rho_{n-1,n'-1} \tag{5.31}$$

where the linear gain coefficient $\mathcal{A}$, self-saturation coefficient $\mathcal{B}$, and the dimensionless factors $\mathcal{N}$ and $\mathcal{N}'$ are

$$\mathcal{A} = \frac{4g^2}{\lambda_a} \tag{5.32a}$$

$$\mathcal{B} = \frac{32g^4}{\lambda_a^3} \tag{5.32b}$$

$$\mathcal{N}_{n,n'} = \frac{1}{2}(n+n'+2) + \frac{(n-n')^2\mathcal{B}}{16\mathcal{A}} \tag{5.32c}$$

$$\mathcal{N}'_{n,n'} = \frac{1}{2}(n+n'+2) + \frac{(n-n')^2\mathcal{B}}{8\mathcal{A}} \tag{5.32d}$$

If we treat $\mathcal{B}/\mathcal{A} \ll 1$, and expand the Eq. (5.31) to the second lowest order, the master equation in Eq. (5.31) (with cavity loss term) can be treated as the coefficient from of

$$\begin{aligned}\partial_t \rho =& -\frac{\mathcal{A}}{2}\left[aa^\dagger\rho + \rho aa^\dagger - 2a^\dagger\rho a\right] + \frac{\mathcal{B}}{8}\left[\rho(aa^\dagger)^2 + (aa^\dagger)^2\rho - 4a^\dagger\rho aa^\dagger a\right.\\ &\left.-4a^\dagger aa^\dagger\rho a + 6aa^\dagger\rho aa^\dagger\right] + \Gamma_c\mathcal{D}[a]\rho,\end{aligned} \tag{5.33}$$

where the first term is a linear pump to the cavity field process while the second term can be regarded as the reabsorption process. For a laser which is lasing, the cavity should be pumped faster than the loss process. Therefore the lasing threshold is $\mathcal{A} \geq \Gamma_c$.

Here, we would like to stress that the time derivative in Eq. (5.31) is on the coarse time steps. In addition, the laser model we considered is different from the discussion in Chapter 11 of Ref. [121], where in our discussion, there is no population loss out of the laser levels, nor a pumping process to pump the population back to the laser levels. In the more complex laser model of Ref. [121], the population pump into the laser level can be mapped onto the process that the atom is prepared in its initial state and injected into the cavity to interact with the cavity field, while the population loss out of the laser levels can be thought of as the process that the atoms, after interacting to the cavity field for some time period, leave the cavity and no longer interact with the cavity field. This setup is called a micromaser, and via the above mapping we see that the conventional laser model is equivalent to the treatment of a micromaser. If the atoms are initially prepared into a

population inverted states, the laser field effectively experiences an incoherent drive, and the atom beam can be treated as a bath of the laser cavity field. With the atom-bath treatment, it is more natural and easier to derive the linear pump and re-absorption terms in Eq. (5.33). A good reference of the atom-bath treatment of the micromaser model of the conventional laser system is Section 16-17 of Ref. [199].

At last, with the cavity decay terms, the full master equation for the cavity field in Fock basis is

$$\begin{aligned}\partial_t \rho_{n,n'} = &- \frac{\mathcal{N}'_{n,n'}\mathcal{A}}{1+\mathcal{N}_{n,n'}\mathcal{B}/\mathcal{A}}\rho_{n,n'} + \frac{\sqrt{nn'}\mathcal{A}}{1+\mathcal{N}_{n-1,n'-1}\mathcal{B}/\mathcal{A}}\rho_{n-1,n'-1} \\ &- \frac{\Gamma_c}{2}(n+n')\rho_{n,n'} + \Gamma_c\sqrt{(n+1)(n'+1)}\rho_{n+1,n'+1}.\end{aligned} \tag{5.34}$$

The master equation does not mix the components with different $|n-n'|$ (different diagonal bands in density matrix in Fock basis), and it is a three-term recurrent differential equations. The diagonal terms, i.e., terms with $n = n'$, give the photon distribution of the laser field. The first off-diagonal matrix elements, i.e., $|n'-n'| = 1$ terms, gives the laser linewidth, which will be discussed in the following subsection. The steady state of these set of equations can be solved by "detailed balanced" condition. Here we use the diagonal elements as an example, which obey the equation,

$$\partial_t P_n = -\frac{(n+1)\mathcal{A}}{1+(n+1)\mathcal{B}/\mathcal{A}}P_n + \frac{n\mathcal{A}}{1+n\mathcal{B}/\mathcal{A}}P_{n-1} - \Gamma_c n P_n + \Gamma_c(n+1)P_{n+1}, \tag{5.35}$$

where $P_n = \rho_{n,n}$, which is also the probability of having n photon in the cavity field. Note that Eq. (5.35) can also be thought of the probability flow between the states with $(n-1)$, n and $(n+1)$ photons, especially, the first two terms on RHS of Eq. (5.35) is the propability flow from n to $(n+1)$ state and from $(n-1)$ state to n state, which is given by the laser pump process, while the last two terms are the probability flow from the n to $(n-1)$ photon state and from $(n+1)$ to n photon state, which is given by the cavity loss process. In the steady state, since the system probability for different photon number state should be steady, these probability flows should balance with each other. Therefore, we can get the "detailed balance" condition that

$$\Gamma_c n P_n = \frac{n\mathcal{A}}{1+n\mathcal{B}/\mathcal{A}}P_{n-1} \Rightarrow P_n = \frac{\mathcal{A}/\Gamma_c}{1+n\mathcal{B}/\mathcal{A}}P_{n-1}, \tag{5.36}$$

which becomes a recurrence relation between the probability with different photon numbers in the cavity field. Then the steady state photon distribution can be solved by

$$P_m = \prod_{n=1}^{m} \frac{\mathcal{A}/\Gamma_c}{1 + n\mathcal{B}/\mathcal{A}} P_0 \tag{5.37a}$$

$$\sum_{n=0}^{+\infty} P_n = 1. \tag{5.37b}$$

The example of the photon distribution of the laser cavity field for two sets of parameters are shown in Fig. 34. In Fig. 34a we set $\mathcal{A} = 1.2$, the photon distribution of the laser field does not match a Poisson distribution, but as we increase linear pump strength $\mathcal{A}$ to 1.8, the photon distribution becomes more similar to the Poisson distribution.

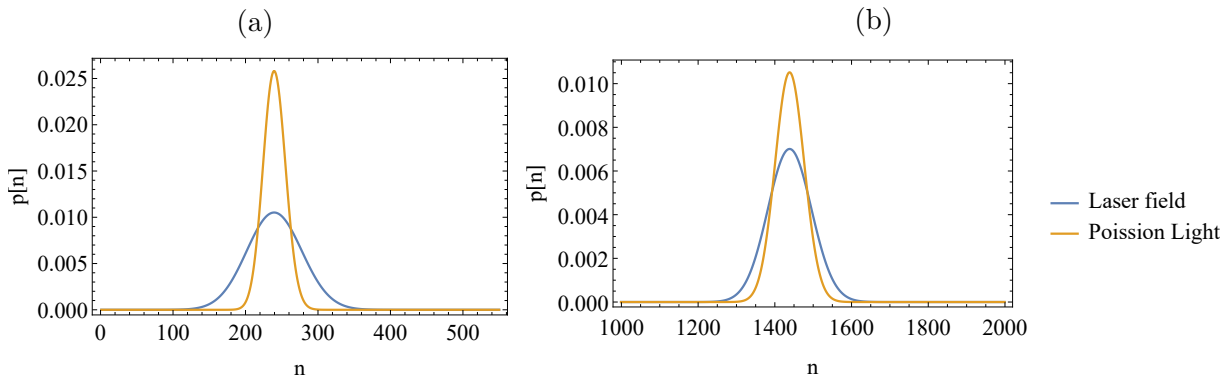

Figure 34: The photon distribution of the laser light and the Poisson distribution with the same mean photon number. For both subplots, we set $\Gamma_c = 1.0$ and $\mathcal{B} = 0.001$. In (a) $\mathcal{A} = 1.2$ and in (b) $\mathcal{A} = 1.8$. Notice that the laser is far above the threshold, the laser distribution is similar to a Poisson distribution.

Finally, we want to stress that in the model of our linear Josephson micromaser shown in Fig. 32, there is only a single two-level atom which interacts with the cavity field. Therefore, the dynamics of the laser system is exactly modeled by the master equation in Eq. (5.23). Note that the Josephson micormaser directly maps to a "single-atom" maser. All the discussion on the photon distribution and the linewidth can be directly solved by solving the dynamics of the atom and the cavity field, i.e., Eq. (5.23).

5.3.2 Conventional laser linewidth, Schawlow-Townes limit

The laser linewidth is related to the fluctuations, in time, of the phase of the laser light field. The spectrum of the light field is given by the Fourier transform of the two-time correlation function of the field, i.e., $\langle E(t+\tau)E(t)\rangle$, or equivalently, $\langle a^\dagger(t+\tau)a(t)\rangle$. If the light field is perfectly coherent, i.e., $\langle a^\dagger(t+\tau)a(t)\rangle \sim \exp(i\omega\tau)$, the spectrum of the light field is a delta function, which has zero linewidth. On the other hand, if there is phase noise, the two-time correlation function decays, and the linewidth is given by the decay rate of the two-time correlation function $\langle a^\dagger(t+\tau)a(t)\rangle$. To compute the two-time correlation function, we assume that the Born-Markov approximation still applies to this system, and apply the quantum regression theorem [see Section 2.5]. Because we only care about the time-decay of the two time correlation function, i.e., the $c_j(\tau)$'s in Eqs. (2.39) and (2.40), we can obtain these time-dependent factors by solving the single-time average $\langle a(t+\tau)\rangle$ instead. This is equivalent to computing $\rho_{n,n-1}(t+\tau)$ or $\rho_{n-1,n}(t+\tau)$. An analytical solution of the laser linewidth can be derived using the detailed balance condition, similar to the solution of the photon distribution of the laser field.

To use the detailed balance condition to solve the equations for the first off-diagonal elements $\rho_{n-1,n}(t+\tau)$, Eq. (5.34) needs to be rewritten in the form of

$$\partial_t \rho_{n,n+1} = -\frac{1}{2}\mu_n \rho_{n,n+1} + c_{n-1}\rho_{n-1,n} + d_{n+1}\rho_{n+1,n+2} - (c_n + d_n)\rho_{n,n+1} \tag{5.38}$$

where μ_n, c_n and d_n are coefficients that depends on n. With the detailed balance condition $c_n\rho_{n,n+1} = d_{n+1}\rho_{n+1,n+2}$, we can assume the solution of the elements of the density operator is in the form of $\rho_{n,n+1} = e^{-D_n(t)}\rho_{n,n+1}(t=0)$. We can plug back this tentative solution into Eq. (5.38), and expand to the lowest order to get a solution for $D(t) \sim \frac{1}{2}Dt$, where D is the linewidth of the laser field,

$$D = \mu_n \sim \frac{1}{4}\left(\frac{\mathcal{A}+\Gamma_c}{\langle n\rangle} - \frac{3\mathcal{B}/2 + \mathcal{B}^2/(16\mathcal{A})}{\langle n\rangle(1+\langle n\rangle\mathcal{B}/\mathcal{A})}\right) \sim \frac{\mathcal{A}+\Gamma_c}{4\langle n\rangle}. \tag{5.39}$$

Based on the above expression of the laser linewidth, the phase noise of the laser light comes from two different sources, the gain process and loss process [197, 200]. Because when the

laser is active, the laser must be above the threshold, i.e., $\mathcal{A} \geq \Gamma_c$. Therefore there is a limit on the laser linewidth, called the Schawlow-Townes limit,

$$D_{\mathrm{ST}} = \frac{\Gamma_c}{2\langle n \rangle}. \tag{5.40}$$

Here we comment on obtaining the laser linewidth with numerical methods. One can extract the laser linewidth by directly evaluating the two-time correlation function, $\langle a^\dagger(t+\tau)a(t)\rangle$. The Fourier transform of the two-time correlation function gives the spectrum of the laser line, which should be have a Lorentzian form, and the linewidth can be extracted from this spectrum. Another way to calculate the linewidth is to apply the quantum regression theorem and numerically solve the time evolution of the cavity field when the cavity field is initialized to some initial state, e.g. a coherent state with a definite phase. After solving the cavity state, extract the time evolution of the off-diagonal elements of the density matrix $\rho_{n,n+1}$ and fit it to an exponential decay, where the decay constant is the linewidth of the cavity field. The last method, which is heavily used in our discussion, is to treat the laser system master equation in a form

$$\partial_t \rho = \hat{\mathcal{L}}\rho, \tag{5.41}$$

where $\hat{\mathcal{L}}$ is the super-operator which acts on the density operator of the system. The real part of the eigenvalues of $\hat{\mathcal{L}}$ must be either zero or negative, corresponding to either steady state or decaying solutions. For laser systems the spectrum of the super-operator $\hat{\mathcal{L}}$ should have exactly one eigenstate ρ_0 with a zero eigenvalue, i.e., $\hat{\mathcal{L}}\rho_0 = 0$. This eigenstate, ρ_0, corresponds to the steady state of the laser system. The rest of the eigenstates should all have trace zero. Let ρ_1 be the eigenstate with the largest real part, or the smallest $|\mathrm{Re}(\lambda)|$ among all the other eigenvalues, s.t. $\hat{\mathcal{L}}\rho_1 = \lambda_1\rho_1$. The linewidth of the laser field is well approximated by $|\mathrm{Re}(\lambda_1)|$. With the quantum regression theorem, the laser linewidth can be extracted by the phase diffusion of the electric field ($\langle a(t)\rangle$) instead. The short-time phase diffusion performance, which is given by the large $|\mathrm{Re}(\lambda_1)|$, only contributes to the large frequency components. Especially when the laser linewidth is narrow, it is well approximated by the the eigenvalue with smallest $|\mathrm{Re}(\lambda)|$.

In Fig. 35, we use the numerics to obtain the spectrum of the super-operators for the 2-level incoherently driven single atom-cavity laser model for our Josephson micromaser shown

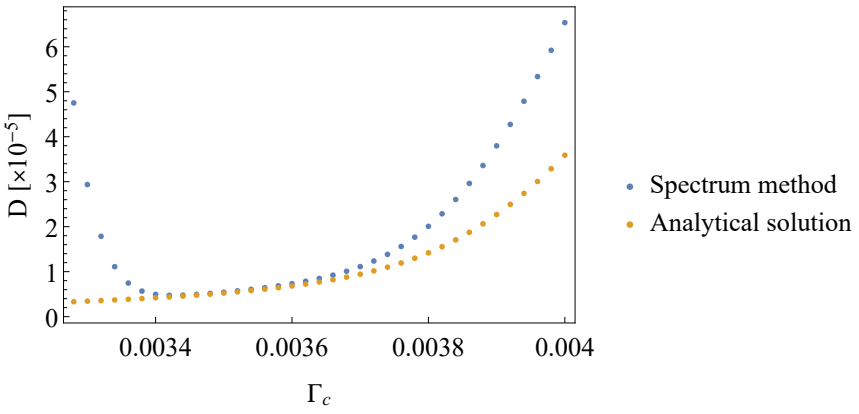

Figure 35: The conventional Josephson micromaser linewidth as we tune the cavity linewidth Γ_c. We set $g = 0.1$, $\lambda_a = 10.0$. The blue dots are the numerical calculation from the spectrum of the super-operator, while the orange dots are from the analytical solution in Eq. (5.39).

in Fig. 32. We direct solve the spectrum of the super-operator by truncating the photon number inside the cavity at 350 photons and find the linewidth of the laser, which is shown as the blue dots. We further set $\lambda_a = 10$, and the atom-cavity coupling strength $g = 0.1$ and tune the cavity bare linewidth, Γ_c. Note that at small Γ_c, especially at $\Gamma_c < 0.0034$, the linewidth from the spectrum method increases greatly from the predicted analytical result from Eq. (5.39), which is shown as the orange dots in Fig. 35. This occurs because the mean number of photons in the cavity reaches the truncation threshold of 350 photons, and hence the cavity state represented in this truncated space has a larger error as compared to the true state. But in moderate parameters, when the photon is in the order of $\sim$ 100 to 200 photons, the spectrum solution matches the analytical solution perfectly. As Γ_c increases, the laser approaching the lasing threshold and the mean photon number inside the cavity drops to $\langle n \rangle < 5$, which causes the analytical solution diverges from the laser linewidth in Eq. (5.39).

5.3.3 Using nonlinear coupling between cavity and atom to circumvent the Schawlow-Townes limit

In Ref. [197], it was shown that by using the Susskind operator

$$\hat{e} = \sum_n |n-1\rangle\langle n|, \tag{5.42}$$

to replace the normal photon lowering operator a in the cavity-bath coupling Hamiltonian, the linewidth of the cavity field can be suppressed by a factor of 1/2. Compared with the normal photon operator

$$a = \sum_n \sqrt{n}|n-1\rangle\langle n|, \tag{5.43}$$

the Susskind operator does not have any Boson amplification. If the Susskind operator is applied to the cavity-atom coupling, the time for a full swap of the excitation from the atom to the cavity does not depend on the cavity photon number. Consequently, the cavity field gain process using the $\hat{e}^\dagger$ does not introduce any phase noise to the cavity field. This can also be seen from the fact that the Susskind operator can be treated as the exponential of the phase operator [197, 198].

In order to verify the prediction that the linewidth of a laser can be reduced to 1/2 the Schawlow-Townes limit, we take our single-atom laser model of the Josephson micromaser and replace the atom cavity coupling Hamiltonian $g\left(\sigma_+ a + a^\dagger \sigma_-\right) \rightarrow g\left(\sigma_+ e + e^\dagger \sigma_-\right)$. We numerically find the spectrum of the resulting superoperator, and obtain the linewidth using the eigenvalue with the largest non-zero real part. The resulting linewidth (in units of the Schawlow-Townes linewidth) is plotted as a function of pump strength in Fig. 36. The figure shows that once the pump strength becomes sufficiently strong (i.e., beyond the lasing threshold), the linewidth becomes fixed to 1/2 the Schawlow-Townes limit. This is indeed the expected result from Eq. (5.39) after we turn off the atom-cavity noise by setting $\mathcal{A} = 0$.

Inspired by Wiseman's discussion in Ref. [197], we argue that if the system-bath coupling is also nonlinear, such that the loss of the cavity is described by the dissipator $\mathcal{D}[\hat{e}]\rho$, instead of the linear loss dissipator $\mathcal{D}[a]\rho$, the phase noise of the cavity field from the loss process can also be reduced. Therefore, the cavity linewidth can be further suppressed, even beyond 1/2 of the Schawlow-Townes limit.

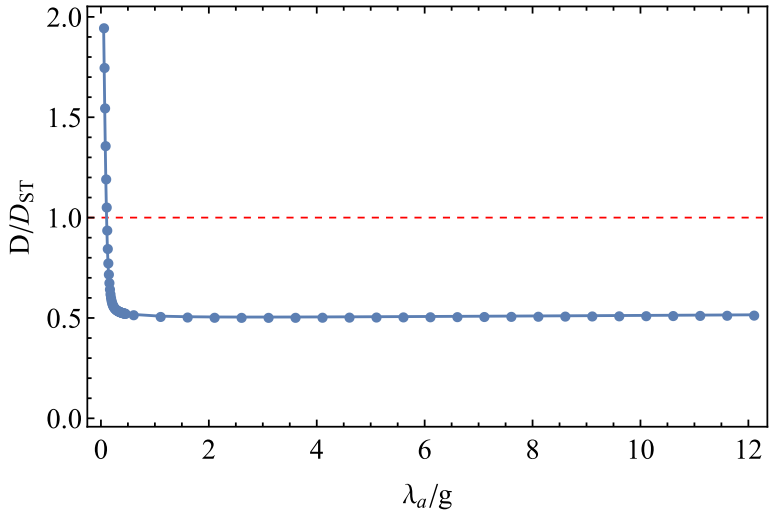

Figure 36: The linewidth of the single-atom laser with the Susskind operator for the atom-cavity coupling. We see the linewidth is suppressed to be 1/2 of the Schawlow-Townes limit.

To examine our hypothesis, we take our single-atom laser model of the Josephson micromaser, and replace both the the atom-cavity coupling (as Wiseman suggested in Ref. [197]) and the cavity dissipator by the equivalent terms with $a \to e$. In order to stabilize the cavity field, we also add a weak normal loss to the cavity (i.e., a conventional dissipator $\mathcal{D}[a]\rho$). The system is described by

$$\partial_t \rho = -i[v_{\rm NL}, \rho] + \lambda_a \mathcal{D}[\sigma_+]\rho + \Gamma_{\rm NL}\mathcal{D}[\hat{e}]\rho + \Gamma_c \mathcal{D}[a]\rho \tag{5.44}$$

where the nonlinear coupling Hamiltonian is

$$v_{\rm NL} = g\left(\sigma_+ \hat{e} + \sigma_- \hat{e}^\dagger\right), \tag{5.45}$$

the incoherent drive to the two-level atom and the normal cavity loss are given in Eq. (5.17b) and (5.17a), and the nonlinear loss term is

$$\mathcal{D}[\hat{e}]\rho = -\frac{1}{2}\left(\hat{e}^\dagger \hat{e}\rho + \rho \hat{e}^\dagger \hat{e} - 2\hat{e}\rho\hat{e}^\dagger\right). \tag{5.46}$$

As the cavity loss process is no longer dominated by Γ_c, we generalize the definition of the Schawlow-Townes limit by replacing $\langle n\rangle\Gamma_c$ by the laser luminosity

$$D_{\rm ST} = \frac{1}{4\langle n\rangle}\frac{P_{\rm out}}{\hbar\omega\langle n\rangle}, \tag{5.47}$$

where $P_{\rm out}$ is the output power of the laser and ω is the output laser light frequency. The term $P_{\rm out}/(\hbar\omega)$ is the emission rate of the photons from the cavity. In the current system, the modified Schawlow-Townes limit is

$$D_{\rm ST} = \frac{1}{4\langle n\rangle^2}\left(\Gamma_c {\rm Tr}[a\rho a^\dagger] + \Gamma_{\rm NL}{\rm Tr}[\hat{e}\rho\hat{e}^\dagger]\right). \tag{5.48}$$

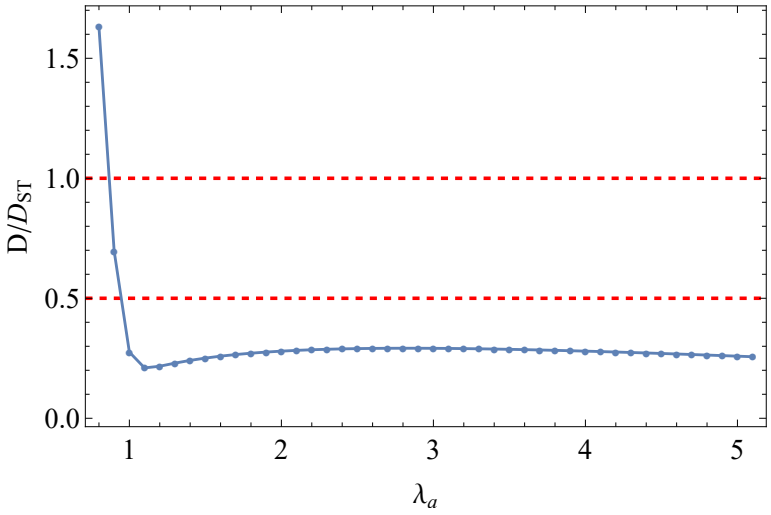

Figure 37: The linewidth of the nonlinear laser. The laser system is described by the master equation Eq. (5.44). The phase noise from both the pump process and loss process are suppressed. The parameters we choose are $\Gamma_c = 0.005$, $\Gamma_{\rm NL} = 0.3$ and $g = 1.0$.

The linewidth of laser with the nonlinear coupling given by the Susskind operator $\hat{e}$ for both the cavity-atom coupling and cavity-bath coupling is shown in Fig. 37. The linewidth of this nonlinear laser is much narrower than the Schawlow-Townes limit, even below the 1/2 of the Schawlow-Townes limit found in Ref. [197].

Note that the essence of the Susskind operator $\hat{e}$ is that it lacks the Boson amplification. Even though there are already works [197, 201, 202, 203, 204, 205] looking at various ways

to construct the Susskind operator in physical system, as far as we know (1) we are the first to apply the Susskind operator to cavity-bath coupling in laser systems and (2) we have come up with a completely novel way to implement the Susskind operator using superconducting circuit systems. In the following sections, we discuss our approach for building an approximate Susskind operator using the nonlinearity properties of Josephson junctions.

5.4 Nonlinear cavity-bath coupling in Josephson micromaser

5.4.1 Model of the cavity-to-transmission line coupler

In this subsection, we introduce the circuit model for the nonlinear coupling between the cavity and the transmission line and construct the corresponding quantum Hamiltonian.

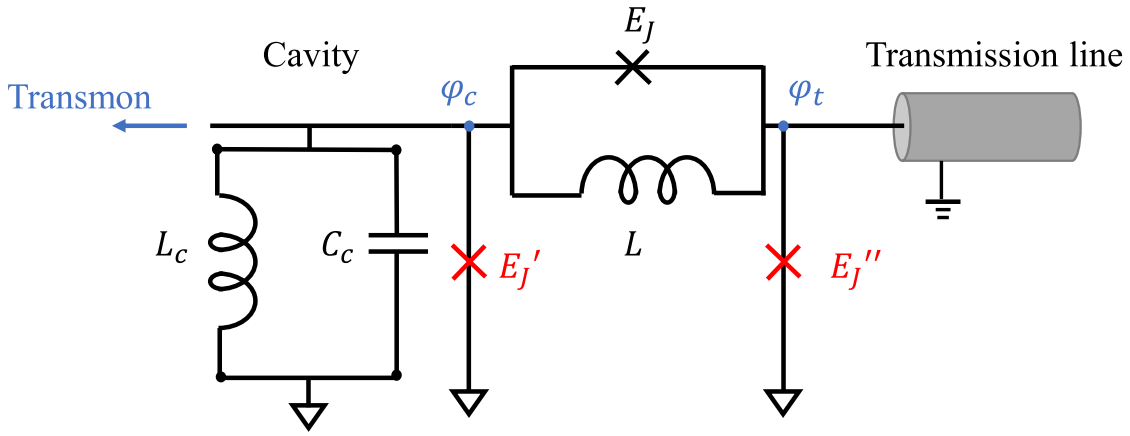

Figure 38: The proposed circuit model for introducing nonlinear coupling between the cavity and the transmission line. The Josephson junctions labeled as red are π-junctions, which are to compensate the dispersion of the cavity field and the transmission line brought by the nonlinear coupling circuit.

The coupling circuit between the cavity and the transmission line is shown in Fig. 38. The goal of the discussion in this section is to understand the cavity-transmission line nonlinear coupling, and treat the transmission line as the bath of the system and trace out from the system dynamics to get the master equation for the cavity field. Therefore, in this discussion,

we ignore the modeling of the artificial atom that is used to pump the cavity in the first place, and focus on the cavity and the transmission line.

Further, we assume the weak coupling regime, in which the energy scale of the coupling circuit E_J is much weaker than the energy scale given by the cavity frequency $\omega = 1/\sqrt{L_c C_c}$. In the weak coupling regime, the typical master equation treatment is still applicable.

In addition, on the first pass we will ignore the π-junction in Fig. 38. These junctions are included in the circuit in order to compensate for the nonlinear dispersive shift of the cavity induced by the Josephson junctions in the coupling circuit. The energy scale of these π-junctions is the same order as the coupling circuit, and hence we can ignore the effect of these junctions in the lowest order treatment.

5.4.2 The quantization of cavity field

The Josephson micomaser cavity is modeled by an LC resonator. The classical Lagrangian of the cavity consists of the energy of the capacitor, which is treated as the kinetic energy, and the energy of the linear inductor, which is treated as the potential energy. The classical Lagrangian is

$$\mathcal{L}_c = \frac{1}{2} C_c \dot{\Phi}_c^2 - \frac{1}{2L_c} \Phi_c^2, \tag{5.49}$$

where Φ_c is the flux across the linear inductor, which is related to the phase on the cavity node φ_c via $\Phi_c = \phi_0 \varphi_c$, where $\phi_0 = \hbar/(2e)$ is the flux quantum. If we treat the node flux Φ_c as the general coordinate, the momentum is

$$p_c = \frac{\partial \mathcal{L}}{\partial \dot{\Phi}_c} = C_c \dot{\Phi}_c = Q_c \tag{5.50}$$

where Q_c is the charge across the capacitor. The Hamiltonian of the LC resonator is

$$H_c = \frac{Q_c^2}{2C_c} + \frac{\Phi_c^2}{2L_c}. \tag{5.51}$$

With this quadratic Hamiltonian of the LC resonator, it can be quantized similar to the Harmonic oscillator,

$$\hat{Q}_c = -i \sqrt{\frac{\hbar}{2Z_c}} \left(\hat{a} - \hat{a}^\dagger \right) \tag{5.52a}$$

$$\hat{\Phi}_c = \sqrt{\frac{\hbar Z_c}{2}} \left(\hat{a} + \hat{a}^\dagger\right) \tag{5.52b}$$

where Z_c is the characteristic impedance of the LC resonator, $Z_c = \sqrt{L_c/C_c}$. The Hamiltonian is $H_c = \hbar\omega_c \hat{a}^\dagger \hat{a}$. The frequency of the LC resonator is $\omega_c = 1/\sqrt{L_c C_c}$. The voltage on the cavity node is $V_c = \dot{\Phi}_c$ and the current flow in the LC resonator, i.e., through the capacitor, is $I_c = \dot{Q}_c$. We can express the voltage and current operators using the raising and lowering operators via

$$\hat{V}_c = -\frac{i}{\hbar}[\hat{\Phi}_c, H_c] = -i\omega\sqrt{\frac{\hbar Z_c}{2}} \left(\hat{a} - \hat{a}^\dagger\right), \tag{5.53a}$$

$$\hat{I}_c = -\frac{i}{\hbar}[\hat{Q}_c, H_c] = \omega\sqrt{\frac{\hbar}{2Z_c}} \left(\hat{a} + \hat{a}^\dagger\right). \tag{5.53b}$$

As the coupling circuit are inductive elements, we will focus on the phase of the cavity node,

$$\hat{\varphi}_c = \tilde{\phi}_{c0} \left(\hat{a} + \hat{a}^\dagger\right), \tag{5.54}$$

where $\tilde{\phi}_{c0}$ is a dimenionless quantity defined as

$$\tilde{\phi}_{c0} = \frac{1}{\phi_0}\sqrt{\frac{\hbar Z_c}{2}}. \tag{5.55}$$

5.4.3 Treatment of the transmission line

The basic equation to model a perfect transmission line is the telegrapher's equation. To construct the telegrapher's equation we consider a single segment of the transmission line is [see Fig. 39]. The current flow in this segment is $I(x)$ and the voltage at the beginning of the segment is $V(x)$. The effective inductance of this segment is Ldx and the effective capacitance is Cdx. Note that here L and C are inductance and capacitance per unit length.

We obtain the current flow through the inductor using Faraday's law

$$I(x,t) = -\frac{1}{Ldx}\int_{-\infty}^{t} d\tau \left(V(x+dx,\tau) - V(x,\tau)\right). \tag{5.56}$$

The currents through the inductors and capcitors are connected by Krikoff's law, e.g. on node B we obtain

$$I(x,t) - I(x+dx,t) = I_c(t) = (Cdx)\frac{dV(x+dx,t)}{dt}. \tag{5.57}$$

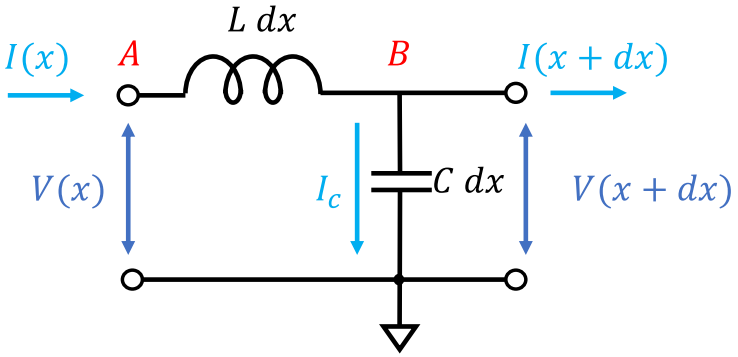

Figure 39: The lumped element model for the lossless transmission line. The unit length inductance of the transmission line is given by L, while the unit capacitance is C. The current flow and the voltage across the transmission line are I and V.

Taking partial derivative with respect to time t on both sides of Eq. (5.56) and dividing by dx on both sides of Eq. (5.57), and then taking the limit $dx \to 0$ of both equations, we get the telegrapher's equation

$$\frac{\partial V(x,t)}{\partial x} = -L\frac{\partial I(x,t)}{\partial t} \tag{5.58a}$$

$$\frac{\partial I(x,t)}{\partial x} = -C\frac{\partial V(x,t)}{\partial t}. \tag{5.58b}$$

Further, if we define the generalized flux as

$$\Phi(x,t) = \int_{-\infty}^{t} d\tau V(x,\tau), \tag{5.59}$$

and note that $I = \frac{dQ}{dt}$ where Q is a charge quantity, the equations for the generalized flux and charge are in the same form of the Telegrapher's equations in Eq. (5.58).

In telegrapher's equations in Eq. (5.58), we can take partial derivative with respect to x in Eq. (5.58a) and get

$$\partial_x^2 V(x,t) + LC\,\partial_t^2 V(x,t) = 0 \tag{5.60a}$$

$$\partial_x I(x,t) = -C\,\partial_t V(x,t), \tag{5.60b}$$

which is a wave equation of both $V(x,t)$ and $I(x,t)$. Note that the wave speed is $v_p = 1/\sqrt{LC}$ and the character impedance of the transmission line is $Z_T = \sqrt{L/C}$.

The transmission line can also be treated using Lagrangian dynamics. The transmission line Lagrangian and Hamiltonian dynamics follows the discussion in Ref. [206]. By using the node flux as the generalized coordinates, the Lagrangian of the transmission line segment is

$$d\mathfrak{L} = \frac{Cdx}{2}\dot{\Phi}^2(x+dx) - \frac{1}{2Ldx}\left(\Phi(x+dx) - \Phi(x)\right)^2 \tag{5.61}$$

In the continuous limit where $dx \to 0$, the Lagrangian density is $\mathcal{L} = \frac{d\mathfrak{L}}{dx}$. The transmission line Lagrangian is

$$\mathcal{L} = \frac{C}{2}\dot{\Phi}^2(x) - \frac{1}{2L}\left[\partial_x \Phi(x)\right]^2 \tag{5.62a}$$

$$\mathfrak{L} = \int_0^l \mathcal{L} dx \tag{5.62b}$$

where l is the total length of the transmission line.

The canonical momentum with respect to the flux along the transmission line is

$$\pi(x) = \frac{\partial \mathfrak{L}}{\partial \dot{\Phi}(x)} = C\dot{\Phi}(x) = q(x) \tag{5.63}$$

which is the charge density along the transmission line. With Legendre transformation, the transmission line Hamiltonian using the generalized flux and the charge density along the transmission line becomes

$$H = \int_0^l \mathcal{H}(x,t) dx \tag{5.64a}$$

$$\mathcal{H} = \pi(x,t)\dot{\Phi}(x,t) - \mathcal{L}(x,t) = \frac{q^2(x,t)}{2C} + \frac{1}{2L}\left[\partial_x \Phi(x,t)\right]^2 \tag{5.64b}$$

The equation of motion can be constructed using the Lagrange equation as

$$\frac{d}{dt}\left(\frac{\partial \mathcal{L}}{\partial \dot{\Phi}}\right) + \frac{d}{dx}\left(\frac{\partial \mathcal{L}}{\partial(\partial_x \Phi)}\right) - \frac{\partial \mathcal{L}}{\partial x} = 0. \tag{5.65}$$

With the Lagrangian density in Eq. (5.62), the EOM using the generalized node flux $\Phi(x,t)$ is

$$C\ddot{\Phi}(x) - \frac{1}{L}\partial_x^2 \Phi(x) = 0 \tag{5.66}$$

Notice that the EOM of the transmission line using the node general flux is still a wave equation. The wave speed is $v_p = 1/\sqrt{LC}$. Similarly, the EOM can also be derived using Hamiltonian dynamics as

$$\dot{\Phi}(x) = \frac{\delta \mathcal{H}}{\delta q} = \frac{q(x)}{C} \tag{5.67a}$$

$$\dot{q}(x) = -\frac{\delta \mathcal{H}}{\delta \Phi} = -\left(\frac{\partial}{\partial \Phi} - \partial_x \frac{\partial}{\partial(\partial_x \Phi)}\right)\mathcal{H} = \frac{1}{L}\partial_x^2 \Phi(x). \tag{5.67b}$$

To use the transmission line as a bath, we assume that the transmission line is infinitely long. However, for ease of discussion, we will follow the discussion of the box quantization of the free space electromagnetic wave, i.e., we assume the transmission line has a finite size l and quantize the field of the transmission line, then take the limit $l \to \infty$ for the infinite transmission line.

5.4.3.1 Transmission line eigenmodes with periodic boundary conditions We assume that the left end of the transmission line is at $x = 0$ and the right end is $x = l$. The eigenmode solution of the transmission line with length l depends on the boundary conditions on both ends. In our discussion, we at first assume the transmission line has periodic boundary condition on both ends of the transmission line. The eigenmodes of the transmission line can be assumed to have the form of propagating waves

$$\Phi(x,t) = \sum_k \Phi_k(t) = \sum_k \phi(k,t) e^{ikx}, \tag{5.68}$$

where k is the wave-vector, and the EOM [Eq. (5.66)] is

$$\ddot{\phi}(k,t) + v_p^2 k^2 \phi(k,t) = 0. \tag{5.69}$$

Solving the above equation, the dispersion relation is

$$\omega_k = v_p |k| \tag{5.70}$$

and ω_k is the frequency of the k mode of the transmission line. We note that the frequency is always non-negative while k can be either positive or negative. The right propagating modes are the modes with positive k, while left propagating modes are the modes with negative k.

Because the generalized flux should be real valued, the normal modes should satisfy

$$\phi(k) = \phi^*(-k). \tag{5.71}$$

Further, note that on the length l transmission line with periodic boundary conditions, the wave vector can be chosen as $k = 2\pi n/l$, where n is an integer. The orthogonality relation of the normal modes is

$$\frac{1}{l}\int_0^l \Phi_{k_1}(x)\Phi_{k_2}(x)dx = \phi(k_1)\phi(-k_1)\delta(k_1,-k_2) = |\phi(k_1)|^2\delta(k_1,-k_2) \tag{5.72}$$

5.4.3.2 The effect of open boundary condition For a more realistic consideration, we consider the case in which both ends of the transmission line are open. When the transmission line is open, there is no current flowing through (or out of) both ends of the transmission line. In telegrapher's equation Eq. (5.58a), if we perform the integral with respect to time and use the definition of the generalized flux $\Phi(x,t) = \int^t V(s,\tau)d\tau$,

$$\partial_x\Phi(x,t) = -L\, I(x,t). \tag{5.73}$$

If we use the sine and cosine functions as the normal mode basis for the modes,

$$\Phi(x,t) = \sum_k \left(\alpha_k(t)\cos(kx) + \beta_k(t)\sin(kx)\right), \tag{5.74}$$

and applying the boundary condition for the current at $x = 0$, i.e., $I(0,t) = 0$,

$$\partial_x\Phi(x,t)|_{x=0} = \sum_k (k\beta_k)e^{-i\omega_k t} = 0 \tag{5.75}$$

we obtain $\beta_k = 0$, $\forall k$. Therefore, the normal modes can only be cosines. While on the other boundary $x = l$, similarly, we have

$$\sum_k [-k\alpha_k \sin(kl)] = 0, \tag{5.76}$$

which results $kl = \pi n$, where n is an integer. So the normal modes of the transmission line with open boundary conditions are

$$\Phi(x,t) = \sum_k \Phi_k(x,t) = \sum_k \phi_{\mathrm{obc}}(k,t)\cos(kx) \tag{5.77}$$

Because the normal modes $\Phi_k(x)$ should be real, $\phi_{\text{obc}}(k)$ are real. Compared with the normal modes expression in periodic boundary condition, we effectively assumes $\phi_k = \phi_{-k}$ for expression in Eq. (5.68) to make the normal mode profiles exactly match the Eq. (5.77). So if the realistic transmission line is considered to have open-ends, the periodic boundary condition on the transmission line is still somewhat applicable. We just need to force $\phi(k) = \phi(-k)$ to get open boundary condition solutions[1]. Therefore, in the following we will only focus on the transmission line with periodic boundary condition.

5.4.4 Transmission line field 2nd quantization

Here we still consider the periodic boundary condition for the transmission line, in which the general flux field can be expressed in k-space normal modes as Eq. (5.68). Similarly, the canonical momentum density function can also be written as

$$q(x,t) = \sum_k q(k,t) e^{ikx} \tag{5.78}$$

The transmission line Hamiltonian can be expressed as

$$\begin{aligned} H &= \int_0^l dx \sum_{k,k'=-\infty}^{+\infty} \left[\frac{1}{2C} q(k,t) q(k',t) - \frac{k\,k'}{2L} \phi(k,t) \phi(k',t) \right] e^{i(k+k')x}, \\ &= \sum_{k=-\infty}^{+\infty} l \left[\frac{1}{2C} q(k,t) q(-k,t) + \frac{k^2}{2L} \phi(k,t) \phi(-k,t) \right] \end{aligned} \tag{5.79}$$

where we use the orthogonal relation

$$\int_0^l e^{i(k+k')x} dx = l\delta(k,-k'), \quad \{k,k'\} = \frac{2\pi}{l}\{n,n'\} \tag{5.80}$$

where n and n' are integers.

With the help of the relation

$$\sum_{k=-\infty}^{+\infty} \{q(-k,t)\phi(k,t) - q(k,t)\phi(-k,t)\} = 0, \tag{5.81}$$

[1]Note that the k values differs by a factor of 2 in periodic boundary condition with the open boundary condition case. When treating the open boundary conditions using the result of the periodic boundary condition results, we have to be careful about these factors. However, as we are coupling to the phase (and not the current) the analytical parametric dependence is identical.

and use the fact that the fields are real, i.e., $\phi(k,t) = \phi(-k,t)$ and $q(k,t) = q(-k,t)$, the Hamiltonian of the transmission line can be written as

$$H = \sum_{k=-\infty}^{+\infty} A^*(k,t)A(k,t) \tag{5.82}$$

where the auxiliary field $A(k,t)$ is defined as

$$A(k,t) = \sqrt{l}\left[\sqrt{\frac{1}{2C}}q(k,t) + i\sqrt{\frac{k^2}{2L}}\phi(k,t)\right]. \tag{5.83}$$

Apply the inverse transformation of Eqs. (5.68) and (5.78), the auxiliary field can be expressed as

$$A(k,t) = \frac{1}{\sqrt{l}}\int_0^l \left[\frac{1}{\sqrt{2C}}q(x,t) + i\sqrt{\frac{k^2}{2L}}\phi(x,t)\right] e^{-ikx}dx. \tag{5.84}$$

The Poisson bracket of the fields satisfies

$$[q(x), q(x')]_{\mathrm{PB}} = 0 = [\phi(x), \phi(x')]_{\mathrm{PB}} \tag{5.85a}$$

$$[\phi(x), q(x')]_{\mathrm{PB}} = \delta(x - x'). \tag{5.85b}$$

The Poisson bracket for the auxiliary field is

$$[A^*(k),\, A(k)]_{\mathrm{PB}} = -i\frac{1}{2\sqrt{CL}}\left(|k| + |k'|\right)\delta(k,k') = -i\omega_k\delta(k,k'), \tag{5.86}$$

where we use the speed of the wave in the transmission line $v_p = 1/\sqrt{CL}$ and the dispersion relation $\omega_k = v_p|k|$. Then we can normalize the field by define

$$\alpha(k,t) = \frac{1}{\sqrt{\omega_k}}A(k,t), \tag{5.87}$$

where Poisson bracket for the new field $\alpha(k,t)$ is

$$[\alpha^*(k), \alpha(k')]_{\mathrm{PB}} = -i\delta(k,k'). \tag{5.88}$$

With the canonical quantization process, we promote $\alpha(k,t)$ as operator $\sqrt{\hbar}\hat{a}_k(t)$, and promote the Poisson bracket [Eq. (5.88)] to commutation relation

$$[\hat{a}_k^\dagger(t), \hat{a}_{k'}(t)] = \delta(k,k') \tag{5.89}$$

The quantized Hamiltonian for the transmission line is

$$H = \sum_k \frac{\hbar\omega_k}{2}\left(\hat{a}_k^\dagger(t)\hat{a}_k(t) + \hat{a}_k(t)\hat{a}_k^\dagger(t)\right). \tag{5.90}$$

Note that the time-evolution of the operators $a_k(t)$ is given by the Heisenberg equation

$$\partial_t \hat{a}_k(t) = \frac{1}{i\hbar}[\hat{a}_k(t), H(t)] = -i\omega_k \hat{a}_k(t) \tag{5.91}$$

if we define $\hat{a}_k = \hat{a}_k(t=0)$, the time-evolution of operator $\hat{a}_k(t) = \hat{a}_k e^{-i\omega_k t}$. The quantized field for field $\phi(k)$ and $q(k)$ is given by

$$\hat{q}(k) = \sqrt{\frac{\hbar\omega_k C}{2l}}\left(\hat{a}_k + \hat{a}_{-k}^\dagger\right) \tag{5.92a}$$

$$\hat{\phi}(k) = -i\sqrt{\frac{\hbar Z v_p}{2l\omega_k}}\left(\hat{a}_k - \hat{a}_{-k}^\dagger\right) \tag{5.92b}$$

where $v_p = 1/\sqrt{LC}$ is the wave speed along the transmission line, $Z = \sqrt{L/C}$ is the characteristic impedance of the transmission line. Similarly, the fields $\phi(x)$ and $q(x)$ are

$$\hat{q}(x) = \sum_{k=-\infty}^{+\infty} \sqrt{\frac{\hbar\omega_k C}{2l}}\left(\hat{a}_k e^{ikx} + \hat{a}_k^\dagger e^{-ikx}\right) \tag{5.93a}$$

$$\hat{\phi}(x) = -i\sum_{k=-\infty}^{+\infty} \sqrt{\frac{\hbar Z v_p}{2l\omega_k}}\left(\hat{a}_k e^{ikx} - \hat{a}_k^\dagger e^{-ikx}\right) \tag{5.93b}$$

where in the second term of the both equations, we redefine the wave-vector k to be $-k$.

5.4.5 Quantized coupling Hamiltonian

In the discussion in Section 5.4.1, the classical coupling Hamiltonian can be written as

$$H = -E_{\mathrm{J}} \cos\left(\varphi_c - \varphi_T\right) + \frac{\phi_0^2}{2L}\left(\varphi_c - \varphi_T\right)^2 + E'_{\mathrm{J}} \cos(\varphi_c) + E''_{\mathrm{J}} \cos(\varphi_T), \tag{5.94}$$

where the coupling Josephson junction energy E_{J}, the coupling linear inductance L, the π-junction Josephson energy E'_{J} and the node phases φ_c and φ_T are labeled in Fig. 38. The π-junctions are used to correct the dispersion given by the nonlinear coupling between the cavity and the transmission line. Here we will ignore these two π junctions at the beginning of the discussion. Further, we define a dimensionless parameter $r = \frac{\phi_0^2}{2L}/E_{\mathrm{J}}$, such that the coupling Hamiltonian without the π junctions is

$$H/E_{\mathrm{J}} = -\cos\left(\varphi_c - \varphi_T\right) + r\left(\varphi_c - \varphi_T\right)^2. \tag{5.95}$$

To consider the quantized nonlinear coupling Hamiltonian, we can replace the node phase on cavity side, φ_c, by the dimenionless LC resonator flux in Eq. (5.52b) and the node phase on transmission line site φ_T can be substitute by the dimenioness field operator at $x = 0$ in Eq. (5.93b)[2],

$$\hat{\varphi}_c = \tilde{\varphi}_c\left(\hat{a} + \hat{a}^\dagger\right) \tag{5.96a}$$

$$\hat{\varphi}_T = -i\sum_k \tilde{\varphi}_T(k)\left(\hat{b}_k - \hat{b}_k^\dagger\right) \tag{5.96b}$$

where we use $\hat{a}$, $\hat{b}$ for operators in the LC resonator and the transmission line, respectively. The dimensionless parameters $\tilde{\varphi}_c$ and $\tilde{\varphi}_T(k)$ are defined as

$$\tilde{\varphi}_c = \frac{1}{\phi_0}\sqrt{\frac{\hbar Z_c}{2}}, \qquad \tilde{\varphi}_T(k) = \frac{1}{\phi_0}\sqrt{\frac{\hbar Z_T}{2}}\sqrt{\frac{v_p}{l\omega_k}} \tag{5.97}$$

where Z_c is the impedance of the LC resonantor, Z_T is the characteristic impedance of the transmission line, v_p is the wave speed along the transmission line, l is the length of the transmission line, ω_k is the frequency of the k mode of the transmission line.

[2]We assume the coupling circuit connects to one end of the transmission line which is $x = 0$.

Let us estimate the the ratio of the parameters $\tilde{\varphi}_c$ and $\tilde{\varphi}_T$

$$\frac{\tilde{\varphi}_T}{\tilde{\varphi}_c} = \sqrt{\frac{Z_T}{Z_c}}\sqrt{\frac{v_p}{l\omega_k}}. \tag{5.98}$$

The impedance of the cavity and the transmission line are of the same order, however, the second term is ~ 0.080 for a 1 m long transmission line with microwave speed v_p approximated by the speed of light and the mode frequency at 7.5 GHz. Because the typical bandwidth for the system-bath coupling of quantum optics systems is only a small fraction of the optical frequency (in this case 7.5 GHz), so with the above parameters, the parameter $\tilde{\varphi}_T(k)$ can be treated as a small parameter compared with $\tilde{\varphi}_c$ for all the modes in the the bandwidth of the system-bath coupling. Therefore, we may expanded the system-bath coupling Hamiltonian ($\cos(\Delta\hat{\varphi})$ term) in the order of bath operators.

The phase difference across the coupling circuit after second quantization is

$$\Delta\hat{\varphi} \equiv \hat{\varphi}_c - \hat{\varphi}_T = \tilde{\varphi}_c\left(\hat{a} + \hat{a}^\dagger\right) + i\sum_k \tilde{\varphi}_T(k)\left(\hat{b}_k - \hat{b}_k^\dagger\right). \tag{5.99}$$

The cavity-transmission line coupling Hamiltonian

$$H/E_\mathrm{J} = -\cos\left(\Delta\hat{\varphi}\right) + r\left(\Delta\hat{\varphi}\right)^2, \tag{5.100}$$

and can be expanded in orders of transmission line field operators. Notice that the nonlinear coupling between the transmission line and the cavity field is provided by the Josephson junction (first term). The nonlinear coupling can be expanded using the transformation in Eq. (5.10) as

$$\cos\left(\Delta\hat{\varphi}\right) = \frac{1}{2}\left(e^{i\hat{\varphi}_c - i\hat{\varphi}_T} + e^{-i\hat{\varphi}_c + i\hat{\varphi}_T}\right) = \frac{1}{2}\left(e^{i\hat{\varphi}_c}e^{-i\hat{\varphi}_T} + e^{-i\hat{\varphi}_c}e^{i\hat{\varphi}_T}\right), \tag{5.101}$$

where in the second term we use the fact that the cavity operators commute with the transmission line operators. Further, because the transmission line operators satisfy

$$[\hat{b}_k, \hat{b}_{k'}^\dagger] = \delta(k, k'), \tag{5.102}$$

the exponential of the field operators can be simplified as

$$e^{i\hat{\varphi}_T} = \prod_k e^{\tilde{\varphi}_T(k)\left(\hat{b}_k - \hat{b}_k^\dagger\right)},\ e^{-i\hat{\varphi}_T} = \prod_k e^{-\tilde{\varphi}_T(k)\left(\hat{b}_k - \hat{b}_k^\dagger\right)} \tag{5.103}$$

The nonlinear coupling given by Eq. (5.101) can be expanded as the normal ordered terms in the order of transmission line operators using Eq. (5.15),

$$e^{i\hat{\varphi}_c} = e^{-\tilde{\varphi}_c^2/2} e^{i\tilde{\varphi}_c \hat{a}^\dagger} e^{i\tilde{\varphi}_c \hat{a}}, \tag{5.104a}$$

$$e^{-i\hat{\varphi}_c} = e^{-\tilde{\varphi}_c^2/2} e^{-i\tilde{\varphi}_c \hat{a}^\dagger} e^{-i\tilde{\varphi}_c \hat{a}}, \tag{5.104b}$$

$$e^{\hat{\varphi}_T(k)} = e^{-\tilde{\varphi}_T^2(k)/2} e^{-\tilde{\varphi}_T \hat{b}_k^\dagger} e^{\tilde{\varphi}_T \hat{b}_k}, \tag{5.104c}$$

$$e^{-\hat{\varphi}_T(k)} = e^{-\tilde{\varphi}_T^2(k)/2} e^{\tilde{\varphi}_T \hat{b}_k^\dagger} e^{-\tilde{\varphi}_T \hat{b}_k}. \tag{5.104d}$$

Expanding each term with operators using the expansion of exponential function we get

$$e^{\pm i\hat{\varphi}_c} = e^{-\tilde{\varphi}_c^2/2} \sum_{n,m=0}^{\infty} \frac{(\pm i\tilde{\varphi}_c)^{n+m}}{n! \cdot m!} \left(\hat{a}^\dagger\right)^n \hat{a}^m \tag{5.105a}$$

$$e^{\pm\hat{\varphi}_T(k)} = e^{-\tilde{\varphi}_T^2(k)/2} \sum_{n,m=0}^{\infty} (\mp 1)^n (\pm 1)^m \frac{\tilde{\varphi}_T^{n+m}(k)}{n! \cdot m!} \left(\hat{b}_k^\dagger\right)^n \hat{b}_k^m. \tag{5.105b}$$

With the expansion of the operators given in Eqs. (5.101), (5.103), (5.104) and (5.105), we can expand the nonlinear coupling Hamiltonian in the order of transmission line field operators. The expansion of Eq. (5.100) to third order in field operators yields

$$H/E_{\mathrm{J}} = h_{\mathrm{sys}} + h_{\mathrm{tl}} + h_1 + h_2 + h_3 + ... \tag{5.106}$$

where h_{sys} and h_{tl} are the dimensionless Hamiltonian acting solely on the cavity field and the transmission line, respectively. The cavity-transmission line coupling is expanded in orders of the transmission line field operators and the first, second and third order terms are labeled as h_1, h_2 and h_3.

$$h_{\mathrm{sys}} = -\left(\prod_k e^{-\tilde{\varphi}_T^2(k)/2}\right) \frac{1}{2}\left(e^{i\hat{\varphi}_c} + e^{-i\hat{\varphi}_c}\right) + r\hat{\varphi}_c^2 \equiv -\mathcal{C}_{\mathrm{TL}} \cos\left(\hat{\varphi}_c\right) + r\hat{\varphi}_c^2, \tag{5.107a}$$

$$h_{\mathrm{TL}} = -e^{-\tilde{\varphi}_c^2/2} \frac{1}{2}\left(e^{i\hat{\varphi}_T} + e^{-i\hat{\varphi}_T}\right) + r\hat{\varphi}_T^2 \equiv -\mathcal{C}_c \cos\left(\hat{\varphi}_T\right) + r\hat{\varphi}_T^2, \tag{5.107b}$$

where $\mathcal{C}_{\mathrm{TL}}$ and $\mathcal{C}_c$ are two constants. Notice that h_{sys} and h_{tl}, induced by the coupling circuit, contributes new nonlinearities to the cavity and the transmission line. These nonlinearities, especially the nonlinearity of the cavity field, will degrade the laser performance by adding shifting the cavity frequency as the number of photons in the cavity increases. To compensate

the dispersion of the cavity field and the transmission line, we include two π junctions as shown in Fig. 38, in which the Josephson energies satisfy

$$E'_{\mathrm{J}} = \mathcal{C}_{\mathrm{TL}} E_{\mathrm{J}}, \quad E''_{\mathrm{J}} = \mathcal{C}_{\mathrm{c}} E_{\mathrm{J}}. \tag{5.108}$$

These π-junctions cancel out the non-linear contributions of h_{sys} and h_{tl} that lead to dephasing. Consequently, in the following discussion we focus on the remaining terms, which are the cavity-transmission line coupling terms h_1, h_2 and h_3.

Next, we move on to h_1, h_2, and h_3 terms of Eq. (5.106)

$$h_1 = -\frac{\mathcal{C}_{\mathrm{TL}}}{2} \sum_k \tilde{\varphi}_T(k) \left\{ (b_k^\dagger - b_k) e^{i\hat{\varphi}_c} + (b_k - b_k^\dagger) e^{-i\hat{\varphi}_c} \right\} \tag{5.109a}$$

$$= -i\mathcal{C}_{\mathrm{TL}} \sum_k \tilde{\varphi}_T(k) (b_k^\dagger - b_k) \sin(\hat{\varphi}_c) + 2ir\hat{\varphi}_c \sum_k \tilde{\varphi}_T(k) \left(b_k - b_k^\dagger \right),$$

$$h_2 = -\mathcal{C}_{\mathrm{TL}} \left\{ \sum_k \frac{\tilde{\varphi}_T^2(k)}{2} \left(b_k^2 + \left(b_k^\dagger \right)^2 - b_k^\dagger b_k \right) \right. \tag{5.109b}$$

$$\left. + {\sum_{k,q}}' \tilde{\varphi}_T(k) \tilde{\varphi}_T(q) \left(b_k b_q + b_k^\dagger b_q^\dagger - 2 b_k^\dagger b_q \right) \right\} \left[\cos(\hat{\varphi}_c) - 1 \right],$$

$$h_3 = -i\mathcal{C}_{\mathrm{TL}} \left\{ \sum_k \frac{\tilde{\varphi}_T^3(k)}{6} \left[\left(b_k^\dagger \right)^3 - 3 \left(b_k^\dagger \right)^2 b_k + 3 b_k^\dagger b_k^2 - b_k^3 \right] \right. \tag{5.109c}$$

$$+ {\sum_{k,q}}' \frac{\tilde{\varphi}_T^2(k) \tilde{\varphi}_T(q)}{2} \left[\left(b_k^\dagger \right)^2 + b_k^2 - 2 b_k^\dagger b_k \right] \left(b_q^\dagger - b_q \right)$$

$$\left. + {\sum_{k,q,p}}' \tilde{\varphi}_T(k) \tilde{\varphi}_T(q) \tilde{\varphi}_T(p) \left(b_k^\dagger - b_k \right) \left(b_q^\dagger - b_q \right) \left(b_p^\dagger - b_p \right) \right\} \sin(\hat{\varphi}_c),$$

where the summation $\sum_k$ is from $-\infty$ to $+\infty$, the summations with prime ${\sum}'_{k,q}$ and ${\sum}'_{k,q,p}$ omit the terms in which any of the summation indices are equal. The phase operator $\hat{\varphi}_c$ is given in Eq. (5.96a) and the dimensionless constant for transmission line node phase quantization $\tilde{\varphi}_T(k)$ is given in Eq. (5.97). Similarly, the higher order terms can also be expanded and calculated.

5.4.6 Master equation for the nonlinear loss of the cavity

Here we treat the cavity field as our "system" and the transmission line field as the "bath". In this section, we focus on the nonlinear coupling introduced by the coupling circuit given by Fig. 38 and trace out the dynamics of the bath degrees of freedom (DOFs) and derive the master equation for the cavity field.

First, we want to point out that throughout the derivation we have assumed that the coupling strength is weak compared to the system dynamics (which is given by the optical frequency of the cavity field, typically in the GHz range for superconducting circuits). We have also assumed that the number of the photons in the cavity is not so large as to make the effective coupling strength exceed the optical frequency of the cavity (due to Boson enhancement). In this regime, the rotating wave approximation applies and we can remove the terms that do not conserves the excitation number in the coupling Hamiltonian. Note that the transmission line has an infinite number of k-modes, which behave as a bath that is much larger than the system itself. We, therefore, make the usual assumption that the system-bath coupling strength and the density of states in the bandwidth of system-bath coupling is smooth. The coupling bandwidth (noted as θ) is assumed to be larger than the frequency scale for dynamics of the system-bath coupling, but smaller than the frequency scale for dynamics of the system itself (optical frequency). This hierarchy of frequency scales allows us to apply the Born-Markov approximation, i.e., that the bath has no memory.

Next, using the rotating wave approximation and Born-Markov approximation, we will go through the derivation of the master equation by tracing out the bath DOFs (similar to the derivation of master equation in Chapter 8 of Ref. [121]). We will proceed from h_1 to h_2 and h_3, identifying the quantum jump operators for the cavity field induced by the cavity-bath coupling.

The general procedures for the following derivation is listed below:

1. From the target order nonlinear coupling Hamiltonian terms, expand the Hamiltonian into a polynomial function of operators.

2. Apply the rotating wave approximation to the system-bath coupling Hamiltonian by dropping the terms that do not conserve the excitation number.

3. Expand the equation of motion of the system-bath density operator to second order in coupling Hamiltonian. Apply Born-Markov approximation and trace out the bath degrees of freedoms. Because the operational temperature of the superconducting circuit devices is typically in 10 mK range, and the frequency of the laser system is in the range of 5 to 10 GHz, the thermal excitation is negligible, we will treat the transmission line as a vacuum bath for the laser cavity.

5.4.6.1 Jump operators for the cavity induced by coupling to the transmission line: first order terms The first order coupling Hamiltonian terms is given by Eq. (5.109a). We begin by expanding the sine function of the cavity field operators $\sin(\hat{\varphi}_c)$

$$\begin{aligned}\sin(\hat{\varphi}_c) &= \frac{1}{2i}\left(e^{i\hat{\varphi}_c} - e^{-i\hat{\varphi}_c}\right) = \frac{e^{-\tilde{\varphi}_c^2/2}}{2i}\left(e^{i\tilde{\varphi}_c\hat{a}^\dagger}e^{i\tilde{\varphi}_c\hat{a}} - e^{-i\tilde{\varphi}_c\hat{a}^\dagger}e^{-i\tilde{\varphi}_c\hat{a}}\right) \\ &= e^{-\tilde{\varphi}_c^2/2}\left[\sum_{m,n=0}^{+\infty}\frac{1-(-1)^{m+n}}{2i}\frac{(i\tilde{\varphi}_c)^{m+n}}{m!\cdot n!}\left(a^\dagger\right)^n a^m\right]\end{aligned} \tag{5.110}$$

Using this expansion and applying the rotating wave approximation to h_1 of Eq. (5.109a), and restoring dimensions of energy, we obtain

$$\begin{aligned}H_1 = -iE_{\mathrm{J}}\mathcal{C}_{\mathrm{TL}}e^{-\tilde{\varphi}_c^2/2}\sum_k\sum_{n=0}^{\infty}(-1)^n\frac{\tilde{\varphi}_T(k)\tilde{\varphi}_c^{2n+1}}{n!\cdot(n+1)!}\Big[b_k^\dagger\left(a^\dagger\right)^n a^{n+1} \\ -b_k\left(a^\dagger\right)^{n+1}a^n\Big] + 2irE_{\mathrm{J}}\tilde{\varphi}_c\sum_k\tilde{\varphi}_T(k)\left(a^\dagger b_k - b_k^\dagger a\right).\end{aligned} \tag{5.111}$$

Defining the nonlinear operator for the cavity field

$$\hat{A}_1 = \mathcal{C}_{\mathrm{TL}}e^{-\tilde{\varphi}_c^2/2}\sum_{n=0}^{\infty}(-1)^n\frac{\tilde{\varphi}_c^{2n+1}}{n!\cdot(n+1)!}\left(a^\dagger\right)^n a^{n+1} + 2r\tilde{\varphi}_c a, \tag{5.112}$$

and the coupling strength

$$\kappa_k = E_{\mathrm{J}}\tilde{\varphi}_T(k)/\hbar, \tag{5.113}$$

the first order Hamiltonian can be re-written as

$$H_1 = -i\sum_k\hbar\kappa_k\left(b_k^\dagger\hat{A} - b_k\hat{A}^\dagger\right). \tag{5.114}$$

Applying the Born-Markov approximation, similar to the discussion in Section 2.3, we obtain the master equation for the first order term

$$\partial_t \rho(t) = -\frac{i}{\hbar}[H_{\rm sys}, \rho(t)] - \frac{\Gamma_1}{2}\left(\hat{A}^\dagger \hat{A}\rho + \rho \hat{A}^\dagger \hat{A} - 2\hat{A}\rho(t)\hat{A}^\dagger\right) \tag{5.115}$$

where

$$\Gamma_1 = \frac{E_{\rm J}^2}{\hbar^2}\left(\frac{\hbar Z_T}{2\phi_0^2}\right)\frac{1}{\omega_c}. \tag{5.116}$$

Before we further examine if the dissipator $\mathcal{D}[\hat{\mathcal{A}}]$, i.e., the last bracket of the master equation, gives the desired nonlinear loss to the cavity field to suppress the linewidth of the cavity field, a few remarks about estimating the constants contained in the nonlinear operator expression is useful.

First, we want to estimate $\mathcal{C}_{\rm TL}$, which is given by Eq. (5.107). In the quantum optics regime, we assume that the transmission line has a large length, where we can assume $l \to \infty$. In this limit, we can approximate the summation of k by the integral of k as

$$\sum_k \to \frac{1}{2\pi}\int dk. \tag{5.117}$$

Further, in quantum optics regime, especially for the system that Born-Markov approximation applies, the cavity frequency is the dominant frequency to the coupling bandwidth θ and the system-bath coupling strength. Here we explicitly assume that the cutoff frequencies for the system-bath coupling are $\omega_L = \omega_c - \theta/2$ and $\omega_H = \omega_c + \theta/2$, while the corresponding cutoff wave-vectors are k_L and k_H[3]. The constant $\mathcal{C}_{\rm TL}$ can be calculated as

$$\begin{aligned}
\mathcal{C}_{\rm TL} &= \prod_k e^{-\frac{\tilde{\varphi}_T(k)}{2}} = \exp\left[-\frac{1}{2}\sum_{k=k_L}^{k_H}\left(\frac{1}{\phi_0^2}\frac{\hbar Z_T}{2}\right)\frac{1}{kl}\right] \\
&\to \exp\left[-2\frac{1}{4\pi}\left(\frac{1}{\phi_0^2}\frac{\hbar Z_T}{2}\right)\int_{k_L}^{k_H}\frac{1}{k}dk\right] \\
&= \exp\left(-\frac{1}{\phi_0^2}\frac{\hbar Z_T}{4\pi}\right)\frac{\omega_H}{\omega_L}.
\end{aligned} \tag{5.118}$$

[3]Here there will be another factor of 2, which is because of the coupling to the left-propagating modes and the right-propagating modes.

Next, we adopt the assumption that $\theta/\omega_c \ll 1$, so the ratio ω_H/ω_L can be expanded in the order of θ/ω_c, and $\mathcal{C}_{\rm TL}$,

$$\mathcal{C}_{\rm TL} = \exp\left(-\frac{1}{\phi_0^2}\frac{\hbar Z_T}{4\pi}\right)\left[1+\frac{\theta}{\omega_c}+\frac{\theta^2}{2\omega_c^2}+o\left(\frac{\theta^3}{\omega_c^3}\right)\right]. \tag{5.119}$$

If we choose the characteristic impedance of the transmission line as $Z_T = 50\ \Omega$. the lowest order approximation of the parameter $\mathcal{C}_{\rm TL}$ is 0.9961.

The constant $\mathcal{C}_{\rm c}$ can also be directly calculated with the given circuit parameters

$$\mathcal{C}_c \equiv \exp\left[-\frac{1}{2}\frac{1}{\phi_0^2}\frac{\hbar Z_c}{2}\right]. \tag{5.120}$$

This constant, if we assume the cavity impedance is 50 Ω, is 0.9880.

To further examine the nonlinear property of the cavity operator $\hat{A}$, we assume the transmission line has the characteristic impedance $Z_T = 50\ \Omega$, cavity field (LC resonator) has impedance $Z_c = 50\ \Omega$. The ratio parameter $r = 0.4$. The parameters are summarized in Table 5. We plot the matrix element of nonlinear $\hat{A}$ operator, $\langle n|\hat{A}|n+1\rangle$, as a function of cavity state photon number n in Fig. 40. We observe that there is a sweet spot, at $n \sim 100$, for which $langlen|\hat{A}|n+1\rangle$ is almost independent of the photon number. In this sweet spot, the operator $\hat{A}$ approximates the Susskind operator $\hat{e}$. As we demonstrate in Section 5.3.3, this property of $\hat{A}$ decreases the laser linewidth much in the same way that $\hat{e}$ did the same in Section 5.3.3.

Table 5: Chosen circuit parameters and the derived constants in the nonlinear system jump operator $\hat{A}$ in Eq. (5.112) for Fig. 40.

Parameters	Z_T	Z_c	r	$\tilde{\varphi}_c$	$\mathcal{C}_c$	$\mathcal{C}_{\rm TL}$
Value	50 Ω	50 Ω	0.4	0.1560	0.9880	0.9961

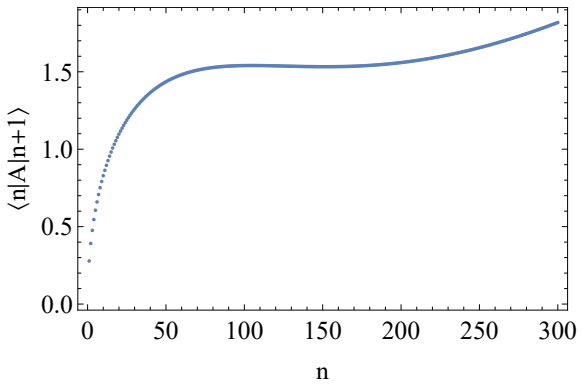

Figure 40: Transition amplitude of nonlinear cavity operator $\hat{A}$ given in Eq. (5.112) with parameters given in Table 5. We notice the flatten region in the transition amplitude $\langle n|\hat{A}|n+1\rangle$ as a function of the state photon number n.

5.4.6.2 Second order terms The second order term in the expansion of the coupling Hamiltonian is given by Eq. (5.109b). Under the rotating wave approximation (and restoring dimensions), the second order term is

$$\begin{aligned}
&H_2/(-E_{\mathrm{J}}\mathcal{C}_{\mathrm{TL}}\mathcal{C}_c) = \\
&-\left(\sum_k \frac{\tilde{\varphi}_T^2(k)}{2}\left(b_k^\dagger\right)^2 + \sum_{k,q}{}' \tilde{\varphi}_T(k)\tilde{\varphi}_T(q) b_k^\dagger b_q^\dagger\right)\sum_n \frac{(-1)^n\tilde{\varphi}_c^{2n+2}}{n!\cdot(n+2)!}\left(a^\dagger\right)^n a^{n+2} \\
&-\left(\sum_k \frac{\tilde{\varphi}_T^2(k)}{2} b_k^2 + \sum_{k,q}{}' \tilde{\varphi}_T(k)\tilde{\varphi}_T(q) b_k b_q\right)\sum_n \frac{(-1)^n\tilde{\varphi}_c^{2n+2}}{n!\cdot(n+2)!}\left(a^\dagger\right)^{n+2} a^n \\
&-\left(\sum_k \tilde{\varphi}_T^2(k) b_k^\dagger b_k + \sum_{k,q}{}' 2\tilde{\varphi}_T(k)\tilde{\varphi}_T(q) b_k^\dagger b_q\right)\sum_n \frac{(-1)^n\tilde{\varphi}_c^{2n}}{(n!)^2}\left(a^\dagger a\right)^n .
\end{aligned} \tag{5.121}$$

where the summation $\sum'$ does not contains the terms that have the same indices.

Suppose the density operator of the cavity is given by $\rho(t)$ and the transmission line is assumed to be a vacuum bath. the master equation given by the nonlinear coupling Hamiltonian H_2 in Eq. (5.121) is

$$\partial_t\rho(t) = -\frac{i}{\hbar}\mathrm{Tr}_B[H_2(t), R(t_0)] - \frac{1}{\hbar^2}\mathrm{Tr}_B\int_{t_0}^t [H_2(t),[H_2(\tau),R(\tau)]]\,d\tau \tag{5.122}$$

where R is the density operator for the system (cavity) and the bath (transmission line), which can be approximated by $R(t) \sim \rho(t) \otimes \rho_B$ and $\rho_B = |\text{vac}\rangle\langle\text{vac}|$ where $|\text{vac}\rangle$ is the vacuum state of the bath (transmission line). The partial trace of the bath DOFs is

$$\text{Tr}_B\{\cdot\cdot\} = \sum_{\{n_{k_1}, n_{k_2}, \cdots\}} \langle n_{k_1}, n_{k_2}, ...| \cdot\cdot |n_{k_1}, n_{k_2}, ...\rangle \tag{5.123}$$

where $|n_{k_1}, n_{k_2}, ...\rangle = |n_{k_1}\rangle|n_{k_2}\rangle...$, $|n_{k_i}\rangle$ is the n_{k_i}-photon Fock state of the mode $k = k_i$.

Note that because in H_2, all the terms are aligned in the normal order, the first term in Eq. (5.122) is zero. We will focus on the second term of Eq. (5.122). After expansion of the commutation relation, the Eq. (5.122) is

$$\begin{aligned}\dot{\rho} = -\frac{1}{\hbar^2}\text{Tr}_B \int_{t_0}^{t} d\tau \{&H_2(t)H_2(\tau)\rho(\tau)\otimes\rho_B + \rho(\tau)\otimes\rho_B H_2(\tau)H_2(t) \\ &-H_2(t)\rho(\tau)\otimes\rho_B H_2(\tau) - H_2(\tau)\rho(\tau)\otimes\rho_B H_2(t)\}\end{aligned} \tag{5.124}$$

Note that the Hamiltonian H_2 should be considered as the interaction picture Hamiltonian, where the transformation is $U = \exp(H_0)$, where H_0 is

$$H_0 = \hbar\omega_c a^\dagger a + \sum_k \hbar\omega_k \; b_k^\dagger b_k \tag{5.125}$$

Next, we will work term by term in Eq. (5.124) to get master equation for the cavity field.

We start from the term

$$T_3 \equiv \frac{1}{\hbar^2}\int_{t_0}^{t} d\tau \text{Tr}_B \left\{H_2(t)\rho(\tau)\otimes\rho_B H_2(\tau)\right\}. \tag{5.126}$$

As the transmission line is assumed to be a vacuum bath, and the coupling Hamiltonian H_2 is in normal order, the partial trace will kill all the terms that contains lowering operators for the bath DOFs. The Hamiltonian terms that survive in T_3 partial trace is

$$\frac{H_{2,1,(\text{I})}(t)}{(E_\text{J}\mathcal{C}_\text{TL}\mathcal{C}_c)} \equiv h_{2,1,(\text{I})}(t) = \sum_k h_{2,1,kk,(\text{I})} + {\sum_{k,q}}' h_{2,1,kq,(\text{I})} \tag{5.127a}$$

$$h_{2,1,kk,(\text{I})}(t) = \frac{\tilde{\varphi}_T^2(k)}{2}\left(b_k^\dagger\right)^2 \hat{A}_2 e^{i2(\omega_k-\omega_c)t} \tag{5.127b}$$

$$h_{2,1,kq,(\text{I})}(t) = \tilde{\varphi}_T(k)\tilde{\varphi}_T(q) b_k^\dagger b_q^\dagger \hat{A}_2 e^{i(\omega_k+\omega_q-2\omega_c)t}, \tag{5.127c}$$

where the cavity nonlinear operator $\hat{A}_2$ is defined as

$$\hat{A}_2 = \sum_n \frac{(-1)^n \tilde{\varphi}_c^{2n+2}}{n! \cdot (n+2)!} \left(a^\dagger\right)^n a^{n+2} \tag{5.128}$$

and the Eq. (5.126) is

$$\begin{aligned} \frac{T_3\,\hbar^2}{(E_{\rm J}\mathcal{C}_{\rm TL}\mathcal{C}_c)^2} = \int_{t_0}^{t} d\tau \Bigg\{ & \sum_k \langle 2_k | h_{2,1,kk,(\rm I)}(t) | {\rm vac}\rangle \rho \langle {\rm vac} | h^\dagger_{2,1,kk,(\rm I)}(\tau) | 2_k \rangle \\ & + \sum_{k,q}{}' \langle 1_k, 1_q | h_{2,1,kq,(\rm I)}(t) | {\rm vac}\rangle \rho \langle {\rm vac} | h^\dagger_{2,1,kq,(\rm I)}(\tau) | 1_k, 1_q \rangle \Bigg\}, \end{aligned} \tag{5.129}$$

where we apply the bath state orthogonality relations and remove all the zero terms. Further, the term

$$\langle 2_k | h_{2,1,kk,(\rm I)}(t) | {\rm vac}\rangle = \frac{\sqrt{2}\tilde{\varphi}_T^2(k)}{2} \hat{A}_2 e^{i2(\omega_k - \omega_c)t} \tag{5.130a}$$

$$\langle 1_k, 1_q | h_{2,1,kq,(\rm I)}(t) | {\rm vac}\rangle = \tilde{\varphi}_T(k)\tilde{\varphi}_T(q) \hat{A}_2 e^{i(\omega_k + \omega_q - 2\omega_c)t} \tag{5.130b}$$

For the first term, which is involved in the time integral of the first line of Eq. (5.129) (noted as $T_{3,1}$), after apply the Born-Markov approximation, and define $k_c = \omega_c / v_p$ and take Eq. (5.117), the term $T_{3,1}$ is

$$T_{3,1} = (\mathcal{C}_{\rm TL}\mathcal{C}_c)^2 \frac{E_{\rm J}^2}{\hbar^2} \frac{l}{2\pi v_p} \int_{t_0}^{t} d\tau \int_{\omega_L}^{\omega_H} d\omega_k \frac{\tilde{\varphi}_T^4(k)}{2} \hat{A}_2 \rho(\tau) \hat{A}_2^\dagger e^{i2(\omega_k - \omega_c)t} \tag{5.131a}$$

$$= (\mathcal{C}_{\rm TL}\mathcal{C}_c)^2 \frac{1}{8} \left(\frac{\hbar Z_T}{2\phi_0^2}\right) \frac{E_{\rm J}^2}{\hbar^2 \omega_c} \tilde{\varphi}_T^2(k_c) \hat{A}_2 \rho(t) \hat{A}_2^\dagger \tag{5.131b}$$

$$= \Gamma_{2,1} \hat{A}_2 \rho(t) \hat{A}_2^\dagger. \tag{5.131c}$$

Similar to the definition of the nonlienar operator of the cavity field in first order coupling, we can redefine the nonlinear operator for second order as

$$\hat{A}_2' = (\mathcal{C}_{\rm TL}\mathcal{C}_c) \hat{A}_2 \tag{5.132}$$

and then the associated rate is

$$\hat{\Gamma}'_{2,1} = \frac{1}{(\mathcal{C}_{\rm TL}\mathcal{C}_c)^2} \Gamma_{2,1} = \frac{1}{8} \left(\frac{\hbar Z_T}{2\phi_0^2}\right) \frac{E_{\rm J}^2}{\hbar^2 \omega_c} \tilde{\varphi}_T^2(k_c) \tag{5.133}$$

Compared with the rate associated with the first order coupling Hamiltonian, Γ_1 [see Eq. (5.116)], the rate associated with this term is

$$\Gamma'_{2,1}/\Gamma_1 = \frac{1}{8}\tilde{\varphi}_T^2(k_c). \tag{5.134}$$

For a realistic setup, where we assume the transmission is 1 m long, the cavity frequency is 7.5 GHz, and the speed of microwave along the transmission line is speed of light, and the characterestic impedance of the transmission line is 50 Ω, the quantization parameter $\tilde{\varphi}_T(k_c) \sim 0.0124$. So this process is much slower than the first order coupling, which is controlled by the small parameter $\tilde{\varphi}_T^2(k_c)$, which is equivalent to the small parameter $\frac{2\pi v_p}{\omega_c l}$ [see Eq. (5.141)]. Especially, as the transmission line $l \to \infty$ (approaching theoretical limit), this term $\to 0$.

The second line of the Eq. (5.129) (noted as $T_{3,2}$) is

$$T_{3,2} = (\mathcal{C}_{\text{TL}}\mathcal{C}_c)^2 \frac{E_{\text{J}}^2}{\hbar^2}\left(\sum_{k,q} - \sum_k \delta_{k,q}\right)\tilde{\varphi}_T^2(k)\tilde{\varphi}_T^2(q)\hat{A}_2 e^{i(\omega_k+\omega_q-2\omega_c)(t-\tau)} \tag{5.135}$$

Note the second summation term is similar to the calculation in Eq. (5.131), and it is $2\Gamma_{2,1}\hat{A}_2\rho(t)\hat{A}_2^\dagger$.

The first summation term

$$\begin{aligned} T_{3,2} + 2\Gamma_{2,1}\hat{A}_2\rho(t)\hat{A}_2^\dagger = (\mathcal{C}_{\text{TL}}\mathcal{C}_c)^2 \frac{E_{\text{J}}^2}{\hbar^2}\frac{l^2}{(2\pi v_p)^2}\int_{t_0}^{t} d\tau \int_{\omega_L}^{\omega_H} d\omega_k \int_{\omega_L}^{\omega_H} d\omega_q \\ \times \left\{\tilde{\varphi}_T^2(k)\tilde{\varphi}_T^2(q)\hat{A}_2\rho(\tau)\hat{A}_2^\dagger e^{i(\omega_k+\omega_q-2\omega_c)t}\right\} \end{aligned} \tag{5.136}$$

With Born-Markov approximation, we replace $\tilde{\varphi}_T k$ and $\tilde{\varphi}_T q$ by the central frequency mode $k_c = \omega_k/v_p$, and because of the fast oscillation term $e^{i(\omega_k+\omega_q-2\omega_c)t}$, only the modes that satisfies $\omega_k + \omega_q = 2\omega_c$ will have large contribution, we can approximate the integral of two modes frequencies by $\theta\int d\bar{\omega}$ where $\bar{\omega} = (\omega_k + \omega_q)/2$, and θ is the coupling bandwidth. Then the integral in Eq. (5.137a) is

$$\begin{aligned} T_{3,2} + 2\Gamma_{2,1}\hat{A}_2\rho(t)\hat{A}_2^\dagger = (\mathcal{C}_{\text{TL}}\mathcal{C}_c)^2 \frac{E_{\text{J}}^2}{\hbar^2}\frac{l^2\theta}{(2\pi v_p)^2}\tilde{\varphi}_T^4(k_c)\int_{t_0}^{t} d\tau \int d\bar{\omega} \\ \times \left\{\hat{A}_2\rho(\tau)\hat{A}_2^\dagger e^{2i(\bar{\omega}-\omega_c)t}\right\} \end{aligned} \tag{5.137a}$$

$$= (\mathcal{C}_{\rm TL}\mathcal{C}_c)^2 \frac{1}{4\pi}\left(\frac{\hbar Z_T}{2\phi_0^2}\right)^2 \frac{E_{\rm J}^2}{\hbar^2\omega_c}\frac{\theta}{\omega_c}\hat{A}_2\rho(t)\hat{A}_2^\dagger \tag{5.137b}$$

$$\equiv \Gamma_{2,2}\hat{A}_2\rho(t)\hat{A}_2^\dagger \tag{5.137c}$$

Note that this term is also slow compared to the first order dynamics. Similarly, to consistently compare with the first order rate in Eq. (5.116), we redefine the cavity operator $\hat{A}$ as Eq. (5.132) and the rate associated rate $\Gamma'_{2,2}$ as

$$\Gamma'_{2,2} = \frac{1}{(\mathcal{C}_{\rm TL}\mathcal{C}_c)^2}\Gamma_{2,2} = \frac{1}{4\pi}\left(\frac{\hbar Z_T}{2\phi_0^2}\right)^2 \frac{E_{\rm J}^2}{\hbar^2\omega_c}\frac{\theta}{\omega_c} \tag{5.138}$$

and then the ratio for the rates

$$\frac{\Gamma'_{2,2}}{\Gamma_1} = \frac{1}{4\pi}\left(\frac{\hbar Z_T}{2\phi_0^2}\right)\frac{\theta}{\omega_c}, \tag{5.139}$$

where if the transmission line impedance is 50 Ω, the term $\left(\frac{\hbar Z_T}{2\phi_0^2}\right) \sim 0.1560$ and in the quantum optics system assumption, $\theta/\omega_c \ll 1$. So this second order coupling dynamics is also slower than the first order coupling dynamics, and is controlled by the small parameter θ/ω_c.

Similarly, we can perform the same preocedure for the other three terms and obtain the master equation induced by H_2

$$\partial_t\rho(t) = -\Gamma_2\mathcal{D}[\hat{A}_2]\rho(t) \tag{5.140a}$$

$$\mathcal{D}[\hat{A}_2]\rho(t) = -\frac{1}{2}\left(\hat{A}_2^\dagger\hat{A}_2\rho + \rho\hat{A}_2^\dagger\hat{A}_2 - 2\hat{A}_2\rho(t)\hat{A}_2^\dagger\right) \tag{5.140b}$$

$$\hat{A}_2 = \mathcal{C}_{\rm TL}\mathcal{C}_c\sum_n \frac{(-1)^n\tilde{\varphi}_c^{2n+2}}{n!\cdot(n+2)!}\left(a^\dagger\right)^n a^{n+2} \tag{5.140c}$$

$$\Gamma_2 = \left[\frac{1}{4\pi}\left(\frac{\hbar Z_T}{2\phi_0^2}\right)^2\frac{E_{\rm J}^2}{\hbar^2\omega_c}\right]\left[\frac{\theta}{\omega_c} - \frac{\pi v_p}{2l\omega_c}\right] \tag{5.140d}$$

Finally, I want to note that the above derivation is valid when the length of the transmission line is large. This is consistent with the Born-Markov approximation. We assume in a coupling bandwidth $\theta \ll \omega_c$, the number of modes in this bandwidth is still much greater

than the system DOFs, so the transmission line must be considered to be long, in which the integer

$$n_c \equiv \frac{k_c l}{2\pi} = \frac{\omega_c l}{2\pi v_p} \gg 1, \tag{5.141}$$

such that we can find an other integer n_θ which satisfies $|n_\theta - n_c| \gg 1$ and $n_\theta/n_c \ll 1$. In the regime where $l \to \infty$, the rate of the quantum process given by H_2 nonlinear system-bath coupling is given by $\Gamma'_{2,2}$ term [Eq. (5.138)], and is controlled by small parameter θ/ω_c which does not depend on the length of the transmission line.

5.4.6.3 Third order terms Similar to the discussion in Section 5.4.6.2, after we apply the rotating-wave approximation, the third order Hamiltonian is given by

$$\begin{aligned}
\frac{H_3}{E_J \mathcal{C}_c \mathcal{C}_{\rm TL}} =& i\left\{\left(\sum_k \frac{\tilde{\varphi}_T^3(k)}{6}(b_k^\dagger)^3 + \sum_{k,q}{}' \frac{\tilde{\varphi}_T(k)\tilde{\varphi}_T(q)}{2}(b_k^\dagger)^2 b_q^\dagger \right.\right. && \text{(5.142a)}\\
&\left.\left. + \sum_{k,q,p}{}' \tilde{\varphi}_T(k)\tilde{\varphi}_T(q)\tilde{\varphi}_T(p) b_k^\dagger b_q^\dagger b_p^\dagger\right) \sum_n \frac{(-1)^n \tilde{\varphi}_c^{2n+3}}{n!\cdot(n+3)!}(a^\dagger)^n a^{n+3} - h.c.\right\} \\
&-i\left\{\left[\sum_k \frac{\tilde{\varphi}_T^3(k)}{2}(b_k^\dagger)^2 b_k + \sum_{k,q}{}' \tilde{\varphi}_T^2(k)\tilde{\varphi}_T(q)\left(b_q^\dagger b_k^\dagger b_k + \frac{1}{2}(b_k^\dagger)^2 b_q\right)\right.\right. && \text{(5.142b)}\\
&\left.\left. + \sum_{k,q,p}{}' 6\tilde{\varphi}_T(k)\tilde{\varphi}_T(q)\tilde{\varphi}_T(p) b_k^\dagger b_q^\dagger b_k\right] \sum_n \frac{(-1)^n \tilde{\varphi}_c^{2n+1}}{n!\cdot(n+1)!}(a^\dagger)^n a^{n+1} - h.c.\right\}
\end{aligned}$$

Follow the same argument in Section 5.4.6.2, the only Hamiltonian term that contributes to the system dynamics when the bath is in vacuum state is the first term in Eq. (5.142a). We can define a system nonlinear operator

$$\hat{A}_3 = \mathcal{C}_c \mathcal{C}_{\rm TL} \sum_n \frac{(-1)^n \tilde{\varphi}_c^{2n+3}}{n!\cdot(n+3)!}(a^\dagger)^n a^{n+3}. \tag{5.143}$$

In Eq. (5.142a), there are three terms, the first term, $\sum_k \frac{\tilde{\varphi}_T^3(k)}{6}(b_k^\dagger)^3$ term, will give a Lindblad term in master equation of cavity field as $\mathcal{D}[\hat{A}_3]\rho(t)$ with rate $\Gamma_{3,1}$. This process is further suppressed by the small parameter $1/n_c$ [see Eq. (5.141)] as

$$\frac{\Gamma_{3,1}}{\Gamma_1} \propto n_c^{-2} = \left(\frac{2\pi v_p}{\omega_c l}\right)^2. \tag{5.144}$$

The second term, $\sum_{k,q}(b_k^\dagger)^2 b_q^\dagger$ term, will give a Lindbald term $\mathcal{D}[\hat{A}_3]\rho(t)$ with rate $\Gamma_{3,2}$,

$$\frac{\Gamma_{3,2}}{\Gamma_1} \propto \frac{1}{n_c}\frac{\theta}{\omega_c} = \left(\frac{2\pi v_p}{\omega_c l}\right)\frac{\theta}{\omega_c}, \tag{5.145}$$

where θ is the coupling bandwidth. The third term $\sum_{k,q,p} b_k^\dagger b_q^\dagger b_p^\dagger$ givens the same Lindblad term with rate $\Gamma_{3,3}$,

$$\frac{\Gamma_{3,3}}{\Gamma_1} \propto \frac{\theta^2}{\omega_c^2}. \tag{5.146}$$

In the limit where $l \to \infty$, the third term is dominant, but is still further suppressed by θ/ω_c, even compared with the second order dynamics.

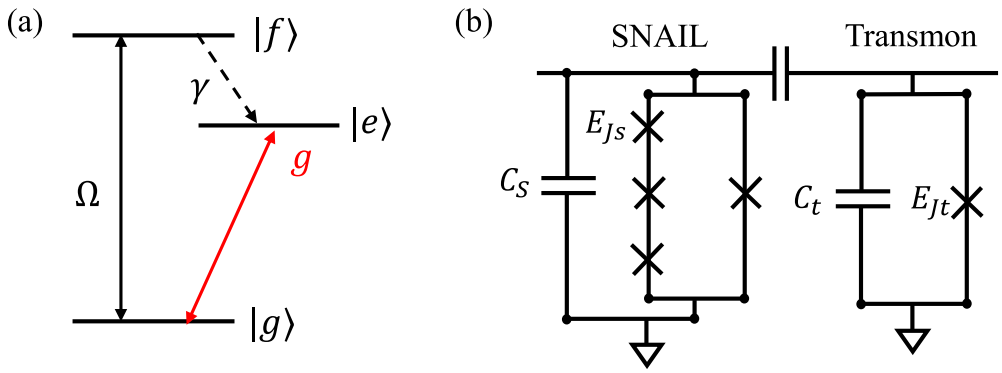

Figure 41: In (a), we show the three-level model of the laser pump media (atom) where only coherent drives are permitted. In (b), we show the circuit diagram of the SNAIL qubit and transmon qubit composite system, in which the effective incoherent drive of the transmon qubit can be achieved.

5.5 Engineering an artificial atom with population inversion

Previously we assumed that there is an incoherent pump process that induces population inversion. In this chapter we will analyze how to build such an incoherent pump.

As a first, more realistic, step is to consider a three-level-atom model [see Fig. 41] for the pump media, where the transition between the ground state $|g\rangle$ and the second excited state

$|f\rangle$ is coherently driven while the second excited state experiences a fast decay to the excited state $|e\rangle$. If the decay process is sufficiently fast, as the population of the atom is driven to the state $|f\rangle$ it quickly relaxes to $|e\rangle$ to achieve population inversion on the lasing levels $|g\rangle$ and $|e\rangle$. However, the transition between $|g\rangle$ and $|f\rangle$ for a transmon qubit is forbidden by selection rules, and thus it cannot be easily pumped. Therefore, we propose adding a SNAIL qubit to the transmon qubit to form a composite system. The key feature of the SNAIL qubit is that it has third order nonlinearity that makes the $|g\rangle \rightarrow |f\rangle$ transition allowed.

The level structure of the two qubit system is shown in Fig. 42. Because the transmon qubit is a strongly anharmonic oscillator, we use $|g_t\rangle$, $|e_t\rangle$ and $|f_t\rangle$ to represent its ground, first and second excited states, respectively. The SNAIL qubit is a weak nonlinear device, where we use $|0_s\rangle$, $|1_s\rangle$ and $|2_s\rangle$, etc to represent the states of the SNAIL qubit system.

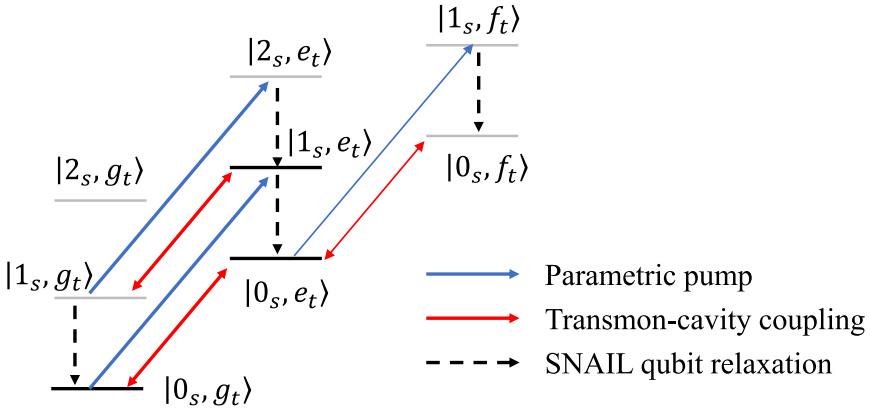

Figure 42: The level structure of the SNAIL qubit and the transmon qubit. The gray thin lines are the levels that are weekly populated in the pumping scheme discussed in Section 5.5. The blue line is the parametric drive on the composite system, the red arrow show the transition of the composite system due to the coupling to the laser cavity. The dashed arrow shows the relaxation process of the SNAIL qubit. The think solid lines show the transition that are in resonance, while the thin solid lines show the ones that are not in resonance (because of the anharmonicity of the transmon qubit).

When the SNAIL qubit (operator $\hat{s}$ for the SNAIL qubit), which has third order nonlinearity, couples to the transmon qubit (operator $\hat{t}$ for the transmon qubit), the state of the transmon qubit and the SNAIL qubit forms dressed states, i.e., $\hat{s}'$ and $\hat{t}'$. In the dressed

state basis, the third order nonlinearity of the SNAIL qubit provides the nonlinear coupling between the dressed states of the transmon qubit and the SNAIL qubit. Especially, the term $\hat{s}'^{\dagger}\hat{s}'\hat{t}'$ can be used to parametrically drive both the SNAIL qubit and the transmon qubit such that the composite system experiences a two-photon drive to excite the SNAIL qubit and the transon qubit at the same time. This transition is shown in Fig. 42 as the blue arrows. If the SNAIL qubit couples to a lossy cavity, such that the relaxation of the SNAIL qubit [see Fig. 42, black dashed arrows] is fast compare to the pump process (and also the transmon-cavity coupling, see Fig. 42 red arrows), the SNAIL qubit and the transmon qubit can form an effective three-level atom, in which the ground state ($|g\rangle$ in Fig. 41a) is the state $|0_s g_t\rangle$, and the state $|f\rangle$ in Fig. 41a is the excited state for both the qubits, i.e., $|1_s, e_t\rangle$ and the state $|e\rangle$ in Fig. 41(a) is the state $|0_s, e_t\rangle$ in Fig. 42.

The Hamiltonian of a SNAIL qubit coupled to a transmon qubit is

$$H = H_{\mathrm{T}} + H_{\mathrm{S}} + H_{\mathrm{couple}} \tag{5.147a}$$

$$H_{\mathrm{T}} = \omega_t \hat{t}^{\dagger}\hat{t} + k_t \hat{t}^{\dagger}\hat{t}^{\dagger}\hat{t}\hat{t} \tag{5.147b}$$

$$H_{\mathrm{S}} = \omega_s \hat{s}^{\dagger}\hat{s} + g_3\left(\hat{s}^{\dagger}\hat{s}^{\dagger}\hat{s} + \hat{s}^{\dagger}\hat{s}\hat{s}\right) \tag{5.147c}$$

$$H_{\mathrm{couple}} = g_2\left(\hat{s}^{\dagger}\hat{t} + \hat{t}^{\dagger}\hat{s}\right) \tag{5.147d}$$

where $\hat{s}$ ($\hat{t}$) is the operator for the SNAIL qubit and the transmon qubit. We truncate the Hamiltonian of the transmon qubit and the SNAIL qubit to the lowest order nonlinearity, and we further ignore the third order nonlinear terms $\hat{s}^{\dagger}\hat{s}^{\dagger}\hat{s}^{\dagger}$ and $\hat{s}\hat{s}\hat{s}$ in SNAIL qubit Hamiltonian, as these terms are far-off detuned and should have small effect on the overall dynamics. We further assume that the SNAIL qubit and transmon qubit modes are strongly detuned compared with the linear coupling, i.e., $2\Delta = |\omega_s - \omega_t| \gg g_2$, which causes the modes of the transmon and SNAIL qubits to be weakly dressed. In the dressed basis, the third order nonlinearity of the bare SNAIL mode gives third order nonlinear coupling between the dressed SNAIL and transmon modes as $H_3 = s'^{\dagger}s't' + h.c.$, where s' and t' are the dressed SNAIL and transmon mode operators. When we drive the SNAIL mode with a classical drive

$$H_{\mathrm{d}} = \Omega_d \exp\left[i\left(\omega_s + \omega_t\right)t\right]s + h.c., \tag{5.148}$$

In the dressed basis, the classical drive on the bare SNAIL mode causes the SNAIL mode has a fast oscillating component with frequency $(\omega_s + \omega_t)$. This components, through the third order nonlinear coupling H_3, the dressed SNAIL and transmon mode undergo a parametric two-photon pump process (see blue arrows in Fig. 42).

If we further couples the SNAIL mode with a lossy cavity, which causes the bare SNAIL mode to have a fast decay compared to the pump process, e.g., from $|0_s, g_t\rangle$ to $|1_s, e_t\rangle$, the population pumped to $|1_s, e_t\rangle$ fast relaxes to state $|0_s, e_t\rangle$. With the coherent pump (blue arrow in Fig. 42) and the loss process (black dashed arrows in Fig. 42), it effective enables an incoherent drive to the transmon qubit. Further, as the population builds up on state $|0_s, e_t\rangle$, because the transmon qubit is a strong nonlinear device, the two-photon transition $|0_s, e_t\rangle$ to $|1_s, f_t\rangle$ is far detuned from the classical pump frequency, which makes the state $|1_s, f_t\rangle$ and $|0_s, f_t\rangle$ is weakly populated.

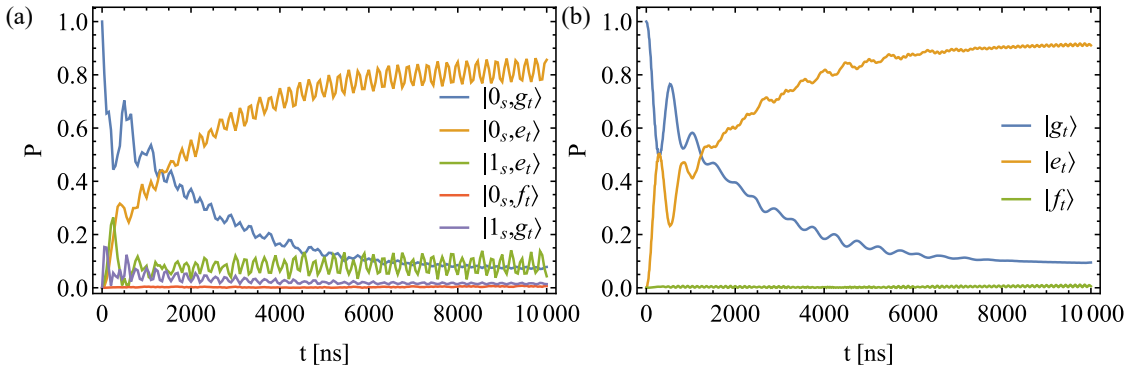

Figure 43: The population of the composite quantum system and the transmon qubit with coherent drive on the SNAIL qubit. In (a) we plot the population on the composite system levels $|0_s, g_t\rangle$ (blue line), $|0_s, e_t\rangle$ (orange line), $|1_s, e_t\rangle$ (green line), $|0_s, f_t\rangle$ (vermilion line) and $|1_s, g_t\rangle$ (purple line) with coherent drive on the SNAIL mode. Except the state $|0_s, g_t\rangle$, $|0_s, e_t\rangle$ and $|0_s, g_t\rangle$, the other states are weakly populated. In (b), we plot the population on the transmon qubit. The population of the transmon qubit is pumped from the ground state $|g_t\rangle$ (blue line) to $|e_t\rangle$ (orange line). The higher state $|f_t\rangle$ (green line) is rarely populated. Parameters chosen: $\omega_s/2\pi = 7.2$ GHz, $\omega_t/2\pi = 6.7$ GHz, $g_2/2\pi = 0.05$ GHz, $g_3/2\pi = 0.05$ GHz, $\Omega_d/2\pi = 2.0$ GHz, $\gamma/2\pi = 5$ MHz, $k/2\pi = -0.3$ GHz.

The whole composite quantum system can be described by the master equation

$$\partial_t \rho_{St} - i[H + H_d, \rho_{St}] + \gamma \mathcal{D}[s]\rho_{St} \tag{5.149a}$$

$$\mathcal{D}[s]\rho_{St} = -\frac{1}{2}\left(s^\dagger s \rho_{St} + \rho_{St} s^\dagger s - 2 s \rho_{St} s^\dagger\right) \tag{5.149b}$$

where ρ_{St} is the density operator for the composite system of the coupled SNAIL and transmon qubits, the system Hamiltonian is in Eq. (5.147), and the classical drive Hamiltonian is in Eq. (5.148) and Eq. (5.149b) is the dissipation of the SNAIL mode.

The dynamics of the composite quantum system in presence of the coherent drive can be obtained by solving the master equation Eq. (5.149). As the higher levels of the composite systems are weakly populated, we truncated the Hilbert space of the SNAIL qubit to maximally allow 6 photons, and transmon qubit for 3 photons and numerically time-evolve the master equation Eq. (5.149) in the truncated Hilbert space.

In the numerical calculation, we set the SNAIL qubit to have mode frequency $\omega_s/(2\pi) = 7.2$ GHz with third order nonlinearity $g/(2\pi) = 50$ MHz, while the transmon qubit to have mode frequency $\omega_t/(2\pi) = 6.7$ GHz with fourth order nonlinear strength $k/(2\pi) = -0.3$ GHz. The linear coupling strength between two qubits is $g_2/(2\pi) = 50$ MHz. The SNAIL qubit is coherently pumped by a classical drive with $\Omega_d/(2\pi) = 2.0$ GHz. The relaxation for the SNAIL mode is $\gamma/(2\pi) = 5$ MHz. The population of the lower excitation states for the composite systems are shown in Fig. 43a. In Fig. 43a, the population of the state $|0_s, g_t\rangle$ is pumped to state $|1_s, e_t\rangle$ and then relaxes to $|0_s, e_t\rangle$, which effectively drives the population from $|0_s, g_t\rangle$ to state $|0_s, e_t\rangle$. For a long enough pumping time, the population will be pumped into level $|0_s, e_t\rangle$. We also notice that the population for the state $|0_s, g_t\rangle$, $|0_s, e_t\rangle$ and $|1_s, g_t\rangle$ is fast oscillating[4]. This is caused by the classical drive on the SNAIL qubit such that the SNAIL mode has a fast oscillating components with frequency $(\omega_s + \omega_t)$. In Fig. 43b, we plot the population of the ground, first and second excited states of the transmon qubit. The population on the transmon qubit is pumped from the ground state $|g_t\rangle$ to $|e_t\rangle$. From both plots in Fig. 43, the higher excited states of the composite systems (e.g., $|0_s, f_t\rangle$ and $|1_s, g_t\rangle$) has little population, especially the second excited state of the transmon qubit $|f_t\rangle$, which justifies the truncation of the composite system Hilbert space in our numerical calculation.

[4] we did not sample the population curves in Fig. 43a extremely fine to capture the correct oscillation frequency for better view of the long-time behavior of all the curves.

5.6 Transmon qubit-cavity nonlinear coupling

In this section, we introduce a nonlinear coupling circuit for coupling the artificial atom to the cavity. The circuit is very similar to the one discussed in Section 5.4.5. In this section, in order to simplify the discussion, we treat the artificial atom as a two-level system (a transmon qubit) with an incoherent pump that generates level inversion. The detailed discussion of the more realistic model of the pump media and the pump process is be discussed in the Section 5.5.

5.6.1 Model discussion

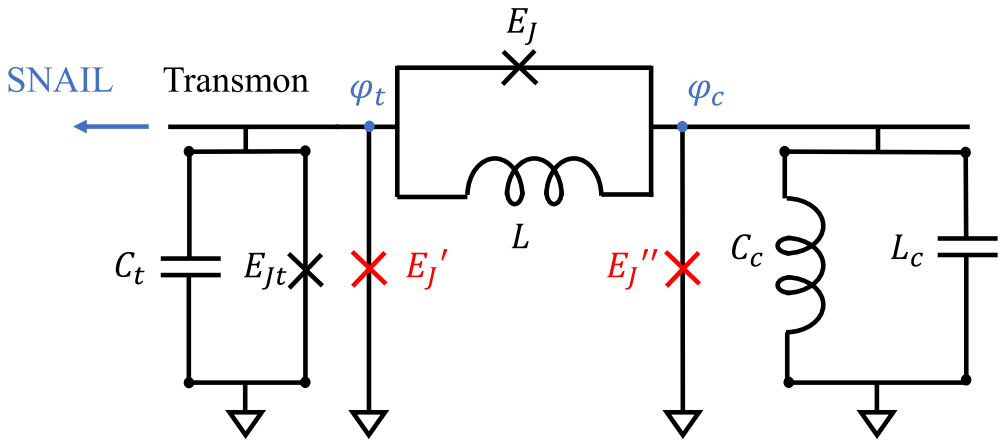

Figure 44: The circuit model for the nonlinear coupling between the transmon qubit and the cavity. The red junctions are π-junctions, which is to compensate the extra nonlinearity induced to the transmon qubit and the cavity field due to the coupling circuit.

The proposed atom-cavity nonlinear coupling circuit is shown in Fig. 44. We assume the coupling given by the nonlinear circuit model is weak compared to the optical frequencies, i.e., the frequency of the transmon qubit and the frequency of the cavity light. The nonlinear coupling strength is controlled by the coupling Josephson junction energy, which is labeled as E_{J} and the linear inductance L in Fig. 44.

In our model, the cavity field is modeled by an LC resonator. After second quantization, the node phase φ_c of the cavity is given by Eq. (5.96a). The node phase of the transmon

qubit φ_t is

$$\hat{\varphi}_t = \tilde{\varphi}_t \sigma_x \tag{5.150}$$

where $\tilde{\varphi}_t = \frac{1}{\phi_0}\sqrt{\frac{\hbar Z_t}{2}}$ and $Z_t = \sqrt{\frac{L_{\mathrm{J_t}}}{C_t}}$ is the impedance of the transmon qubit, σ_x is the x Pauli matrix. The nonlinear coupling Hamiltonian is

$$H_{ac} = -E_{\mathrm{J}} \cos(\hat{\varphi}_c - \hat{\varphi}_t) + r_{ac} E_{\mathrm{J}} (\hat{\varphi}_c - \hat{\varphi}_t)^2 + E'_{\mathrm{J}} \cos(\hat{\varphi}_t) + E''_{\mathrm{J}} \cos(\hat{\varphi}_c), \tag{5.151}$$

where we assume $r_{ac} = \frac{\phi_0^2}{2LE_{\mathrm{J}}}$, which is the ratio of the linear inductance energy and the Josephson energy of the coupling circuit.

5.6.2 Nonlinear cavity operator under rotating wave approximation

Similarly, we can also adopt the treatment of the operator cosines discussed in Section 5.2.2 and 5.2.3 to construct a nonlinear operator for the cavity field under rotating wave approximation. Especially, for the term $\cos(\hat{\varphi}_c - \hat{\varphi}_t)$. Also we note that the transmon qubit operators and the cavity operators commute,

$$\begin{aligned} \cos(\hat{\varphi}_c - \hat{\varphi}_t) &= \frac{1}{2}\left(e^{-i\hat{\varphi}_t} e^{i\hat{\varphi}_c} + e^{i\hat{\varphi}_t} e^{-i\hat{\varphi}_c}\right) \\ &= \frac{1}{2} e^{-\tilde{\varphi}_c^2/2} \left(e^{-i\hat{\varphi}_t} e^{i\tilde{\varphi}_c a^\dagger} e^{i\tilde{\varphi}_c a} + e^{i\hat{\varphi}_t} e^{-i\tilde{\varphi}_c a^\dagger} e^{-i\tilde{\varphi}_c a}\right). \end{aligned} \tag{5.152}$$

Note that

$$\exp\left(i\tilde{\varphi}_t \sigma_x\right) = \cos(\tilde{\varphi}_t) + i \sin(\tilde{\varphi}_t)\sigma_x \tag{5.153a}$$

$$\exp\left(-i\tilde{\varphi}_t \sigma_x\right) = \cos(\tilde{\varphi}_t) - i \sin(\tilde{\varphi}_t)\sigma_x, \tag{5.153b}$$

We can separate a term in the nonlinear coupling from expansion of Eq. (5.152) that is solely acting on the cavity field, denoted as H_c

$$H_c = -E_{\mathrm{J}} \cos(\tilde{\varphi}_t) \cos(\hat{\varphi}_c), \tag{5.154}$$

which introduce dispersion to the cavity field. We again employ π-junctions with Josephson energy $E'_{\mathrm{J}} = E_{\mathrm{J}} e^{-\tilde{\varphi}_c^2}$ and $E''_{\mathrm{J}} = E_{\mathrm{J}} \cos(\tilde{\varphi}_t)$ to compensate this nonlinearity of the transmon

qubit and the cavity field. After we absorb the extra linear frequency shifts into the Hamiltonian of the transmon qubit and the cavity, the nonlinear coupling Hamiltonian becomes

$$H_{ac} = -E_{\mathrm{J}}\sigma_x \left\{ \sin(\tilde{\varphi}_t) \sin\left[\tilde{\varphi}_c(a^\dagger + a)\right] + 2r\tilde{\varphi}_t\tilde{\varphi}_c(a^\dagger + a) \right\}. \tag{5.155}$$

After applying the rotating wave approximation, the atom-cavity coupling is

$$H_{ac,\mathrm{RWA}} = -E_{\mathrm{J}} \left(\sigma_+ \hat{A}_a + \sigma_- \hat{A}_a^\dagger \right), \tag{5.156}$$

with the cavity nonlinear operator

$$\hat{A}_a = \mathcal{C}_c \sin(\tilde{\varphi}_t) \sum_n \frac{(-1)^n \tilde{\varphi}_c^{2n+1}}{n! \cdot (n+1)!} (a^\dagger)^n a^{n+1} + 2r_{ac}\tilde{\varphi}_t\tilde{\varphi}_c a, \tag{5.157}$$

where $\mathcal{C}_c$ is defined in Eq. (5.120).

Again, we will estimate the magnitude of the parameter $\tilde{\varphi}_t$ for guidance. In experimental settings, the frequency of the transmon qubit is in GHz range, while the Josephson junction critical current can range from 10 nA to 10 μA. Note that

$$\tilde{\varphi}_t = \frac{1}{\phi_0}\sqrt{\frac{\hbar Z_t}{2}} = \sqrt{\frac{\hbar\omega_t}{\phi_0 I_c}} \tag{5.158}$$

where ω_t is the transmon frequency, I_c is the junction critical current. The parameter $\tilde{\varphi}_t$ is to vary in the range of 0.04 to 1.23. Especially, if the critical current is 100 nA and the transmon frequency is 7.5 GHz, the $\tilde{\varphi}_t \sim 0.389$. Notice that in Eq. (5.157), the factor $\tilde{\varphi}_t$ controls relative magnitude of the factor before linear term a to the factor before higher order nonlinear terms. By tuning this parameter, we can make the linear term to balance the nonlinear terms to give the Boson amplification reduction region in Fig. 45.

Again, we examine the transition amplitude from the cavity photon number state $|n+1\rangle$ to $|n\rangle$ by this operator, i.e., $\langle n|\hat{A}_a|n+1\rangle$. The set of circuit parameters are given in Table 6.

Next, we verify our derivation of the $\hat{A}_a$ operator by comparing it with a numerical derivation. Since there is only as single cavity mode being considered, we can truncate the normal photon operators a in a finite dimensional Hilbert space, i.e., manually add a restriction that the photon number in the cavity must be below N. Then we can express the coupling Hamiltonian in Hilbert space $\mathcal{H}_{ac} = \mathcal{H}_a \otimes \mathcal{H}_{c,\mathrm{trunc}}$, where $\mathcal{H}_a$ is the Hilbert space

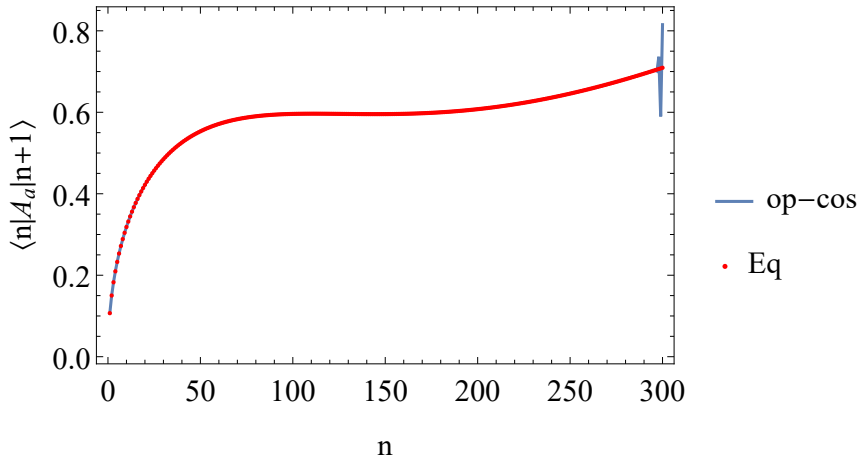

Figure 45: The transition amplitude of the nonlinear operator for the cavity field $\hat{A}_a$, which is given by Eq. (5.157). We compare the analytical solution from Eq. (5.157) (red dots) with the exact matrix representation of the nonlinear coupling Hamiltonian in Eq. (5.156) (blue line).

of the two-level atom and $\mathcal{H}_{c,\text{trunc}}$ is the truncated Hilbert space of the cavity photon field. With the finite dimensional Hilbert space $\mathcal{H}_{ac}$, the phase difference operator $\Delta\hat{\varphi} = \hat{\varphi}_c - \hat{\varphi}_t$ can be expanded as a finite dimensional matrix in the orthonormal basis $\{|g\rangle \otimes |n\rangle,\ |e\rangle \otimes |n\rangle\}$ where $|g\rangle$ and $|e\rangle$ is the ground and excited state of the atom, $|n\rangle$ is the photon number state of the cavity. With the matrix representation of the operator $\Delta\hat{\varphi}$, its eigen-basis can be found, noted as $\{|\psi_i\rangle\}$, with corresponding eigenvalues $\{\lambda_i\}$. Then the cosine of the phase difference operator can be expressed using the eigenbasis as

$$H_{ac}/E_\text{J} \sim -\cos(\Delta\hat{\varphi}) + r_{ac}\Delta\hat{\varphi}^2 = \sum_i \left[\cos(\lambda_i) + r_{ac}\lambda_i^2\right] |\psi_i\rangle\langle\psi_i|, \tag{5.159}$$

where we ignore the term for the π-junction as it does not contribute to the coupling between the cavity mode and the transmon qubit.

After apply the rotating wave approximation, to compare with the operator given in Eq. (5.157), we also calculate the transition amplitude, however for both the atom and the photon states, as $\langle e, n|H_{ac}/E_\text{J}|g, n+1\rangle$, which is plotted as the blue line in Fig. 45. The

Table 6: Chosen circuit parameters and the derived constants in the nonlinear system jump operator $\hat{A}_a$ in Eq. (5.157) for Fig. 45.

Parameters	ω_c	I_c	Z_c	r_{ac}
Value	7.5 GHz	0.1 μA	50 Ω	0.4
Parameters	Z_t	$\tilde{\varphi}_t$	$\tilde{\varphi}_c$	$\mathcal{C}_c$
Value	155.1 Ω	0.3886	0.1560	0.9880

oscillation around $n \sim 300$ is because of the truncation we make. But compare with the operator expansion approach [Eq. (5.157)] the two transition amplitudes matches perfectly. This shows support for our operator expansion approach. Further, from the transition amplitude plot, there exists a region for the cavity photon that the transition between nearby photon number states given by the nonlinear operator $\hat{A}_a$ does not have the Boson amplification (or Boson amplification is largely suppressed), which is the key for further suppressing the laser linewidth beyond the Schawlow-Townes limit [197].

5.7 The suppression of the Josephson micromaser linewdith beyond Schawlow-Townes limit

In this section, we construct a theoretical model for the laser system. The model discussed in this section is build from real circuit elements: Josephson junctions, inductors, capacitors and transmission lines, and consequently it is very close to what can be build in the lab with real superconducting circuits. However, the model does still lacks certain details: precise modeling for the pump process for the transmon qubit, a model of transmission line bandwidth, and capacitors between the transmon qubit and the cavity as well as the cavity and the transmission line. The main goal of this section is to build a realistic theoretical proof of concept model which is easy to analyze and which demonstrates that

a laser system with the nonlinear couplings can have laser linewidth significantly narrower than the Schawlow-Townes limit of classical laser theory.

5.7.1 2-level incoherent pump atom model for the Josephson laser

The model of the Josephson nonlinear laser system is similar to the atomic laser model shown in Fig. 33, except that the coupling between the atom and cavity and the dissipation process of the cavity is nonlinear, given by the nonlinear cavity operators in Eq. (5.157) and Eq. (5.112), respectively. In this mode, the transmon qubit is modeled by the two-level atom. The pump process discussed in Section. 5.5 is modeled by an incoherent pump process from the ground state to the excited state. The cavity is again modeled by a single-mode photon field. The coupling between the transmon qubit and the cavity field is given by the nonlinear coupling in Eq. (5.156). The cavity couples to a photon bath, which is a model for the transmission line discussed in the Section 5.4. The dissipation process can be modeled by a Lindblad term as Eq. (5.115) with nonlinear bath operator given in Eq. (5.112). The system can be described by the master equation,

$$\partial_t \rho(t) = -i[H_0 + H_{ac}, \rho(t)] - \Gamma_p \mathcal{D}[\sigma_+]\rho(t) - \Gamma_c \mathcal{D}[\hat{A}_1]\rho(t) \tag{5.160a}$$

$$H_0 = \frac{1}{2}\omega_t \sigma_z + \omega_c a^\dagger a \tag{5.160b}$$

$$H_{ac} = g\left(\sigma_+ \hat{A}_a + \hat{A}_a^\dagger \sigma_-\right) \tag{5.160c}$$

$$\mathcal{D}[\sigma_+]\rho(t) = -\frac{1}{2}\left[\sigma_-\sigma_+\rho(t) + \rho(t)\sigma_-\sigma_+ - 2\sigma_+\rho(t)\sigma_-\right] \tag{5.160d}$$

$$\mathcal{D}[\hat{A}_1]\rho(t) = -\frac{1}{2}\left[\hat{A}_1^\dagger \hat{A}_1 \rho(t) + \rho(t)\hat{A}_1^\dagger \hat{A}_1 - 2\hat{A}_1 \rho(t) \hat{A}_1^\dagger\right] \tag{5.160e}$$

$$\hat{A}_1 = \frac{\mathcal{C}_{\mathrm{TL}}\mathcal{C}_c}{\mathcal{C}_{\mathrm{TL}}\mathcal{C}_c + 2r} \sum_{n=0}^{\infty} (-1)^n \frac{\tilde{\varphi}_c^{2n}}{n! \cdot (n+1)!} \left(a^\dagger\right)^n a^{n+1} + \frac{2r\tilde{\varphi}_c}{\mathcal{C}_{\mathrm{TL}}\mathcal{C}_c + 2r} a \tag{5.160f}$$

Note that compared with Eq. (5.112), we redefine the nonlinear cavity operator $\hat{A}_1$. In the new definition in Eq. (5.160f), by dividing the constant factor $(\mathcal{C}_{\mathrm{TL}}\mathcal{C}_c + 2r)\tilde{\varphi}_c$ to make sure the lowest term (a) has coefficient 1, which is easier to compare with a normal cavity loss term.

5.7.2 Beyond the Schawlow-Townes limit

At first, we will focus on the transmon qubit-cavity coupling under rotating wave approximation. Then we will move to the more general discussion by including terms that are dropped in rotating wave approximation, the higher order loss terms for the cavity field, etc.

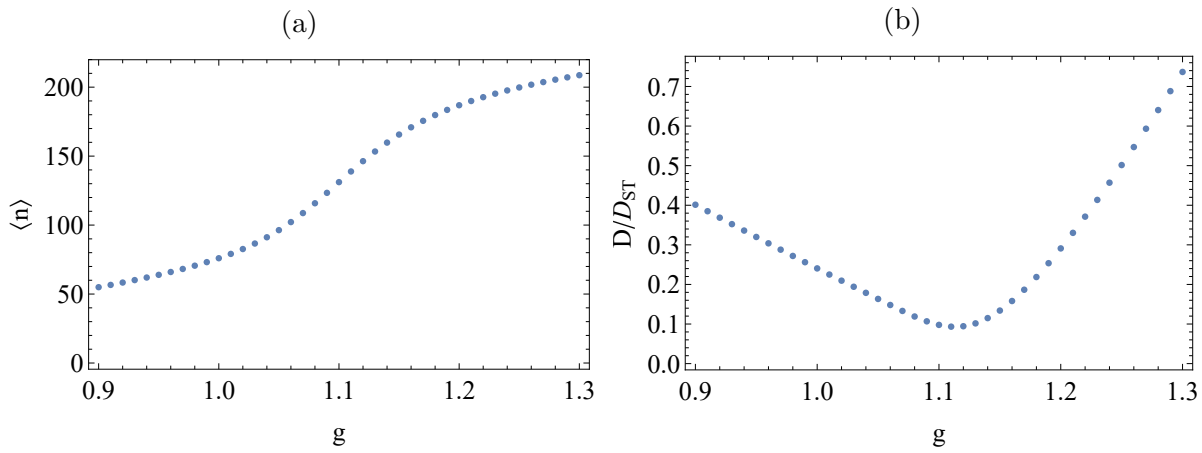

Figure 46: The mean photon number $\langle n \rangle$. (a) and the linewidth of the cavity field D in unit of Schawlow-Townes limit D_{ST} (b). At the narrowest point the laser linewidth is 9.2% of the Schawlow-Townes limit.

With the above approximation, we set pump strength $\Gamma_p = 1.0$, and $\Gamma_c = 0.01228$ and sweep the transmon qubit-cavity coupling strength g. The mean photon number and the linewidth of the laser light (in the unit of the Standard limit) are plotted in Fig. 46. We observe in Fig. 46a, at $g \sim 1.12$, the mean photon number is in the flattened region of the nonlinear cavity operator, as shown in Fig. 40. At the same coupling strength, we observe in Fig. 46b, that the linewidth of the laser reaches the narrowest point with respect to the Schawlow-Townes limit, becoming just 9.2% of D_{ST}. The photon distribution in the cavity at $g = 1.12$ is plotted in Fig. 47. Compared with the photon distribution of a conventional laser, in which the photon distribution is a Poisson distribution, the photon distribution in Fig. 47 has distortion in the regime where the transition amplitude is flat for the nonlinear coupling operator. We summarize all the parameters used for Fig. 47 in Table 7.

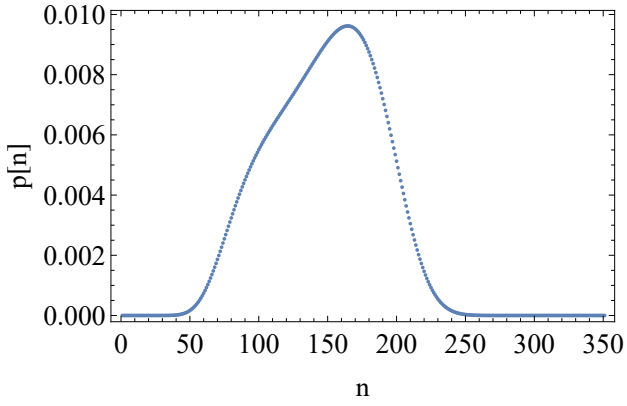

Figure 47: The photon distribution of the proposed nonlinear Josephson micromaser using the nonlinear coupling circuit. The photon distribution in the cavity is calculated using the parameters $g = 1.12$, $\Gamma_p = 1.0$ and $\Gamma_c = 0.01228$.

5.7.3 Non-excitation number conserving terms in atom-cavity coupling and higher-order cavity loss processes

In this section, we explore some complication of the model. We focus on the non-excitation-number-conserving terms in the atom-cavity nonlinear coupling and the effects of the higher order terms in the cavity loss process. We show that the non-excitation-number-conserving terms in the atom-cavity coupling does not have an obvious effect on the system dynamics, which justifies our treatment of the laser system.

First, the atom-cavity coupling has terms that do not conserves the excitation number that were dropped in the rotating wave approximation. In Fig. 48a, we compare the atom-cavity coupling with rotating wave approximation (excitation number conserving terms only) and the coupling with not only excitation number conserving terms, but also the two-photon and three-photon processes (excitation number change is less than 3). We observe that there is essentially no difference between the two calculations thus validating the rotating wave approximation. In Fig. 48b, we add second order terms in the cavity-bath coupling. In the calculation, we set $\theta/\omega_c = 0.5$, we still don't identify any observable difference and thus conclude that the higher order terms do not affect the linewidth very much.

Table 7: Chosen circuit parameters, the derived constants and the dynamical parameters in the nonlinear system for Fig. 47.

Parameters	ω_c	I_c	Z_c	r_{ac}	Z_t
Value	7.5 GHz	0.1 μA	50 Ω	0.41	155.1 Ω
Parameters	$\tilde{\varphi}_t$	$\tilde{\varphi}_c$	$\mathcal{C}_c$	Z_T	$\mathcal{C}_T$
Value	0.3886	0.1560	0.9880	155.1 Ω	0.9961
Parameters	r	g	Γ_p	Γ_c	
Value	0.42	1.12	1.0	0.01228	

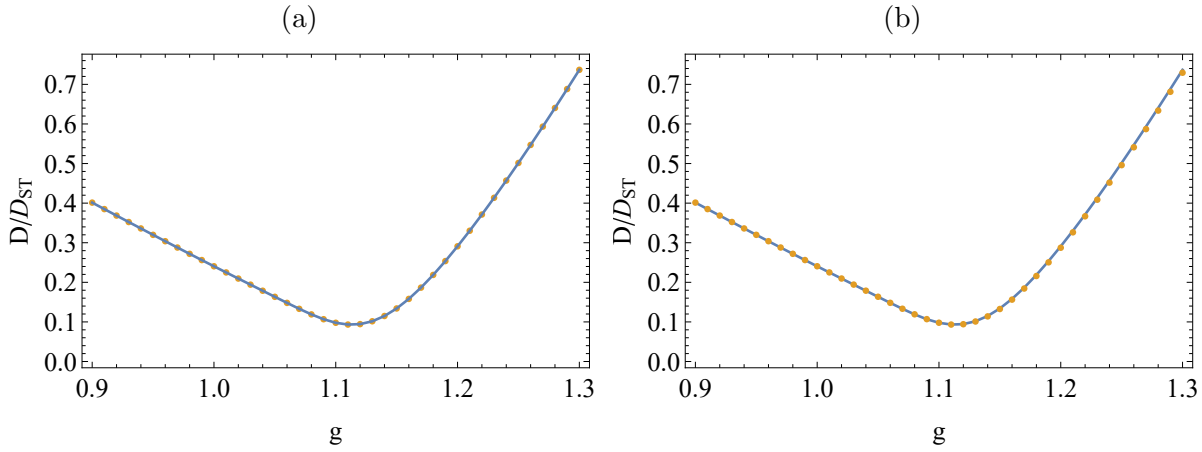

Figure 48: We add extra terms to system dynamics and check their effect on the laser linewidth. In (a), we add terms that do not respect the rotating wave approximation on the atom-cavity coupling. In (b), we add the Lindblad term that corresponds to the second order terms in the transmission line field operators. We assume the coupling bandwidth $\theta/\omega_c = 0.5$. In both subplots, the blue line is the original solution without complications. The orange dots are the linewidth calculated with the complication. Adding these terms does not affect the linewidth solution much.

5.8 Summary

In this chapter, we presented the theory of a narrow-linewidth Josephson micromaser, in which we use a transmon qubit as the pump media, and strongly coupled it to a microwave resonator to achieve lasing. The quantum system Hamiltonian and bath environment can be engineered to achieve more powerful quantum manipulation on the system. Specifically, we use a transmon-type qubit with SNAIL element to bath engineer the transmon qubit to achieve an effective incoherent drive on the transmon qubit to obtain population inversion. We further take advantages of the nonlinear coupling provided by the Josephson junctions in superconducting circuit to construct a Josephson micromaser that emits quantum light. By carefully engineering the nonlinear coupling between the transmon qubit and the maser cavity (resonator), as well as between the maser cavity (resonator) and the transmission line (the bath), the emitted light from the nonlinear Josephson micromaser system has a narrow linewidth that is beyond the Schawlow-Townes limit, the standard linewidth of the conventional laser with linear coupling. For the parameters we chose, the linewidth of the nonlinear Josephson micromaser can be $\sim 10\%$ of the Schawlow-Townes limit.

Our work on the nonlinear Josephson micromaser not only provides a pathway to on-chip narrow-linewidht Josephson micromasers for quantum computing applications, but also shows the power of the nonlinearity of the Josephson junctions in circuit-QED systems. As a strongly nonlinear element in superconducting circuit system, Josephson junctions can provide more versatile nonlinear couplings which are hard to obtain in normal cavity-QED systems. It also opens a new regime of quantum optics, a regime with relative strong nonlinearity between the atom and cavity, which provides more tools for quantum manipulation of the quantum states of superconducting circuit systems.

6.0 Robust manipulation of light using topologically protected plasmonic modes

In this chapter, we explore how to use Su-Shrieffer-Heeger model plasmonic topological modes to manipulate light. We provide an in-depth analysis of the topological defect modes, similar to the ones experimentally observed in [113, 114], and propose applications of these modes in plasmonic systems. We show that the proposed setup allows us not only to guide light but also to robustly manipulate it by shifting the topological defect modes, as a function of axial position, inside the structure. Using full 3D finite-difference-time-domain (FDTD) solutions of the Maxwell equations, we demonstrate a beam splitter and a spatial mode filter (that couples light from a pair of bulk modes to a pair of topological defect modes). Further, we analyze tolerance to manufacturing defects. While topological robustness to disorder that is invariant in the axial direction (i.e., time-independent disorder in electronic systems) has been extensively studied before, here we analyze tolerance to disorder that varies in the axial direction (i.e., time-dependent disorder in electronic systems). We investigate two types of defects: (a) defects in nanowire positions, that violate sublattice symmetry exponentially weakly and (b) defects in nano-wire diameter, that violate sublattice symmetry strongly. Using the 3D FDTD calculations we show that our structures are very tolerant to type (a) defects and reasonably tolerant to type (b) defects with transverse length-scales comparable to inter-nanowire spacing, as long as the axial length-scales are larger than the inverse topological band gap.

6.1 Finite-Difference-Time-Domain method for numerical simulation of electromagnetic field evolution

Finite-Difference-Time-Domain (FDTD) method is one of the most important numerical methods of computational electromagnetism. It is also the main numerical method we used in this project. Compared with other numerical methods of computational electro-

magnetism like the Finite Element Method (FEM), Finite Difference Frequency Domain (FDFD) methods, FDTD method focus more on the time-evolution of the electromagnetic (EM) field inside the region of interests, which is more suitable to work with problems of EM wave propagation. In this section, we briefly introduce the essence of the FDTD method, including how to use finite difference to approximate the derivatives, the Yee grid and Yee algorithm for time-evolve the EM field. The discussion in this section is influenced by the discussion in Refs. [207, 208, 209].

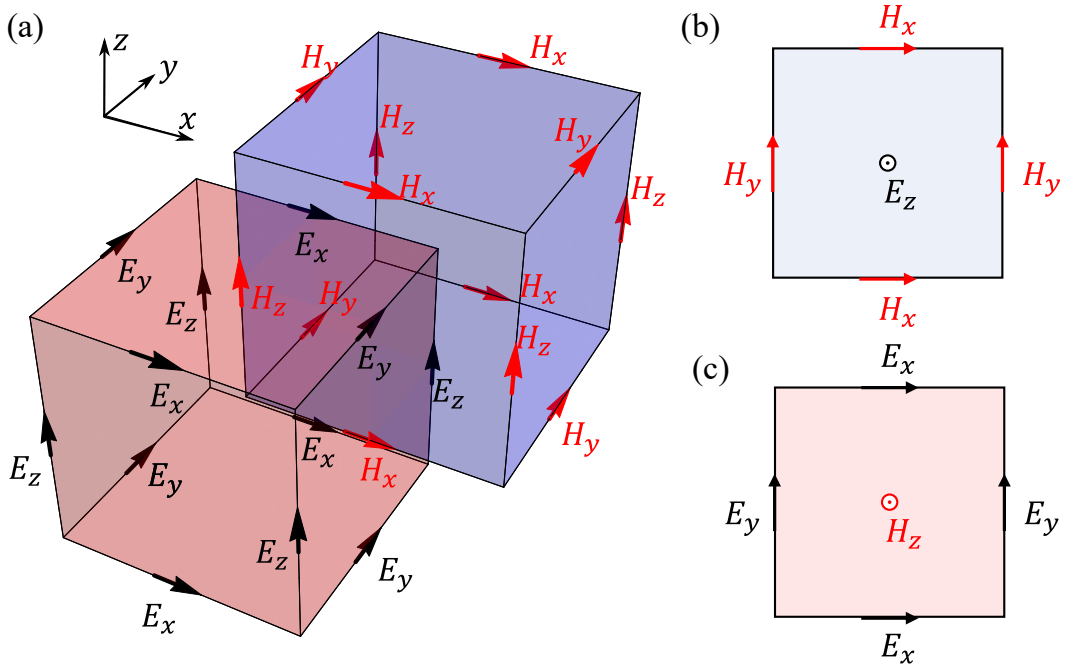

Figure 49: Visualization of the Yee grids. In (a) we show the Yee grid in 3D with both the **E** and **H** components. In (b) and (c), we show the 2D plane for the TE and TM components of the EM fields.

In classical electrodynamics, the electromagnetic field is described by the Maxwell equation [210],

$$\nabla \times \mathbf{E} = -\frac{1}{\mu}\frac{\partial}{\partial t}\mathbf{H} \tag{6.1a}$$

$$\nabla \cdot \mathbf{D} = \rho \tag{6.1b}$$

$$\nabla \times \mathbf{H} = \frac{\mathbf{D}}{\partial t} + \mathbf{J} \tag{6.1c}$$

$$\nabla \cdot \mathbf{B} = 0 \tag{6.1d}$$

where ρ is the free charge density, $\mathbf{E}$, $\mathbf{D}$, $\mathbf{B}$ and $\mathbf{H}$ are electric field and electric displacement field, magnetic flux density and magnetic field, respectively. The $\mathbf{E}$, $\mathbf{D}$, $\mathbf{B}$ and $\mathbf{H}$ are connected through the media permittivity ϵ and permeability μ,

$$\mathbf{D} = \epsilon\mathbf{E} \qquad \mathbf{B} = \mu\mathbf{H}. \tag{6.2}$$

In general, the permittivity ϵ and permeability μ are tensors, i.e., $D_i = \epsilon_{ij}E_j$ where i, j can be x, y, z.

In a realistic system when a solution of the EM field is needed, in most of the cases, the system itself is so complected that an analytical solution of Maxwell equations [Eq. (6.1)] with the boundary conditions is impossible. We need numerical methods to approximate the exact solution of Maxwell equations, a set of coupled partial differential equations. FDTD is one of these numerical methods, especially for simulating the time-evolution of the EM field (e.g. light propagation).

To approximate the EM field and the Maxwell equations, we recall that a continuous function $f(x)$ can be approximated by the values on a set of discrete sampling point, e.g. $\{f(x_1),\, f(x_2), ...f(x_n)\}$. The derivative of the function $f(x)$, which is defined as

$$\frac{d}{dx}f(x_0) = \lim_{\Delta x \to 0} \frac{f(x_0 + \Delta x) - f(x_0)}{\Delta x}, \tag{6.3}$$

can also be approximated by a finite difference,

$$\frac{d}{dx}f(x_0) \sim \frac{\Delta f(x_0)}{\Delta x} = \frac{f(x_0 + \Delta x) - f(x_0)}{\Delta x}. \tag{6.4}$$

Note that there are multiple ways to approximate the (1st order) function derivatives using finite difference. The Eq. (6.4), as it uses the point $x = x_0 + \Delta x$ which is in the forward direction of the point $x = x_0$, is referred as forward difference formula. Similarly, there are backward difference as

$$\frac{\Delta f(x_0)}{\Delta x} = \frac{f(x_0) - f(x_0 - \Delta x)}{\Delta x}, \tag{6.5}$$

and central difference as

$$\frac{\Delta f(x_0)}{\Delta x} = \frac{f(x_0 + \Delta x) - f(x_0 - \Delta x)}{2\Delta x}, \tag{6.6}$$

Different finite difference formulas will result in different approximation accuracy. To approximate the accuracy of these finite differences, we expand the function around the point of interest $x = x_0$ as,

$$f(x_0 \pm \Delta x) = f(x_0) \pm \frac{df(x_0)}{dx}\Delta x + \frac{1}{2}\frac{d^2 f(x_0)}{dx^2}\Delta x^2 \pm \frac{1}{6}\frac{d^3 f(x_0)}{dx^3}\Delta x^3 + ... \tag{6.7}$$

The forward difference is

$$\frac{\Delta f(x_0)}{\Delta x} = \frac{df(x_0)}{dx} + \frac{1}{2}\frac{d^2 f(x_0)}{dx^2}\Delta x + ... \tag{6.8}$$

With Eq. (6.8), using the forward difference formula to approximate the function derivative gives an error $o(\Delta x)$. Similarly, the backward difference also gives an error $o(\Delta x)$. However, the central difference has better performance, as the Δx^2 term in the Taylor expansion [Eq. (6.7)] is canceled, which gives an error $o(\Delta x^2)$ for the approximated differentiation value.

To get more accurate approximation to the function derivatives, we can include more nearby points in the finite difference formula, by canceling more higher order terms in the Taylor expansion. The examples can be found in [208]. Further, the higher order derivatives of the function can also be approximated by finite difference. One of the most commonly used formula for second order derivative is

$$\frac{d^2}{dx^2}f(x_0) \sim \frac{\Delta^2 f(x_0)}{\Delta x^2} = \frac{f(x_0 + \Delta x) + f(x_0 - \Delta x) - 2f(x_0)}{\Delta x^2} \tag{6.9}$$

which gives an accuracy $o(\Delta x^2)$

In FDTD method, the central difference for spacial derivative is applied to approximate the spacial partial derivatives in Maxwell equations for numerically solving the equations. To optimize the memory usage of the numerical method (i.e., the number of grid points but still get a descent accuracy), Kane Yee, in his famous work Ref. [211], proposed to use the staggered grids for the electric and magnetic fields. This method of meshing the EM field and the corresponding updating rules are called Yee algorithm. Here for simplicity, we introduce the Yee grid and the update rules without source, i.e., $\mathbf{J} = 0$ and the media is isotropic i.e., the permittivity ϵ and permeability μ of the media are scalers. The more detailed description with source current and charge can be found in Ref. [207].

The Yee grid in 3D for all components of electric field **E** and magnetic field **H** are shown in Fig 49(a). The Electric field and the magnetic field components are not sampled with the same grid mesh. Instead, they are sampled on the different middle points of the edges of two staggered cubic cells. The slice cut along xy plane of these two cells are plotted in Fig. 49(b) (blue) and 49(c) (red). For a TE light propagating along the z direction, the field components E_z, H_x, H_y are important, which corresponds to the plane shown in Fig. 49(b), while for TM light propagating along z direction, the field components H_z, E_x, E_y are important, which corresponds to Fig. 49(c). We refer these two surfaces of the Yee-grid as TE surface and TM surface.

We assume the mesh is equal-spacing, i.e., the Yee cells have unit length Δx, Δy and Δz, respectively. We further assume the sampling of the EM field has a constant time interval Δt. The grid point location can be rewritten as $(x, y, z) = (i\Delta x, j\Delta y, k\Delta z)$ and the time $t = l\Delta t$, where i, j, k can be integers and half integers while l can only be integers. For simplicity, we will use these indices to label the field components in our following discussion of the update rule of Yee algorithm and further assume all the indices can only be integer.

According to the Yee grid shown in Fig. 49(a), if we assume the E_z components are at the mesh points (i, j, k), where i, j, k are all integers, [noted as $E_z(i, j, k, l)$, l is for time], the rest of the field components are meshed as $H_x(i, j-1/2, k, l)$, $H_y(i-1/2, j, k, l)$ [see Fig. 49(b)], $H_z(i-1/2, j-1/2, k+1/2, l)$, $E_x(i-1/2, j, k+1/2, l)$ and $E_y(i, j-1/2, k+1/2, l)$ [see Fig. 49(c)].

Let's focus on the Maxwell equations [Eq. (6.1)] to understand how the finite difference approximated Maxwell equations are constructed for numerical time-evolve the EM field. The curl relations [Eqs. (6.1a) and (6.1c)] in the Maxwell equations are re-written in component form as

$$\partial_y E_z - \partial_z E_y = -\frac{1}{\mu_x} H_x \tag{6.10a}$$

$$\partial_z E_x - \partial_x E_z = -\frac{1}{\mu_y} H_y \tag{6.10b}$$

$$\partial_x E_y - \partial_y E_x = -\frac{1}{\mu_z} H_z \tag{6.10c}$$

for Eq. (6.1a) and

$$\partial_y H_z - \partial_z H_y = \epsilon_x E_x \tag{6.11a}$$

$$\partial_z H_x - \partial_x H_z = \epsilon_y E_y \tag{6.11b}$$

$$\partial_x H_y - \partial_y H_x = \epsilon_z E_z \tag{6.11c}$$

for Eq. (6.1c). Because in FDTD method, the time evolve the EM field from previous time steps to the further time is the key question. So the most intuitive approach to approximate the partial derivatives with respect to time is to use the backward difference and treat the EM field components on the current time step as the quantities that are waiting to be solved [1]. With the Yee-grid shown in Fig. 49(a), it is natural to use the central difference formula to approximate the spatial partial derivatives. The approximated finite difference equations are

$$\begin{aligned} &\frac{\Delta E_z(i, j+1, k, l-1)}{\Delta y} - \frac{\Delta E_y(i, j-\frac{1}{2}, k+\frac{1}{2}, l-1)}{\Delta z} \\ &\quad = -\frac{1}{\mu_x(i, j-\frac{1}{2}, k)} \frac{\Delta H_x(i, j-\frac{1}{2}, k, l)}{\Delta t} \end{aligned} \tag{6.12a}$$

$$\begin{aligned} &\frac{\Delta E_x(i-\frac{1}{2}, j, k+\frac{1}{2}, l-1)}{\Delta z} - \frac{\Delta E_z(i, j, k, l-1)}{\Delta x} \\ &\quad = -\frac{1}{\mu_y(i-\frac{1}{2}, j, k)} \frac{\Delta H_y(i-\frac{1}{2}, j, k, l)}{\Delta t} \end{aligned} \tag{6.12b}$$

$$\begin{aligned} &\frac{\Delta E_y(i+1, j+\frac{1}{2}, k+\frac{1}{2}, l-1)}{\Delta x} - \frac{\Delta E_x(i+\frac{1}{2}, j+1, k+\frac{1}{2}, l-1)}{\Delta y} \\ &\quad = -\frac{1}{\mu_z(i+\frac{1}{2}, j+\frac{1}{2}, k+\frac{1}{2})} \frac{\Delta H_z(i+\frac{1}{2}, j+\frac{1}{2}, k+\frac{1}{2}, l)}{\Delta t} \end{aligned} \tag{6.12c}$$

for Eq. (6.1a) and

$$\frac{\Delta H_z(i-\frac{1}{2}, j+\frac{1}{2}, k-\frac{1}{2}, l-1)}{\Delta y} - \frac{\Delta H_y(i-\frac{1}{2}, j, k, l-1)}{\Delta z} \tag{6.13a}$$

[1] There is no restriction that we cannot use the central difference formula for time derivatives. With central difference formula, we add a set of new unknown parameters into the set of difference equations, which are the field components in the future time step. The method is no longer explicit, i.e., we need to solve the whole set linear equations to get the EM field on current and future time steps instead of only solving a single equation to update the field component on a grid point. The implicit method will be much slower than the explicit method we discussed in the main text. However, the implicit method can be more numerically stable than the explicit one. The stability of these two numerical methods is beyond the scope of this discussion, but can be found in Ref. [207].

$$= \epsilon_x(i, j - \frac{1}{2}, k - \frac{1}{2}) \frac{\Delta E_x(i - \frac{1}{2}, j, k - \frac{1}{2}, l)}{\Delta t}$$
$$\frac{\Delta H_x(i, j - \frac{1}{2}, k, l - 1)}{\Delta z} - \frac{\Delta H_z(i + \frac{1}{2}, j - \frac{1}{2}, k - \frac{1}{2}, l - 1)}{\Delta x} \tag{6.13b}$$
$$= \epsilon_y(i, j - \frac{1}{2}, k - \frac{1}{2}) \frac{\Delta E_y(i, j - \frac{1}{2}, k - \frac{1}{2}, l)}{\Delta t}$$
$$\frac{\Delta H_y(i + \frac{1}{2}, j, k, l - 1)}{\Delta x} - \frac{\Delta E_x(i, j + \frac{1}{2}, k, l - 1)}{\Delta y} = \epsilon_z(i, j, k) \frac{\Delta E_z(i, j, k, l)}{\Delta t} \tag{6.13c}$$

for Eq. (6.1c). where the field finite difference is defined as

$$\frac{\Delta E_\alpha(i_x, j_y, k_z, l_t)}{\Delta x} = \frac{E_\alpha(i_x + 1, j_y, k_z, l_t) - E_\alpha(i_x, j_y, k_z, l_t)}{\Delta x} \tag{6.14}$$

where $\alpha = x, y, z$ and i_x, j_y, k_z, l_t can be integers and half integers depends on the Yee grid of the specific field component. The finite differences for y, z and t are similar. Notice that on the left hand side of the Eqs. (6.12) and (6.13), all the field components are on the previous time step $(l - 1)$, while on the right hand side the only unknown quantities are the field components at the corresponding grid point for the current time step. Providing the EM field information for previous time step, the EM field on the grid points at current time step can be explicitly solved by the Eq. (6.12) and (6.13). Then we can time-evolve the EM field using the finite difference equations till the finish time step.

6.2 Guiding light using topological defect modes

Consider a system that is almost translationally invariant along the axial, i.e., z-direction. Our goal is to describe paraxial modes, time-harmonic electromagnetic waves that propagate at small angles to the z-axis. For paraxial TM-modes it is natural to focus on the transverse components of the electric field [212, 213] and to separate out the fast oscillating part, $E_x = \psi_x(x, y, z)e^{i\beta_0 z}$ and $E_y = \psi_y(x, y, z)e^{i\beta_0 z}$, where $\beta_0 = \omega/c$. The propagation of paraxial TM-modes is governed by the paraxial Schrödinger equation (see appendix for details)

$$\left[-\frac{c}{2\beta_0} \nabla_\perp^2 + V \right] \begin{pmatrix} \psi_x \\ \psi_y \end{pmatrix} = i\, c\, \partial_z \begin{pmatrix} \psi_x \\ \psi_y \end{pmatrix}, \tag{6.15}$$

where, $\nabla_\perp^2 = \partial_x^2 + \partial_y^2$, $V(x, y, z)$ describes the position of the metal nanowires, and we have neglected $\partial_z^2 \psi_{\{x,y\}}$ as per the paraxial approximation. Eq. (6.15) has the form of the two-dimensional time-dependent Schrödinger equation with $c\,\partial_z \to \partial_t$, $\psi_{\{x,y\}}$ – the wave function, and $H \equiv -(c/2\beta_0)\nabla_\perp^2 + V(x, y, z)$ – the Hamiltonian operator. Thus, stationary states of H become the TM modes of paraxial light that propagate along the z-direction and the eigenenergies $\mathcal{E}$ of H become the z-wavenumbers $\beta_z = \beta_0 - \epsilon/c$. In [112], Rechtsman et al showed that this analogy can be used to gain intuition about the topological structure of electromagnetic waves by mapping solutions of the Schrödinger equation with non-trivial topology onto the Helmholtz equation.

Let us now consider the SSH model, which was originally used for studying electrons in polyacetylene. The backbone of polyacetylene is a chain of carbon atoms with staggered single and double bonds, schematically depicted in Fig. 50(a). (Here, we assume that the pattern of single and double bonds does not have intrinsic dynamics, but is instead a prescribed function of time.) The discretized version of the Hamiltonian describing the hopping of spinless electrons along the backbone of polyacetylene is

$$H_{\text{SSH}} = -\sum_i t_{i,i+1} \left(c_i^\dagger c_{i+1} + c_{i+1}^\dagger c_i \right) \tag{6.16}$$

where the operator c_i ($c_i^\dagger$) annihilates (creates) an electron on the i-th carbon atom and the hopping matrix element $t_{i,i+1} = t_1(t_2)$ if the bond between sites i and $i+1$ is a single (double) bond. The unit cell of this model consists of a two atom dimer. Let us assume the hopping strength within a dimer is t_1 and the hopping strength between the atoms belonging to two nearby dimers is t_2. Applying the Fourier transform to the Hamiltonian, i.e., $c_{2n} = \sum_k a_k e^{ikRn}$ and $c_{2n+1} = \sum_k b_k e^{ikRn}$, where k is the wave vector, R is the unit cell size, and n is the unit cell index, we obtain

$$H_{\text{SSH}} = -\sum_k \left(t_1 + t_2 e^{-ikR} \right) a_k^\dagger b_k + h.c. \tag{6.17}$$

This Hamiltonian can be written as a 2×2 matrix $H_k = \vec{h}(k) \cdot \vec{\sigma}$, where $\vec{\sigma} = \{\sigma_x, \sigma_y\}$ is a vector of Pauli matrices and $\vec{h}(k) = \{t_1 + t_2 \cos(kR), t_2 \sin(kR)\}$. Note that $||\vec{h}(k)||$ is non-zero throughout the Brillouin zone, indicating that the two bands of the SSH model never

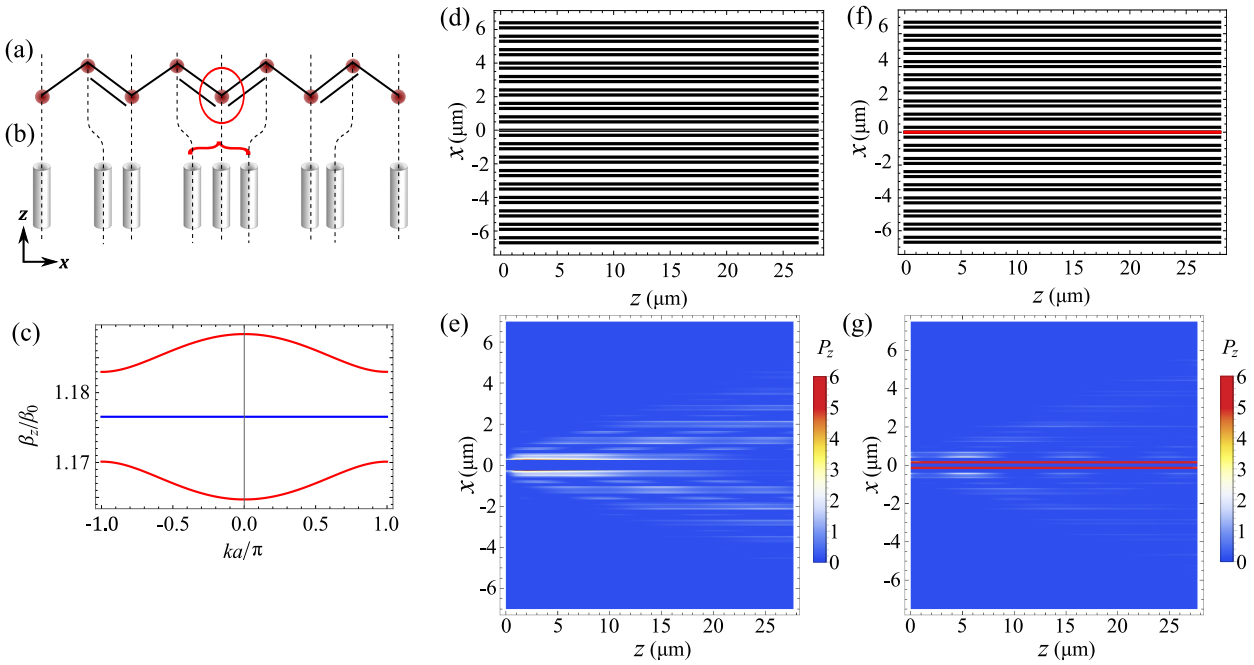

Figure 50: (a) Single-double bond pattern in a polyacetylene chain with a kink defect. The red disks show the carbon atoms. (b) Analogous nanowire array with staggered spacing and a kink defect. (c) Staggered nanowire spacing leads to a band gap for the bulk modes (red), the topological defect mode appears in the middle of the band gap (blue). (d,f) The positions of nanowires in the array without (d) and with (f) a domain wall. (e,g) Spreading of light in the nanowire array without (e) and with (g) a domain wall. The topological defect mode bound to the domain wall is observed guiding light in (g). For this figure we used $\epsilon = -45.83 + 2.49 \times 10^{-9} i$ (the real part of the permittivity is identical to that of silver and the imaginary part was chosen to be very small to highlight the guidance by the topological defect mode.) Geometry parameters used: diameter 200 nm, center-to center spacing 300 and 500 nm, wavelength $\lambda = 1\,\mu$m.

touch. As k traverses the Brillouin zone in 1D, going from $-\pi/R$ to π/R, $\vec{h}(k)$ goes around a circle centered at t_1 with radius t_2. The number of times this trajectory winds around the origin is a topological invariant, being either 0 if $t_1 < t_2$ or 1 if $t_1 > t_2$, corresponding to the two distinct topological phases of the SSH chain. The winding number is directly

related to the Zak phase $\phi_{\text{Zac}} = \int_{-\pi/R}^{\pi/R} \langle\psi|i\partial_k|\psi\rangle\, dk$, which is the 1D equivalence of the Berry phase in higher dimensions [214, 215]. The existence of a topologically protected mode at the boundary of two topologically distinct domains is prescribed by the Atiyah-Singer index theorem [216].

A domain wall in the single-bond double-bond pattern of the chain, as depicted in Fig. 50(a), is a topological defect: locally changing the bond strength around the kink cannot eliminate it as the single- double-bond pattern is a non-local property. Domain walls can, however, be eliminated in pairs by moving them towards each other, as the single-double-bond pattern far away from where the domain walls are being merged is not effected by the merger. Moreover, each domain wall must host a mid-gap state, a topological defect mode, that is localized in the vicinity of the domain wall.

We now investigate the optical equivalent of the SSH topological defect modes in plasmonic crystals. Consider a plasmonic crystal that consists of an array of parallel nanowires with staggered spacing as depicted in Fig. 50(b). The Helmholtz-Schrödinger analogy tells us that for each eigenmode of the SSH Hamiltonian Eq. (6.16), there is an equivalent electromagnetic mode in the plasmonic crystal. We note that the fermionic commutation relations do not play a role here as we are considering the non-interacting case; hence, we can replace the operator $c_i^\dagger$ that creates an electron in a carbon atom atomic orbital by the operator $b_i^\dagger$ that create a surface plasmon on the i-th nanowire. (We present the details of the connection between the continuous and discrete Hamiltonians in the appendix.) Thus the band gap in the electronic system maps onto a β_z gap in the plasmonic system. Moreover, electronic states that are localized on domain walls (and appear inside the band gap) map directly onto guided plasmonic states that propagate along the domain walls in the z-direction [and appear in the β_z gap, see Fig. 50(c)].

Now consider injecting a spatially truncated plane wave into a plasmonic crystal with staggered spacing but no domain walls [Fig. 50(d)]. This is equivalent to injecting an electron into polyacetylene using a local probe like an STM tip. Because the electron is being injected locally, it overlaps many k-modes, and hence the electron wave-packet will spatially spread out as time advances. Similarly, the plasmonic wave packet will expand in the transverse direction as it advances along the z-direction. To illustrate this expansion we introduce the

normalized Poynting vector P_z in the x-z plane that cuts through the middle of the nanowire array

$$P_z(x, y = 0, z) = \frac{\vec{S}(x, y = 0, z) \cdot \hat{z}}{\int dx\, dy\, \vec{S}(x, y, z) \cdot \hat{z}}, \tag{6.18}$$

where $\vec{S}$ is the non-normalized Poynting vector and $\hat{z}$ is the unit vector along the z-direction. Figure 50(e) shows the spreading out of a plasmonic wave-packet obtained using 3D FDTD simulation of the plasmonic crystal. Completing the analogy, the group velocity of the electron in polyacetylene corresponds to the opening angle of the light cone in the plasmonic crystal.

The introduction of a topological defect into the plasmonic crystal [see Fig. 50(b)] gives rise to a localized mode. We expect that light injected in the vicinity of the topological defect couples both to the localized defect mode as well as to the bulk modes. We plot the results of injecting a truncated plane wave into a plasmonic crystal with a topological defect [Fig. 50(f)] in Fig. 50(g). In accord with our expectations, we observe that light coupled into the bulk modes forms a diffracting fan, while light coupled into the topological mode propagates without spreading transversely.

We comment that light guided by a topological defect mode is spatially concentrated. As a figure of merit, we consider the quantity $\lambda^2 P_z$, where λ is the free space wavelength, which measures how much the light is squeezed spatially as compared with diffraction limited optics ($\lambda^2 P_z \approx 1$ at diffraction limit). Plasmonic confinement of light in the topologically guided mode of the structure depicted in Fig. 50(g) results in $\lambda^2 P_z \approx 16.6$.

6.3 Manipulation of light using topological defect modes

In the electronic system, there are two well-established operations for manipulating topological defect modes: (i) shifting the position of a topological domain wall causes the associated topological defect mode to be carried along with the domain wall, and (ii) pairs of domain walls can be nucleated and pulled apart, causing two of the bulk modes to be turned into topological defect modes. In this section, we explicitly apply these operations to achieve

topological manipulation of light in the plasmonic crystal of metal nanowires.

In the Helmholtz-Schrödinger correspondence, ∂_t is mapped to $c\partial_z$, so that time dependent manipulation in the electronic system is mapped onto axial dependent manipulation in the plasmonic crystal. For instance, the time-dependent shifting of domain walls in the electronic picture is mapped to the shifting of the domain walls as a function of the axial position z in the plasmonic crystal, which we achieve through the variation of the nanowire spacing as a function of z.

6.3.1 Topological spatial mode filter

Nucleating two domain walls in the middle of the SSH chain and adiabatically moving them apart results in a spectral flow in which a pair of delocalized electronic states, one from the upper bulk band and one from the lower, are adiabatically transformed into the two mid-gap states spatially localized on the domain walls. We take advantage of this spectral flow to perform spatial mode filtering of light using a plasmonic crystal.

Specifically, we design a plasmonic crystal with a pair of domain walls that are created inside the array and shifted apart as a function of z, see Fig. 51(a). Two of the bulk modes at the input side ($z = 0$) of the array are mapped into the two topological defect modes on the output side ($z = 200\,\mu$m) by the spectral flow, see Fig. 51(b). If one of these two bulk modes is injected into the array, after propagation, the maximum of the light intensity on the output side will be strongly localized around the kinks. To verify this behavior, we perform full 3D FDTD simulations of the structure depicted in Fig. 51(a), and plot the results in Fig. 51(c). We observe that the majority of the light flux is indeed guided into the topological defect modes. On the other hand, if we inject any other bulk mode on the input side it will be rejected by the mode filter and the output light flux in the vicinity of the domain walls will be small (see appendix). We note that the topological defect modes are not always in the center of the band-gap [see Fig. 51(e)] as we are locally slightly breaking the sub-lattice symmetry. Indeed, topological protection endows our device with robustness against exactly these types of perturbations.

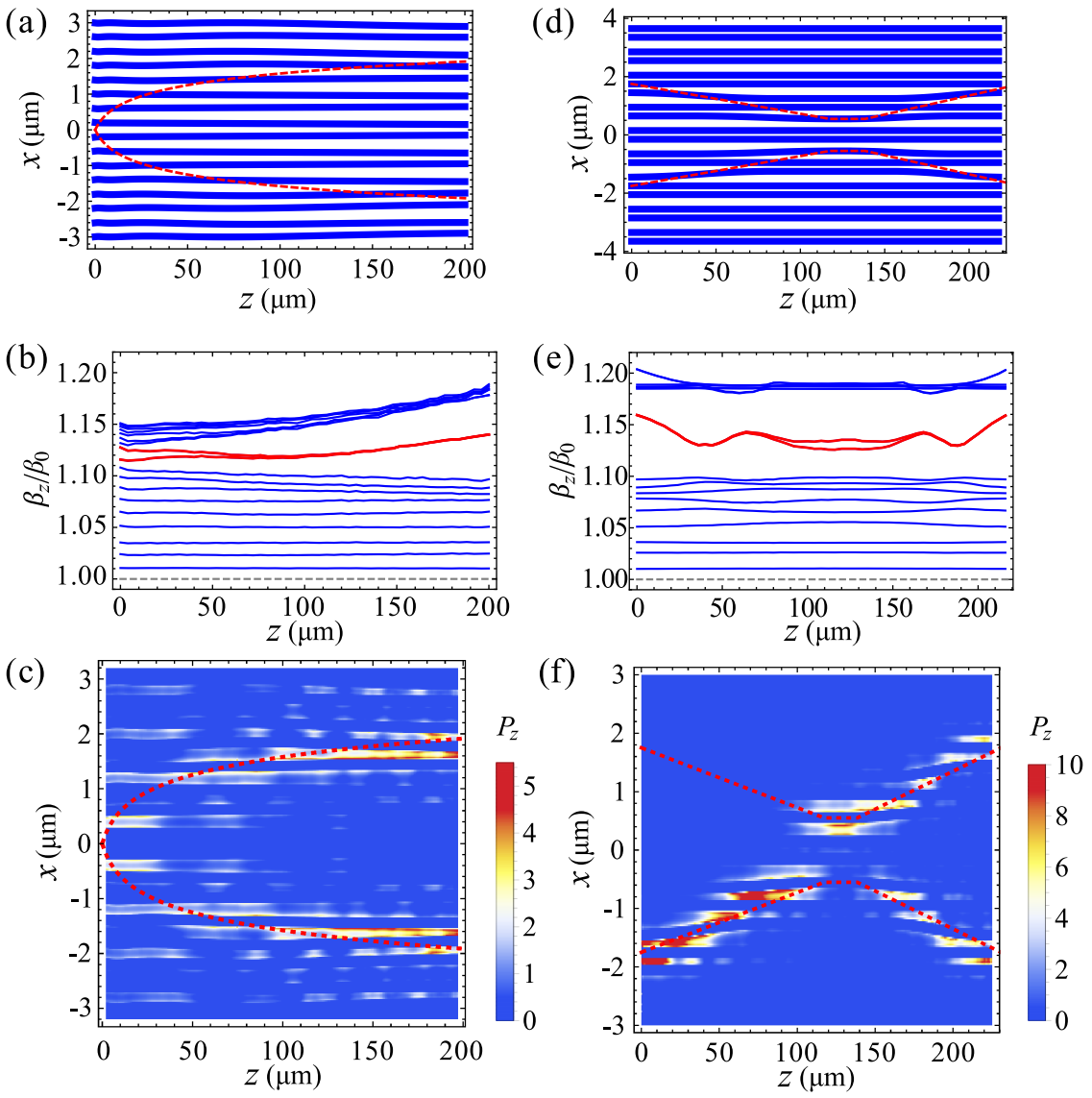

Figure 51: (a,d) Nanowire array geometry for a spatial mode filter (a) and a beam splitter (d). Blue lines indicate the positions of the nanowires and red dashed lines the position of the kinks. (b,e) Spectral flow of bulk modes (blue) and the topological defect modes (red) as a function of z for the spatial mode filter (b) and the beam splitter (e). (c,f) Light propagation through the spatial mode filter (c) and the beam splitter (f), red dashed lines indicate the position of the kinks (see text). Parameters used are same as Fig. 50.

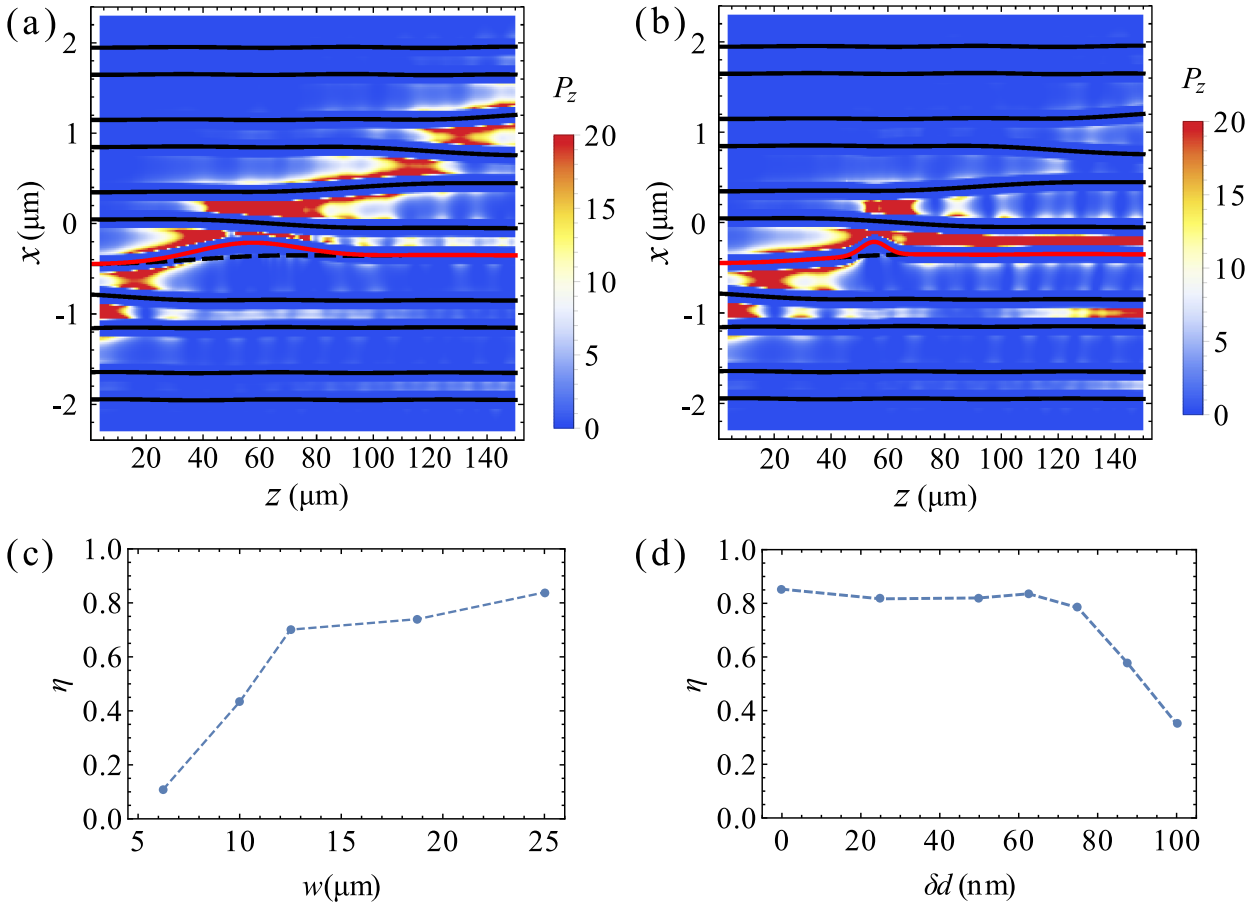

Figure 52: (a,b) Topological defect mode propagation in a nanowire array with a perturbation. The red nanowire is shifted away from its original position indicated by the black dashed line. The smoothness parameter is $w = 25\,\mu m$ in (a) and $w = 6.25\,\mu$m in (b). (see text for details) (c) Fraction of flux retained in the topological defect mode η in a structure with a shifted nanowire perturbation. We vary the smoothness parameter w and fix the displacement parameter $\delta x = 150\,$nm. (d) η in a structure with a nanowire diameter perturbation, the nanowire diameter parameter δd is varied and $w = 25\,\mu$m is fixed. Materials and nanowire geometry parameters are same as Fig. 50.

6.3.2 Beam splitter with topological defect modes

Consider the geometry of a nanowire array depicted in Fig. 51(d): two domain walls that are well separated spatially on the input and output sides of the structure are brought close together in the middle of the structure. The propagation of the two topological defect modes can be described by the Landau-Zener Hamiltonian, in which the coupling is controlled by the spatial separation of the domain walls. The spectral flow of the array along the z direction is shown in Fig. 51(e). When the domain walls are well separated, the topological defect modes are non-interacting, and hence both are in the middle of the gap. As the domain walls are moved closer, the topological defect modes begin to interact and the degeneracy is broken. By controlling the interaction strength and the length of the interaction region it is possible to construct a 50-50 beam splitter. We perform 3D FDTD simulation of the beam splitter in which we inject light into one of the defect modes on the input side and observe an equal superposition of light in the two defect modes on the output side [see Fig. 51(f)].

6.4 Tolerance to perturbations in wire placement and diameter

Consider a structure in which a topological defect mode is guided by a kink that is being shifted as a function of z [see Fig. 52]. To test the tolerance of the light manipulation to perturbations (e.g. manufacturing defects), we measure the amount of light that leaks from the topological defect mode into the bulk modes due to perturbations in the plasmonic nanowire structure. This is a particularly stringent test of mode transport fidelity, as perturbations near the domain wall can affect the structure of the defect mode directly as well as how the defect mode hops from nanowire-to-nanowire as the domain wall is shifted. As it is not possible to test the tolerance to all kinds of perturbations, we focus on two specific types that are likely to occur in experimental situations: meander of a single nanowire and distortions in the diameter of a single nanowire. We note that topological robustness only protect defect modes when they are moved infinitely slowly. In a realistic plasmonic system we would rather move the defect modes as fast as possible to avoid absorption losses which

has the potential to break the adiabatic approximation. It is the tolerance of light manipulation rather than topological mode robustness protected by the chiral symmetry that is examined in this section.

In Figs. 52(a) and 52(b), we compare the results of 3D FDTD simulation for two test structures in which we displace one of the nanowires by the addition of a meander $M(z) = \delta x\, e^{-(z-z_0)^2/w^2}$. In Fig. 52(a) the meander is smooth with $w = 25\,\mu$m, while in Fig. 52(b) the meander is abrupt with $w = 6.25\,\mu$m. The positions of unperturbed wires are indicated with black lines, the original position of the perturbed wire is indicated with black dashed line and its new position with the red line. The color scale shows P_z for light that is injected into the topological defect mode on the left side of the structure. We observe that if the meander is sufficiently smooth the topological mode remains guided along the domain wall [Fig. 52(a)]. However, if the meander is too abrupt there is significant leakage of light into the bulk modes [Fig. 52(b)].

What role does topological protection play here? The spectral flow calculation (see Appendix D) shows that the topological defect mode β_z shifts as $M(z)$ becomes large. This feature is due to the existence of next-nearest-neighbor (NNN) coupling between the nanowires which breaks the sublattice symmetry. As the NNN coupling is exponentially small, the topological defect mode is well protected from nanowire meander disorder (see Appendix D for details).

Despite the topological protection from perturbations that respects sub-lattice symmetry, these perturbations can still break adiabaticity (i.e., an abrupt meander) to give heavy leakage. This is a consequence of the fact that while topological protection ensures that the defect mode is pinned to the middle of the topological band-gap, the wave function of the topological mode still depends on the perturbation. Thus if the perturbation is turned on sufficiently abruptly, on a length scale $\approx \Delta\beta_z$, adiabaticity will break down. To quantify the amount of leakage caused by a perturbation, we introduce the quantity η,

$$\eta = \frac{1}{2}\int dx\, dy\, (\vec{E}_\alpha \times \vec{H} + \vec{E} \times \vec{H}_\alpha) \cdot \hat{z}, \tag{6.19}$$

where $\vec{E}_\alpha$ and $\vec{H}_\alpha$ are the electric and magnetic fields that correspond to the guided mode ($\eta = 1$ perfect guidance, $\eta = 0$ complete leakage). In Fig. 52(c) we plot η as a function of

the smoothness parameter w. We observe a dramatic loss of adiabaticity for $w \lesssim 10\mu m$.

Perturbations of the nanowire diameter, as opposed to position, are potentially more problematic as these explicitly break the sublattice symmetry [by affecting the plasmon self-energy]. We investigate a series of structures similar to the one depicted in Fig. 52(a), but instead of shifting the red wire, we modify its diameter $D(z) = D_0 - \delta d\, e^{-(z-z_0)^2/w^2}$, where $D_0 = 200\,\text{nm}$ is the unperturbed diameter. We plot η as a function of δd in Fig. 52(d). We observe robustness to small perturbations followed by a sharp drop in η for large perturbations. The loss of transport fidelity is again associated with the loss of adiabaticity. However, due to the sublattice symmetry breaking nature of the perturbation, the loss of adiabaticity occurs prematurely as the defect mode is pushed close to the edge of the topological band-gap. That is the defect mode is indeed protected from small perturbations in the nanowire diameter (and other non-avoidable symmetry-breaking perturbations) by the topological band gap.

In summary, the device is quite tolerant to perturbations in both the nanowire position and diameter. Indeed, the device is very tolerant to nanowire position errors, which preserves the chiral symmetry if the NNN interaction is ignored. In order to see strong leakage from the topological defect mode into the bulk modes we need to displace a nanowire until it is almost touching its neighbor. The device is more sensitive to nanowire diameter which breaks the chiral symmetry, however it is still tolerant to diameter errors of $\sim 30\%$.

6.5 Detailed discussion and calculation of the topological plasmonic system

6.5.1 The paraxial Schrödinger equations

The propagation of electromagnetic waves is governed by the Helmholtz equation

$$\left(\nabla^2 + \frac{\omega^2}{c^2}\epsilon\right)\left\{\begin{array}{c}\vec{E}\\ \vec{B}\end{array}\right\} = -\left\{\begin{array}{c}\nabla\left(\epsilon^{-1}\nabla\epsilon\cdot\vec{E}\right)\\ \epsilon^{-1}\nabla\epsilon\times\left(\nabla\times\vec{B}\right)\end{array}\right\} \tag{6.20}$$

where $\epsilon(x,y,z)$ is the position-dependent relative permittivity, $\vec{E}(x,y,z)$, $\vec{B}(x,y,z)$ are the electric and magnetic field components, and the right hand side encodes the boundary con-

ditions at the metal-air interface. For the case of dielectric waveguides, the dielectric constant tends to vary gently, and hence the terms on the right hand side of Eq. (6.20) can be neglected. Therefore it is natural to obtain the paraxial Schödinger equation from the Helmholtz equation for E_z. For metallic structures variations of ϵ cannot be neglected. However, for structures that are translationally invariant in z-direction, $\nabla\epsilon$ only has transverse components. Hence, it is natural to focus on the transverse components E_x and E_y, as the Helmholtz equations for those components have closed form. For TM-modes propagating at small angles to the z-axis it is natural to implement the paraxial approximation, which leads us to the paraxial Schrödinger equation, Eq. (6.15). The potential energy operator, that appears in Eq. (6.15), is given by

$$V(x,y,z) = \frac{\omega}{2}(1-\epsilon) + c \begin{pmatrix} \nabla_x \left(\frac{\nabla_x \epsilon}{\epsilon}\right) & \nabla_x \left(\frac{\nabla_y \epsilon}{\epsilon}\right) \\ \nabla_y \left(\frac{\nabla_x \epsilon}{\epsilon}\right) & \nabla_y \left(\frac{\nabla_y \epsilon}{\epsilon}\right) \end{pmatrix},$$

where the second term accounts for the boundary conditions at the metal-air interface.

6.5.2 Connecting the continuous and discrete Helmholtz equations

In this subsection, we connect the continuous description of electromagnetic waves shown in Eq. (6.15) with the discrete description of the SSH model given by the Hamiltonian

$$H_{\text{SSH}} = -\sum_i t_{i,i+1}\left(c_i^\dagger c_{i+1} + c_{i+1}^\dagger c_i\right) + v_i c_i^\dagger c_i. \tag{6.21}$$

This Hamiltonian is an extension of Eq. (6.16), where we have added the on-site energy v_i which will be used to describe the plasmon self-energy. We note that this connection is only precise in the limit of weak coupling (i.e., when the distance between nanowires is sufficiently large compared to the wavelength of light). In the strong coupling limit the topological properties of the Helmholtz equation remain intact but the tight-binding model can no longer be used to accurately describe light propagation. Consequently we use full 3D FDTD solutions of the Helmholtz equation throughout the main text.

Our strategy to make the connection is to (1) describe the plasmon "self-energy" by modeling a single nanowire, and (2) describe the plasmon hopping by modeling two nanowires.

We begin by considering a single nanowire of the type that makes up the plasmonic crystal. The single nanowire has a well defined plasmon mode, i.e., a radially symmetric solution of Eq. (6.15) of the form $\psi(x, y, z) = \psi_1(x, y)e^{i\beta_1 z}$. We can capture the plasmon self-energy β_1, by setting $v_i = c(\beta_0 - \beta_1)$ in Eq. (6.21).

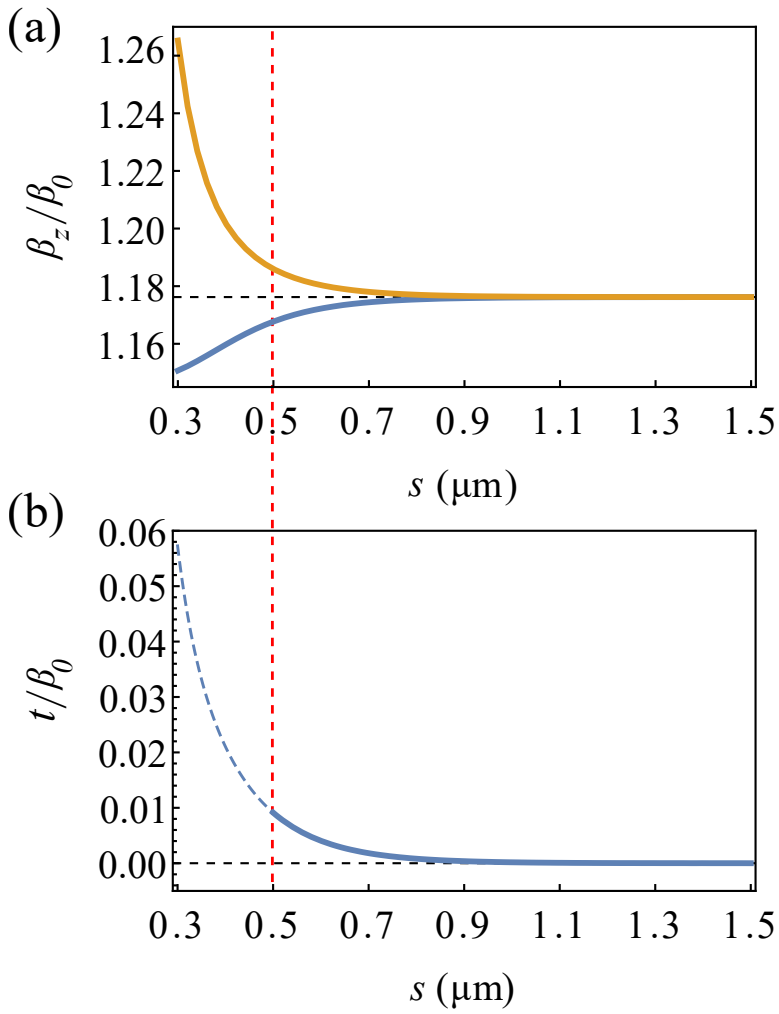

Figure 53: (a) The splitting of the symmetric and antisymmetric plasmon modes (for $\lambda = 1\,\mu$m in vacuum) in a system of two parallel silver nanowires with 100 nm radius, as a function of the nanowire center-to-center separation s. The black dashed line indicates the single nanowire eigenvalue β_1. (b) Extracted tight-binding parameter t as a function of spacing between two nanowires. The tight-binding model starts to break down when the spacing between the two nanowire goes below $0.5\,\mu$m (indicated by the dashed red line).

Next, we consider the plasmon modes of a system of two parallel nanowires separated by distance s. The plasmon spectrum is now composed of two modes $\psi_{\pm}$ with eigenvalues $\beta_{\pm}$. These are approximately the symmetric $\psi_{+} \approx (\psi_1(x + s/2, y) + \psi_1(x - s/2, y))/\sqrt{2}$ and the antisymmetric $\psi_{-} \approx (\psi_1(x + s/2, y) - \psi_1(x - s/2, y))/\sqrt{2}$ combinations of the single nanowire modes. Comparing this spectrum with the spectrum of the two site discrete model, we identify $t = (\beta_{+} - \beta_{-})/2$. In Fig. 53(a) we plot β_z of the symmetric and antisymmetric modes obtained using the Helmholtz equations as a function of s. We observe that the splitting of the symmetric and antisymmetric modes with respect to the single-nanowire β_1 (black dash line) is even for $s > 0.5\,\mu$m and hence we can extract the tight binding parameter t. For $s < 0.5\,\mu$m the splitting becomes uneven signaling the breakdown of the tight binding model. We plot the extracted tight-binding parameter $t = (\beta_{+} - \beta_{-})/2$, which is applicable for $s > 0.5\,\mu$m, in Fig. 53(b).

6.5.3 Mode filtering

In Fig. 54 we demonstrate an example of mode rejection by the mode filter. We inject a mode that is not adiabatically connected to the two topological defect modes in the structure. The light flux spreads out over the whole structure except for the area in the vicinity of the two topological defects.

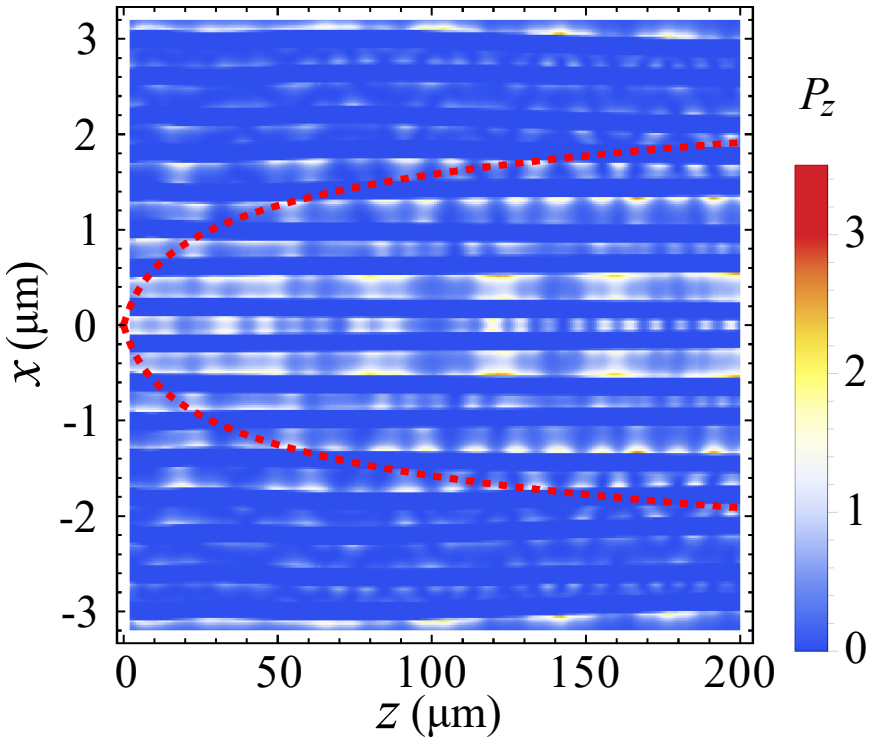

Figure 54: Mode rejection by the mode filtering nanowire array. On the input (left) side of the nanowire array, a bulk mode that is orthogonal to the two select modes, is injected into the nanowire array. On the output (right) side there is essentially no light in the vicinity of the two topological defect modes.

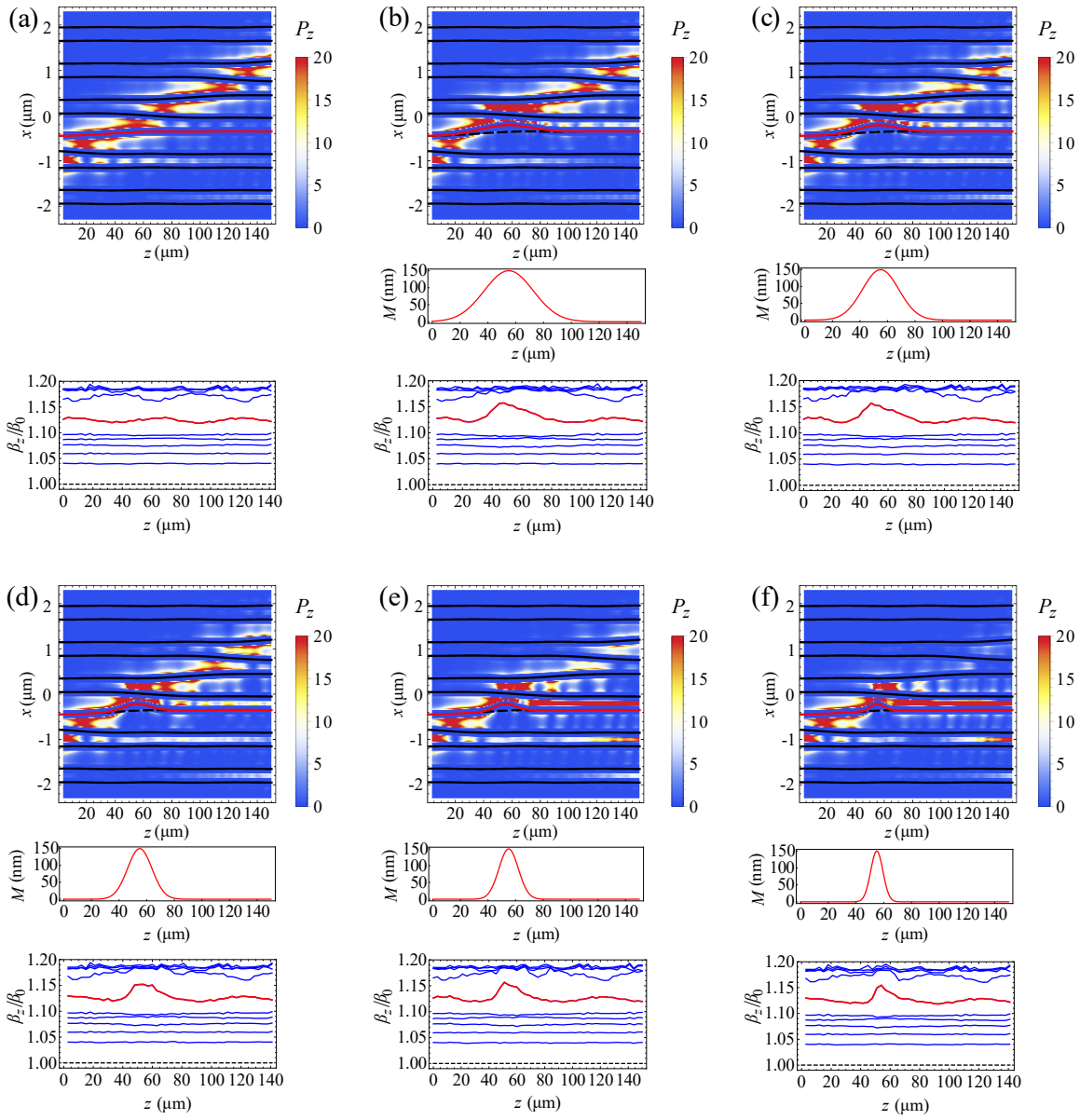

Figure 55: Light propagation along structures with a perturbation on the position of one of the nanowires. (a) Light flux (top panel) and the spectral flow (bottom panel) in a structure with no perturbation. (b)-(f) Light flux (top panel), meander $M(z)$ (middle panel), and spectral flow (bottom panel) in structures with one of the nanowires displaced from its original position (dashed line in top panel) to a new position (red line in top panel). The nanowire is displaced by $\delta x = 150$ nm over a width of $w = 25.00\,\mu$m (b), $18.75\,\mu$m (c), $12.50\,\mu$m (d), $10.00\,\mu$m (e), $6.25\,\mu$m (f).

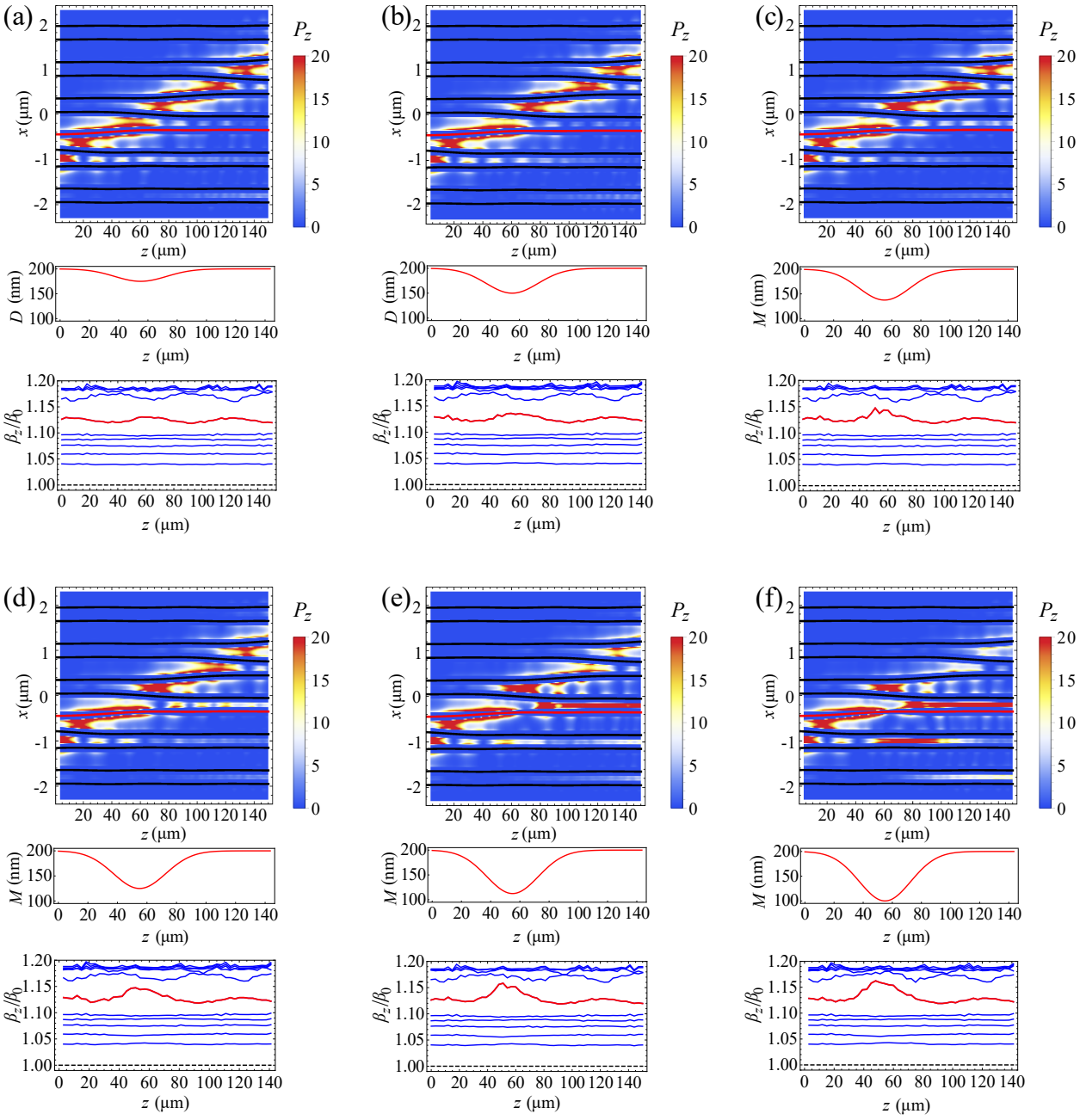

Figure 56: Same as Fig. 55, except we perturb the diameter $D(z)$ of the red nanowire. We fix the perturbation width at $w = 25\mu$m, and shrink the nanowire diameter by $\delta D = 25.0\,$nm (a), $\delta D = 50.0\,$nm (b), $\delta D = 62.5\,$nm (c), $\delta D = 75.0\,$nm (d), $\delta D = 87.5\,$nm (e), $\delta D = 100\,$nm (f).

6.5.4 Tolerance to fabrication error

In this set of figures we provide additional data for the same set of structures that were used to construct Fig. 52 of the main text. The data demonstrate the tolerance of the topological defect mode manipulation against perturbation in nanowire position and diameter. The top panel of Fig 55(a) shows the light flux computed using 3D FDTD in a structure with a single topological defect shifting across the nanowire array. Light is injected into the topological defect mode on the left side of the array. The light is guided in the middle of the nanowire array and remains confined to the topological defect until it exits the array on the right side. The bottom panel of Fig 55(a) shows the spectral flow of the β_z spectrum as a function of position along the wire (similar to Figs. 51(b) and 51(e) of the main text). The spectrum plot shows that the defect mode is well separated from the bulk modes throughout the structure.

Next, we test tolerance to perturbations by displacing the red nanowire by a Gaussian with maximum displacement of δx and a width w. In Figs. 55(b)-55(f) we plot the light flux, wire displacement, and the spectral flow of the β_z spectrum as a function of z for $\delta x = 150$ nm and w ranging from $25\,\mu$m to $6.25\,\mu$m. From the light flux plots (top panels), we observe that the light intensity is well guided when $w \gtrsim 12.5\,\mu$m. For $w \lesssim 10.00\,\mu$m, light flux heavily leaks into the bulk modes. The reason for this, is the breaking of adiabaticity as $w \lesssim 1/\Delta\beta_z$.

Figure. 56 is similar to Fig. 55, except we perturb the diameter D of the red nanowire. The unperturbed nanowire has a diameter of 200 nm, and we shrink it by 25.0nm to 100.0 nm in Figs. 56(a)-56(f). The perturbation profiles have a fixed width of $25\,\mu$m. Topological mode guidance starts to break down when the diameter shrinks by 87.5 nm as the β_z of the guided mode is approaching the bulk spectrum.

We note that the topological defect modes in Fig. 55 are shifted slightly from the middle of the band gap when we introduce disorder on the nanowire position. This shift is caused by the exponentially weak next-nearest-neighbor (NNN) hopping of the plasmons, which breaks the sub-lattice symmetry. Indeed, the effect of the NNN interaction on the energy of the topological defect mode (in polyacetylene) has been studied before [217, 218, 219, 220].

6.5.5 Decay of the topological defect mode

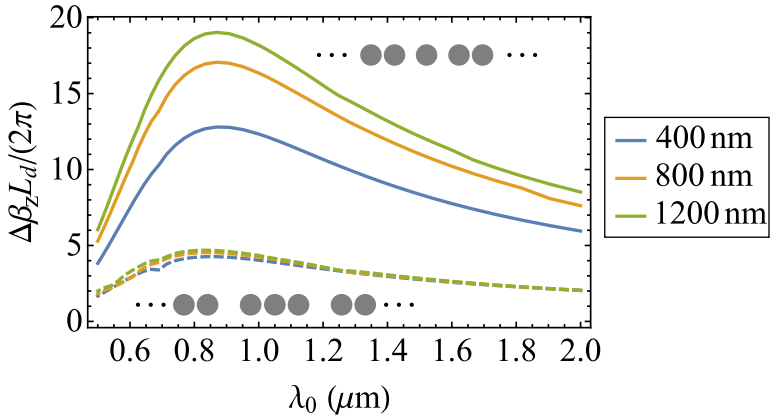

Figure 57: The Figure of Merit ($\Delta\beta L_d/(2\pi)$) as a function of the free space wavelength (λ_0) for a silver nanowire array with nanowire diameter 400 nm, 800 nm and 1200 nm. The major and minor surface-to-surface spacing is 350 nm and 50 nm respectively. The dashed lines show the topological defect with minor spacing around the defect while the solid lines show the topological defect with major spacing, as indicated in the insets.

In this section, we compute the decay length of the topological defect modes using complex susceptibility for silver nanowire structures. We use Lumerical Mode Solution numerical eigenmode solver to obtain complex β_z and extract the decay length for two types of topological defects (see Fig. 57 inset). Specifically, we simulate a nanowire array consisting of 7 nanowires with periodic boundary conditions. The nanowires have a diameter of either 400, 800, or 1200 nm and staggered surface-to-surface spacing of 50 nm and 350 nm. The key figure of merit is FOM $= \Delta\beta_z L_d/(2\pi)$. Here, $\Delta\beta_z$ is the topological band gap, which sets the length scale for adiabatic manipulation of topological defects; $L_d = 1/\mathrm{Im}[\beta_z]$ is the decay length for the topologically guided mode.

In Fig. 57 we plot the FOM as a function of free space wavelength (λ_0) for two flavors of topological defects: domain wall with major spacing (solid lines) and domain wall with minor spacing (dashed lines). We observe that FOM for topological defects with major spacing is larger than the FOM for defects with minor spacing. The reason for this is the large penetration of the electric field into the nanowires for the kink with minor spacing [see

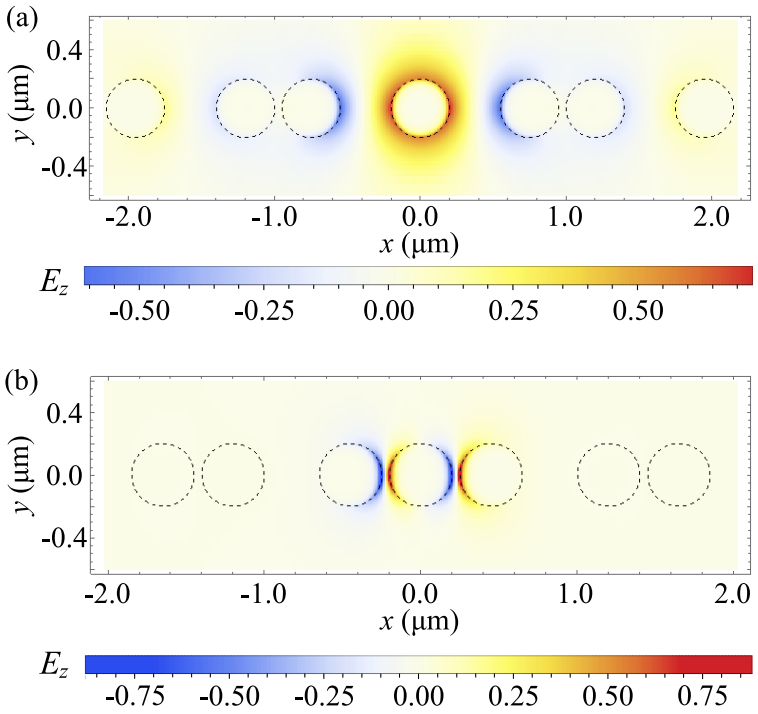

Figure 58: The electric field z component (E_z) of the topological defect mode around two kinds of defects, (a) a topological defect with major spacing, and (b) a defect with minor spacing. The E_z field is calculated based on a 400 nm diameter silver nanowire array with a staggered surface-to-surface spacing 50 nm and 350 nm. The dashed circles show the position of the nanowires.

plots of the mode structure, Fig. 58]. We also observe that the FOM has a broad maximum around 900 nm, which defines an optimal wavelength for silver structures. The maximum is a result of the competition between the topological band gap (which decreases with increasing wavelength) and the decay length (which increases with increasing wavelength). Finally, we observe that the FOM for domain wall with major spacing is larger for larger diameter nanowires, which is a consequence of the suppression of L_d as the wire diameter becomes smaller than wavelength.

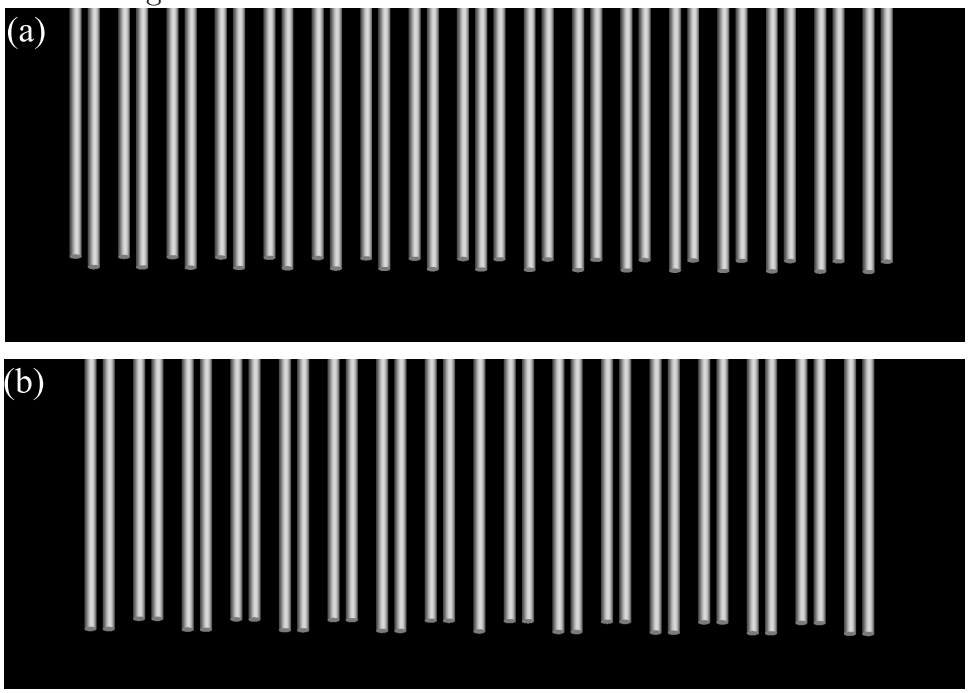

Figure 59: The schematic nanowire array geometry at the beginning of an array with minor-spacing defect (a), and major-spacing defect (b). The beginning of the nanowire array is staggered to match the phase different between the nearby nanowires in topological defect mode. The length difference between the nanowire is determined by the exaction method and plasmonic mode wavelength in the nanowire array.

6.5.6 Phase matching to improve coupling to the topological defect mode

Finally, we make a remark regarding Ref. [114], which claims to experimentally detect topologically guided modes in the type of structures that we propose. We found that the

analysis carried out in Ref. [114] is flawed. Specifically, (i) there is breakdown of the coupled-mode theory, which predicts velocities of modes that are faster than the speed of light (ii) there is zero overlap of the injected mode with the topological mode in minor-spacing defect array due to symmetry reasons.

The the self-energy in the coupled mode theory results in the real part of mode index $\beta = 1.047k_0$, where k_0 is the free space wavenumber. According to their coupled mode theory calculation, the lower band edge reaches $\beta_z \approx \beta - 0.225\,k_0$, which corresponds to $\beta_z \approx 0.822k_0$. This value of the mode index indicates that the mode is propagating faster than the speed of light, which signals the breakdown of the coupled mode theory.

The topological protected defect modes in major-spacing case is symmetric while minor-spacing case tends to have an anti-symmetric nature [see Fig. 58]. In real experiment, if the plasmonic mode is injected directly into the beginning of the nanowire array without any modification of the plasmonic field, the mode is likely to be symmetric and fails to couple to the topological defect mode in minor-spacing case. Here we proposed a way of modifying the length of the nanowires at the beginning of the nanowire array to induce phase difference between the nanowires [see Fig. 59], in order to improve topological mode coupling efficiency. If we assume a truncated plane wave injected into the plasmonic nanowire arrays shown in Fig. 59 from above and the plasmon is excited at the edges of each nanowire, in order the achieve the π-phase shift between the defect nanowire and the nearby nanowires [see Fig. 58], the nanowire length difference should be $\Delta l = \pi/\beta$, where β is the wave-number of the plasmonic mode. The different staggered pattern in minor-spacing defect array [Fig. 59(a)] and major-spacing defect array [Fig. 59(b)] is because of the distinct phase profile of the topological defect modes in these two nanowire arrays.

6.6 Outlook and summary

One of the key issue of plasmonic devices is the absorption of light due to finite optical conductivity in metals and hence a small but finite imaginary part of the dielectric constant. A useful figure of merit is FOM $= \Delta\beta_z L_d/(2\pi)$ the product of the decay length and the

topological band gap. The FOM counts how many adiabatic operations we can do on a topologically guided mode before it decays by $1/e$. The proposed topological mode filter and beam splitter both require ~ 50 operations. For silver nanostructures with $\lambda \sim 900\,\mathrm{nm}$ (in vacuum), we find that the FOM $\sim 5 - 20$ depending on the details of the structure (see appendix). From the experimental perspective, these are appealing length scales due to the availability of lasers and the ease of nano-fabrication. Moreover, for demonstration purposes the attenuation is quite reasonable. Applications would require further optimization of the structure to limit attenuation.

In summary, we have provided an in-depth analysis of the plasmonic analogue of the topological protected defect modes in the SSH model theoretically. We have explored using topological defect modes to manipulate light. Specifically, we numerically demonstrated the functionality of two devices: a mode filter and a beam splitter. Moreover, we showed that light manipulation is tolerant to fabrication errors in nanowire diameter and very tolerant to fabrication errors in nanowire displacement.

7.0 Conclusions

To conclude, we summarize the key results of the theoretical investigation on the quantum systems discussed in this thesis.

In Chapter 3, we investigate the electronic structures of the Nitrogen-Vacancy centers in diamond. With the understanding of the electronic structures and the transitions between the electronic states of NV centers, inspired by Ref. [136], we proposed two-qubit quantum gates for pairs of NV centers in diamond heralded on a single scattered photon. We modeled the coupling between NV centers and the diamond waveguide for light collection to analyze the gate fidelity and success rate. With the photon collection efficiency approaching ~ 0.85, the gate fidelity can reach ~ 0.97, when we impose a photon collection window of 0.1 times of averaged state-flipping transition rates.

In Chapter 4, we investigated the dynamics of a Josephson Ring Modulator based Josephson parametric amplifier (JPA). Using the circuit input-output relations, we modeled the response of the JPA and the reflection gain of the amplifier beyond the linear approximation. We notice that the saturation performance of JPA is controlled by the nonlinearity provided by the Josephson junctions, not only the lowest order (3rd order nonlinearity), but also more higher order nonlinearities. To further optimize the saturation power of the device, we proposed to use the outer linear inductance to diluting the higher order nonlinear couplings. We numerically optimize the JPA and achieve ~ 15 dB saturation power improvement. The analytical model for the Josephson devices discussed in this paper also helps to explain and model the other physical processes and similar devices in Prof. Michael Hatridge's lab.

In Chapter 5, we present the theory of a narrow-linewidth Josephson micromaser. We show that using a transmon-type qubit with SNAIL element to bath engineer the transmon qubit to achieve an effective incoherent drive on the transmon qubit to make it population inversion. We further take advantages of the nonlinear coupling provided by the Josephson junctions in superconducting circuit to construct a Josephson micromaser that emits quantum light. By carefully engineering the nonlinear coupling between the transmon qubit and the maser cavity (resonator), as well as between the maser cavity (resonator) and the

transmission line (the bath), the emitted light from the nonlinear Josephson micromaser system has a narrow linewidth that is beyond the linewidth of the Schawlow-Townes limit, the standard linewidth of the conventional laser with linear coupling. In the parameters we chose, the linewidth of the nonlinear Josephson micromaser can be ~ 0.10 times of the Schawlow-Townes limit.

In Chapter 6, we focus on the plamsonic nanowire system that consists of paraxial nanowire arrays. In these nanowire arrays where the paraxial approximation is applied, the plasmon propagation along the axial direction can be mapped to the time-evolution of the lower dimensional quantum system. we designed the geometry of the nanowire arrays to map the plasmon propagation to Su-Schrieffer-Heeger model, where the edge modes in plasmonic array maps to the topologically protected modes in SSH model. We use the topological mode in the plamonic array to robustly manipulate the light. Specifically, we proposed a topological waveguide, a spatial mode filter and a beam splitter, and check the functionality of the proposed devices by 3D FDTD numerical method.

Bibliography

[1] Richard P. Feynman. Simulating physics with computers. *International Journal of Theoretical Physics*, 21(6):467–488, Jun 1982.

[2] Seth Lloyd. Universal quantum simulators. *Science*, 273(5278):1073–1078, 1996.

[3] I. M. Georgescu, S. Ashhab, and Franco Nori. Quantum simulation. *Rev. Mod. Phys.*, 86:153–185, Mar 2014.

[4] Bela Bauer and Chetan Nayak. Analyzing many-body localization with a quantum computer. *Phys. Rev. X*, 4:041021, Nov 2014.

[5] Michael Schreiber, Sean S. Hodgman, Pranjal Bordia, Henrik P. Lüschen, Mark H. Fischer, Ronen Vosk, Ehud Altman, Ulrich Schneider, and Immanuel Bloch. Observation of many-body localization of interacting fermions in a quasirandom optical lattice. *Science*, 349(6250):842–845, 2015.

[6] Jae-yoon Choi, Sebastian Hild, Johannes Zeiher, Peter Schauß, Antonio Rubio-Abadal, Tarik Yefsah, Vedika Khemani, David A. Huse, Immanuel Bloch, and Christian Gross. Exploring the many-body localization transition in two dimensions. *Science*, 352(6293):1547–1552, 2016.

[7] Tiff Brydges, Andreas Elben, Petar Jurcevic, Benoît Vermersch, Christine Maier, Ben P. Lanyon, Peter Zoller, Rainer Blatt, and Christian F. Roos. Probing rényi entanglement entropy via randomized measurements. *Science*, 364(6437):260–263, 2019.

[8] K. A. Landsman, C. Figgatt, T. Schuster, N. M. Linke, B. Yoshida, N. Y. Yao, and C. Monroe. Verified quantum information scrambling. *Nature*, 567(7746):61–65, Mar 2019.

[9] L. García-Álvarez, I. L. Egusquiza, L. Lamata, A. del Campo, J. Sonner, and E. Solano. Digital quantum simulation of minimal AdS/CFT. *Phys. Rev. Lett.*, 119:040501, Jul 2017.

[10] Ryan Babbush, Dominic W. Berry, and Hartmut Neven. Quantum simulation of the sachdev-ye-kitaev model by asymmetric qubitization. *Phys. Rev. A*, 99:040301, Apr 2019.

[11] Frank Arute, Kunal Arya, Ryan Babbush, Dave Bacon, Joseph C. Bardin, Rami Barends, Rupak Biswas, Sergio Boixo, Fernando G. S. L. Brandao, David A. Buell, Brian Burkett, Yu Chen, Zijun Chen, Ben Chiaro, Roberto Collins, William Courtney, Andrew Dunsworth, Edward Farhi, Brooks Foxen, Austin Fowler, Craig Gidney, Marissa Giustina, Rob Graff, Keith Guerin, Steve Habegger, Matthew P. Harrigan, Michael J. Hartmann, Alan Ho, Markus Hoffmann, Trent Huang, Travis S. Humble, Sergei V. Isakov, Evan Jeffrey, Zhang Jiang, Dvir Kafri, Kostyantyn Kechedzhi, Julian Kelly, Paul V. Klimov, Sergey Knysh, Alexander Korotkov, Fedor Kostritsa, David Landhuis, Mike Lindmark, Erik Lucero, Dmitry Lyakh, Salvatore Mandrà, Jarrod R. McClean, Matthew McEwen, Anthony Megrant, Xiao Mi, Kristel Michielsen, Masoud Mohseni, Josh Mutus, Ofer Naaman, Matthew Neeley, Charles Neill, Murphy Yuezhen Niu, Eric Ostby, Andre Petukhov, John C. Platt, Chris Quintana, Eleanor G. Rieffel, Pedram Roushan, Nicholas C. Rubin, Daniel Sank, Kevin J. Satzinger, Vadim Smelyanskiy, Kevin J. Sung, Matthew D. Trevithick, Amit Vainsencher, Benjamin Villalonga, Theodore White, Z. Jamie Yao, Ping Yeh, Adam Zalcman, Hartmut Neven, and John M. Martinis. Quantum supremacy using a programmable superconducting processor. *Nature*, 574(7779):505–510, 2019.

[12] Jerry Chou and Jay Gambetta. Quantum takes flight: Moving from laboratory demonstrations to building systems. `https://www.ibm.com/blogs/research/2020/01/quantum-volume-32/`.

[13] Jeremy Hsu. CES 2018: Intel's 49-qubit chip shoots for quantum supremacy. `https://spectrum.ieee.org/tech-talk/computing/hardware/intels-49qubit-chip-aims-for-quantum-supremacy`, Jan 2018.

[14] Rigetti website. `https://rigetti.com/`.

[15] Allison Linn. With new Microsoft breakthroughs, general purpose quantum computing moves closer to reality. `https://news.microsoft.com/features/new-microsoft-breakthroughs-general-purpose-quantum-computing-moves-closer-reality/`.

[16] K. Wright, K. M. Beck, S. Debnath, J. M. Amini, Y. Nam, N. Grzesiak, J.-S. Chen, N. C. Pisenti, M. Chmielewski, C. Collins, K. M. Hudek, J. Mizrahi, J. D. Wong-Campos, S. Allen, J. Apisdorf, P. Solomon, M. Williams, A. M. Ducore, A. Blinov, S. M. Kreikemeier, V. Chaplin, M. Keesan, C. Monroe, and J. Kim. Benchmarking an 11-qubit quantum computer. *Nature Communications*, 10(1):5464, Nov 2019.

[17] D-Wave announces D-Wave 2000Q quantum computer and first system order. https://www.dwavesys.com/press-releases/d-wave%C2%A0announces%C2%A0d-wave-2000q-quantum-computer-and-first-system-order.

[18] M.A. Nielsen and I.L. Chuang. *Quantum Computation and Quantum Information*. Cambridge Series on Information and the Natural Sciences. Cambridge University Press, 2000.

[19] T.H. Cormen, C.E. Leiserson, R.L. Rivest, and C. Stein. *Introduction to Algorithms*. Computer science. MIT Press, 2009.

[20] H.R. Lewis and C.H. Papadimitriou. *Elements of the Theory of Computation*. Prentice-Hall Software Series. Prentice-Hall, 2nd edition, 1998.

[21] Ding-Zhu Du and Ker-I Ko. *Theory of Computational Complexity*. John Wiley & Sons, Incorporated, Somerset, US, 2014.

[22] M. Sipser. *Introduction to the Theory of Computation*. Cengage Learning, 3rd edition, 2012.

[23] P. W. Shor. Algorithms for quantum computation: Discrete logarithms and factoring. In *Proceedings of the 35th Annual Symposium on Foundations of Computer Science*, SFCS '94, pages 124–134, Washington, DC, USA, 1994. IEEE Computer Society.

[24] Peter W. Shor. Polynomial-time algorithms for prime factorization and discrete logarithms on a quantum computer. *SIAM Journal on Computing*, 26(5):1484–1509, 1997.

[25] Lov K. Grover. A fast quantum mechanical algorithm for database search. In *Proceedings of the Twenty-eighth Annual ACM Symposium on Theory of Computing*, STOC '96, pages 212–219, New York, NY, USA, 1996. ACM.

[26] Daniel R. Simon. On the power of quantum computation. *SIAM Journal on Computing*, 26(5):1474–1483, Oct 1997.

[27] Lance Fortnow and John Rogers. Complexity limitations on quantum computation. *Journal of Computer and System Sciences*, 59(2):240 – 252, 1999.

[28] A. Chi-Chih Yao. Quantum circuit complexity. In *Proceedings of 1993 IEEE 34th Annual Foundations of Computer Science*, Proceedings of 1993 IEEE 34th Annual Foundations of Computer Science, pages 352–361, 1993.

[29] Stephen A. Fenner, Frederic Green, Steven Homer, and Randall Pruim. Determining acceptance possibility for a quantum computation is hard for the polynomial hierarchy. *Proceedings of the Royal Society of London. Series A: Mathematical, Physical and Engineering Sciences*, 455:3953 – 3966, 1998.

[30] Barbara M. Terhal and David P. DiVincenzo. Adaptive quantum computation, constant depth quantum circuits and arthur-merlin games. *Quantum Inf. Comput.*, 4:134–145, 2004.

[31] Scott Aaronson. The equivalence of sampling and searching. *Theory of Computing Systems*, 55:281–298, 2013.

[32] Aram W. Harrow and Ashley Montanaro. Quantum computational supremacy. *Nature*, 549(7671):203–209, Sep 2017.

[33] Edward Farhi and Aram Wettroth Harrow. Quantum supremacy through the quantum approximate optimization algorithm. *arXiv: Quantum Physics*, 2016.

[34] Zhihui Wang, Stuart Hadfield, Zhang Jiang, and Eleanor G. Rieffel. Quantum approximate optimization algorithm for maxcut: A fermionic view. *Phys. Rev. A*, 97:022304, Feb 2018.

[35] Leo Zhou, Sheng-Tao Wang, Soonwon Choi, Hannes Pichler, and Mikhail D. Lukin. Quantum approximate optimization algorithm: Performance, mechanism, and implementation on near-term devices. *Phys. Rev. X*, 10:021067, Jun 2020.

[36] F. Jelezko, T. Gaebel, I. Popa, A. Gruber, and J. Wrachtrup. Observation of coherent oscillations in a single electron spin. *Phys. Rev. Lett.*, 92:076401, Feb 2004.

[37] F. Jelezko, T. Gaebel, I. Popa, M. Domhan, A. Gruber, and J. Wrachtrup. Observation of coherent oscillation of a single nuclear spin and realization of a two-qubit conditional quantum gate. *Phys. Rev. Lett.*, 93:130501, Sep 2004.

[38] M. V. Gurudev Dutt, L. Childress, L. Jiang, E. Togan, J. Maze, F. Jelezko, A. S. Zibrov, P. R. Hemmer, and M. D. Lukin. Quantum register based on individual electronic and nuclear spin qubits in diamond. *Science*, 316(5829):1312–1316, 2007.

[39] P. Neumann, N. Mizuochi, F. Rempp, P. Hemmer, H. Watanabe, S. Yamasaki, V. Jacques, T. Gaebel, F. Jelezko, and J. Wrachtrup. Multipartite entanglement among single spins in diamond. *Science*, 320(5881):1326–1329, 2008.

[40] Gopalakrishnan Balasubramanian, Philipp Neumann, Daniel Twitchen, Matthew Markham, Roman Kolesov, Norikazu Mizuochi, Junichi Isoya, Jocelyn Achard, Johannes Beck, Julia Tissler, Vincent Jacques, Philip R. Hemmer, Fedor Jelezko, and Jörg Wrachtrup. Ultralong spin coherence time in isotopically engineered diamond. *Nature Materials*, 8(5):383–387, May 2009.

[41] J. M. Taylor, P. Cappellaro, L. Childress, L. Jiang, D. Budker, P. R. Hemmer, A. Yacoby, R. Walsworth, and M. D. Lukin. High-sensitivity diamond magnetometer with nanoscale resolution. *Nature Physics*, 4(10):810–816, Oct 2008.

[42] J. R. Maze, P. L. Stanwix, J. S. Hodges, S. Hong, J. M. Taylor, P. Cappellaro, L. Jiang, M. V. Gurudev Dutt, E. Togan, A. S. Zibrov, A. Yacoby, R. L. Walsworth, and M. D. Lukin. Nanoscale magnetic sensing with an individual electronic spin in diamond. *Nature*, 455(7213):644–647, Oct 2008.

[43] P. Neumann, I. Jakobi, F. Dolde, C. Burk, R. Reuter, G. Waldherr, J. Honert, T. Wolf, A. Brunner, J. H. Shim, D. Suter, H. Sumiya, J. Isoya, and J. Wrachtrup. High-precision nanoscale temperature sensing using single defects in diamond. *Nano Letters*, 13(6):2738–2742, Jun 2013.

[44] G. Davies, M. F. Hamer, and William Charles Price. Optical studies of the 1.945 ev vibronic band in diamond. *Proceedings of the Royal Society of London. A. Mathematical and Physical Sciences*, 348(1653):285–298, 1976.

[45] R T Harley, M J Henderson, and R M Macfarlane. Persistent spectral hole burning of colour centres in diamond. *Journal of Physics C: Solid State Physics*, 17(8):L233–L236, mar 1984.

[46] N.R.S. Reddy, N.B. Manson, and E.R. Krausz. Two-laser spectral hole burning in a colour centre in diamond. *Journal of Luminescence*, 38(1):46 – 47, 1987.

[47] N.B. Manson and C. Wei. Transient hole burning in n-v centre in diamond. *Journal of Luminescence*, 58(1):158 – 160, 1994.

[48] A. Gruber, A. Dräbenstedt, C. Tietz, L. Fleury, J. Wrachtrup, and C. von Borczyskowski. Scanning confocal optical microscopy and magnetic resonance on single defect centers. *Science*, 276(5321):2012–2014, 1997.

[49] A. Dräbenstedt, L. Fleury, C. Tietz, F. Jelezko, S. Kilin, A. Nizovtzev, and J. Wrachtrup. Low-temperature microscopy and spectroscopy on single defect centers in diamond. *Phys. Rev. B*, 60:11503–11508, Oct 1999.

[50] Rosa Brouri, Alexios Beveratos, Jean-Philippe Poizat, and Philippe Grangier. Photon antibunching in the fluorescence of individual color centers in diamond. *Opt. Lett.*, 25(17):1294–1296, Sep 2000.

[51] Christian Kurtsiefer, Sonja Mayer, Patrick Zarda, and Harald Weinfurter. Stable solid-state source of single photons. *Phys. Rev. Lett.*, 85:290–293, Jul 2000.

[52] L. Childress, M. V. Gurudev Dutt, J. M. Taylor, A. S. Zibrov, F. Jelezko, J. Wrachtrup, P. R. Hemmer, and M. D. Lukin. Coherent dynamics of coupled electron and nuclear spin qubits in diamond. *Science*, 314(5797):281–285, 2006.

[53] E Togan, Y Chu, a S Trifonov, L Jiang, J Maze, L Childress, M V G Dutt, a S Sørensen, P R Hemmer, a S Zibrov, and M D Lukin. Quantum entanglement between an optical photon and a solid-state spin qubit. *Nature*, 466(7307):730–734, aug 2010.

[54] P. Neumann, R. Kolesov, B. Naydenov, J. Beck, F. Rempp, M. Steiner, V. Jacques, G. Balasubramanian, M. L. Markham, D. J. Twitchen, S. Pezzagna, J. Meijer, J. Twamley, F. Jelezko, and J. Wrachtrup. Quantum register based on coupled electron spins in a room-temperature solid. *Nature Physics*, 6(4):249–253, Apr 2010.

[55] Lucio Robledo, Lilian Childress, Hannes Bernien, Bas Hensen, Paul F. A. Alkemade, and Ronald Hanson. High-fidelity projective read-out of a solid-state spin quantum register. *Nature*, 477(7366):574–578, Sep 2011.

[56] P. C. Maurer, G. Kucsko, C. Latta, L. Jiang, N. Y. Yao, S. D. Bennett, F. Pastawski, D. Hunger, N. Chisholm, M. Markham, D. J. Twitchen, J. I. Cirac, and M. D. Lukin. Room-temperature quantum bit memory exceeding one second. *Science*, 336(6086):1283–1286, 2012.

[57] T. H. Taminiau, J. Cramer, T. van der Sar, V. V. Dobrovitski, and R. Hanson. Universal control and error correction in multi-qubit spin registers in diamond. *Nature Nanotechnology*, 9(3):171–176, Mar 2014.

[58] H. Bernien, B. Hensen, W. Pfaff, G. Koolstra, M. S. Blok, L. Robledo, T. H. Taminiau, M. Markham, D. J. Twitchen, L. Childress, and R. Hanson. Heralded entanglement between solid-state qubits separated by three metres. *Nature*, 497(7447):86–90, May 2013. Letter.

[59] B. Hensen, H. Bernien, A. E. Dreau, A. Reiserer, N. Kalb, M. S. Blok, J. Ruitenberg, R. F. L. Vermeulen, R. N. Schouten, C. Abellan, W. Amaya, V. Pruneri, M. W. Mitchell, M. Markham, D. J. Twitchen, D. Elkouss, S. Wehner, T. H. Taminiau, and R. Hanson. Loophole-free bell inequality violation using electron spins separated by 1.3 kilometres. *Nature*, 526(7575):682–686, Oct 2015. Letter.

[60] Netanel H. Lindner and Terry Rudolph. Proposal for pulsed on-demand sources of photonic cluster state strings. *Phys. Rev. Lett.*, 103:113602, Sep 2009.

[61] Donovan Buterakos, Edwin Barnes, and Sophia E. Economou. Deterministic generation of all-photonic quantum repeaters from solid-state emitters. *Phys. Rev. X*, 7:041023, Oct 2017.

[62] M. H. Devoret, A. Wallraff, and J. M. Martinis. Superconducting qubits: A short review, 2004.

[63] B.D. Josephson. Possible new effects in superconductive tunnelling. *Physics Letters*, 1(7):251 – 253, 1962.

[64] Jens Koch, Terri M. Yu, Jay Gambetta, A. A. Houck, D. I. Schuster, J. Majer, Alexandre Blais, M. H. Devoret, S. M. Girvin, and R. J. Schoelkopf. Charge-insensitive qubit design derived from the cooper pair box. *Phys. Rev. A*, 76:042319, Oct 2007.

[65] J. A. Schreier, A. A. Houck, Jens Koch, D. I. Schuster, B. R. Johnson, J. M. Chow, J. M. Gambetta, J. Majer, L. Frunzio, M. H. Devoret, S. M. Girvin, and R. J. Schoelkopf. Suppressing charge noise decoherence in superconducting charge qubits. *Phys. Rev. B*, 77:180502, May 2008.

[66] L. DiCarlo, M. D. Reed, L. Sun, B. R. Johnson, J. M. Chow, J. M. Gambetta, L. Frunzio, S. M. Girvin, M. H. Devoret, and R. J. Schoelkopf. Preparation and measurement of three-qubit entanglement in a superconducting circuit. *Nature*, 467(7315):574–578, Sep 2010.

[67] M. D. Reed, L. DiCarlo, S. E. Nigg, L. Sun, L. Frunzio, S. M. Girvin, and R. J. Schoelkopf. Realization of three-qubit quantum error correction with superconducting circuits. *Nature*, 482(7385):382–385, Feb 2012.

[68] J. E. Mooij, T. P. Orlando, L. Levitov, Lin Tian, Caspar H. van der Wal, and Seth Lloyd. Josephson persistent-current qubit. *Science*, 285(5430):1036–1039, 1999.

[69] T. P. Orlando, J. E. Mooij, Lin Tian, Caspar H. van der Wal, L. S. Levitov, Seth Lloyd, and J. J. Mazo. Superconducting persistent-current qubit. *Phys. Rev. B*, 60:15398–15413, Dec 1999.

[70] I. Chiorescu, Y. Nakamura, C. J. P. M. Harmans, and J. E. Mooij. Coherent quantum dynamics of a superconducting flux qubit. *Science*, 299(5614):1869–1871, 2003.

[71] J. Q. You, Xuedong Hu, S. Ashhab, and Franco Nori. Low-decoherence flux qubit. *Phys. Rev. B*, 75:140515, Apr 2007.

[72] Jonas Bylander, Simon Gustavsson, Fei Yan, Fumiki Yoshihara, Khalil Harrabi, George Fitch, David G. Cory, Yasunobu Nakamura, Jaw-Shen Tsai, and William D. Oliver. Noise spectroscopy through dynamical decoupling with a superconducting flux qubit. *Nature Physics*, 7(7):565–570, Jul 2011.

[73] Long B. Nguyen, Yen-Hsiang Lin, Aaron Somoroff, Raymond Mencia, Nicholas Grabon, and Vladimir E. Manucharyan. High-coherence fluxonium qubit. *Phys. Rev. X*, 9:041041, Nov 2019.

[74] N. E. Frattini, U. Vool, S. Shankar, A. Narla, K. M. Sliwa, and M. H. Devoret. 3-wave mixing josephson dipole element. *Applied Physics Letters*, 110(22):222603, 2017.

[75] N. E. Frattini, V. V. Sivak, A. Lingenfelter, S. Shankar, and M. H. Devoret. Optimizing the nonlinearity and dissipation of a snail parametric amplifier for dynamic range. *Phys. Rev. Applied*, 10:054020, Nov 2018.

[76] V.V. Sivak, N.E. Frattini, V.R. Joshi, A. Lingenfelter, S. Shankar, and M.H. Devoret. Kerr-free three-wave mixing in superconducting quantum circuits. *Phys. Rev. Applied*, 11:054060, May 2019.

[77] V. V. Sivak, S. Shankar, G. Liu, J. Aumentado, and M. H. Devoret. Josephson array mode parametric amplifier, 2019.

[78] T. Yamamoto, K. Inomata, M. Watanabe, K. Matsuba, T. Miyazaki, W. D. Oliver, Y. Nakamura, and J. S. Tsai. Flux-driven josephson parametric amplifier. *Applied Physics Letters*, 93(4):042510, 2008.

[79] Lafe Spietz, Kent Irwin, Minhyea Lee, and José Aumentado. Noise performance of lumped element direct current superconducting quantum interference device amplifiers in the 4–8 ghz range. *Applied Physics Letters*, 97(14):142502, 2010.

[80] J. Y. Mutus, T. C. White, E. Jeffrey, D. Sank, R. Barends, J. Bochmann, Yu Chen, Z. Chen, B. Chiaro, A. Dunsworth, J. Kelly, A. Megrant, C. Neill, P. J. J. O'Malley, P. Roushan, A. Vainsencher, J. Wenner, I. Siddiqi, R. Vijay, A. N. Cleland, and John M. Martinis. Design and characterization of a lumped element single-ended superconducting microwave parametric amplifier with on-chip flux bias line. *Applied Physics Letters*, 103(12):122602, 2013.

[81] X. Zhou, V. Schmitt, P. Bertet, D. Vion, W. Wustmann, V. Shumeiko, and D. Esteve. High-gain weakly nonlinear flux-modulated josephson parametric amplifier using a squid array. *Phys. Rev. B*, 89:214517, Jun 2014.

[82] O. Naaman, D. G. Ferguson, and R. J. Epstein. High saturation power josephson parametric amplifier with ghz bandwidth, 2017.

[83] N. Bergeal, F. Schackert, M. Metcalfe, R. Vijay, V. E. Manucharyan, L. Frunzio, D. E. Prober, R. J. Schoelkopf, S. M. Girvin, and M. H. Devoret. Phase-preserving amplification near the quantum limit with a josephson ring modulator. *Nature*, 465:64, May 2010.

[84] N. Bergeal, R. Vijay, V. E. Manucharyan, I. Siddiqi, R. J. Schoelkopf, S. M. Girvin, and M. H. Devoret. Analog information processing at the quantum limit with a josephson ring modulator. *Nature Physics*, 6:296, Feb 2010. Article.

[85] G. Liu, T.-C. Chien, X. Cao, O. Lanes, E. Alpern, D. Pekker, and M. Hatridge. Josephson parametric converter saturation and higher order effects. *Applied Physics Letters*, 111(20):202603, 2017.

[86] Baleegh Abdo, Flavius Schackert, Michael Hatridge, Chad Rigetti, and Michel Devoret. Josephson amplifier for qubit readout. *Applied Physics Letters*, 99(16):162506, 2011.

[87] Baleegh Abdo, Archana Kamal, and Michel Devoret. Nondegenerate three-wave mixing with the josephson ring modulator. *Phys. Rev. B*, 87:014508, Jan 2013.

[88] C. Macklin, K. O'Brien, D. Hover, M. E. Schwartz, V. Bolkhovsky, X. Zhang, W. D. Oliver, and I. Siddiqi. A near–quantum-limited josephson traveling-wave parametric amplifier. *Science*, 350(6258):307–310, 2015.

[89] T. C. White, J. Y. Mutus, I.-C. Hoi, R. Barends, B. Campbell, Yu Chen, Z. Chen, B. Chiaro, A. Dunsworth, E. Jeffrey, J. Kelly, A. Megrant, C. Neill, P. J. J. O'Malley, P. Roushan, D. Sank, A. Vainsencher, J. Wenner, S. Chaudhuri, J. Gao, and John M. Martinis. Traveling wave parametric amplifier with josephson junctions using minimal resonator phase matching. *Applied Physics Letters*, 106(24):242601, 2015.

[90] A. B. Zorin. Josephson traveling-wave parametric amplifier with three-wave mixing. *Phys. Rev. Applied*, 6:034006, Sep 2016.

[91] C. L. Kane and E. J. Mele. Quantum spin hall effect in graphene. *Phys. Rev. Lett.*, 95:226801, Nov 2005.

[92] B. Andrei Bernevig and Shou-Cheng Zhang. Quantum spin hall effect. *Phys. Rev. Lett.*, 96:106802, Mar 2006.

[93] Liang Fu and C. L. Kane. Topological insulators with inversion symmetry. *Phys. Rev. B*, 76:045302, Jul 2007.

[94] Andreas P. Schnyder, Shinsei Ryu, Akira Furusaki, and Andreas W. W. Ludwig. Classification of topological insulators and superconductors in three spatial dimensions. *Phys. Rev. B*, 78:195125, Nov 2008.

[95] Alexei Kitaev. Periodic table for topological insulators and superconductors. *AIP Conference Proceedings*, 1134(1):22–30, 2009.

[96] M. Z. Hasan and C. L. Kane. *Colloquium* : Topological insulators. *Rev. Mod. Phys.*, 82:3045–3067, Nov 2010.

[97] Markus König, Steffen Wiedmann, Christoph Brüne, Andreas Roth, Hartmut Buhmann, Laurens W. Molenkamp, Xiao-Liang Qi, and Shou-Cheng Zhang. Quantum spin hall insulator state in hgte quantum wells. *Science*, 318(5851):766–770, 2007.

[98] Chetan Nayak, Steven H. Simon, Ady Stern, Michael Freedman, and Sankar Das Sarma. Non-abelian anyons and topological quantum computation. *Rev. Mod. Phys.*, 80:1083–1159, Sep 2008.

[99] Faxian Xiu, Liang He, Yong Wang, Lina Cheng, Li-Te Chang, Murong Lang, Guan Huang, Xufeng Kou, Yi Zhou, Xiaowei Jiang, Zhigang Chen, Jin Zou, Alexandros Shailos, and Kang L. Wang. Manipulating surface states in topological insulator nanoribbons. *Nat Nano*, 6(4):216–221, Apr 2011.

[100] K. Nakayama, K. Eto, Y. Tanaka, T. Sato, S. Souma, T. Takahashi, Kouji Segawa, and Yoichi Ando. Manipulation of topological states and the bulk band gap using natural heterostructures of a topological insulator. *Phys. Rev. Lett.*, 109:236804, Dec 2012.

[101] A. R. Mellnik, J. S. Lee, A. Richardella, J. L. Grab, P. J. Mintun, M. H. Fischer, A. Vaezi, A. Manchon, E.-A. Kim, N. Samarth, and D. C. Ralph. Spin-transfer torque generated by a topological insulator. *Nature*, 511(7510):449–451, Jul 2014. Letter.

[102] F. D. M. Haldane and S. Raghu. Possible realization of directional optical waveguides in photonic crystals with broken time-reversal symmetry. *Phys. Rev. Lett.*, 100:013904, Jan 2008.

[103] Alexander B. Khanikaev, S. Hossein Mousavi, Wang-Kong Tse, Mehdi Kargarian, Allan H. MacDonald, and Gennady Shvets. Photonic topological insulators. *Nat Mater*, 12(3):233–239, Mar 2013.

[104] Ling Lu, Liang Fu, John D. Joannopoulos, and Marin Soljacic. Weyl points and line nodes in gyroid photonic crystals. *Nat Photon*, 7(4):294–299, Apr 2013.

[105] Scott A. Skirlo, Ling Lu, and Marin Soljačić. Multimode one-way waveguides of large chern numbers. *Phys. Rev. Lett.*, 113:113904, Sep 2014.

[106] Alexander Poddubny, Andrey Miroshnichenko, Alexey Slobozhanyuk, and Yuri Kivshar. Topological majorana states in zigzag chains of plasmonic nanoparticles. *ACS Photonics*, 1(2):101–105, 2014.

[107] Ling Lu, Chen Fang, Liang Fu, Steven G. Johnson, John D. Joannopoulos, and Marin Soljačić. Symmetry-protected topological photonic crystal in three dimensions. *Nature Physics*, 12(4):337–340, 2016.

[108] Sunkyu Yu, Xianji Piao, Jiho Hong, and Namkyoo Park. Metadisorder for designer light in random systems. *Science Advances*, 2(10), 2016.

[109] Stefano Longhi. Non-hermitian bidirectional robust transport. *Phys. Rev. B*, 95:014201, Jan 2017.

[110] Zheng Wang, Yidong Chong, J D Joannopoulos, and Marin Soljacić. Observation of unidirectional backscattering-immune topological electromagnetic states. *Nature*, 461(7265):772–5, 2009.

[111] M. Hafezi, S. Mittal, J. Fan, A. Migdall, and J. M. Taylor. Imaging topological edge states in silicon photonics. *Nat Photon*, 7(12):1001–1005, Dec 2013.

[112] Mikael C. Rechtsman, Julia M. Zeuner, Yonatan Plotnik, Yaakov Lumer, Daniel Podolsky, Felix Dreisow, Stefan Nolte, Mordechai Segev, and Alexander Szameit. Photonic floquet topological insulators. *Nature*, 496(7444):196–200, Apr 2013.

[113] Andrea Blanco-Redondo, Imanol Andonegui, Matthew J. Collins, Gal Harari, Yaakov Lumer, Mikael C. Rechtsman, Benjamin J. Eggleton, and Mordechai Segev. Topological optical waveguiding in silicon and the transition between topological and trivial defect states. *Phys. Rev. Lett.*, 116:163901, Apr 2016.

[114] Qingqing Cheng, Yiming Pan, Qianjin Wang, Tao Li, and Shining Zhu. Topologically protected interface mode in plasmonic waveguide arrays. *Laser & Photonics Reviews*, 9(4):392–398, 2015.

[115] Ivan S. Sinev, Ivan S. Mukhin, Alexey P. Slobozhanyuk, Alexander N. Poddubny, Andrey E. Miroshnichenko, Anton K. Samusev, and Yuri S. Kivshar. Mapping plasmonic topological states at the nanoscale. *Nanoscale*, 7(28):11904–11908, 2015.

[116] Weifeng Zhang, Xianfeng Chen, and Fangwei Ye. Plasmonic topological insulators for topological nanophotonics. *Opt. Lett.*, 42(20):4063–4066, Oct 2017.

[117] A. J. Heeger, S. Kivelson, J. R. Schrieffer, and W. P. Su. Solitons in conducting polymers. *Rev. Mod. Phys.*, 60:781–850, Jul 1988.

[118] W. P. Su, J. R. Schrieffer, and A. J. Heeger. Solitons in polyacetylene. *Phys. Rev. Lett.*, 42:1698–1701, Jun 1979.

[119] Felix Bleckmann, Zlata Cherpakova, Stefan Linden, and Andrea Alberti. Spectral imaging of topological edge states in plasmonic waveguide arrays. *Phys. Rev. B*, 96:045417, Jul 2017.

[120] Shaolin Ke, Bing Wang, Hua Long, Kai Wang, and Peixiang Lu. Topological edge modes in non-hermitian plasmonic waveguide arrays. *Opt. Express*, 25(10):11132–11143, May 2017.

[121] Marlan O. Scully and M. Suhail Zubairy. *Quantum Optics*. Cambridge University Press, 1997.

[122] C.W. Gardiner, C.W. Gardiner, and P. Zoller. *Quantum Noise: A Handbook of Markovian and Non-Markovian Quantum Stochastic Methods with Applications to Quantum Optics*. Springer series in synergetics. Springer, 2000.

[123] C.W. Gardiner. *Handbook of Stochastic Methods for Physics, Chemistry, and the Natural Sciences*. Springer complexity. Springer, 2004.

[124] Andrew J. Daley. Quantum trajectories and open many-body quantum systems. *Adv. Phys.*, 63(2):77–149, mar 2014.

[125] Klaus Mølmer, Yvan Castin, and Jean Dalibard. Monte carlo wave-function method in quantum optics. *J. Opt. Soc. Am. B*, 10(3):524–538, Mar 1993.

[126] N. Y. Yao, L. Jiang, A. V. Gorshkov, Z.-X. Gong, A. Zhai, L.-M. Duan, and M. D. Lukin. Robust quantum state transfer in random unpolarized spin chains. *Phys. Rev. Lett.*, 106:040505, Jan 2011.

[127] C. Cabrillo, J. I. Cirac, P. García-Fernández, and P. Zoller. Creation of entangled states of distant atoms by interference. *Phys. Rev. A*, 59:1025–1033, Feb 1999.

[128] S. Bose, P. L. Knight, M. B. Plenio, and V. Vedral. Proposal for teleportation of an atomic state via cavity decay. *Phys. Rev. Lett.*, 83:5158–5161, Dec 1999.

[129] L.-M. Duan, M. D. Lukin, J. I. Cirac, and P. Zoller. Long-distance quantum communication with atomic ensembles and linear optics. *Nature*, 414(6862):413–418, Nov 2001.

[130] Xun-Li Feng, Zhi-Ming Zhang, Xiang-Dong Li, Shang-Qing Gong, and Zhi-Zhan Xu. Entangling distant atoms by interference of polarized photons. *Phys. Rev. Lett.*, 90:217902, May 2003.

[131] Sean D. Barrett and Pieter Kok. Efficient high-fidelity quantum computation using matter qubits and linear optics. *Phys. Rev. A*, 71:060310, Jun 2005.

[132] Xu Bo Zou and W. Mathis. Conditional quantum phase gate using distant atoms and linear optics. *Phys. Rev. A*, 71:042334, Apr 2005.

[133] Yuan Liang Lim, Almut Beige, and Leong Chuan Kwek. Repeat-until-success linear optics distributed quantum computing. *Phys. Rev. Lett.*, 95:030505, Jul 2005.

[134] K. C. Lee, M. R. Sprague, B. J. Sussman, J. Nunn, N. K. Langford, X.-M. Jin, T. Champion, P. Michelberger, K. F. Reim, D. England, D. Jaksch, and I. A. Walmsley. Entangling macroscopic diamonds at room temperature. *Science*, 334(6060):1253–1256, 2011.

[135] W. Pfaff, B. J. Hensen, H. Bernien, S. B. van Dam, M. S. Blok, T. H. Taminiau, M. J. Tiggelman, R. N. Schouten, M. Markham, D. J. Twitchen, and R. Hanson. Unconditional quantum teleportation between distant solid-state quantum bits. *Science*, 345(6196):532–535, 2014.

[136] I. E. Protsenko, G. Reymond, N. Schlosser, and P. Grangier. Conditional quantum logic using two atomic qubits. *Phys. Rev. A*, 66:062306, Dec 2002.

[137] M. W. Doherty, N. B. Manson, P. Delaney, and L. C L Hollenberg. The negatively charged nitrogen-vacancy centre in diamond: The electronic solution. *New J. Phys.*, 13:025019, 2011.

[138] Marcus W. Doherty, Neil B. Manson, Paul Delaney, Fedor Jelezko, J??rg Wrachtrup, and Lloyd C L Hollenberg. The nitrogen-vacancy colour centre in diamond. *Phys. Rep.*, 528(1):1–45, 2013.

[139] Michał Horodecki, Paweł Horodecki, and Ryszard Horodecki. General teleportation channel, singlet fraction, and quasidistillation. *Phys. Rev. A*, 60:1888–1898, Sep 1999.

[140] Michael A Nielsen. A simple formula for the average gate fidelity of a quantum dynamical operation. *Physics Letters A*, 303(4):249 – 252, 2002.

[141] Michael A. Nielsen. Optical quantum computation using cluster states. *Phys. Rev. Lett.*, 93:040503, Jul 2004.

[142] S.C. Benjamin, B.W. Lovett, and J.M. Smith. Prospects for measurement-based quantum computing with solid state spins. *Laser & Photonics Reviews*, 3(6):556–574, 2009.

[143] Austin G. Fowler, Matteo Mariantoni, John M. Martinis, and Andrew N. Cleland. Surface codes: Towards practical large-scale quantum computation. *Phys. Rev. A*, 86:032324, Sep 2012.

[144] Earl T. Campbell, Barbara M. Terhal, and Christophe Vuillot. Roads towards fault-tolerant universal quantum computation. *Nature*, 549:172, Sep 2017.

[145] Audrius Alkauskas, Bob B Buckley, David D Awschalom, and Chris G Van de Walle. First-principles theory of the luminescence lineshape for the triplet transition in diamond nv centres. *New Journal of Physics*, 16(7):073026, 2014.

[146] A. Batalov, C. Zierl, T. Gaebel, P. Neumann, I.-Y. Chan, G. Balasubramanian, P. R. Hemmer, F. Jelezko, and J. Wrachtrup. Temporal coherence of photons emitted by single nitrogen-vacancy defect centers in diamond using optical rabi-oscillations. *Phys. Rev. Lett.*, 100:077401, Feb 2008.

[147] Michael J. Burek, Nathalie P. de Leon, Brendan J. Shields, Birgit J. M. Hausmann, Yiwen Chu, Qimin Quan, Alexander S. Zibrov, Hongkun Park, Mikhail D. Lukin, and Marko Lončar. Free-standing mechanical and photonic nanostructures in single-crystal diamond. *Nano Letters*, 12(12):6084–6089, 2012. PMID: 23163557.

[148] Peter Lodahl, Sahand Mahmoodian, and Soren Stobbe. Interfacing single photons and single quantum dots with photonic nanostructures. *Rev. Mod. Phys.*, 87(2):347–400, 2015.

[149] A. A. Clerk, M. H. Devoret, S. M. Girvin, Florian Marquardt, and R. J. Schoelkopf. Introduction to quantum noise, measurement, and amplification. *Rev. Mod. Phys.*, 82:1155–1208, Apr 2010.

[150] W. H. Louisell, A. Yariv, and A. E. Siegman. Quantum fluctuations and noise in parametric processes. i. *Phys. Rev.*, 124:1646–1654, Dec 1961.

[151] J. P. Gordon, W. H. Louisell, and L. R. Walker. Quantum fluctuations and noise in parametric processes. ii. *Phys. Rev.*, 129:481–485, Jan 1963.

[152] Carlton M. Caves. Quantum limits on noise in linear amplifiers. *Phys. Rev. D*, 26:1817–1839, Oct 1982.

[153] M. A. Castellanos-Beltran and K. W. Lehnert. Widely tunable parametric amplifier based on a superconducting quantum interference device array resonator. *Applied Physics Letters*, 91(8):083509, 2007.

[154] M. A. Castellanos-Beltran, K. D. Irwin, G. C. Hilton, L. R. Vale, and K. W. Lehnert. Amplification and squeezing of quantum noise with a tunable josephson metamaterial. *Nature Physics*, 4:929, Oct 2008.

[155] M. Hatridge, R. Vijay, D. H. Slichter, John Clarke, and I. Siddiqi. Dispersive magnetometry with a quantum limited squid parametric amplifier. *Phys. Rev. B*, 83:134501, Apr 2011.

[156] N. Roch, E. Flurin, F. Nguyen, P. Morfin, P. Campagne-Ibarcq, M. H. Devoret, and B. Huard. Widely tunable, nondegenerate three-wave mixing microwave device operating near the quantum limit. *Phys. Rev. Lett.*, 108:147701, Apr 2012.

[157] R. Vijay, D. H. Slichter, and I. Siddiqi. Observation of quantum jumps in a superconducting artificial atom. *Phys. Rev. Lett.*, 106:110502, Mar 2011.

[158] J. E. Johnson, C. Macklin, D. H. Slichter, R. Vijay, E. B. Weingarten, John Clarke, and I. Siddiqi. Heralded state preparation in a superconducting qubit. *Phys. Rev. Lett.*, 109:050506, Aug 2012.

[159] C. Eichler, D. Bozyigit, and A. Wallraff. Characterizing quantum microwave radiation and its entanglement with superconducting qubits using linear detectors. *Phys. Rev. A*, 86:032106, Sep 2012.

[160] A. Metelmann and A. A. Clerk. Quantum-limited amplification via reservoir engineering. *Phys. Rev. Lett.*, 112:133904, Apr 2014.

[161] Lafe Spietz, Kent Irwin, and José Aumentado. Superconducting quantum interference device amplifiers with over 27 ghz of gain-bandwidth product operated in the 4–8 ghz frequency range. *Applied Physics Letters*, 95(9):092505, 2009.

[162] T. C. Chien, O. Lanes, C. Liu, X. Cao, P. Lu, S. Motz, G. Liu, D. Pekker, and M. Hatridge. Multiparametric amplification and qubit measurement with a kerr-free josephson ring modulator, 2019.

[163] A. Metelmann and A. A. Clerk. Nonreciprocal photon transmission and amplification via reservoir engineering. *Phys. Rev. X*, 5:021025, Jun 2015.

[164] Q. Zhong, S. K. Ozdemir, A. Eisfeld, A. Metelmann, and R. El-Ganainy. Exceptional points-based optical amplifiers, 2019.

[165] Archana Kamal, Adam Marblestone, and Michel Devoret. Signal-to-pump back action and self-oscillation in double-pump josephson parametric amplifier. *Phys. Rev. B*, 79:184301, May 2009.

[166] Christopher Eichler and Andreas Wallraff. Controlling the dynamic range of a josephson parametric amplifier. *EPJ Quantum Technology*, 1(1):2, Jan 2014.

[167] Bogdan A. Kochetov and Arkady Fedorov. Higher-order nonlinear effects in a josephson parametric amplifier. *Phys. Rev. B*, 92:224304, Dec 2015.

[168] Ananda Roy and Michel Devoret. Quantum-limited parametric amplification with josephson circuits in the regime of pump depletion. *Phys. Rev. B*, 98:045405, Jul 2018.

[169] D.M. Pozar. *Microwave Engineering, 4th Edition*. Wiley, 2011.

[170] Saeed Khan, A. Metelmann, and Hakan Türeci. Quantum nonlinear dynamics of nondegenerate parametric amplification beyond the stiff-pump approximation. In *APS March Meeting Abstracts*, Jan 2019.

[171] Leonardo Ranzani and José Aumentado. Graph-based analysis of nonreciprocity in coupled-mode systems. *New Journal of Physics*, 17(2):023024, feb 2015.

[172] K. M. Sliwa, M. Hatridge, A. Narla, S. Shankar, L. Frunzio, R. J. Schoelkopf, and M. H. Devoret. Reconfigurable josephson circulator/directional amplifier. *Phys. Rev. X*, 5:041020, Nov 2015.

[173] Y. Nakamura, Yu. A. Pashkin, and J. S. Tsai. Coherent control of macroscopic quantum states in a single-cooper-pair box. *Nature*, 398(6730):786–788, Apr 1999.

[174] D. Vion, A. Aassime, A. Cottet, P. Joyez, H. Pothier, C. Urbina, D. Esteve, and M. H. Devoret. Manipulating the quantum state of an electrical circuit. *Science*, 296(5569):886–889, 2002.

[175] John M. Martinis, S. Nam, J. Aumentado, and C. Urbina. Rabi oscillations in a large josephson-junction qubit. *Phys. Rev. Lett.*, 89:117901, Aug 2002.

[176] Morten Kjaergaard, Mollie E. Schwartz, Jochen Braumüller, Philip Krantz, Joel I.-J. Wang, Simon Gustavsson, and William D. Oliver. Superconducting qubits: Current state of play. *Annual Review of Condensed Matter Physics*, 11(1):369–395, 2020.

[177] Yuriy Makhlin, Gerd Schön, and Alexander Shnirman. Quantum-state engineering with josephson-junction devices. *Rev. Mod. Phys.*, 73:357–400, May 2001.

[178] I. Chiorescu, P. Bertet, K. Semba, Y. Nakamura, C. J. P. M. Harmans, and J. E. Mooij. Coherent dynamics of a flux qubit coupled to a harmonic oscillator. *Nature*, 431(7005):159–162, Sep 2004.

[179] A. Wallraff, D. I. Schuster, A. Blais, L. Frunzio, R.-. S. Huang, J. Majer, S. Kumar, S. M. Girvin, and R. J. Schoelkopf. Strong coupling of a single photon to a superconducting qubit using circuit quantum electrodynamics. *Nature*, 431(7005):162–167, Sep 2004.

[180] J. Johansson, S. Saito, T. Meno, H. Nakano, M. Ueda, K. Semba, and H. Takayanagi. Vacuum rabi oscillations in a macroscopic superconducting qubit *lc* oscillator system. *Phys. Rev. Lett.*, 96:127006, Mar 2006.

[181] D. I. Schuster, A. A. Houck, J. A. Schreier, A. Wallraff, J. M. Gambetta, A. Blais, L. Frunzio, J. Majer, B. Johnson, M. H. Devoret, S. M. Girvin, and R. J. Schoelkopf. Resolving photon number states in a superconducting circuit. *Nature*, 445(7127):515–518, Feb 2007.

[182] S M Girvin, M H Devoret, and R J Schoelkopf. Circuit QED and engineering charge-based superconducting qubits. *Physica Scripta*, T137:014012, dec 2009.

[183] S. M. Girvin. *Circuit QED: superconducting qubits coupled to microwave photons.* Oxford University Press, 2014.

[184] Noriyuki Hatakenaka and Susumu Kurihara. Josephson cascade micromaser. *Phys. Rev. A*, 54:1729–1732, Aug 1996.

[185] P. Barbara, A. B. Cawthorne, S. V. Shitov, and C. J. Lobb. Stimulated emission and amplification in josephson junction arrays. *Phys. Rev. Lett.*, 82:1963–1966, Mar 1999.

[186] E. Il'ichev, N. Oukhanski, A. Izmalkov, Th. Wagner, M. Grajcar, H.-G. Meyer, A. Yu. Smirnov, Alec Maassen van den Brink, M. H. S. Amin, and A. M. Zagoskin. Continuous monitoring of rabi oscillations in a josephson flux qubit. *Phys. Rev. Lett.*, 91:097906, Aug 2003.

[187] L. Ozyuzer, A. E. Koshelev, C. Kurter, N. Gopalsami, Q. Li, M. Tachiki, K. Kadowaki, T. Yamamoto, H. Minami, H. Yamaguchi, T. Tachiki, K. E. Gray, W.-K. Kwok, and U. Welp. Emission of coherent thz radiation from superconductors. *Science*, 318(5854):1291–1293, 2007.

[188] D. A. Rodrigues, J. Imbers, and A. D. Armour. Quantum dynamics of a resonator driven by a superconducting single-electron transistor: A solid-state analogue of the micromaser. *Phys. Rev. Lett.*, 98:067204, Feb 2007.

[189] Julian Hauss, Arkady Fedorov, Carsten Hutter, Alexander Shnirman, and Gerd Schön. Single-qubit lasing and cooling at the rabi frequency. *Phys. Rev. Lett.*, 100:037003, Jan 2008.

[190] S Ashhab, J R Johansson, A M Zagoskin, and Franco Nori. Single-artificial-atom lasing using a voltage-biased superconducting charge qubit. *New Journal of Physics*, 11(2):023030, feb 2009.

[191] M. C. Cassidy, A. Bruno, S. Rubbert, M. Irfan, J. Kammhuber, R. N. Schouten, A. R. Akhmerov, and L. P. Kouwenhoven. Demonstration of an ac josephson junction laser. *Science*, 355(6328):939–942, 2017.

[192] Steven H. Simon and Nigel R. Cooper. Theory of the josephson junction laser. *Phys. Rev. Lett.*, 121:027004, Jul 2018.

[193] J. Q. You, Yu-xi Liu, C. P. Sun, and Franco Nori. Persistent single-photon production by tunable on-chip micromaser with a superconducting quantum circuit. *Phys. Rev. B*, 75:104516, Mar 2007.

[194] O. Astafiev, K. Inomata, A. O. Niskanen, T. Yamamoto, Yu. A. Pashkin, Y. Nakamura, and J. S. Tsai. Single artificial-atom lasing. *Nature*, 449(7162):588–590, Oct 2007.

[195] Fei Chen, Juliang Li, A. D. Armour, E. Brahimi, Joel Stettenheim, A. J. Sirois, R. W. Simmonds, M. P. Blencowe, and A. J. Rimberg. Realization of a single-cooper-pair josephson laser. *Phys. Rev. B*, 90:020506, Jul 2014.

[196] C. Rolland, A. Peugeot, S. Dambach, M. Westig, B. Kubala, Y. Mukharsky, C. Altimiras, H. le Sueur, P. Joyez, D. Vion, P. Roche, D. Esteve, J. Ankerhold, and F. Portier. Antibunched photons emitted by a dc-biased josephson junction. *Phys. Rev. Lett.*, 122:186804, May 2019.

[197] H. M. Wiseman. Light amplification without stimulated emission: Beyond the standard quantum limit to the laser linewidth. *Phys. Rev. A*, 60:4083–4093, Nov 1999.

[198] Leonard Susskind and Jonathan Glogower. Quantum mechanical phase and time operator. *Physics Physique Fizika*, 1:49–61, Jul 1964.

[199] M. Sargent, M.O. Scully, and W.E. Lamb. *Laser Physics*. Advanced book program. Addison-Wesley, 1974.

[200] S.M. Barnett, S. Stenholm, and D.T. Pegg. A new approach to optical phase diffusion. *Optics Communications*, 73(4):314 – 318, 1989.

[201] Daniel K. L. Oi, Václav Potoček, and John Jeffers. Nondemolition measurement of the vacuum state or its complement. *Phys. Rev. Lett.*, 110:210504, May 2013.

[202] Luke C G Govia, Emily J Pritchett, and Frank K Wilhelm. Generating nonclassical states from classical radiation by subtraction measurements. *New Journal of Physics*, 16(4):045011, apr 2014.

[203] Serge Rosenblum, Orel Bechler, Itay Shomroni, Yulia Lovsky, Gabriel Guendelman, and Barak Dayan. Extraction of a single photon from an optical pulse. *Nature Photonics*, 10(1):19–22, Jan 2016.

[204] Mark Um, Junhua Zhang, Dingshun Lv, Yao Lu, Shuoming An, Jing-Ning Zhang, Hyunchul Nha, M. S. Kim, and Kihwan Kim. Phonon arithmetic in a trapped ion system. *Nature Communications*, 7(1):11410, Apr 2016.

[205] Jennifer C J Radtke, Daniel K L Oi, and John Jeffers. Linear quantum optical bare raising operator. *Journal of Physics B: Atomic, Molecular and Optical Physics*, 50(21):215501, oct 2017.

[206] A. A. Clerk, M. H. Devoret, S. M. Girvin, Florian Marquardt, and R. J. Schoelkopf. Introduction to quantum noise, measurement, and amplification. *Rev. Mod. Phys.*, 82:1155–1208, Apr 2010.

[207] A. Taflove and S.C. Hagness. *Computational Electrodynamics: The Finite-difference Time-domain Method*. Artech House antennas and propagation library. Artech House, 2005.

[208] A.Z. Elsherbeni and V. Demir. *The Finite-difference Time-domain Method for Electromagnetics with MATLAB Simulations*. SciTech Pub., 2009.

[209] A. Taflove, A. Oskooi, and S.G. Johnson. *Advances in FDTD Computational Electrodynamics: Photonics and Nanotechnology*. Artech House antennas and propagation library. Artech House, 2013.

[210] John. D. Jackson. *Classical Electrodynamics*. John Wiley, 3rd edition, 1998.

[211] Yee. Kane. Numerical solution of initial boundary value problems involving maxwell's equations in isotropic media. *IEEE Transactions on Antennas and Propagation*, 14(3):302–307, 1966.

[212] W. Huang, C. Xu, S. T. Chu, and S. K. Chaudhuri. The finite-difference vector beam propagation method: analysis and assessment. *Journal of Lightwave Technology*, 10(3):295–305, Mar 1992.

[213] W. P. Huang and C. L. Xu. Simulation of three-dimensional optical waveguides by a full-vector beam propagation method. *IEEE Journal of Quantum Electronics*, 29(10):2639–2649, Oct 1993.

[214] M. V. Berry. Quantal phase factors accompanying adiabatic changes. *Proc. R. Soc. Lond. A*, 392(1802):45–57, 1984.

[215] J. Zak. Berry's phase for energy bands in solids. *Phys. Rev. Lett.*, 62:2747–2750, Jun 1989.

[216] M. F. Atiyah and I. M. Singer. The index of elliptic operators: I. *Annals of Mathematics*, 87(3):484–530, 1968.

[217] Xiao Yi. Note on the electron-hole symmetry breaking of the energy band structure of polyacetylene. *Communications in Theoretical Physics*, 14(2):209, 1990.

[218] Z. J. Li, Z. An, K. L. Yao, and Z. G. Li. Effects of the second and third neighbor hopping interactions on the electronic states of soliton in polyacetylene. *Zeitschrift für Physik B Condensed Matter*, 92(2):195–197, 1993.

[219] Linhu Li, Zhihao Xu, and Shu Chen. Topological phases of generalized su-schrieffer-heeger models. *Phys. Rev. B*, 89:085111, Feb 2014.

[220] Brajesh Narayan. End modes in arrays of modulated su–schrieffer–heeger chains. *Pramana*, 87(2):25, 2016.